Endoscopic Cheap Optical Transducers (CHOTs) for On-Wing Ultrasonic Inspection

by Victoria Ageeva, MSc, BSc

Thesis submitted to The University of Nottingham
for the degree of Doctor of Philosophy, March 2016

Abstract

The instrumentation and the developments presented in this thesis aim to address the challenges associated with in-service non-destructive testing of aeroengine components, imposed by severe restrictions on component accessibility.

In-service non-destructive testing (NDT) is essential to ensure early detection of service-induced damage and prevent catastrophic failures of such safety-critical aeroengine components as turbine/compressor blades and disks, increasing the safety of operations and dramatically reducing the cost of engine changes. The main concern during their inspection is detection of fatigue cracking, typically initiated on the surface of the part. The application of inspection techniques used during overhaul to on-wing testing is restricted both by the complex, spatially-confined access to the components and the inaccessibility of the high-stress concentration surfaces in the full engine assembly. Two routinely-used techniques providing a solution to these challenges are the use of endoscopes for access and surface acoustic waves to inspect parts of the assembly.

CHOTs are optically-activated ultrasonic transducers located on the surface of a sample, that use laser illumination to remotely generate and detect ultrasound, providing a non-contact wireless alternative to conventional piezoelectric transducers (PZTs). The benefits of optical activation are paired with fibre-optic light delivery in an endoscopic pulser – a simple portable ultrasonic inspection system with flexible instrumentation, beneficial for testing hard-to-reach components in locations with limited access or hazardous environments.

This thesis presents the instrumentation of the endoscopic pulser and the development of the self-adhesive portable CHOTs (SA CHOTs) to complement its potential field application by enabling transducer delivery to components in-service and application to large and curved parts, previously limited by laboratory-based direct on-sample CHOT fabrication. The developed transducers overcome frequent barriers for industrial adaptation of fully-optical inspection systems presented by the sample surface conditions such as reflectivity and roughness. The NDT capabilities of the CHOTs endoscopic pulser are demonstrated by performing detection of machined slots on controlled aluminium samples and representative industrial parts using 4–5 MHz surface acoustic waves. System capabilities for active structural health monitoring (SHM) as well as inspection of samples in motion are demonstrated.

Although in its present configuration the size of the endoscope exceeds practical access requirements, the potential of the system for further development and miniaturisation is discussed.

Acknowledgements

With the conclusion of my work come both feelings of achievement and relief as well as a heartfelt gratitude to all those without whom I would not have had the courage to undertake this journey, those who inspired and supported me not only during but also long before it began.

First and foremost, I owe my deepest gratitude to my supervisor Professor Matthew Clark for his extraordinary support and guidance that helped to shape my research, and without whose imagination, big heart, selflessness and wit the Applied Optics Group and my time with it would not have been the same.

My research would not have been possible without the Dorothy Hodgkin Postgraduate Award, and I would like to gratefully acknowledge the funding received towards my PhD from the University of Nottingham and Rolls-Royce plc, and thank them for the opportunity it gave me.

My sincere thanks goes to Professor Michael G Somekh and Assistant Professor Steve Sharples for their advice and feedback, Mr. David C Wright from Rolls-Royce plc. for the endless supply of ideas and challenges during this project, and Dr Theodosia Stratoudaki for supervision and practical guidance with laser ultrasonics. A special thank you goes to Dr Richard J Smith for stepping in at the most critical stage to oversee the conclusion of my work, for discussions and encouragement, and for his time spent fighting my use of articles.

I would like to thank the other members of the Applied Optics Group and the university staff, in particular my colleagues Fernando, Leo and Rikesh for the shared expertise and friendship, and Ms Lihua Sun for her brilliant work and the friendly support she has given me.

I am profoundly grateful to Professor Valentin Kozintsev from BMSTU for his counsel and guidance at the start of my academic career, and would also like to acknowledge my outstanding school teachers Dmitry Malinovsky and Taisia Komarova whose enthusiasm and high standards inspired my academic confidence and competitive drive.

My most heartfelt thanks go to my family – my parents Marina and Sergey whose love and support have enabled me to succeed, and my husband Tam who survived the writing up period, sacrificing our living room and social life, and has been the source of strength throughout the years in all my endeavours (which must require endless patience) and never stopped encouraging me to boldly go wherever my dreams take me.

This has been a time of an immense personal growth, sustained effort, absolute frustration and equal rewards, and I am thankful you were all there to share it with me.

Contents

List of Figures

Chapter 1

Introduction

The work presented in this thesis aims to address the challenges of in-situ non-destructive testing (NDT) of aeroengine components. This is achieved by using cheap optical transducers (CHOTs) in combination with fibre-optic operation in an all-optical non-contact ultrasonic inspection system with flexible instrumentation.

Developed at the Applied Optics Group, the University of Nottingham, CHOTs [1] allow non-contact remote generation and detection of ultrasound using laser illumination, and are characterised by a simple and compact optical arrangement with environmentally-robust operation.

The work presented covers four areas associated with the development of the practical inspection system for the target application: the endoscopic instrumentation, the fabrication/application of the transducers to the test parts, characterisation of their performance and demonstration of the NDT capabilities using surface acoustic waves (SAWs) and representative aeroengine components. Although discussed within the aerospace context, the application of the endoscopic pulser and the portable CHOTs developed in this work can be extended to NDT in other challenging applications requiring inspection of safety-critical components with spatially-confined or complex access paths, or located in hazardous environments, such as the nuclear industry.

1.1 Ensuring airworthiness in aerospace

An aircraft represents a complex system composed of a multitude of parts, with over thirty five thousand components in the engine alone. The industrial requirements for current and next generation aircraft are driven by the demand for more time- and cost-efficient operation and minimisation of the industrial environmental impact, with targets to reduce emission levels by 75–90% and noise by 65% by the year 2050. These, combined with the desired reduction of fuel consumption and

provision of more flights place increasing demands on the components of aeroengines, pushing their operation to increasingly-higher temperatures and cyclic loading.

Extensive maintenance is required to prevent operational and/or catastrophic failures due to service-induced damage or wear of the safety-critical components. Preventative maintenance consists of the scheduled regular inspections and downtime of the aircraft for overhaul as well as the use of non-destructive testing and active structural health monitoring while in-service.

The structural integrity of the turbine and compressor blades of an aeroengine, subjected to extreme temperatures and stresses and prone to fatigue and stress-corrosion cracking, is of primary concern as their failure has catastrophic consequences for the integrity of the whole engine. It is advantageous to perform repetitive monitoring of the engine components while it remains in service to provide early-stage damage detection independent of the scheduled overhaul. In this case an assessment can be made as to whether the engine can continue service, continue with more frequent checks or the part should be removed. Such inspections dramatically reduce the cost of engine changes due to suspected damage and premature removal of acceptable parts according to the maintenance schedule based on the component life-time. The requirements for lower operation costs, including the reduction of time and cost of in-service operations without impairing passenger safety, create the need for testing methods and instrumentation able to provide reliable, real-time on-wing inspection.

The conventional inspection practices employed in aerospace NDT and the challenges of their application for in-situ aeroengine testing are outlined below.

1.1.1 Conventional inspection practices for non-destructive testing

The purpose of non-destructive testing in aerospace, described in the Aviation Maintenance Technician Handbook [2], is 'to determine the airworthiness of a component without damaging it'. The frequency and type of inspection with the description of specific testing procedures are provided by the aeronautical publications that guide the operation, maintenance and repair of the aircraft and its components, including the manufacturer's service bulletins and manuals, FAA (US) and CAA (UK) regulations, airworthiness directives and advisory circulars. A brief description of the most common techniques employed in aerospace NDT is presented below, their detailed description can be found in [2–4] and an overview of future development trends in [5].

Visual inspection

Visual inspection consists of the direct observation of the inspected area in bright light with the naked eye or by using a magnifying glass or a mirror. Although it is the cheapest method, which

constitutes around 80% of performed inspections, the detection capability is limited to surface defects which are big enough to be visually identified.

Liquid penetrant inspection

The penetrant inspection method is based on the application of a liquid penetrant (paint, fluorescent dye) to a thoroughly-cleaned surface of the sample where it enters and fills any defects open to the surface. After the excess penetrant is removed and the surface is dried, the application of the developer draws out the dye to reveal the presence of the flaws. The use of this technique enhances visible contrast of surface defects (by colour contrast or fluorescence) that can be missed during a simple visual inspection. The inspection is limited to non-porous materials and detection of surface flaws. It requires surface preparation and is time consuming.

Magnetic particle inspection

Magnetic particle inspection requires ferromagnetic materials and magnetisation of the test part. The ferromagnetic particles applied to the surface of the magnetised test component become trapped in the areas of the magnetic flux leakage produced by the flaw. The shape and location of the near-surface defects is indicated with this method, including detection of flaws not open to the surface. Surface cleaning and visual observations are required as well as the demagnetisation of the inspected component after the test.

Eddy current testing

This method requires electrically-conducting samples and can be used to detect surface and subsurface defects, and can operate through coatings. The alternating current in the coil of the probe produces a changing magnetic field that, when placed in close proximity to the sample, induces the circular flow of eddy currents on and below the surface. The interaction of the secondary magnetic field produced by the eddy currents with the field of the probe changes the impedance of the coil and can be measured as a change of voltage. The presence of the defects interrupts the flow of eddy currents affecting the measured output. This method does not require surface preparation and can be non-contact.

Ultrasonic testing

Ultrasonic testing consists of observation and analysis of the transmitted or reflected high-frequency sound waves originated in or sent through a structure. The changes experienced by the propagating wave and observed in the detected signal are indicative of the material condition and discontinuities

present in the propagation medium. This is a very versatile method without specific requirements to the material properties or surface condition. It can be used for the inspection of surface and bulk material, including detection of flaws, dimensional measurements and material characterisation. The conventional techniques require a good contact with the sample and the use of couplants such as oil or gel to introduce the wave into the structure.

Radiography

The radiographic techniques are based on the differential absorption of penetrating γ- or X-ray radiation in the sample or their assembly. The differences in thickness, density, shapes and absorption characteristics are displayed as a variation of contrast in the image created by the unabsorbed radiation that passes through the part. The image is recorded on film or fluorescent screens and represents a planar projection. It is an expensive method with associated health hazards. It is used predominantly to detect cracks along the axis of the ray but not planar defects. The use of *computed tomography* produces cross-sectional sample views which allows the location and measurement of flaws within the structure independent of their orientation.

Thermography

The thermal and infrared methods are based on obtaining an image of the temperature distribution on the surface of the test part (in a steady state) or the measurement of the infrared emission from the surface when a temperature gradient is created by the application of a pulsed heat source. The presence of the defects is indicated by the non-uniformities in the detected distributions.

Laser-based methods

- *Digital holography* creates a three-dimensional image of the test part using interference of the reference laser beam with the beam scattered from the component. The reconstructed image can be superimposed onto the test part producing interference fringes in the locations with displacement deviations from the original recording.
- *Shearography* is a variation of the holographic method that includes stressing of the component between multiple image exposures to increase sensitivity. This method provides remote full field inspection and is often used on composite materials.
- *Laser ultrasonics* uses laser beams to remotely generate and detect ultrasound. The generation is achieved via optical absorption and the thermoelastic effect, with detection frequently employing interferometric techniques. The use of lasers is fully remote, allows operation on a variety of materials and fast scanning of large areas. The main advantages over the contact

ultrasonic alternative is the absence of a couplant (remoteness) and the ability to operate with complex geometries.

Practical considerations

Some of the main factors underlying the choice of a particular inspection method are the critical nature of the component, the type and possible location/orientation of the defect, the material and part accessibility. The simplicity and sensitivity of the techniques range from simple flaw indication/detection to full measurement and characterisation, with some suitable for field applications, and others necessitating part removal and complete disassembly.

From the description above, it can be seen that most techniques require parts to be accessible for close visual examination or contact, and some degree of surface preparation (e.g. cleaning, oiling, magnetisation, or heating). Additional restrictions are placed on operational materials (conducting, ferroelectric, or non-porous) and orientation of the flaws. Some methods may be time-consuming and impractical in confined spaces, or expensive and hazardous. Whereas some (such as visual, penetrant, eddy current) are highly-portable and can be used in-situ for inspection of internal areas, others, such as radiography, allow inspection of the entire engine or the airframe without disassembly.

The FAA advisory circular 43.13-1B [3] gives a brief description of the most common types of flaws required to be detected, classified as corrosion, inherent flaws, primary and secondary processing or finishing flaws, and the flaws developed in-service. The last group of defects is formed during aircraft/aeroengine service due to the ageing effects of time, flight cycles and operation conditions.

Current aircraft mostly use metallic and composite materials, with additive-layer-manufactured (ALM) parts entering service in the near future. The main consideration for composite materials used in the skin and wings of an aircraft is the detection of delaminations, disbonds and impact damage. The major concern with metallic parts of the aeroengine is metal fatigue, associated with cyclic loading, and corrosion. The stresses produced by repeated application and removal of load cycles (take offs and landings) result in the initiation and growth of cracks in the highly-stressed areas until their eventual fracture. Early detection of fatigue cracking is therefore a primary aim of inspection. Although written more than forty years ago, the review by J.R. Barton and F.N. Kusenberger [6] provides a comprehensive description of the inspection practices employed for testing of the aeroengine turbines with regard to fatigue damage detection.

The on-site application of the techniques is typically manual, time- and labour-consuming. To address this, continuous efforts have been directed towards greater automation and the use of robotic and crawling systems for on-site inspections [7, 8]. Some examples include the multifunc-

tion automated crawling system (MACS) [9], able to deliver a range of NDT techniques on-site, and the current MIRoR project at the University of Nottingham targeting the development of a miniaturised robot to perform inspection and repairs within hazardous environments or industrial confined spaces, such as aeroengines. Owing to their non-contact nature and ability for fast inspection of large areas and parts of complex geometry, automated laser-ultrasonic scanning systems have been increasingly applied to inspection of composite materials [10]. One example is a laser-ultrasonic inspection system LUIS [11] for automated inspection of wing and fuselage panels.

1.1.2 On-wing testing of the aeroengine assembly

A typical gas turbine engine consists of the fan section providing the air intake, the compressor section pressurising the air, the combustion section burning the air/fuel mixture, and the turbine section driven by the expanded gas to rotate the fan and compressor and provide thrust through the exhaust. Each section includes a series of pressure stages consisting of consequent pairs of rotor blades and stator vanes attached to the rotor and stator disks. These are connected to the rotating shafts or the outer casing. A simplified diagram illustrating the internal layout and component arrangement in the assembled engine is presented in figure 1.1. The extreme operational conditions of the aeroengine blades at temperatures reaching $1,600$ °C and rotation speeds of up to $10,000$ rpm (high-pressure turbine) necessitate the use of advanced material alloys (Ti, Ni superalloys) and complex blade designs to enable cooling, as well as regular monitoring of their structural integrity.

The airworthiness of an aeroengine and its components is assured by a combination of the following inspections:

- *Scheduled inspections* are part of the maintenance schedule based on engine cycles or flight time, running alongside the general aircraft maintenance. These are performed during overhaul and include full disassembly to detect, repair or replace damaged parts, using visual, structural NDT and dimensional testing.

- *Non-scheduled inspections* are performed to assess the damage by foreign objects or part/engine serviceability after the exceedance of the maximum power or operational temperature limits, to diagnose the cause of defects.

- *Special inspections* are performed as the engine continues in service to monitor potential problem areas/components highlighted by the regular or overhaul inspections.

The requirements for the NDT techniques used to detect fatigue damage in-situ are similar to the methods used at overhaul but with severe restrictions imposed by component accessibility. The increased complexity of engine designs to satisfy the demanded performance requirements presents

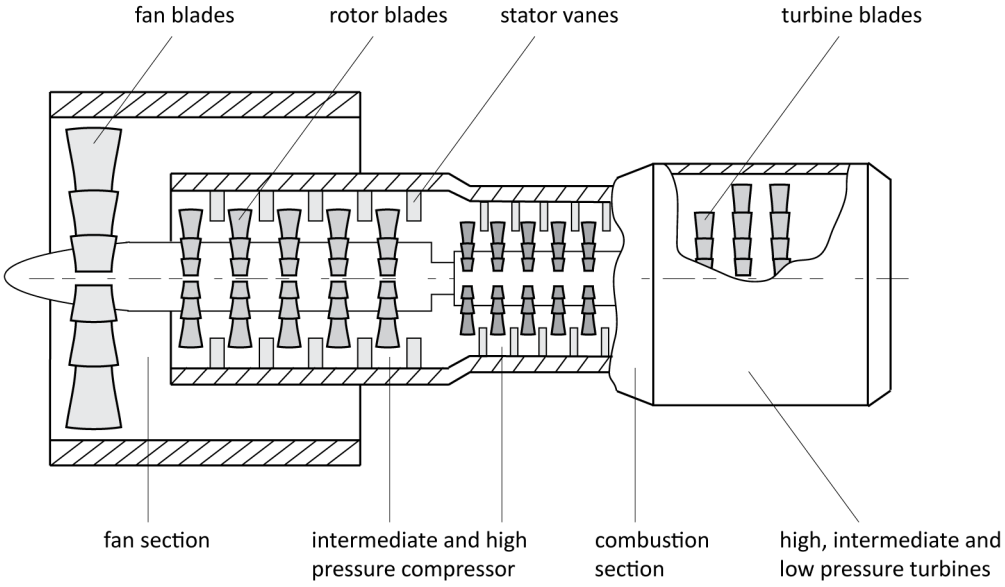

Figure 1.1: Schematic diagram illustrating the internal layout and test geometry of a typical turbofan gas turbine engine in cross section (stator vanes – only single element shown for clarity).

a challenge for in-situ inspections and contributes to their ongoing development. A large number of parts located in close proximity and in multiple stages (e.g. 16 stages in the compressor section, 68 turbine blades), often inaccessible within the assembly, are required to be inspected in confined spaces and via complex access paths.

A typical solution routinely used with visual inspection and even repairs of compressors, combustion sections and turbines is the use of the endoscopes (borescopes and fibrescopes) allowing navigation to the test part and inspection of internal areas of the engine otherwise inaccessible without extensive disassembly. The endoscopes can use optical fibres or cameras to transmit the image, have light sources, articulation, and interchangeable tools for repair. Their use enables the determination of the airworthiness of hard-to-reach components in the engine installed in service, thereby decreasing the time and cost of inspection and the downtime of the aircraft. In 1998 the on-wing use of the blending borescope inspection system (Pratt & Whitney) combining visual inspection and repair tools was estimated to provide cost savings of $\$360,000$ per engine (or $\$19,440,000$ per year) compared to the teardown cost [12]. On older aircraft the hot section of turbine engines could be accessed via the hole from the removed igniter, whereas modern designs provide specially-installed inspection ports at a number of locations in the casings for access to the rotating and combustion sections of the engine. The rotating shafts can be additionally turned into the desired position either manually or by using an air-driven motor for the ease of inspection.

Providing a solution to the access challenges, the use of borescopes is being increasingly combined with other NDT techniques such as dye penetrant [13] and eddy current [14] testing to expand in-situ inspection capabilities. The use of in-situ testing methods is however largely limited to the techniques requiring direct surface access and visual inspection.

The common service-induced defects of aeroengine blades are stress-corrosion, overstress and fatigue cracks, primarily initiated on the surface of the part, and in such high-stress concentration areas as the fillet radius of a blade dovetail. These areas are inaccessible for direct surface inspection on-wing as their surfaces are partially obstructed by other parts of the assembly. Figure 1.2 illustrates the typical geometry of the blade/disk assembly and the associated inspection challenges.

The use of ultrasonic techniques, in particular surface acoustic waves, is often the only acceptable method for detection of defects in parts of the assembly with no direct surface access. Specifically-designed piezoelectric transducers enable inspection of the critical parts of the engine blades on-wing [6] and can be combined with the endoscopic delivery [15]. This method however requires the use of customised clip-on probes and couplants, with the repeatability of results greatly affected by the quality of contact with the test part.

1.2 Fibre-coupled optically-excited ultrasonic transducers (CHOTs) for remote non-destructive testing

In this work the ability of the surface waves to detect distant defects and inspect parts without disassembly is combined with endoscopic operation and non-contact generation and detection of ultrasound. The use of laser ultrasonics [16] permits remote operation on samples of complex

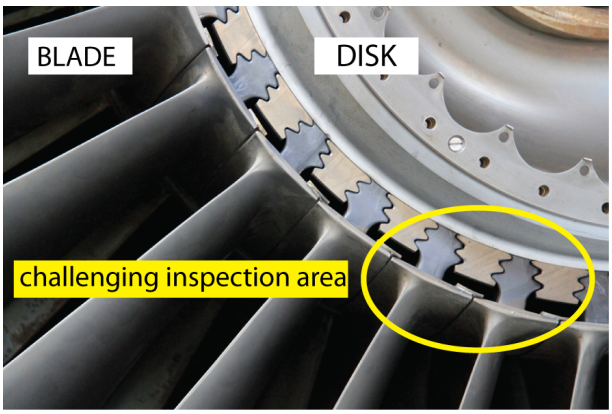

Figure 1.2: Photograph of a typical blade/disk assembly illustrating high-stress-concentration areas challenging for inspection in-situ.

shapes without the use of couplants, provides repeatable results independent of coupling quality or angle of approach, additionally allowing inspection of moving objects [17] and operation at large stand-off distances. It generally does not require surface preparation and provides immediate results. Furthermore, light delivery by optical fibres enables flexible instrumentation and remote inspection which is beneficial in hazardous, spatially-confined or high-temperature environments.

Cheap optical transducers (figure 1.3) are an optically-activated alternative to the conventional piezoelectric transducers, based on principles of laser ultrasonics. They are nanometre-height metal patterns located on the surface of the component and activated remotely by laser illumination, operating in the thermoelastic regime without damage to the part. The g-CHOT uses pulsed laser illumination to generate ultrasound via spatially-modulated absorption of the incident radiation. The d-CHOT operates as a local on-sample interferometer using continuous-wave (CW) probing laser illumination, and translating the surface displacement caused by the propagating wave into intensity modulation of the returning light. Both CHOTs can be used independently, combined with other techniques, or in a coupled configuration. With minimal surface impact, CHOTs can be integrated into the structure, used in large numbers or as disposable transducers.

The use of CHOTs removes the need for additional optical elements used by other laser-ultrasonic techniques, and environmental stabilisation required for the interferometric detection, resulting in a compact optical arrangement. The benefit of the technique is the ultrasonic transduction and sensing performed locally on the sample itself, with the instrumentation used simply for light delivery and collection to and from the transducers. The use of collimated illumination allows flexible stand-off distances and does not require complicated alignment. These properties make CHOTs a suitable technique for the basis of a simple, portable non-contact laser-ultrasonic

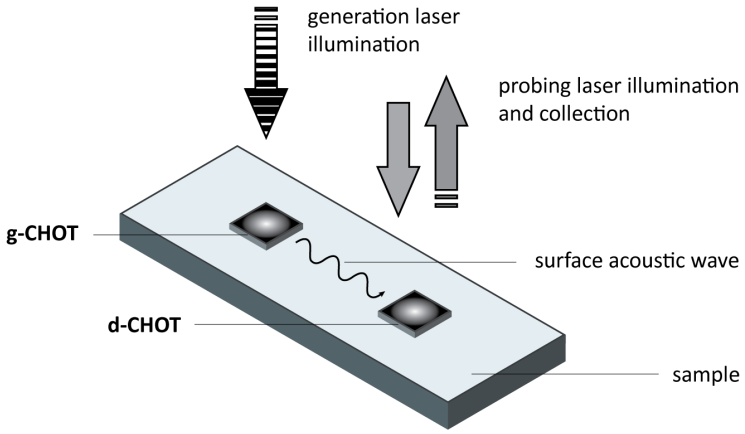

Figure 1.3: Schematic diagram demonstrating laser generation and detection of SAWs with CHOTs.

inspection system for industrial applications.

The practical capabilities of laser ultrasonics are greatly enhanced by the use of optical fibres, allowing inspection of hard-to-reach components located out of direct line of sight or in hazardous environments [18]. Pairing the benefits of the laser ultrasonics and the compact optical arrangement and system simplicity offered by CHOTs with the operation via optical fibres creates great potential for remote ultrasonic inspection of critical aeroengine components on-wing. Furthermore, it could potentially enable continuous-pass testing of the moving components where the instrumentation is kept stationary, dramatically reducing the time and cost of inspection. Figure 1.4 illustrates the concept of on-wing inspection with endoscopic CHOTs.

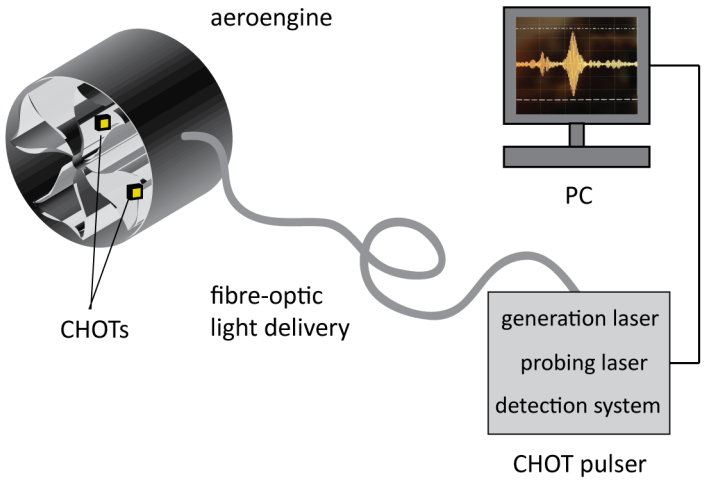

Figure 1.4: On-wing inspection of aeroengine components using endoscopic CHOTs: concept.

1.3 Thesis objectives and layout

This chapter outlined common practices and the types of inspection used in the aerospace industry to ensure the safe operation of the aircraft and prevent operational failures. It also illustrated the need for and the challenges of in-service on-wing inspection of such safety-critical components as the aeroengine blades. The combined use of CHOTs with fibre-optic light delivery was proposed for the creation of a simple, portable non-contact ultrasonic testing system enabling repeatable inspection of hard-to-reach components in locations with spatially-confined or complex access.

The thesis contains four distinct subjects: CHOTs' instrumentation, their fabrication, characterisation and application to NDT. In view of the considered application, this work was limited to the use of surface acoustic waves on metal samples, and frequencies characteristic of the required inspection: 4–5 MHz.

The aims of the work were:

- pairing of the CHOTs operation with optical-fibre light delivery (endoscopic pulser);
- upgrading of the transducer fabrication method to enable transducer application onto industrial parts and overcome the restrictions imposed by the laboratory-based application used previously;
- quantitative characterisation of the transducer performance to enable evaluation of the system component requirements and practical system capabilities;
- demonstration of the inspection capabilities of the system as a whole on representative industrial samples.

The thesis structure is organised as follows. Chapter 2 provides the general background of ultrasonic inspection in non-destructive testing, with particular attention to the use of the Rayleigh waves, and their application to the aerospace sector and in-situ inspection. The conventional ultrasonic generation and detection methods are reviewed, followed by an outline of the principles of laser ultrasonics and a review of the techniques for generation and detection of surface waves. The operation principles, design, fabrication and practical-use consideration of CHOTs for surface waves are discussed in Chapter 3, where previous work in the field is reviewed. An alternative fabrication concept is proposed to create a portable CHOT on film carriers allowing transducer transfer and application to components in-situ.

The endoscopic instrumentation and system elements are presented in Chapter 4 and are followed by the presentation of the fabrication procedure to produce CHOTs on film carriers and the corresponding results in Chapter 5. The performance of the fabricated portable CHOTs and the CHOTs produced with the previously-used method is characterised and compared in Chapter 6. The NDT capabilities of the overall system are demonstrated in Chapter 7, using CHOTs in pulse-echo and pitch-catch configurations on a range of controlled and representative industrial samples. The results of a comparative inspection with a conventional piezoelectric transducer are provided where possible. Additionally, the potential of the technique for structural health monitoring is demonstrated.

Finally, the main contributions of the performed work, its limitations and suggestions for further development are summarised in Chapter 8.

Chapter 2

Background

Ultrasonic techniques have found broad use in a range of fields from medicine and biology to science and engineering where the diversity of their application includes imaging and microscopy, measurement, detection, therapy, particle manipulation, cleaning, and even welding.

In medicine ultrasound is commonly used for diagnostic imaging [19], therapeutic treatment [20] and prevention, for instance pre-natal scanning using transducer arrays and the removal of kidney stones and cancer tumours with high power ultrasound, or stroke prevention by measuring the blood flow to the brain. The latest research in acoustic trapping saw ultrasound being used in analytical chemistry and cell biology, applied to tissue engineering, bio-sensing and targeted drug delivery [21]. The development of acoustic microscopy allows imaging and characterisation of bio– and engineering materials at nano-scales, above the resolution of the optical techniques [22].

In engineering, ultrasonic inspection is one of the most widely-used methods for non-destructive testing and structural health monitoring of engineered parts to detect the nucleation, development or presence of defects such as cracks and delaminations, the presence of voids, take dimensional measurements, perform material characterisation and process monitoring.

The underlying principle, common to all ultrasonic tests, consists of observation and analysis of the transmitted or reflected high-frequency elastic waves originated in or sent through a structure. The changes experienced by the propagating wave and observed in the detected signal are indicative of the condition and characteristics of the propagation medium.

The first section of this chapter provides a background review of principles and types of ultrasonic inspection commonly used for non-destructive testing, reviews the main properties of Rayleigh waves and their use in the aerospace applications, and concludes with an overview and comparison of ultrasonic generation and detection methods.

The second part presents the principles of laser ultrasonics enabling remote non-contact gen-

eration and detection of ultrasound, with a review of the relevant techniques used with surface acoustic waves.

2.1 Ultrasonic inspection in NDT

2.1.1 Ultrasound and wave modes

Sound is a mechanical pressure wave propagating in a medium as particle oscillations from some initially-applied disturbance. Its propagation can be described in terms of Hooke's law and the theory of elasticity [23], with the wave parameters determined by the properties of the propagation medium. The frequency of the wave f and its wavelength Λ in particular material are related via the sound velocity c in that material as:

$$f = \frac{c}{\Lambda} \tag{2.1}$$

Based on its frequency content, the range of sound is divided into *infrasound* (below 20 Hz), *acoustic* range (20 Hz–20 kHz) and *ultrasound*, with frequencies exceeding 20 kHz. Although ultrasonic frequencies as high as hundreds of GHz reaching into THz range have been achieved [24], most NDT and SHM applications rarely operate above 200 MHz, primarily due to the frequency-dependent material attenuation that limits the propagation distance at these frequencies. Additionally, the grain sizes of some engineering materials introduce 'structural' noise and scatter into the high-frequency signals [25]. Defects can be completely obscured by material micro-structure scattering for frequencies with a wavelength/grain-size ratio below three [26]. Although restricting NDT applications, these effects enable studies of material structure and attenuation.

Based on the geometry of the test part and accessibility of the inspected region, the most appropriate mode of ultrasonic inspection can be chosen from three principal wave modes supported in elastic solids: *longitudinal* (compression), *transverse* (shear) and *surface/guided* waves. The propagation of different modes in the same material occurs with different velocities, determined by the appropriate elastic constant characterising the stress-strain relation in a particular mode:

$$c_l = \sqrt{\frac{E(1-\nu)}{\rho(1+\nu)(1-2\nu)}} \qquad \text{and} \qquad c_t = \sqrt{\frac{E}{2\rho(1+\nu)}} \equiv \sqrt{\frac{G}{\rho}}$$

where c_l and c_t are the longitudinal and the transverse wave velocities, E and G are the Young's and the shear modulii respectively, ν is the Poisson's ratio, and ρ is the material density.

The velocity of the surface waves is typically in the range of 0.87–0.95 of a shear wave, and is determined as: $c_R = [(0.87 + 1.12\nu)/(1+\nu)]c_t$. For example, in aluminium the longitudinal, shear and surface wave velocities are: c_l= 6,374 m/s, c_t= 3,111 m/s, c_R= 2,906 m/s [27].

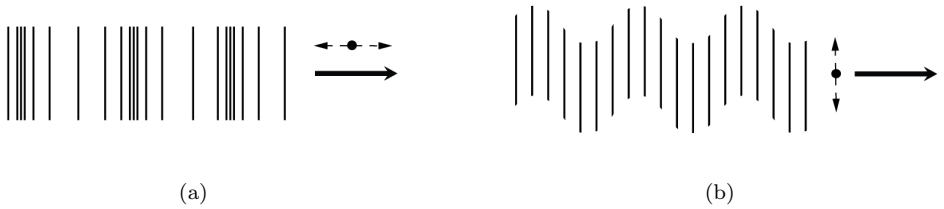

Figure 2.1: Longitudinal (a) and transverse (b) waves, shown with corresponding particle motion.

Bulk waves

Longitudinal and transverse waves propagate into and through the body of material, and are known collectively as bulk waves. In longitudinal waves the particle oscillations are parallel to the direction of propagation (material contractions and extensions), and orthogonal in transverse waves (material shear). The latter are restricted to the acoustically-solid materials as the molecular structure does not allow their efficient propagation in air. In NDT the bulk waves are commonly used for thickness measurements, inspection of bulk of material for internal defects, and imaging.

Surface and guided waves

Surface acoustic waves propagate along the surfaces of solid thick materials (Rayleigh – at a free surface, Stoneley – at an interface of two media), with 80% of the wave energy concentrated in the material thickness of one acoustic wavelength [28]. The particle oscillations in surface waves combine both longitudinal and transverse components producing elliptical motion which decreases exponentially with depth of material.

Plate (Lamb) waves propagate throughout the thickness of a solid material layer, guided by its boundaries, in the form of complex symmetrical (extensional) and anti-symmetrical (flexural) modes. The relationship between acoustic wavelength and the plate thickness determines the order of supported modes and their individual velocities, the combination of which for a particular material is represented by dispersion curves. The dispersive properties of the Lamb waves can be used in determination of the coating thickness, however the coexistence of the multiple wave modes complicates signal interpretation for defect detection, and selective-mode generation is preferred.

Due to their properties and ability to propagate large distances and inspect remote regions, the Rayleigh and Lamb waves are extensively used to detect near-surface flaws or delaminations, for integrity assessment of thin-walled components, process monitoring or corrosion mapping. More detailed discussion of the properties and use of the Rayleigh waves in the framework of aerospace NDT is presented in section 2.1.3, whereas the full review of physical properties and applications

of both Rayleigh and Lamb waves can be found in [28].

2.1.2 Inspection principles and typical configurations

Most inspection techniques use ultrasonic signals in the form of a pulse which provides accurate reference points in the time-domain for localisation of damage or thickness gauging, and has a wide spectrum of frequencies for analysis or measurement of frequency-dependent characteristics.

The use of ultrasound for flaw detection utilises the principle of the acoustic wave being partially or fully reflected from a discontinuity or an interface between two acoustically different materials, e.g. a metal sample and an air-filled crack. The amount of energy being reflected or transmitted by the interface depends on the acoustic impedances of the materials [23] $Z = \rho \cdot c$, where ρ and c are the characteristic material density and the sound velocity. Corresponding pressure reflection R and transmission T coefficients for normal incidence are given as:

$$R = \frac{Z_2 - Z_1}{Z_1 + Z_2} \qquad \text{and} \qquad T = \frac{2Z_2}{Z_1 + Z_2}$$

The striking contrast in acoustic impedances of solid materials with air creates serious challenges to launch acoustic waves into the sample (e.g. $Z_{Al} = 1.7$ x 10^7 vs $Z_{air} = 430$). The use of the impedance transitioning layers such as liquid/gel couplants is therefore required to reduce the losses in contact ultrasonic methods (section 2.1.5). The loss in transmission from a 1 MHz PZT transducer into a steel sample is estimated to be 79 dB without and about 1 dB with the couplant [29], and the two-way conversion loss (at 1 MHz and 50 mm distance) without the couplant can reach 189 dB in steel [30].

Depending on the purpose of the inspection, types of the waves used and sample geometry, a number of test configurations could be adopted with different relative positions of the actuator and the receiver, and based on principles of reflection or transmission. Most common of these are *pulse-echo*, *through-transmission* and *pitch-catch* [31], described below and illustrated in figure 2.2.

The use of actuators (such as PZT transducers) to launch acoustic waves into the material defines *active* sensing. In *passive* sensing no external actuators are used, and the sensing is based on listening to the structure itself using a receiver. Passive sensing employs effects such as acoustic emission (20 kHz–1 MHz), where the elastic stresses are originating from a source within the material itself such as during nucleation or propagation of a crack. Such passive methods however cannot detect the existing damage or flaws, and generally require the time history of the previous inspections. They are commonly used for SHM to monitor active damage resulting from fractures, plastic deformations or impacts but are not suitable for NDT.

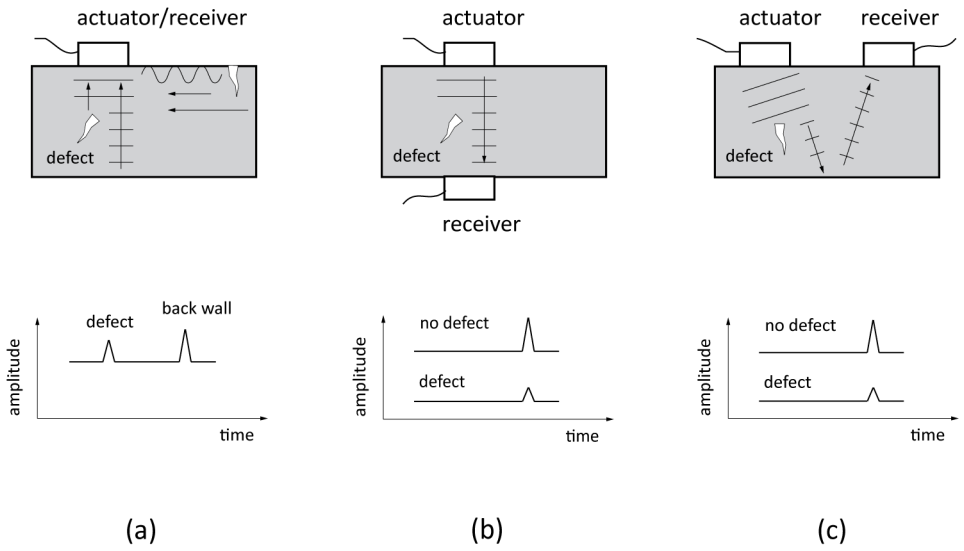

Figure 2.2: Typical inspection configurations and corresponding signals indicating presence of a flaw: (a) pulse-echo; (b) through-transmission; (c) pitch-catch.

Pulse-echo

In the pulse-echo configuration typically the same element acts as an actuator and a receiver requiring a single point of access on the test object, although separate actuators and receivers could also be used. The method is based on detection of the pulse reflected from the object geometry and/or flaws. The presence of flaws is then indicated by the presence of echoes additional to or obscuring those received from the sample geometry with arrival times characteristic of the propagated distance and the ultrasound velocity of the material. The location of flaws and object thickness can be obtained by measuring the arrival times of the echoes for the known velocity. Material characteristics such as velocity and attenuation coefficients can also be determined in this configuration.

Through-transmission and pitch-catch

A through-transmission arrangement uses a separate actuator and receiver placed on the opposite sides of the test object. The presence of a flaw in this configuration is indicated by the reduction in amplitude or complete loss of the transmitted pulse in the received signal. It does not however provide information on the depth-location of the flaw within the object. This arrangement is well suited for testing lossy materials due to the reduction of the travel path, and can be used for velocity and thickness measurements and delamination detection.

Pitch-catch is another transmission-based arrangement where an actuator and a receiver are placed on the same side of the test object and the signal transmitted by the actuator is caught by the receiver in a direct pass or after reflection from the sample geometry/flaws. It can be used with surface waves or with bulk waves at oblique angles of incidence, providing solutions to hard-to-detect orientations of flaws (e.g. parallel to the direction of propagation, at an angle, near-surface).

Other types

The combinations of multiple actuators and multiple receivers on the surface of a test part could also be used with guided waves, in some cases creating a whole network of sensors. Inspection in such an arrangement allows simultaneous monitoring of a large area along different directions and has high potential for structural health monitoring [32].

The test configurations described above could be used with the probe being in contact with the test object or by *immersion testing/scanning* where the test object is placed in a tank with liquid to allow non-contact inspection by a probe submerged in close proximity to the object. This allows automated inspection and scanning of large area components, as is demonstrated by the recent development of '1000 gates' system for inspection of aerospace jet engine discs [33].

Another inspection technique known as *resonance testing* makes use of the unique mechanical resonances of the test object and corresponding resonant frequencies determined by the object geometry and material properties. This type of inspection can be used for quantitative measurement of the thickness of very thin plates, and for qualitative assessment of the part as a whole by analysing the deviations in resonant frequencies from the expected values due to cracks, disbonds or missed processes. The ultrasonic pulse is sent into the structure and its frequency varied until the resonance is achieved or the spectrum of the wide-band pulse sent through the structure is analysed for the changes in the resonant frequencies.

2.1.3 Inspection with Rayleigh waves

The unique properties of Rayleigh waves are beneficial in applications requiring inspection of distant parts of components with limited surface access, parts of an assembly where inspected areas are obstructed, components with curved surfaces, and detection of flaws that might be missed by other methods due to their size, location and orientation.

Propagation

The benefits of using Rayleigh waves for inspection of remote regions are due to their ability to propagate over greater distances than bulk waves. This results from a slower decay in the surface wave amplitudes decreasing as $1/\sqrt{r}$ with distance r, compared to $1/r$ for the bulk waves, producing higher amplitude disturbances for the given power in the wave.

The propagation of the Rayleigh waves is possible on curved surfaces and around corners, with the total wave transmission past the corners with the radii exceeding $1.7 - 2\Lambda_R$ [28]. This enables inspection of the components with complex surface geometries and the regions that are obstructed or behind bends, making surface waves easily accessible for excitation and measurement from any available surface area of the test part. The velocity of the wave is however affected, increasing with curvature of the surface, which should be taken into account when localising the damage.

Of particular benefit for defect detection is the ability of the wave to propagate past the cracks independently of their depth (the transmission coefficient is close to 8% for the slots deeper than $1.5\Lambda_R$ [28]).

Localisation

The localisation of the wave in the thin surface layer makes it highly-sensitive to the characteristics of the layer and the surface conditions, affecting wave velocity and attenuation, which can be used for detection of surface flaws and measuring material properties. Small relative dimensions of the interrogating Rayleigh wave (determined by its penetration depth) produce stronger reflections than the bulk waves used for detection of volume defects of similar sizes. The wavelength-dependent penetration depth can be used to probe material condition and properties at different depths by varying the wave frequency.

Defect detection and sizing

The defect detection with surface waves could be performed in pulse-echo or pitch-catch configurations (section 2.1.2) either by detection of an echo from the flaw or by measuring the reduction of the transmitted signal.

The use of Rayleigh waves is not limited merely to flaw detection but can also be employed for accurate defect sizing and characterisation by analysing the interaction of the wave with the surface features [34, 35]. The complex character of this interaction is strongly dependent on the crack–depth/wavelength ratio [28, 36] and includes not only straight-forward reflection and transmission of the wave in the Rayleigh mode, but also mode-conversion [37] and scattering into bulk at the tips and corners of cracks [38], as well as reverberations in slots.

These mechanisms are exploited for the evaluation of the crack penetration depth in a number of approaches. Amplitude-based methods rely on fundamental relationships between the depth of the slot and the amplitudes of the reflected, scattered and transmitted Rayleigh waves. The time-delay measurement methods analyse the depth-dependent transit times of the transmitted, mode-converted or diffracted waves, with the spectral methods additionally exploiting amplitude and transit time dependency on the frequency of the wave [34,35,39,40] to allow the sizing of cracks with depths below Λ_R. Analysis of the power spectral density can also be used for monitoring of crack growth [41].

The demonstration and verification of CHOTs NDT capabilities in the presented work was limited to event of detection, corresponding to intended pass/fail application, without defect sizing. The detection of slots with depths as small as $\Lambda_R/2$ on aluminium samples is shown in Chapter 7.

Aerospace NDT *in-situ*

High sensitivity of surface waves to near-surface conditions makes them a powerful tool for detection and characterisation of defects in components where the initial damage is confined to the surface, such as the development of fatigue and stress-corrosion cracks in turbine and compressor blades of aeroengines.

The feasibility of using surface waves for ultrasonic inspection of aeroengine components was first considered in 1954 and shown as early as 1956 when ultrasonic inspection was introduced by the Royal Danish Airforce. The inspection principle used the pulse-echo arrangement, and the conditions and practicability of using SAWs for compressor and turbine blade testing were reported, demonstrating the detection of cracks in such poorly-accessible and critical areas of a blade as the fillet radius of the root [42]. The potential of SAWs for early detection of fatigue damage and failure prediction had also been shown [43]. The in-situ inspection with surface waves was demonstrated in 1963 by testing of Alison J71 turbojet compressor rotor blades, where 15 out of 167 inspected engines were rejected with a total of 69 cracked blades, amounting to the saving of at least $4 million in engine costs [44]. The use of this ultrasonic technique was reported to reduce the inspection time per stage from 2–3 hours taken with conventionally-used dye-penetrant or magnetic particle tests to 20 minutes [45].

In such applications surface waves are mostly used in a pulse-echo configuration where the echo amplitude and separation are typically analysed. A pass/fail inspection uses a set threshold based on the echo amplitude from a defect of the maximum permissible size and a time-window or a ‘gate’ to select the echoes arriving from the area of interest on the test part. Common practice in aerospace NDT is the use of the reference standards [3] representative of the component that is being tested and often containing a simulated defect. The calibration of the instrument on such

standards provides a sample of the expected ultrasonic response and is used to adjust instrument sensitivity and set the time window. Typical inspection frequencies are used in the range of 0.5–15 MHz [3]. For example, the Rayleigh wave frequencies of 0.4–8 MHz would be required to detect flaws of 0.2–4 mm in depth, based on the maximum allowable repair limits for damaged steel compressor blades in stages 1–4 [46], steel velocity $c_R = 3{,}179$ m/s [27], and detection of the defect with depth $\Lambda_R/2$.

Although the feasibility and effectiveness of the Rayleigh waves for in-situ ultrasonic inspection was demonstrated using contact transducers, considerable efforts were dedicated to custom construction of the probes and fixtures [42, 45, 47]. The probe would be attached to the blade with a pressure spring or other clamp-on mechanism and was required to provide the required angle for mode-conversion from longitudinal to surface waves as well as uniform contact with the surface. 'A Study of Ultrasonics for Flaw Detection in Turbojet Engines', technical report prepared for the Oklahoma City Air Material Area (Tinker Air Force Base) [47] stated the difficulties of placing the transducer in the same location on different blades, difficulty to maintain even pressure and poor repeatability resulting in signal fluctuations and difficulty of result interpretation. The use of non-contact ultrasonics can be expected to overcome the reported difficulties of contact inspection.

Propagation on real surfaces

High sensitivity of Rayleigh waves to surface condition, desirable in terms of inspection, poses a question with regard to practical applications on real components and the effect of the surface quality on the propagation of the wave. Among other factors affecting the propagation of surface waves (grain size, material properties, temperature, etc.) significant contributions to wave attenuation and damping arise from surface finish and loading.

Wave attenuation due to surface roughness results from scattering at surface irregularities and radiation of the wave energy both into the volume (as longitudinal and transverse waves) and secondary Rayleigh waves. The dominating modes and the attenuation coefficients are dependent on the relative dimensions of the Rayleigh wavelength Λ_R and the correlation length of the roughness features a, where the attenuation coefficient varies as the fifth power of frequency in the long wave approximation ($a/\Lambda_R << 1$) and as the fourth power of frequency for the short waves ($a/\Lambda_R >> 1$) [48, 49]. At high frequencies the attenuation is dominated by scattering into the secondary Rayleigh waves and according to [48] attenuation length tends to a constant value dependent on the Poisson ratio.

At longer wavelengths however roughness has a greater impact on the changes in propagation velocity than attenuation, making the wave dispersive [50]. For example, the ratio of the rough/flat surface velocities $c_R/c_{R0} = 0.799$ was reported for Al sample with small roughness ($h^2/a^2 = 0.022$,

h – rms flatness) and $a/\Lambda_R = 1.079$ x 10^{-3} [51]. Although this effect should be taken into account when using time-of-flight methods for flaw localisation, it could be used as a tool to indicate deterioration of the material surface over time.

The inspection efficiency was shown to be affected by surface finish, with the first indications of damage on rough components being detected later in fatigue life. JG Rasmussen [43] reported a 1.8-times difference between the ground and electro-polished surfaces, corresponding to detection at 39.4% of fatigue life on electro-polished and at 72.3% on the ground surface with scratches (sample under dynamic loading, 4 MHz, 2024ST3 Al alloy; 59.6% to 86.6% for unloaded samples).

The presence of surface layers such as liquids, paint, thermal-barrier coating and operational build-up has additional effects. A layer of liquid leads to radiation of acoustic energy into the liquid as compression waves (leaky Rayleigh waves), with significant dependency of the losses onto the thickness of the layer. This limits operational environments for the Rayleigh waves. The formation of the surface build-up layer on turbine blades during operation can present additional challenges in which case the inspection with surface waves can be complemented by transverse waves [42]. No serious effects are expected from a thin paint coating for inspection frequencies under 5 MHz [47].

Considering the ability to detect early fatigue damage at 4 MHz using a PZT [43] the effective propagation distance was reported to exceed 41 cm on a scratched and corroded Al-alloy sample, reduced to 23 cm with applied layer of zinc chromate primer. The use of Rayleigh waves can therefore be reasonably applied for in-situ testing of aerospace components considering moderate roughness and propagation distances and target inspection frequency of 4 MHz.

2.1.4 Typical representation of the test results

Different measurands can be obtained from the ultrasonic data to be presented including arrival times of the echoes (time-of-flight), amplitude or peak-to-peak value of the signal or a particular echo in the region of interest (time-gated), phase or amplitude at particular frequency, velocity, etc. The presentation of the results of the ultrasonic inspection should contain sufficient and appropriate information to allow their interpretation in accordance with the purpose of the inspection. The three main types used to represent the recorded data are *A-scan*, *B-scan* and *C-scan* (figure 2.3), each providing different degrees of detail and ways to analyse the results. All three types of the scans are used in this work to demonstrate particular points that are being discussed. Other types of data acquisition and presentation include P-scan and D-scan used with angled probes and for jointly moving actuators and receivers.

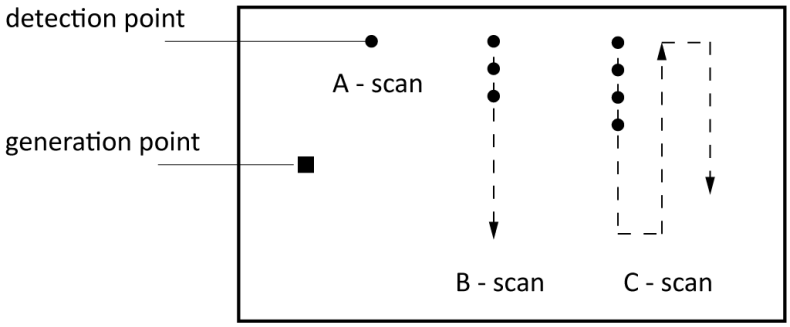

Figure 2.3: Data collection corresponding to representation of results.

A-scan

A-scan plots the amplitude of the signal recorded by the receiver at a single measurement point against time. The time of arrival of the acoustic signal is dependent on the distance travelled and the velocity of the used wave type in a particular material, with the amplitude being indicative of the propagation path, material attenuation and coefficients of reflection or transmission of internal boundaries or flaws. Therefore a range of information can be extracted from A-scans including the presence and location of flaws, their size, layer thickness and properties, etc.

The majority of the results obtained in this work and those typical for a single CHOT actuator and a single receiver are presented in form of A-scans corresponding to detection at a single point.

B-scan

When a number of A-scans are obtained at points along a line on the test object by physically moving the receiver from point to point, a B-scan can be constructed. It allows plotting signal characteristics of interest along the dimensions of the line scan and against time. This provides extra information creating an acoustic slice of the sample at the position of the line scan. The B-scan is presented as an image with spatial and time coordinates and a colour map corresponding to the amplitude of the received signal.

C-scan

Combining a number of B-scans by performing sequential line scans along the second dimension of the test sample, a C-scan is created. The resulting data is a three-dimensional array of the time traces (A-scans) in two spatial coordinates corresponding to positions of the receiver on the

sample. This is the most complete but time and resource consuming scan. The C-scan is presented as an image in two spatial coordinates of the sample with the colour map chosen to represent selected characteristics of the acoustic signal. The time dependency is not shown in C-scans as the plot is bounded by the three-dimensional coordinate system. The detailed time traces can however be analysed separately by using A or B-scan representation. C-scans can be used to display variations in thickness, detection of disbands, imaging, visualisation of acoustic fields. The information presented as B or C-scans is easy to analyse and allows visual recognition of patterns and trends in the data.

2.1.5 Conventional generation and detection methods

The excitation and detection of ultrasound is achieved by the use of an ultrasonic transducer – a device performing conversion between ultrasonic and other types of energy. The operation of a transducer is often reversible (the energy transformation performed in both directions) allowing a single probe to act both as an actuator and as a receiver. The commonly-used methods for generation and detection of ultrasound, their operation principles, benefits and restrictions are summarised below.

Piezoelectric transducers

These ultrasonic transducers employ the direct and converse piezoelectric effects for conversion between the acoustic and electrical energy. Polarised piezoelectric material placed between two conducting plates will induce the change in the electric field as mechanical tensile or compression stresses are applied to it, providing the means for the detection of ultrasound. The application of the alternating electric field to the same material will result in material contractions and expansions enabling the generation of acoustic waves. Phased arrays consisting of multiple transducers enable custom beam modification and steering as well as high resolution imaging that can be used to visualise internal flaws [52].

These are the most common type of the ultrasonic transducers used in NDT offering a wide range of frequencies and ultrasonic modes of operation that could be applied to a range of materials and sample geometries. However, the transfer of the acoustic energy between the sample and the transducer requires a good contact with the sample, and due to the differences in acoustic impedances – a couplant. Transducer operation and the repeatability of inspection results are strongly-dependent on the coupling quality. Another important limitation is the loss of transducer functionality at temperatures above the Curie temperature, restricting the application of a typical lead zirconate titanate (PZT) transducer to under 250–490 °C [31].

Magnetostrictive transducers

The operation principle of the magnetostrictive transducers is similar to that of the piezoelectric transducers but based on the use of ferromagnetic materials and magnetic fields to induce or detect material deformations. Additional abilities include direct initiation of guided waves in rods or wires made from ferrous materials for their inspection or process monitoring.

Electromagnetic acoustic transducers (EMATs)

EMATs offer non-contact generation and detection of acoustic waves by using electromechanical coupling. This allows their use in hostile environments and at high temperatures, however restricting their application to electrically-conducting materials. EMATs operation is based on using a current-conducting coil in the constant magnetic field. Acoustic generation is achieved as an alternating current is passed through the coil placed in close proximity to the test object. The magnetic Lorentz force acts on the induced eddy currents in the material under test resulting in oscillations of the metal lattice. Conversely, the elastic vibrations in the sample introduce a flow of alternating current in the coil.

One of the concerns with the use of EMATs, especially for applications in structural health monitoring is possible electro-magnetic (EM) interference that could adversely affect functioning electronic systems. They are however rather forgiving to the surface roughness and can operate on samples with coatings.

Air-coupled transducers

Air-coupled transducers is a separate branch in the development of the non-contact ultrasonics that couple the acoustic energy between the actuator/receiver and the sample via an air/gas-filled gap. Among the commonly-pursued solutions to overcome the intrinsic difficulties of the efficient acoustic coupling into air are the reduction of the high impedance contrast between the transducer and the air using the resonant matching layers, the reduction of active-element impedance and air-backed transducers.

A separate class is the capacitive (CMUT) and piezoelectric (PMUT) micro-machined ultrasonic transducers, the operation of which is based on the use of the deformable electrode membranes caused to vibrate by the application of the alternating electric field and conversely, producing the flow of alternating current if being deformed. The CMUTs design is that of a parallel-plate capacitor [31], whereas the PMUTs use a membrane resonator coated with electroded piezoelectric film. A comprehensive review of various techniques and designs of the air-coupled transducers, including in NDT context can be found in [30, 53, 54].

Laser and optical

The laser ultrasonic (LU) systems use the interaction of the laser beams with the surface of the sample to generate and detect acoustic waves, providing non-contact remote operation and most ultrasonic modes and wavefronts.

The generation is achieved typically via the thermoelastic effect whereby the radiation of the laser illuminating the surface of the sample is absorbed within a thin surface layer of material and converted to heat, resulting in a rapid thermal expansion of the heated region. Using pulsed, modulated or moving laser sources the material undergoes a series of expansions and contractions that produce propagating elastic stresses inside the structure.

Optical detection is based on using some form of reflection (specular, scatter or diffraction) of the probing optical beam from the surface of the test sample and further analysis of its characteristics. It is therefore often sensitive to surface conditions such as roughness and reflectivity.

The use of lasers enables operation at large distances, on complex and curved surfaces, and easy scanning. This comes, however, at the cost of generally reduced generation efficiency and detection sensitivity compared to conventional contact methods.

More details on the operation principles and specific techniques of laser generation and detection of ultrasound with relation to the current work are provided in section 2.2, whereas a more general and comprehensive review can be found in [16].

Techniques summary and comparison

In addition to the methods described earlier, there is a wide range of hybrid systems using a combination of various techniques, for example – using a laser to remotely excite a PZT element [55] or a MEMS transducer [56], laser generation combined with detection by an air-coupled PZT [57, 58], EMAT [59, 60] or an integrated ultrasonic transducer (IUT) [61], and many more. The trends evident in the development of the ultrasonic techniques in NDT context are driven by the desire for contactless, remote measurements, ability to inspect complex-geometry parts, operation at elevated temperatures, and miniaturised systems for in-situ measurements. Here, the choice of a particular technique or their combination is weighted on the benefits to specific application.

The wide use of the contact bulk transducers is attributed to their high range of applicability, operation frequencies, the ease of use, cost and energy-coupling efficiency, including the highest detection sensitivity among other methods [30]. Although the major limitations of their contact nature have somewhat been overcome with the development of the air-coupled PMUTs and, in part, by the use of the capacitive and inductive PZT hybrid systems [55], the sample penetration and generation efficiency have been compromised (especially for surface waves). The applicability of

contact techniques for testing of non-planar components has been addressed by the the development of a range of flexible (FUT) and integrated ultrasonic transducers [62–66], aided by the rapid advancements in micro-fabrication, MEMS technology and material processes.

Despite EMATs and air-coupled transducers allowing component testing without physical contact with the sample or the need of coupling, among other restrictions (on the type of material, EM interference and parasitic capacitance, high operational voltages) the probe still has to be in close proximity to the test part. In most cases this also imposes restrictions on operational temperatures.

The use of lasers to generate and detect acoustic waves enables remote operation at large distances and in hostile conditions, inspections that could be automated and performed on objects in motion, with high potential for in-situ testing and in industrial applications. The availability of short-pulse lasers enables operation at high frequencies (beneficial for finer defect resolution and restricted in the air-coupled transducers to the lower MHz range), and bandwidths exceeding 100 MHz. However, the laser ultrasonic systems are generally expensive, more complicated to align and have safety considerations. The main drawbacks for their industrial application are reduced detection sensitivity [67] compared to contact methods, and high dependency on surface conditions.

2.2 Laser ultrasonics

In his review of the applicability and transition of laser ultrasonic systems into industry (2004), Jean-Pierre Monchalin [68] concluded that "... laser ultrasonics that was for a long time a laboratory curiosity has definitely now made its transition to industry.", and at the same time "..the developments should continue to improve performance, to make it well adapted to specific inspection..". The persistent presence of dedicated laser ultrasonics sessions at NDT conferences shows acceptance of this technique as a viable means for inspection. However, the development of numerous hybrid systems [69, 70] combining laser generation with some type of non-optical air-coupled detection demonstrates both the desire to exploit the benefits offered by laser ultrasonics and at the same time the reluctance to use optical-based detection methods. The main barriers of the LU techniques slowing down their transition into industries are lower sensitivity of detection, complexity and cost of the systems [67, 68].

The present work draws on a number of approaches developed over the years to increase the efficiency of laser-ultrasonic techniques in pursuit to create the highly-desirable all-optical inspection system. By the combination, extension and adaptation of these techniques for a particular inspection task (Chapter 1), the present work contributes towards further transition of a selected LU technique to industry. This is achieved by overcoming some of the drawbacks limiting industrial

applications of the previous methods and by the demonstration of application-related capabilities. This section outlines the principles of laser ultrasonics and reviews the relevant underlying works in the field.

2.2.1 Principles of laser ultrasonic generation

Unlike contact and air-coupled transducers, the generation with a laser does not require launching acoustic waves across the boundary of two media, with associated losses. Instead, it utilises the material of the sample to act as a transducer, transforming incident radiation into acoustic waves by converting it to heat (via a thermoelastic effect). The laser in this case simply acts as a wireless power-delivery system, similar to the electric pulser used by conventional contact transducers. The efficiency of conversion is determined by material absorption and laser power density which jointly define the generation mechanism that takes place.

In the *thermoelastic* regime (figure 2.4a) the absorbed energy is converted to heat and produces localised material expansions. The resulting thermoelastic strains and stresses set up inside the material are the source of acoustic waves. As radiation is absorbed in a thin layer, the principal stresses are parallel to the surface [71] – a condition favourable for efficient excitation of surface waves [72]. The acoustic generation is achieved when the incident power is modulated in time so as to produce alternating material expansions and rarefactions [73].

The generation in the *ablation* regime (figure 2.4b) is supplementary to the thermoelastic process and begins when the input power density breaches the material melting threshold. Vaporisation of the surface layer and formation of plasma result in ejection of matter from the surface. Combined, the recoil force from evaporation and the pressure from expanding plasma produce

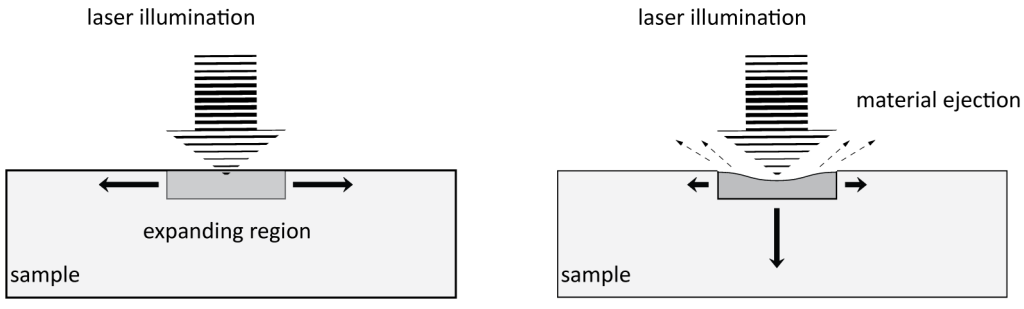

(a) (b)

Figure 2.4: Schematic representation of ultrasonic generation in thermoelastic (a) and ablation (b) regimes; principal stresses are indicated by bold arrows.

normal force directed into the sample, enhancing the generation of bulk waves [71].

Although both mechanisms can be used for excitation of the Rayleigh waves, their application to non-destructive testing evidently prohibits any damage to the sample. The present work and further discussion are therefore restricted to operation in thermoelastic regime.

To produce acoustic waves of sufficient amplitudes and high frequencies in MHz range, a Q-switched laser is commonly used due to its high peak pulse power and short pulse durations. As the generated frequencies are spectral components of the laser pulse, more energy at the higher frequencies is available from the shorter pulses. Acoustic frequency f at which the pulse power-spectrum reaches half-maximum can be estimated (based on Gaussian pulse profile with standard deviation τ [16]) as:

$$f = \frac{0.1874}{\tau}$$

The operation at 4 MHz and 5 MHz in present work therefore requires the pulse duration of under 40 ns to ensure considerable energy at desired frequencies.

Thermoelastic generation

In the thermoelastic regime the origin of the acoustic generation is the temperature gradients introduced by the absorption of input laser radiation, with linear dependency of resulting stress-wave amplitudes on the input power [71, 73]. Limiting interaction of laser illumination to metal samples, the simplified relations during this process are presented below, and the detailed analytical solutions can be found in [74, 75].

Considering a one-dimensional case of a semi-infinite body, the laser irradiation of its surface (plane $z = 0$) with the associated temperature rise ΔT produces a strain ϵ_{zz}:

$$\epsilon_{zz} = \frac{\partial u(z,t)}{\partial z} = \alpha \Delta T(z,t)$$

where $u(z,t)$ is the z component of the particle displacement, and α is the coefficient of linear thermal expansion.

As the expanding volume is constrained by the surrounding material, the stress-strain relation described by Hooke's law includes the corresponding compressional stresses $-B\alpha\Delta T$:

$$\sigma_{zz} = (L + 2G)\epsilon_{zz} - B\alpha\Delta T$$

where σ_{zz} is the total elastic stress, L is the first Lamé parameter, G and B are the shear and bulk modulii of elasticity.

Thus the equation of motion for laser-generated elastic waves u becomes [73]:

$$\rho\frac{\partial^2 u}{\partial t^2} = \frac{\partial \sigma_{zz}}{\partial z} = (L + 2G)\frac{\partial^2 u}{\partial z^2} - B\alpha\frac{\partial T}{\partial z}$$

where the appropriate temperature distribution $T(z,t)$ is found as the solution of the heat conduction problem for the corresponding input energy flux.

Due to finite penetration of the electromagnetic wave, the absorption is localised in a thin surface layer of 'skin depth' δ [16]:

$$\delta = \sqrt{\frac{\lambda_0}{\pi\sigma c\mu}} \tag{2.2}$$

where λ_0 is the optical wavelength in vacuum, σ and μ are the material conductivity and permeability, and c is the velocity of light.

Generally, for near IR radiation and most metals δ is of order of tens of nanometres, and the absorption is around 4–7%. In a simple approximation (without considering thermal conductivity, and for uniform illumination) the temperature rise ΔT and the resulting change of volume ΔV produced by the absorbed energy can be determined as [16, 71]:

$$\Delta T = \frac{E_{absorbed}}{\rho\sigma A\delta} \qquad \text{and} \qquad \Delta V = \frac{3\alpha E_{absorbed}}{\rho\sigma}$$

where $E_{absorbed} = (1-R)E_{incident}$ is the absorbed energy, $E_{incident}$ is the incident energy, R is the reflection coefficient, A is the illuminated area, ρ is the mass density, and $3\alpha/\rho\sigma$ can be described as the thermoelastic coupling factor.

The original experiment by White in 1963 [73] demonstrated generation of easily-detectable elastic waves with a calculated peak surface temperature rise of as little as 0.001 °C corresponding to the absorbed power density $I = 2$ W/cm^2 (pulse length $\tau = 2$ μs) and material absorption $< 10\%$. The pulse duration, power density and thermal properties of the material (conductivity and diffusivity) determine the maximum temperature rise at the surface. Typically, for aluminium and a Q-switched laser operating in the thermoelastic regime ($\tau = 20$ ns, $I = 1.9$ MW/cm^2) this value is close to 100 °C [16], and increases for the shorter pulses carrying the same energy. For metals like aluminium and Q-switched lasers, exceeding the power densities of $\sim 10^7$ W/cm^2 results in material melting and ablation.

Surface acoustic waves

It can be seen that the temperature distribution and strains inside the material resemble the energy distribution on the surface and determine the solution of the equation of motion. The choice of the appropriate illumination thus gives control over the acoustic source.

The temperature gradients produced by the evenly-illuminated surface are directed into the depth of material normal to the surface and are the source of the longitudinal waves. Due to finite size of the laser beam, additional lateral gradients are introduced parallel to the surface enabling generation of shear and surface waves. Such simultaneous generation of multiple acoustic

modes is a distinct feature of laser-generated ultrasound, with the Rayleigh modes dominating in the thermoelastic process. The following ratios of energy distribution between the modes were measured for the material with Poisson ratio of 0.2: Rayleigh/shear = 6.93 and compression/shear = 1.3 [72].

The laser beams of conventional circular symmetry produce surface waves propagating radially away from the source. The directivity of the wave is achieved by expanding the illumination from a spot to a line source [76]. Figure 2.5 demonstrates the directivity comparison for a circular and a line acoustic sources, where the line source is shown to produce two, forward and rearward-travelling, wavefronts with enhanced generation in directions orthogonal to the illuminated line. The Rayleigh wave pulse duration is proportional to the width of the illuminated area, and the amplitude – to the absorbed energy per pulse [77]. Highly-directional SAWs are also desirable in NDT applications, with those generated by linear sources displaying higher sensitivity to flaws [78].

Additionally, the direction of the wave can be controlled by the creation of the linear phased array of point sources [79, 80] activated with the corresponding time delay (figure 2.6) to produce angle $\theta = \sin^{-1}(c_R t/a)$, where a is the distance between the array elements.

2.2.2 Generation of surface acoustic waves: arrays of ultrasonic sources

A number of techniques have been developed in the past four decades to increase the generation efficiency and signal detectability in the LU systems [67, 72]. Two commonly-pursued directions are the increase of the generated surface displacement δ, making signal more easily detectable, and the reduction of the generation and detection bandwidths BW to reduce noise. The relationship

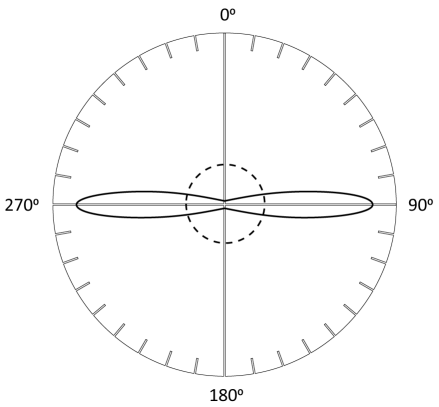

Figure 2.5: Directivity of the Rayleigh wave (Aindow et al 1982): circular source - dashed curve, vertical line source - solid curve.

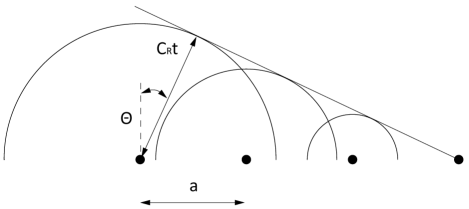

Figure 2.6: Controlling the directivity of the wave by the use of the linear phased array of point sources.

between both factors and the signal detectability for shot-noise limited laser system and probing power P can be described as [67]:

$$SNR = \frac{\text{signal power}}{\text{noise power}} \propto \frac{\delta^2 P}{BW} \tag{2.3}$$

The material ablation threshold places a physical restriction onto permissible input power densities, consequently restricting signal amplitudes achievable without material damage. Distributing the illumination over a larger area allows this restriction to be overcome and deliver threshold levels of input power without the risk of material damage. Further increase in the amplitudes of the generated waves can be achieved by appropriate distribution of acoustic sources to provide superposition of their contributions at a selected location on the sample. For example, the focusing of converging SAWs from annular or arc-shaped acoustic sources [81–84] or the creation of periodic illumination to produce an array of spatially-phased ultrasonic sources [85–88].

Although providing gain in amplitudes and high spatial resolution, the use of focused waves is of limited interest in the current work as it requires scanning to interrogate an area, whereas the use of rectilinear arrays producing plain highly-directional Rayleigh waves is the most suitable for the target application.

At the same time, the use of spatially-distributed arrays provides additional gain from reduction of signal bandwidth, directly proportional to the number of array elements. Temporal modulation of a single source can provide similar bandwidth reduction by creation of a toneburst signal, and a combination of temporal and spatial modulation [79, 80, 89, 90] enables to increase the amplitudes of the generated signal in particular direction/location on the sample, operating similar to a phased array. Similar solutions have been realised for longitudinal waves [91–96].

The temporally-modulated phased arrays use controlled time-delayed activation of the ultrasonic sources which results in somewhat complex electronics and bulky optics, requiring multiple delay lines [90] or laser cavities [95]. Periodic spatial arrays with simultaneous activation, on the other hand, are the simplest to realise and the least expensive, offering a combination of narrowband generation with physical enhancement of signal amplitudes. They are highly suitable for generation of surface waves and industrial applications.

The use of spatially-periodic illumination provides general increase in the generation efficiency due to the introduction of additional lateral constrains by the shadow (cold) zones along the surface [73]. A 20% amplitude increase was reported from a simple introduction of a sharp-edge aperture into an unfocused laser beam [77].

To provide constructive superposition of its elementary contributions, the sources in the array should be appropriately distributed. The highest generation efficiency is achieved by matching of the source separation distance a to the wavelength of the generated SAW $\Lambda_{SAW} = a$. In this case

the stresses generated by a single source at $t = 0$ arrive under the neighbouring source at $t = \Delta t$ determined by the Rayleigh wave velocity c_R, and add in phase. The source separation can then be selected to enhance the generation of the required frequency f_{SAW}:

$$a = \frac{c_R}{f_{SAW}}$$

An 11x increase in signal amplitudes was reported for laser-generated SAW in [85] when this condition was met. Similar peak efficiency condition can be found for generation of Rayleigh waves by a quartz plate with a comb-like metal structure consisting of projections and slots [28], as well as in operation of the inter-digital transducers [97]. Considering Gaussian illumination profile of each source, a line width d can be additionally optimised [87]:

$$d = \frac{\sqrt{2}a}{\pi}$$

The frequency spectrum of the generated wave $G(f)$ is formed from the spectrum of the wave generated by a single source $H(f)$ and the array function $S(f)$ describing the shape, number and separation of the elements [87, 88]:

$$G(f) = H(f) \cdot S(f)$$

For the rectilinear array of evenly-spaced and illuminated sources:

$$S(f) = \frac{\sin(\pi N f_0 \Delta t)}{\sin(\pi f_0 \Delta t)}$$

The bandwidth of the signal generated with such an array is inversely proportional to the number of sources N. Considering first zero-crossings around the fundamental frequency f_0 in the first instance, it can be determined as [87]:

$$BW = \frac{2f_0}{N}$$

The reciprocal increase in SNR follows from equation 2.3 [67, 87, 95], where a joint 8x reduction in bandwidth and 8x increase in total signal levels were reported to produce 64x increase in SNR in [87], and a 9x increase in PTP SAW amplitudes was similarly reported in [95] from a 10-source phased array.

The practical realisations of the laser arrays range from multiple time-delayed laser cavities [95] for temporal modulation to the use of White cell optical delay cavity [94], multiple beam/cavity lasers [79, 91, 95] and arrays of optical fibres [80, 89] for the phased arrays.

The most common configurations for the spatially-distributed arrays with simultaneous activation include the placement of an optical element between the source and the sample (figure 2.7) in the form of alternating transparency masks [70, 85, 98], optical diffraction gratings [87], lenticular arrays [92, 93], holographic diffraction elements [83, 84, 99], or the use of two-beam interference pattern projected onto the sample surface [86, 100, 101].

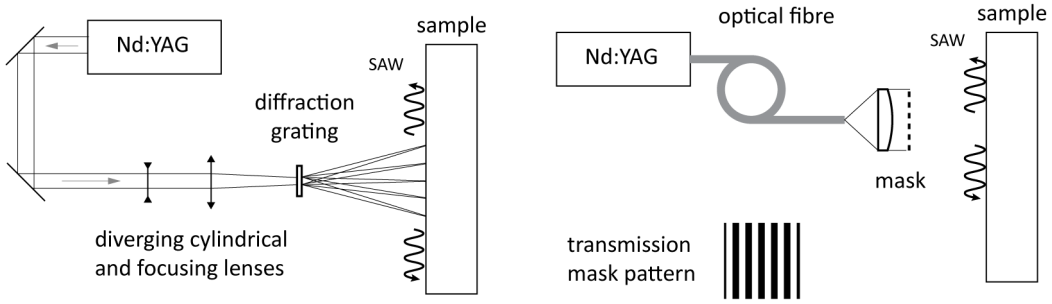

(a) Diffraction grating

(b) Transparency mask

Figure 2.7: Schematic diagram illustrating optical configurations that use optical elements in the path of the illuminating beam to produce linear thermoelastic arrays.

Alternatively, an array of absorbant lines can be created on the sample itself [1,102–105] producing an integrated optically-activated transducer. In this case the desired temperature distribution is created on the sample in the instance of array illumination according to the introduced high/low absorption areas. This technique utilises the increase of the generated wave amplitudes by enhancement of the sample surface absorption at locations of array sources. The effects of enhanced generation by a sample coated with a layer of absorbant materials such as black paint [87, 106], Ti/Al film [85,86], Kodak 'opaque' have been shown and consistently employed.

The benefit of this technique is the ability to operate on transparent samples and to tailor the absorption and generation efficiency to the material of the interrogated sample. As no additional optics are required to form acoustic sources on the sample (e.g. masks), the system can be made compact which is important for limited-space applications. Additionally, the use of collimated beams allows large and flexible stand-off distances, unlike diffractive elements and lenticular arrays where the sample is located in the focal plane.

Chapter 3 presents more details on the design, operation and fabrication of these transducers that constitute the base for present work.

2.2.3 Optical detection of surface waves

The use of lasers for optical detection of ultrasound provides similar benefits to non-contact optical generation, namely – the absence of couplants, large stand-off distances, applicability to a wide range of materials independently of their conducting or magnetic properties, and remote operation. Combined with laser generation, it allows to realise the full potential of remote non-contact ultrasonic inspection.

Optical detection on opaque materials is performed by interrogating the surface, perturbed by the propagating wave, with a probing laser beam and analysing the changes introduced into the reflected or scattered light [16]. The detection efficiency and sensitivity are thus significantly affected by the surface finish and reflectivity which present the main barriers for industrial application [67].

Unlike with laser generation, where operation principle remains the same (and the main efforts are directed to control the ultrasonic source and generation efficiency), the distinctive effects of the propagating wave onto the amplitude, phase or frequency of the interrogating beam can form the base for the detection system [107], separating the techniques according to the sensed parameters. Further development of particular methods pursued the increase in sensitivity of detection [108], frequently employing excessive auxiliary optical and electronic components for signal processing or stabilisation, and producing complex and bulky systems. Additional efforts were therefore made towards the reduction of the overall system size and complexity, restricting industrial applications. Comprehensive reviews of the techniques are offered by [16, 107–109] with descriptions of some industrial applications in [68] and a comparative assessment of the techniques for detection of the Rayleigh waves in particular in [110]. An overview of the main operation principles, and the techniques relevant to the present work is presented below.

Sensing principles

Optical detection of ultrasound is based on sensing of the time-varying changes introduced by the propagating wave into the reflected beam. Consider the propagating surface wave with displacement amplitude δ and wavelength Λ illustrated in figure 2.8 and described by equation 2.4, and the probing field E_{r0} reflected from the surface in the absence of SAW, described by equation 2.5:

$$\delta(x,t) = \delta\cos(\omega_a t + k_a x) \tag{2.4}$$

$$E_{r0} = E_0 \exp[j\,(\omega_{opt} t + k_{opt} z + \phi_0)] \tag{2.5}$$

where $\omega_a = 2\pi f_a$ and $\omega_{opt} = 2\pi\nu$ for acoustic and optical frequencies f_a and ν, $k_a = 2\pi/\Lambda$ and $k_{opt} = 2\pi/\lambda$ are acoustic and optical wavenumbers, E_0, ϕ_0 and λ are the amplitude, phase and wavelength of the reflected optical field respectively, and t is time.

In the presence of the acoustic wave, the optical path of the reflected light ray is reduced by 2δ, introducing the corresponding change of phase into the beam, so that equation 2.5 becomes:

$$\begin{aligned} E_{r1} &= E_1 \exp[j\,(\omega_{opt} t + k_{opt}(z_0 - 2\delta(t)) + \phi_0)] = \\ &= E_1 \exp[j\,(\omega_{opt} t - 2k_{opt}\delta\cos(\omega_a t) + \phi_1)] \end{aligned} \tag{2.6}$$

where $\phi_1 = \phi_0 + k_{opt} z_0$

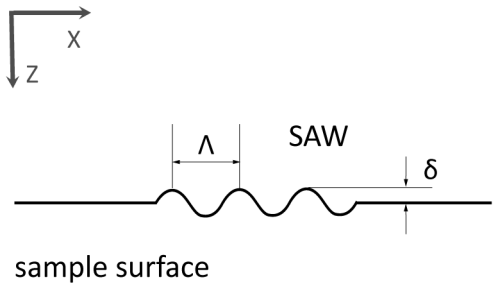

Figure 2.8: Representation of the propagating surface wave geometry.

From equation 2.6 the phase of the reflected beam is seen to be modulated proportionally to the surface displacement amplitude δ at the ultrasonic frequency ω_a. At the same time, the surface disturbance moving with velocity $\frac{d\delta(t)}{dt} = -\delta\omega_a \sin(\omega_a t)$ produces the Doppler frequency shift of the reflected wave proportional to the ultrasonic frequency f_a:

$$E_{r1} = E_1 \exp[j\,(2\pi\,\{\nu + 2k_{opt}\delta f_a \sin(2\pi f_a t)\}\,t))] \tag{2.7}$$

The sensing options provided by equations 2.6 and 2.7 determine the techniques used to collect and process the optical signal and the corresponding system designs for displacement and/or velocity measurements.

2.2.4 Direct, intensity-based detection methods

The first group of methods is based on deflection of the interrogating beam by the propagating acoustic wave, causing intensity variation in a given direction of the photodetector at acoustic frequency f_a, and directly-proportional to the wave amplitude δ. Depending on the ratios of the acoustic wavelength Λ and the size of the beam D, two main configurations are the *knife-edge detection/optical beam deflection* ($\Lambda/2 > D$) and *surface grating diffraction* ($\Lambda < D$).

Knife-edge detection is the simplest method to realise, which is based on sensing the spatial deviation of the returning beam on the photodetectior (figure 2.9a). The deflection of the focused laser beam by the tilt of the propagating wave Θ produces a spatial shift of the returning beam on the photodetector proportional to 2Θ which can be detected by placing a knife-edge into the path of the returning beam, by splitting the beam into two symmetric parts with the use of the differential detection (probe-beam deflection), or by the use of position-sensitive detectors.

Surface-grating diffraction techniques exploit the diffraction of the expanded laser beams at the periodic deformations produced on the surface by the propagating wave (figure 2.9b). These

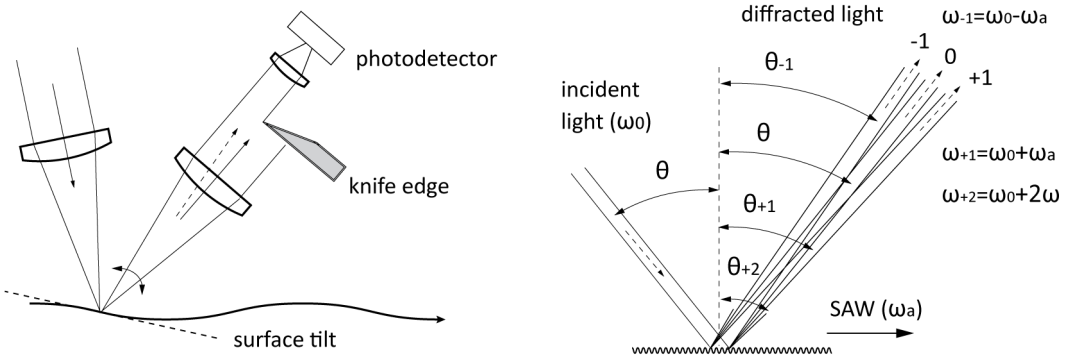

(a) Knife-edge detection

(b) Surface-grating technique

Figure 2.9: Optical detection methods based on beam deflection by SAW.

deformations act as a reflective phase grating splitting the incident beam into the number of orders propagating away from the surface at distinct angles Θ_m, determined by the ratio of the optical λ and acoustic wavelengths. For normal incidence and the number of orders m:

$$sin\Theta_m = \frac{m\lambda}{\Lambda}$$

The distribution of intensities among the orders is determined by the amplitude of the surface displacement δ, and for small displacements $\delta << \lambda$ (where higher order contributions are insignificant), the ratio of the first-order I_1 and zero-order I_0 intensities is described as:

$$\frac{I_1}{I_0} = \left(\frac{2\pi\delta}{\lambda}\right)^2$$

Due to the movement of the wave, the frequency in the diffraction orders is up- or down-shifted by the acoustic frequency as $\nu \pm mf_a$, and their phase is advanced with respect to the main order. In instances where the diffraction orders overlap, their interference produces intensity fluctuations at the acoustic frequency.

A range of detection techniques use well-separated diffraction orders, where the direct measurement of the intensities in the corresponding orders can be used to determine SAW amplitude, velocity or visualise the wave field and propagation [16]. At the same time, the interference in the region of the order overlap can also be used for SAW measurements, for example combining it with the knife-edge configuration to monitor intensity fluctuations. Additionally, optical heterodyne detection can be performed where one of the separated orders is combined with a reference beam on a photodetector, or spatial interference fringes produced by the order overlap are used. The latter technique reported in the original work by Korpel [111] used a transmittance mask with the spatial period equal to the ultrasonic wavelength placed in the overlap region of the 0-th and the

±1 orders, producing intensity fluctuation on the detector during the wave motion.

The comprehensive review of the the diffraction-based probing of the surface waves by Stegeman [112] summarises the techniques and presents the corresponding relations between the properties of the SAW and the diffracted fields.

2.2.5 Phase and velocity-based interferometric detection methods

This separate group of methods uses interferometric systems to convert the phase and frequency modulation of the reflected beam, caused by the propagating SAW (equations 2.6 and 2.7), into a measurable variation of intensity.

Two-beam Michelson interferometer is the simplest example of the interferometric detection of the surface displacement (figure 2.10a). The probing illumination is divided into two paths by a beam splitter, with one beam directed towards the sample and the other travelling to the reference mirror. On their return after the corresponding reflections the beams are recombined and directed to the same photodetector. Representing the reference field in the absence of SAW by equation 2.5, and the object field with the phase modulated by the surface displacement by equation 2.6, the resulting intensity on the detector is expressed as:

$$I_D = \mid E_{r0} + E_{r1} \mid^2 = E_{r0}^2 + E_{r1}^2 + 2E_{r0}E_{r1}\cos\left(\frac{4\pi\delta(t)}{\lambda} + \phi_{st}\right) \tag{2.8}$$

where $\phi_{st} = \frac{2\pi}{\lambda}(z - z_0)$ is a static phase difference between the reference z and the object z_0 paths in the absence of the ultrasonic wave, and λ is the optical wavelength.

Noting the last term in equation 2.8, the detected illumination is seen to be modulated by the surface displacement $\delta(t)$, where for $\delta << \lambda$ the fluctuation of intensity is strongly dependent on

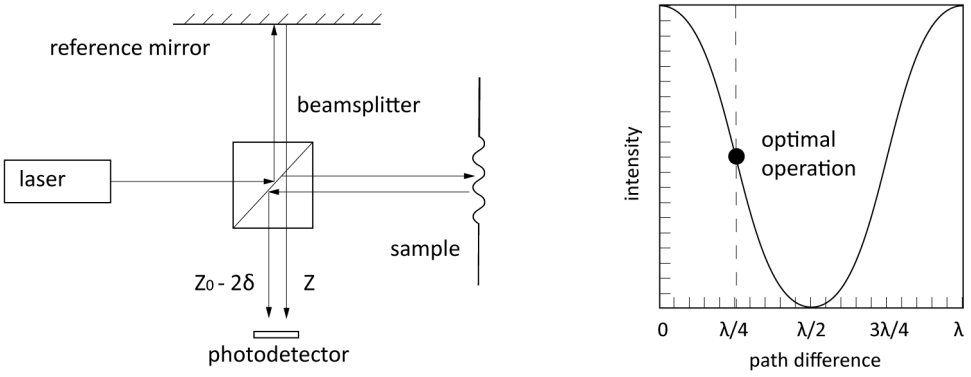

(a) Michelson interferometer

(b) Intensity output as a function of path differnce

Figure 2.10: Interferometric detection of surface displacement with Michelson interferometer.

the static phase difference ϕ_{st}. The optimal operation of the interferometer is achieved when the amplitudes of the recombined beams are equal $E_{r0} = E_{r1}$ to provide the best contrast, and the static phase difference is $\phi_{st} = \pi/2 = \lambda/4$ to ensure the highest sensitivity (figure 2.10b).

The optimal performance and sensitivity of the interferometer are defined by the precisely-controlled physical path difference and depend on its mechanical stability, seriously affected by the ambient vibrations and temperature fluctuations. To overcome this some techniques employ active path stabilisation using electronic feedback from the detector to adjust the position of the mirror. Other methods remove path-length dependency by modifying the optical signal collection and processing. Most of these systems require the use of additional optical elements and electronic circuitry, increasing the size of the system and in some cases slowing down its response at high modulation frequencies.

Heterodyne detection is one of the examples where active stabilisation is not required, making the interferometer more robust to environmental vibrations and better suitable for industrial applications. The signal in heterodyne systems is proportional to the velocity of the wave and is detected by using a frequency-shifting element (such as an acousto-optic modulator) in the reference arm of the interferometer. The detected signal in this case contains a carrier at the frequency of the local oscillator and two Doppler-shifted side bands proportional to the frequency of the ultrasonic signal. The surface displacement produced by the acoustic wave thus causes detectable frequency modulation of the recorded signal, removing dependency on the optical path.

The variety of other types of the interferometric systems and configurations are possible, and have been extensively reviewed in [16, 93, 108, 109].

Whereas the beam-deflection techniques, Michelson-type displacement and heterodyne interferometers are only effective on optically-flat highly-reflective surfaces, the solutions for operation on rough surfaces are provided by the use of a confocal Fabry-Perot interferometer (CFPI) and non-steady state photo-EMF crystals [109, 110] described below.

Confocal Fabry-Perot interferometer consists of an optical cavity where the interference occurs between the multiple copies of the same wavefront reflected from the sample and delayed in time. The specular light field with random phase produced by rough surfaces in this case interferes with its own time-delayed copies, enabling operation on rough samples. The operation principle is based on a change in transmittance of a wavelength-selective cavity with length being multiple of the operation wavelength. The Doppler frequency shift introduced by the propagating wave produces decrease in the output from the cavity, proportional to the acoustic wave velocity.

Photo-refractive crystals and photo-EMF detectors offer cheaper more compact systems, able to operate with diffuse reflections from rough surfaces and providing some compensation of whole-body vibrations [108]. One of the representative examples offering similar performance to CFPI [110] is the interferometer based on the non-steady-state photo-induced electromotive forces (EMF). The interference pattern produced by the reference and the probing beams on the surface of the crystal creates a static space-charge fringe pattern resulting from the diffusion and entrapment of the photo-generated carriers. The shift of the interference fringes caused by the wave motion induces the EMF current across the material proportional to the displacement.

2.2.6 Distributed detector configurations

Similarly to the arrays of ultrasonic sources discussed in section 2.2.2, a directional detection of surface waves can be performed using arrays of optical receivers. The development of the distributed detectors is guided by the same principles applied to the laser generation – distribution of the probing power, allowing increased input without sample damage, and improvement in overall SNR by narrowing the detection bandwidth (equation 2.3). Additional increase in sensitivity can be achieved by matching the bandwidths of the detection system to that of the generated SAW. The coherent addition from the simultaneous detection by the array elements increases the amplitude of the detected signal [113].

The detector arrays are formed by modifying the distribution of the probing beam on the sample, where the transmission masks, diffraction gratings [113] or a set of optical fibres [89] can be used. The use of rectilinear arrays produces a detector with high directional sensitivity towards the normal to its line elements (proportional to $\pi d/\Lambda$, where d is the line width), which can be used for inbuilt discrimination of the unwanted reflections arriving from different angular directions. Appropriately spacing the elements of the array allows to perform frequency-selective detection of SAWs, with the maximum sensitivity achieved for equidistantly-spaced elements with the spacing matching the acoustic wavelength. The array detection using homodyne and heterodyne two-wave mixing holographic interferometer based on photo-refractive crystal was reported in [113], and a heterodyne fibre interferometer in [89].

The excessive optical elements and complex electronic circuitry of the interferometric systems resulting in large system sizes and limited manoeuvrability can be replaced by the use of a simple optical transducer, based on the modified diffraction technique [1, 105]. The transducer, designed as a reflective phase-grating produced on the sample, combines the interferometric performance with the frequency-selective directional detection offered by receiver arrays, without requiring stabilisation or sensitive alignment. Operating with stability of a common-path interferometer, it

can be adapted to industrial environments.

The operation principle is similar to a deformable grating modulator [114], where the electrode array step height is changed by the applied voltage, producing intensity modulation in diffracted light. Similar grating was reported integrated into a CMUT to increase its detection efficiency [115].

More details on the design, operation principle, and fabrication of the optical transducer used in this work are presented in Chapter 3.

2.2.7 Fibre-coupled operation

The benefits of optical generation and detection of ultrasound can be extended even further by the use of optical fibres. The practical advantages include flexibility, ability to guide the illumination to and from the sample over large distances and around obstacles. The small dimensions of the fibres enable access to confined spaces and hard-to-reach components. Optical fibres can provide multiple sources to create phased arrays or detector arrays, used as delay lines in interferometric detection, or act as sensors themselves.

The laser generation of ultrasound via optical fibres has been demonstrated in a number of systems where fibres were used simply for light-delivery [98] (figure 2.7b) or to shape and time-delay the ultrasonic source (as phased-arrays) [80, 89].

In terms of detection, an optical fibre itself can be used as a sensor converting the strains induced in the fibre by acoustic waves into the phase delays or spectral shifts. Such intrinsic fibre sensors can be embedded into the part [116], and form a separate branch of fibre-optic detection.

The use of the fibres as a light-delivery method, with the ultrasonic sensing performed by an external optical/electronic system, can be implemented with most of the described optical

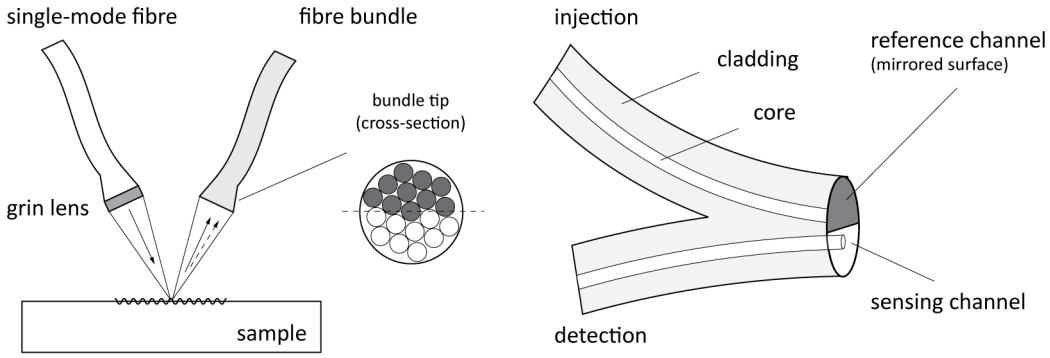

(a) Knife-edge

(b) Michelson fibre interferometer

Figure 2.11: Example of fibre-optic detection systems.

detection techniques. A modified knife-edge method was demonstrated [110] where a split fibre bundle was used for light collection, combined with the differential circuit (figure 2.11a). Various types of optical-fibre interferometers (OFI) have been reported, including CFPI [117, 118], active homodyne and heterodyne interferometers [89, 119], Sagnac-type time-delayed interferometers for SAW and bulk-waves [120, 121]. A retro-reflection of the probing beam off the polished tip of the fibre can be used to create a Fizeau-type interferometer [122, 123] where the static path difference is determined by the tip-to-sample distance, or a two-core optical fibre (figure 2.11b) can be used for Michelson configuration [124]. The use of a thin polymer film on the end of the fibre operating as a small Fabry-Perot interferometer was reported in liquids [125].

In most configurations the fibres form one arm of the interferometer, provide a time-delay or ensure equal paths for multiple beams. The performance and stability of the OFI is therefore sensitive to fibre bends, external pressure and temperature variations, with the common-path interferometers providing the most stability and robustness.

2.2.8 Summary

Since the potential of laser-ultrasonic systems was recognised, further method and system developments were driven towards the increase of the generation and detection efficiencies, practical system applicabilities, enabling operation in industrial environments, reduction of system size and complexity.

The generation of desired acoustic modes was shown to be achieved by the appropriate control of the ultrasonic source, and the efficient generation of the highly-directional Rayleigh waves produced by distributing illumination into an array of line sources. The use of multiple lasers, optical fibres, transmission masks and diffraction gratings have been demonstrated to shape the illumination.

The effects of the surface displacement produced by the acoustic wave onto the amplitude, phase and frequency of the probing beam provide a range of options for the corresponding detection techniques, system designs and signal processing. The choice of a particular technique greatly depends on the required operational requirements and sample surface finish and curvature.

The use of deflection methods is perhaps the simplest, does not require extensive optical elements or complicated electronic circuitry, cheap and relatively robust to the ambient temperature variations or vibrations. Functionality of these systems, heavily-dependent on test geometry, places some limitations on operational frequencies and stand-off distances. As acoustic surface displacements are quite shallow (especially for laser-generated ultrasound), the direct intensity-based sensitivity is also limited. Additionally, the effective operation is only achieved on optically-flat highly-reflective surfaces.

The interferometric systems can operate with higher frequencies but are expensive, usually bulky and not portable, with limited manoeuvrability. Precise alignment is critical for their operation and high sensitivity to environmental conditions (requiring stabilisation schemes) can make them impractical in some applications. Although a number of developed systems show good performance on rough surfaces, most require extensive optical elements and electronic circuitry.

The use of wave-mixing and photo-EMF can offer similar performance and more compact systems, however their slower response restricts operation at high frequencies.

Similarly to the generation of SAW, efficient directional optical detection could be performed by an array of optical receivers formed on the sample surface by using transmission masks or diffraction gratings.

To provide flexibility, access in confined spaces and reduction of system size and complexity, making the LU systems more appealing for industrial applications, both generation and detection of ultrasound can be performed via optical fibres with most of the described techniques. The optical fibre interferometers exist in most of traditional configurations and enable manoeuvrable operation over great distances with smaller probe sizes. Their performance and stability however become dependent on fibre bends and external environmental conditions.

The founding technique for the generation and detection of Rayleigh waves in present work uses spatially-distributed arrays of ultrasonic sources coupled with similar arrays of optical receivers – cheap optical transducers (CHOTs). In both cases the arrays consist of physical metal patterns on the surface of the sample. The generation array shapes the ultrasonic source on the sample and reduces the size of the system by eliminating the need for additional optical elements. The detection array operates similar to a deformable grating modulator, combining interferometric operation with frequency-selective directional detection, without requiring stabilisation or additional optical components. The design, operation and fabrication of CHOTs are discussed in the following chapter.

Chapter 3

Optically-excited ultrasonic transducers (CHOTs)

This chapter provides the description of operational principles, design and fabrication methods of the cheap optical transducers (CHOTs) that use laser activation to generate and detect surface acoustic waves. The present work is an extension of the previously-developed technique described in [1] and [105], operation of which is outlined in context of the considered practical application.

Cheap optical transducers are nanometre-height structures located on the surface of the sample that use spatially-modulated absorption of laser light for generation of acoustic waves, and phase-modulated reflection for ultrasonic detection. Designed as rectilinear arrays they allow efficient, frequency-selective and highly-directional, generation and detection of surface waves, where increased signal gain is achieved by coherent addition of signals from individual array elements and narrow, matched, generation and detection bandwidths.

Located on the sample, CHOTs require only simple collimated illumination producing simplified, compact optical arrangements without requiring additional optical elements to shape the acoustic source and receivers. The use of collimated illumination allows to restrict operation to the thermoelastic regime (by spreading the laser energy over a larger area) and enables flexible stand-off distances. Although requiring to be located on the sample, CHOTs low profile ensures minimal impact onto the surface or operation of the inspected component, where the transducers can remain permanently or be integrated into the structure. Additionally, the fixed locations of the transducers facilitate repeatable measurements over time, with potential for active-SHM applications.

The miniature size and simplicity of the optical arrangement can be easily paired with fibre-optic operation (Chapter 4) to provide flexible access to components in confined spaces or with

complex access paths. As both the ultrasonic transduction and sensing with CHOTs are performed on the sample itself, with the fibres acting solely as light-guiding media, the system provides robust performance with low sensitivity to external environmental factors and vibrations (unlike the optical-fibre interferometers), and without the need for stabilisation.

Large quantities of the transducers can be fabricated at low cost using well-established photolithographic or spray-painting techniques, with a number of recently-investigated methods targeting fabrication in-situ [126].

The use of CHOTs has been previously reported for the investigation of the sample stress states based on velocity measurements [127] and operation with ultrahigh-frequency SAWs [128]. The CHOTs application in this work is extended to flaw detection within the aerospace NDT context.

3.1 Transducer design and operation

Whereas both generation and detection functions could be performed by the same element in conventional contact methods, the disparate nature of the mechanisms employed by optical generation and sensing (Chapter 2) necessitates the differences in CHOTs operation principles, with corresponding function-specific designs. Consequently, a *g-CHOT* is used for generation of acoustic waves using pulsed-laser excitation, and a *d-CHOT* is used to perform sensing, using a continuous wave (CW) probing illumination. Both transducers can operate independently or be combined with other generation/detection methods to exploit particular strengths of individual techniques. Used jointly, the g-CHOT and the d-CHOT form a *coupled* configuration, providing a robust and sensitive system with fully-remote operation. Given certain modifications, a hybrid CHOT performing both functions can be potentially created, although separate optical systems would still be required.

The wave mode, directivity and frequency of CHOT operation are defined by the transducer geometry which can be customised for a particular application or a task to operate with bulk [105] or surface acoustic waves [1] with plane or focused wavefronts. Considering the required inspection task in the proposed application and high sensitivity of the Rayleigh waves to surface flaws, the present work was based on the use of the plane-SAW CHOTs.

3.1.1 Generation of surface acoustic waves: g-CHOT

The generation of surface waves is performed by a *g-CHOT* (figure 3.1). The underlying operation principle consists of controlling the ultrasonic source by appropriately modifying energy distribution on the surface of the sample, where spatially-periodic illumination in the form of the line-source arrays is used to provide enhanced highly-directional generation of the Rayleigh waves.

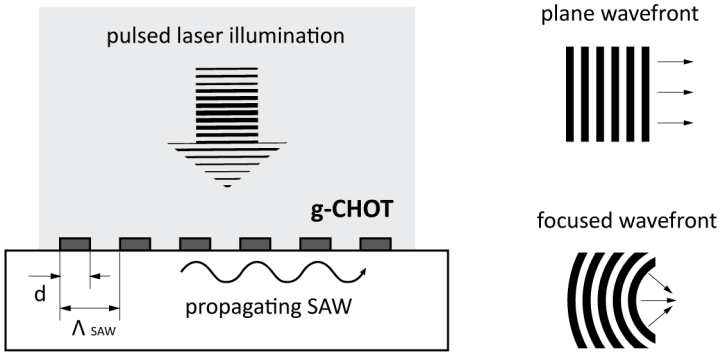

Figure 3.1: Generation of surface acoustic waves with a g-CHOT structure: schematic representation of the sample cross-section (left), and g-CHOT designs for plane and focused SAWs (right).

Instead of using additional optical elements (e.g masks) to produce required temperature distribution, the g-CHOT achieves this by creating periodic areas of high and low absorption which can be produced by appropriate sample patterning. Upon laser illumination, the g-CHOTs can operate both by creating 'hot' zones on weakly-absorbing materials or 'cold' zones on strongly-absorbing substrates, acting as an absorber or reflector respectively. The absorbing g-CHOT removes the dependency of the laser generation process on the absorbing properties of the samples, enhancing generation on otherwise weakly-generating materials and enabling operation on transparent substrates. The techniques to enhance ultrasonic generation by increasing the surface absorption are well known and have been extensively used in the past [85–87, 106]. The use of the periodic absorbing structures for ultrasonic generation has been previously reported in [102, 103, 129–133] with further development of this technique into a g-CHOT described in [1, 105] providing increased control over the characteristics of the generated acoustic waves, and additionally enhancing system performance by pairing it with the d-CHOT detection.

Transducer geometry

The geometry of the transducer pattern determines the wave mode, directivity and frequency of the generated acoustic waves. The g-CHOTs for surface waves use rectilinear arrays consisting of parallel or arc-shaped lines to produce plane, converging/diverging and focused wavefronts (figure 3.1), where the forward- and the rearward-travelling waves are simultaneously generated (Chapter 2). The selective generation enhancement that occurs at the acoustic wavelength matching the spacing of the g-CHOT elements a provides frequency control of the generated wave, considering

wave velocity in material c_R, as:

$$f_{SAW} = \frac{c_R}{a}$$

Therefore, if the Rayleigh wave velocity in the sample material is known, the g-CHOT pattern is designed with the element separation $a = \Lambda_{SAW}$ to produce the desired frequency f_{SAW}.

Here an important operational difference should be noted. Compared to conventional transducers the g-CHOT operates at a fixed wavelength, with operational frequency being further determined by the wave velocity in material. This effect results in the change of central frequency when the same transducer is used on different materials. For example, the g-CHOT designed with the element spacing $a = 625$ μm appropriate to produce 5 MHz SAWs on crown glass with Rayleigh wave velocity of 3,127 m/s, would generate acoustic waves at $f = 4.7$ MHz if titanium sample was used ($c_R = 2{,}958$ m/s). Therefore, when referring to the CHOTs operational frequencies, the material of the sample should be also stated. Similarly, the temperature-induced change of the wave velocity would produce deviations in operational frequency. Considering equally frequency-selective design, similar considerations apply to the operation of the d-CHOT.

Signal frequency spectrum

The frequency spectrum of the generated wave is determined by combined contributions from an individual line source, the spatial distribution of the elements in the array, and the spatial and temporal energy distribution in the illuminating beam.

A single line element of the CHOT (geometry shown in figure 3.1) can be represented by a rectangular function with the width d, and the distribution (location) of elements in the array is further described by a Dirac comb function – a train of equally-spaced Dirac delta functions $\delta(x)$ with the element separation a (for the square wave $a = 2d$):

$$\text{rect}\left(\frac{x}{d}\right) = \begin{cases} 1 & , \mid x \mid \leqslant \frac{d}{2} \\ 0 & , \mid x \mid > \frac{d}{2} \end{cases} \qquad \text{comb}\left(\frac{x}{a}\right) = \sum_{n=-\infty}^{+\infty} \delta(x - na)$$

The number of illuminated sources in the array is additionally determined by the diameter of the laser beam, with the spatial profile described by a Gaussian function $g(x|q)$:

$$g(x|q) = I \cdot \exp\left[-\frac{x^2}{q^2}\right]$$

where $q = Na/2$ is the radius of the laser beam illuminating N lines with the spatial period a, and I is the power density.

A coherent addition of SAWs generated by individual line sources of the g-CHOT array is achieved when the propagation time between two adjacent elements (temporal period) is $\Delta t = \Lambda_{SAW}/c_R$, where the line width of the square-wave CHOT profile is $d_t = \Delta t/2$.

The corresponding components of the time-domain response of the generated SAW and their frequency spectra (defined by the g-CHOT geometry) are:

Time Domain	Frequency Domain
$\text{rect}\left(\frac{t}{d_t}\right) = \begin{cases} 1 & , \mid x \mid \leqslant \frac{\Delta t}{4} \\ 0 & , \mid x \mid > \frac{\Delta t}{4} \end{cases}$	$\text{sinc}(fd_t) = \xi_1 \cdot \frac{\sin(\pi f \Delta t/2)}{\pi f \Delta t/2}$
$\text{comb}\left(\frac{t}{2d_t}\right) = \sum_{n=-\infty}^{+\infty} \delta(t - n\Delta t)$	$\text{comb}(f2d_t) = \xi_2 \cdot \sum_{n=-\infty}^{+\infty} \delta\left(f - \frac{n}{\Delta t}\right)$
$g(t\mid Nd_t) = \exp\left[-\frac{4t^2}{(N\Delta t)^2}\right]$	$G\left(f\mid\frac{1}{Nd_t}\right) = \xi_3 \cdot \exp\left[-\frac{(\pi N \Delta t f)^2}{4}\right]$

where ξ_1, ξ_2, and ξ_3 are constants defining the amplitudes.

Combining the elementary contributions described above and considering temporal characteristics of the laser pulse described by a Gaussian function $g(t|\tau)$, the time-domain response of the generated SAW $y_g(t)$ and the frequency spectrum of the signal $Y_g(f)$ are:

$$y_g(t) \propto \left[\text{rect}\left(\frac{t}{d_t}\right) \otimes \text{comb}\left(\frac{t}{2d_t}\right) \cdot g\left(t\mid Nd_t\right)\right] \otimes g(t|\tau) \tag{3.1}$$

$$Y_g(f) \propto \left[\text{sinc}(fd_t) \cdot \text{comb}(2fd_t) \otimes G\left(f\mid\frac{1}{Nd_t}\right)\right] \cdot G\left(f\mid\frac{1}{\tau}\right) \tag{3.2}$$

where $\otimes$ denotes the operation of convolution, $g(t|\tau) = I \cdot \exp\left(-\xi t^2/\tau^2\right)$ describes Gaussian envelope of the laser pulse with the pulse duration τ measured as a full width at half maximum (FWHM), $\xi = 2.77$, and $G(f|\tau^{-1}) \propto \exp[-(\pi\tau f)^2]$ is the frequency content of the laser pulse.

The terms in [ ] brackets in equations 3.1 and 3.2 are directly defined by the transducer geometry, and their relationships in time and frequency domains are illustrated in figure 3.2 noting characteristic widths of the functions. Denoting these terms as $p(t)$ and $P(f)$ respectively, the generated signal and its frequency spectrum are:

$$\begin{aligned} y_g(t) &= p(t) \otimes g(t|\tau) \\ Y_g(f) &= P(f) \cdot G\left(f\mid\frac{1}{\tau}\right) \end{aligned} \tag{3.3}$$

Figure 3.3 displays theoretical spectra plotted for $N = 10$ line sources, $\Lambda_{SAW} = 625\ \mu m$ designed to operate at 5 MHz on BK7 glass with velocity c_R = 3,127 m/s, and the laser pulse duration $\tau = 10$ ns.

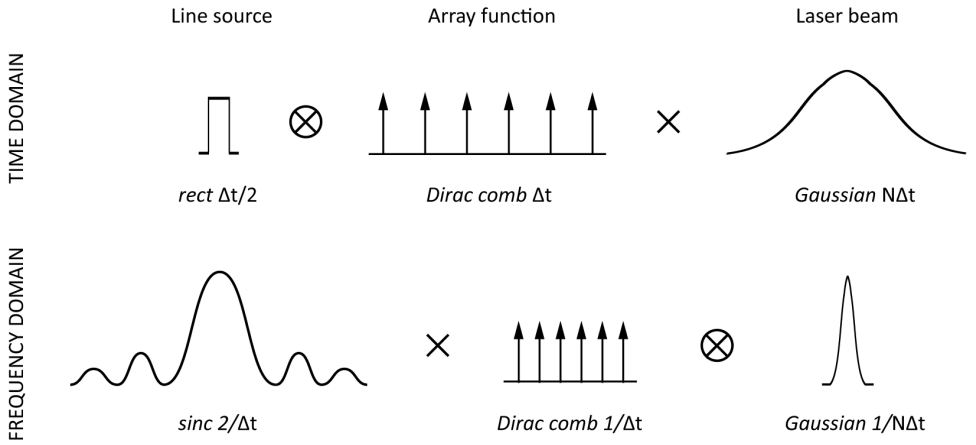

Figure 3.2: Formation of the SAW spectrum by the corresponding g-CHOT geometry.

The relations described above and shown in figures 3.2 and 3.3 essentially demonstrate spectral filtering of the laser pulse by the corresponding geometry of the transducer, where the g-CHOT element shape and the duty cycle d/a determine the envelope function and the present signal harmonics, and the generation frequency is defined by the element spacing. The bandwidth of the generated signal is inversely proportional to the number of illuminated lines N.

The amount of energy in the laser pulse available at the operational frequency of the g-CHOT limits the maximum achievable generation frequencies and sets the requirements to the pulse duration of the laser source. As the spectral content of the pulse is inversely proportional to the pulse duration, the operation at higher frequencies requires the use of shorter pulses. The use

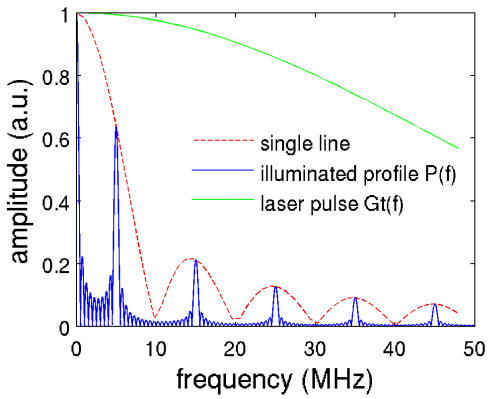

Figure 3.3: Formation of the frequency spectrum of the generated SAW showing theoretical, normalised spectra of a single illuminated line source, a full illuminated g-CHOT profile, and the frequency content of the laser pulse.

of absorbing metal structures to generate 5 GHz SAWs using femto-second lasers was reported in [103], whereas the operation of CHOTs was previously reported at frequencies as high as 82 MHz [127], and modelled up to GHz range [104]. In the present work, the operation frequencies do not exceed 5 MHz, and an 8-ns laser pulse is used (see Chapter 4).

Transducer material

The material of the g-CHOT plays a definitive role in the operation of the transducer, but only when considered alongside the material of the sample and the illumination wavelength. Based on creation of the periodic absorption contrast, the efficient generation on the highly-absorbing substrates necessitates the use of the less-absorbing or reflective g-CHOT materials, whereas for the weakly-absorbing or transparent samples a strongly-absorbing g-CHOT material would be required. For the periodic absorbers the generated surface displacement was shown [102] to be directly proportional both to the absorbed power density and the number of the illuminated sources, thus the generation enhancement can be achieved by increasing the g-CHOT material absorption.

The material absorption of the optical radiation is determined by the complex part of the wavelength-dependent refractive index $n^* = n - i\kappa$, where the real part n defines wave velocity, and κ is the extinction coefficient describing material wave attenuation. The coefficient of absorption for particular sample material and the generation wavelength λ (in vacuum) is found as:

$$\gamma = \frac{4\pi\kappa}{\lambda}$$

Based on the absorption of the substrate material, the function of the g-CHOT as an absorber or a reflector is selected, and the material of the transducer is chosen to provide the highest absorption contrast.

For efficient generation to take place, irrespectively of the g-CHOT role (absorber/reflector), the thickness of the transducer steps should be sufficient to provide maximal contrast. As mentioned in section 2.2, the absorption for most metals occurs within the skin-depth of material, and at near IR wavelength of the commonly-used Nd:YAG lasers can be estimated by using equation 2.2. Although this gives some idea of the required g-CHOT thickness, the optical properties of the metal films [134] are different from bulk metals and are thickness-dependent. A simple estimate of the film thickness based on the optical penetration depth where the transmitted intensity drops to a level of $1/e$ is given by:

$$z_e = \frac{1}{\gamma} = \frac{\lambda}{4\pi\kappa}$$

For a chromium (Cr) g-CHOT ($n^* = 3.544 - 4i$) at $\lambda = 1.064$ μm this gives the depth of $z_e = 42$ nm, compared to the skin-depth of bulk Cr $\delta = 13$ nm ($\delta = \sqrt{(\lambda/(\pi\sigma c\mu)}$, $\sigma = 5.104$ x 10^6 Ω/m,

$\mu_0 = 4\pi$ x 10^{-7} H/m, $\mu_r = 1$, $c = 3$ x 10^8 m/s, and $\mu = \mu_0\mu_r$). Provided the height of the g-CHOT steps exceeds this value, the penetrating radiation is fully absorbed within the transducer. In practice, the film absorption also depends on the deposition method and is frequently required to be thicker than this estimate. For more accurate evaluation of the absorption and the required film thickness, including the effect of the substrate material, a system of the Fresnel coefficients describing the amplitude ratios for the reflected and transmitted fields can be used in combination with the optical matrix transfer method [135]. The reflection R and transmission T coefficients for normal incidence are:

$$R = \frac{n_0 - n_1}{n_0 + n_1} \qquad \text{and} \qquad T = \frac{2n_0}{n_0 + n_1}$$

where n_0 and n_1 are the refraction indices of the interface materials (e.g. air and g-CHOT), and the absorption is accounted for by considering complex index of refraction $n_1^* = n - i\kappa$.

The height of the Cr g-CHOTs used in this work was in the range of 66–80 nm depending on the fabrication conditions, and is stated with the corresponding test results.

The operation principles and the design of the g-CHOT for generation of plane surface waves has been described, outlining the requirements to the transducer geometry and material, as well as to the laser source.

3.1.2 Detection of surface acoustic waves: d-CHOT

The *d-CHOT* is a reflective structure on the surface of the sample facilitating sensing of the ultrasonic wave (figure 3.4). With the geometry almost identical to that of the g-CHOT, the transducer is a rectilinear array of receivers providing frequency-selective and directional detection of the propagating SAW [89, 113]. The operation of the d-CHOT closely resembles the grating optical modulator [114, 136, 137] where the diffraction at a reflective phase grating is used to control the beam intensity and directivity according to an external input. The alteration of the d-CHOT profile by the propagating SAW represents such an input, and the associated changes in the reflected-light intensity provide the means for detection.

Operation principle

More specifically, each cell of the d-CHOT (one spatial period of the grating) represents a miniature common-path interferometer where the reference and the object beams are produced by the reflections from the facets and the grooves of the transducer profile, and the initial (bias) phase difference between them ϕ_{st} is introduced into the probing beam by the d-CHOT step height h. The reflected wavefront is additionally angularly separated into a finite set of the diffraction orders (figure 3.4), with intensity distribution between them determined by the introduced phase differ-

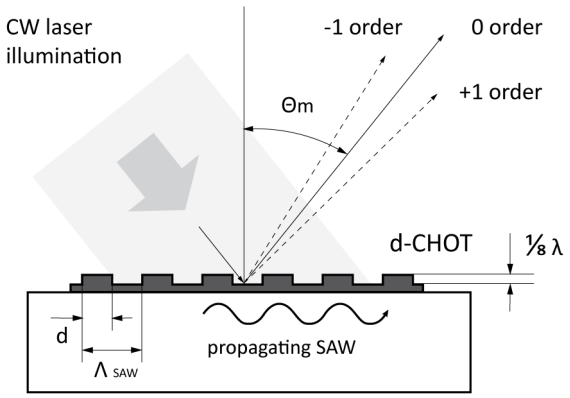

Figure 3.4: Detection of surface acoustic waves with a d-CHOT structure: schematic representation of the sample cross-section.

ence $\phi_{st} = 2kh$ (where $k = 2\pi/\lambda$ is the optical wavenumber). The distortion of the grating by the propagating SAW modifies the optical path difference in the reflected light, causing the change in the intensity distribution between the orders. Good illustration of this effect being used in sensing of displacement, acceleration and strains can be found in [137, 138] and [115]. The detection of ultrasound with the d-CHOT can thus be performed by monitoring the resulting intensity modulation in an isolated diffraction order. Figure 3.5 illustrates the operation principle of the d-CHOT, showing the modification of the transducer profile by the propagating wave and the corresponding change in the order intensities.

Similarly to a g-CHOT, the transduction between the acoustic and the optical waves is performed on the sample, resulting in a miniaturised simplified optical system that is only required to perform light-delivery/collection function. With the path difference between the interfering beams reflected from the top and bottom of the profile corrugation below the optical wavelength, the d-CHOT provides interferometric and robust performance without the need for stabilisation.

Geometrical characteristics

The intensity distribution produced by the illuminated d-CHOT in the far field corresponds to the Fraunhofer diffraction pattern [139] determined by the Fourier transform of the transducer profile geometry. In order to perform effective optical detection of SAW, the design of the d-CHOT accommodates both acoustic and optical inputs by matching the spacing of the transducer elements a to the wavelength of SAW Λ_{SAW}, and selecting their height h to provide the highest sensitivity to surface displacement, determined by the ratio h/λ and the corresponding operation

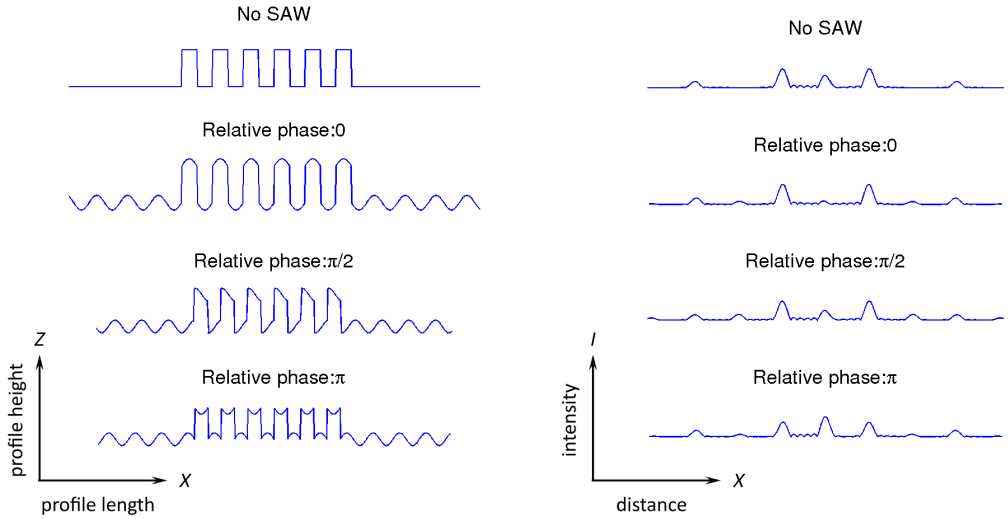

(a) Alteration of the d-CHOT profile

(b) Corresponding change in intensity distribution

Figure 3.5: Operation principle of the d-CHOT showing the alteration of the d-CHOT profile (a) and the corresponding intensity distribution in diffraction orders (b) as a function of the relative phase between the propagating SAW and the d-CHOT grating. The amplitude of the wave is largely exaggerated for illustrative purposes.

point of the transducer $\phi_{st}(h)$.

The locations of the diffraction orders corresponding to constructive interference of the single-element diffraction patterns are described by the grating equation as:

$$\Lambda_{SAW}(\sin(\alpha) + \sin(\Theta_m)) = m\lambda$$

Which for normal incidence becomes:

$$\sin\Theta_m = \frac{m\lambda}{\Lambda_{SAW}} \tag{3.4}$$

where α is the incidence angle of the probing beam with respect to the grating normal, and Θ_m is the diffraction angle defining the position of the m-th diffraction order for $m = 0, \pm1, \pm2...$ etc.

The width of the orders is inversely proportional to the number of the illuminated lines N as: $2\lambda/N\Lambda_{SAW}$. According to the ratio in equation 3.4 the angular separation of the diffracted beams increases with the SAW frequency. This determines the requirements to the numerical aperture and stand-off distance of the collection optics, and places the restriction on operational frequencies of the d-CHOT as the diffraction orders become evanescent at Θ_m approaching 90°. These restrictions however have little impact in the current work, as the highest d-CHOT frequency of 5 MHz on aluminium ($\Lambda_{SAW} = 581$ μm, $c_R = 2{,}905$ m/s) produces the first order deflection of

0.0624° at normal incidence (equivalent to a 1 mm offset per 1 m). A modification of the d-CHOT operation principle described in [128], however, allows operation with ultra-high frequency SAWs ($\Lambda_{SAW} < \lambda$).

Intensity modulation by the propagating wave

The power distribution between the orders is defined by the combination of the d-CHOT element shape, the duty cycle of the grating d/a, and the depth of its profile. The frequency spectrum of the g-CHOT (figure 3.3) with identical geometry, considered in terms of the spatial frequencies, illustrates the energy distribution provided by a single d-CHOT cell. Similarly to the g-CHOT, the d-CHOT relief represents a square-wave grating, where the use of the 50% duty cycle ensures maximum sensitivity to the SAW but suppresses the even harmonics, resulting in the absence of the even diffraction orders. At the same time, this ensures the best interferometric contrast due to the even split of the probing light between the interfering components reflected from the profile steps and the grooves.

The amount of energy directed into particular order as a function of the transducer step height is described by the coefficients C_m of the d-CHOT cell Fourier decomposition $S(x)$:

$$S(x) = \sum_{m=-\infty}^{+\infty} C_m \exp\left(\frac{i2\pi m x}{\Lambda_{SAW}}\right)$$

The zero diffraction order described by the coefficient C_0 represents specular reflection, with intensity I_0 being the average of the reflected field. For the square grating:

$$C_0 = \frac{1}{2}(1 + \exp[i\phi])$$

$$I_0 = |C_0|^2 = \cos^2\left(\frac{\phi}{2}\right)$$

The corresponding coefficients and intensities of the diffracted light are:

$$C_m = (1 - \exp[i\phi])\frac{i}{m2\pi}(1 - \exp[im\pi])$$

$$I_m = |C_m|^2 = 4\sin^2\left(\frac{\phi}{2}\right)\mathrm{sinc}^2\left(\frac{m\pi}{2}\right)$$

where $\phi = \phi_{st} = 2kh$ is the phase difference determined by the height of the d-CHOT steps h.

The total power of the returning beam is split between the specular reflection (zero order) and the diffracted light, so that the sum of the intensities over all diffracted orders $D_\sum$ is:

$$D_\sum = 1 - I_0 = \sin^2\left(\frac{\phi}{2}\right)$$

As the overall intensity of the returning beam remains constant, the change of intensity in the specular direction is compensated by the redistribution of energy into the diffracted light. Table

3.1 shows the intensities of the first four orders as a function of $\phi(h)$, where the phase change $\phi = 2k(h - 2\delta(t))$ introduced by the surface displacement $\delta(t)$ produces the respective change in the order intensities. Figure 3.6a illustrates the corresponding intensity distribution and the energy exchange between the orders with the change of the profile height.

Table 3.1: Intensity distribution among the diffraction orders of the square grating

Phase	I_0	$I_{\pm1}$	$I_{\pm2}$	$I_{\pm3}$
ϕ	$\cos^2\left(\frac{\phi}{2}\right)$	$\frac{4}{\pi^2}\sin^2\left(\frac{\phi}{2}\right)$	0	$\frac{4}{9\pi^2}\sin^2\left(\frac{\phi}{2}\right)$

The monitoring of the specular reflection can be seen to provide the most efficient detection of SAW due to its higher light return and sensitivity to the change of phase. The maximum transducer sensitivity to the surface displacement and response linearity is achieved at $\phi_{st} = \lambda/4$, setting the static operation point of the transducer on the slope of the curve as indicated in figure 3.6b. In practice, this condition is realised by setting the appropriate height of the d-CHOT steps corresponding to $h = \lambda/8$. In this configuration 50% of the incident probing power is directed into the zero order (compared to the maximum achievable intensity in the first order of 41%).

The modulation of the reflected intensity by the propagating SAW produces the maximum signal when the the propagating wave and the d-CHOT profile are out of phase, and the minimum signal when they are in phase (figure 3.5).

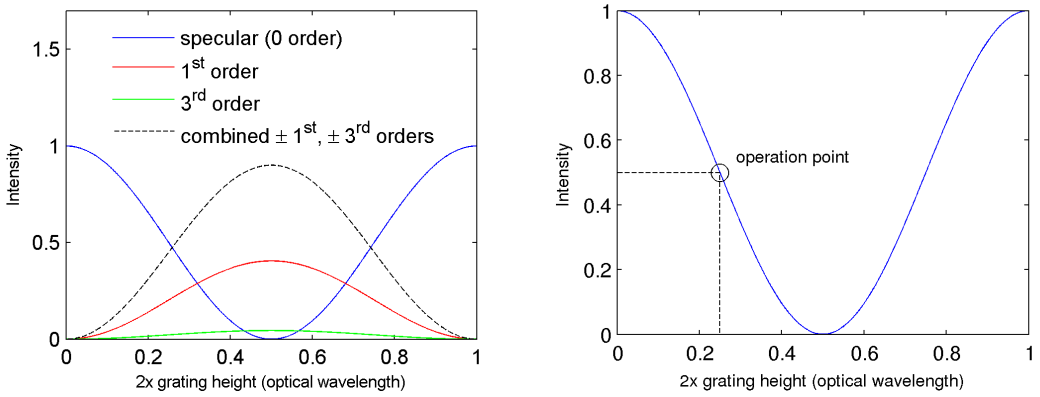

(a) Intensity distribution among the orders

(b) Intensity in the specular reflection

Figure 3.6: Intensity distribution in diffraction orders as a function of $\phi(h)$=2 x step height.

Signal frequency spectrum

The d-CHOT geometry is identical to that of the g-CHOT, described in section 3.1.1, and the frequency-domain response of the illuminated transducer $P(f)$ follows similar considerations:

$$P(f) = \mathrm{sinc}(fd_t) \cdot \mathrm{comb}(2fd_t) \otimes G\left(f|\frac{1}{Nd_t}\right)$$

where d_t is the line width and $2d_t$ is the spatial period of the grating corresponding to the propagation time $\Delta t = \Lambda_{SAW}/c_R$, N is the number of illuminated lines.

In the time domain, the separation of d-CHOT elements Δt ensures a coherent detection of the propagating wave (surface displacement) by successive elements of the grating, and determines the detection efficiency and sensitivity of the transducer to the propagating wave. The frequency content of the detected signal $Y_d(f)$ corresponds to the multiplication of the propagating SAW and the d-CHOT spectra:

$$Y_d(f) = P(f) \cdot Y_g(f)$$

where $Y_g(f)$ is the frequency spectrum of the generated SAW described by equation 3.3.

Similarly to the selective action of the g-CHOT on the spectral content of the laser pulse, the d-CHOT filters the spectrum of the propagating SAW, with the bandwidth inversely proportional to the number of the illuminated lines. As with the g-CHOT, the detection is performed at a fixed wavelength so the changes in material or velocity would result in deviation of operational frequency.

The operation principles and the requirements to the design of the d-CHOT used for detection of plane surface waves have been outlined, including its operational restrictions.

3.1.3 Practical considerations

The CHOTs' operation principles and the required transducer geometry described in the previous sections give rise to a number of specific operational differences and requirements considering practical transducer applications. Although most have been mentioned above, they are summarised in this section to provide a more cohesive view of the CHOTs practical use.

Fixed-wavelength operation

The operation of both transducers (g/d-CHOTs) at a fixed wavelength rather than frequency represents one of the main operational differences with conventional methods. The dependency of the generated frequency on the acoustic velocity of the sample material results in frequency deviations caused by the change of temperature or material of the sample. The customisation of the CHOT geometry is required for individual materials for the optimal performance.

Operational frequency limits

The transducers operate by selectively filtering the frequency content of the generation laser pulse (g-CHOT) or the propagating SAW (d-CHOT). The restrictions on the maximum achievable generation frequencies are placed by the pulse width (bandwidth) of the generation laser, and the detection frequencies are limited by the divergence angle of the diffracted beams.

Fixed-position inspection

The fixed positions of the CHOTs on the sample restrict the inspection region to the field coverage of the transducers, however enable highly-repeatable measurements over time. The use of the diverging fields or multiple/extended CHOTs can widen the inspected region and allow scanning. Additionally, the transducers have to be present on the sample *prior* to the test, and can be embedded into the test part at the fabrication stage.

Sample requirements

The CHOTs operation does not require special sample characteristics (e.g conductivity) and ultrasonic generation can be performed independently of their light absorption properties. The optical detection with the d-CHOT however requires reasonably-smooth surfaces. The latter restriction will be shown to be addressed by the portable CHOTs developed in this work (section 6.2.4).

Excitation and probing

The use of CHOTs requires simple collimated illumination enabling operation in the thermoelastic regime and at large and flexible stand-off distances as no focusing is required. Although the detection at high frequencies produces high deviation of the diffracted beams, the operation of the d-CHOT permits a single order to be used, relaxing the requirements to the collection optics. The operation is possible at oblique angles of incidence and does not require environmental stabilisation. Thus the function of the optical system required by the CHOTs consists of the simple light delivery to and from the transducers.

Whereas CHOTs full potential is best exploited in a coupled configuration, they can operate independently or in combination with other conventional techniques in a pitch-catch or a pulse-echo configurations.

3.2 CHOT fabrication

The fabrication of CHOTs is in essence a straightforward sample-patterning process aiming to produce the appropriate transducer geometry on the surface of the sample. The basic requirements to the fabrication method are the ability to control the dimensions and thickness of the fabricated transducers, ability to operate with required transducer and sample materials and provide sufficient pattern-to-sample bonding. This can be achieved by a large number of techniques, where methods ranging from photolithography to sample etching have been previously used [126].

Although fundamentally different in operation, both types of CHOTs can be generally produced with the same method, equipment and materials, with the addition of an extra step to produce the reflective surface of the d-CHOT. Despite requiring some specialised equipment, this versatility permits transducer manufacture on demand and at the shop floor.

A brief summary of the well-established and more recently-developed CHOT fabrication techniques is provided below, and an alternative fabrication concept to overcome their limitations in the target industrial application is proposed.

3.2.1 On-component fabrication methods

The CHOTs can be produced on the test part by well-established micro-patterning techniques either at component manufacture stage or at a later time provided the required part can be removed from its working position for transducer application. Developed more recently, the laser-based methods enable on-site and potentially in-situ transducer fabrication without the equipment-imposed restrictions of the laboratory-based techniques.

Photolithography

The photolithographic technique [140] illustrated in figure 3.7 is based on the use of the light-sensitive conformal polymer materials, photoresists, to form a positive/negative relief on the surface of the sample corresponding to the transducer geometry. Such relief is commonly created by spin-coating a layer of photoresist onto the sample and exposing it to UV light though a glass transmission mask replicating the required pattern geometry. Depending on whether the positive/ negative type of photoresist was used, the UV-exposed/unexposed areas are removed from the surface of the sample during the development stage. Using a positive photoresist, the exposed areas removed during the development form the imprint of the CHOT pattern in the remaining layer. This is followed by material deposition in a vacuum evaporator or a sputter-coater during which the etched, resist-clear, areas are being filled and the rest of the material is deposited on the layer of the photoresist. During the last, lift-off, stage this layer is chemically removed revealing

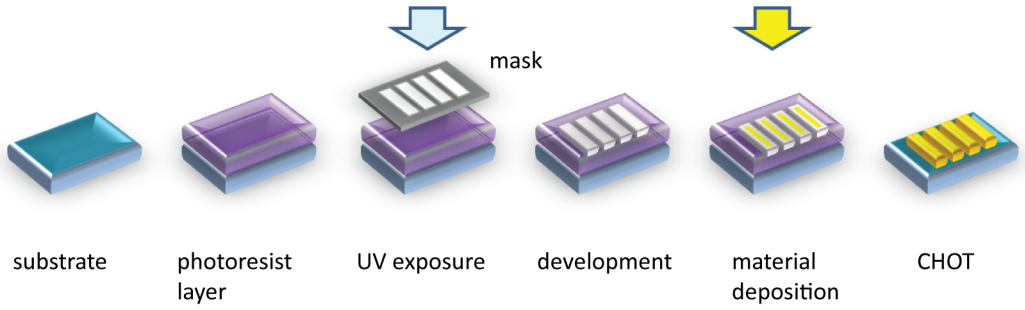

Figure 3.7: Schematic diagram of the photolithographic fabrication of CHOTs.

the created metal profile on the surface of the sample.

The height of the fabricated CHOT features corresponds to the deposited material thickness, and is limited by the thickness of the resist layer. In order to produce the d-CHOT on non-reflective substrates, an additional step includes deposition of highly-reflective material (such as silver for $\lambda = 0.532$ μm) over the fabricated profile.

Although this method offers controllable fabrication with high accuracy and repeatability, producing well-defined pattern features at high resolution, it remains a predominantly laboratory-used technique due to serious restrictions placed by the equipment onto the sample size and curvature, and a time-consuming multi-stage process not desirable in mass-production. It can however be used to produce the master and prototype CHOTs providing the reference for other fabrication techniques, and to produce CHOTs of high frequencies, where structures with frequencies of up to 164 MHz were made on glass.

Direct deposition through a mask

In this method a metal mask with the slots corresponding to the required transducer geometry (elements shape and spacing) is used on the surface of the sample, and the transducer is formed by material deposition through the mask in the vacuum evaporator or a sputter-coater (figure 3.8). The height of the CHOT profile in this case is determined by the amount of the deposited material (coating thickness). The d-CHOT is created in a similar fashion to the previously described technique either by using the reflective material for the transducer itself (if used on a reflective substrate), or by creating a reflective layer over the fabricated structure in additional deposition.

The use of masks to produce CHOTs offers a faster and simpler alternative to the photolithography, with controllable and highly-repeatable results. Although this method permits fabrication on larger samples with some surface curvature, it is limited by the physically-achievable dimensions of the mask features, being most suitable for fabrication of the lower-frequency CHOTs ($<$ 20 MHz

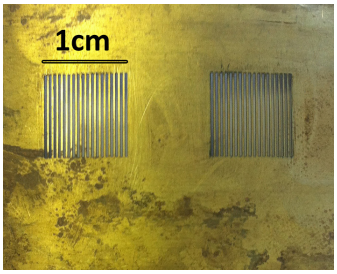

(a) 5 MHz mask for Al, created by laser-etching on brass

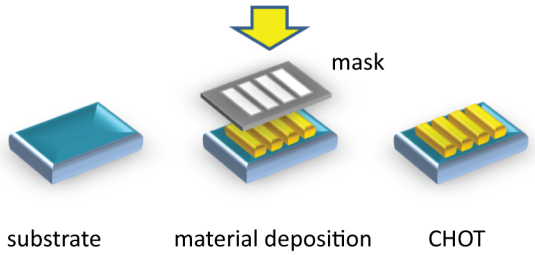

(b) Schematic diagram of the fabrication process

Figure 3.8: Fabrication of CHOTs by direct deposition through masks.

on Al). Similarly to the photolithography, the need to place the sample into the vacuum chamber for metal film deposition restricts the acceptable sizes of the test parts.

Laser deposition: Laser Induced Forward Transfer (LIFT)

The use of the Laser Induced Forward Transfer (LIFT) technique [141,142] allows metal patterning of the substrate without the need for the specialised equipment used for thin film deposition. LIFT is based on the laser vaporisation of the donor material from the transparent carrier placed in close proximity with the sample (figure 3.9a). The donor-material coated on the sample-facing side of the carrier is ablated by the laser pulse focused onto the film/carrier interface, and is being propelled towards the substrate due to the build-up of pressure at the constraint. The pattern is then 'written' onto the substrate by scanning the laser beam across the carrier (or movement of the sample with the carrier) along a path corresponding to the transducer geometry. The resolution of the features produced with LIFT is limited to the diameter of the laser focal spot, and enables controllable and reproducible fabrication of the high-frequency CHOTs. The use of the g-CHOT activation laser to also produce the transducer offers additional benefit of cost reduction.

This technique does not have the sample-size restrictions of the previous methods and can tolerate curved surfaces. Furthermore, its portability permits transducer fabrication on the part on-site, and potentially in-situ as it does not require laboratory facilities. However the need for beam scanning with precise positioning may be hard to achieve for in-situ fabrication in some practical applications.

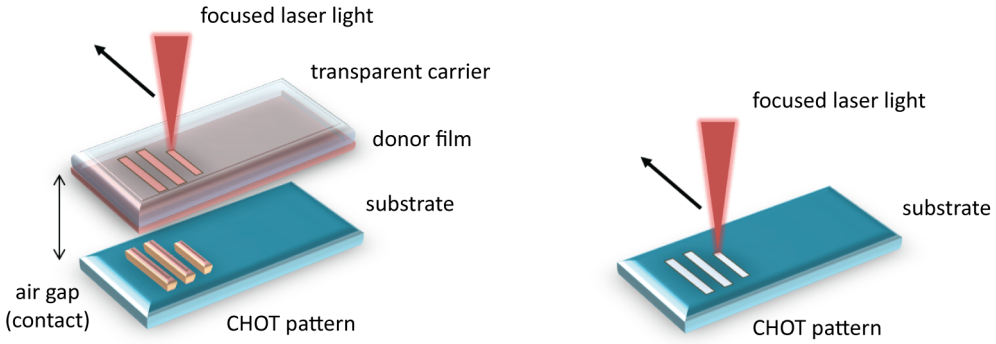

(a) Laser deposition with LIFT

(b) Laser etching

Figure 3.9: Laser-based CHOT fabrication techniques.

Laser etching

It is also possible to use a focused laser beam to etch the CHOTs directly onto the surface of the sample by ablation and scanning the beam or moving the sample to create the required transducer geometry (figure 3.9b). Whereas direct surface etching is not desirable in NDT applications as it in itself introduces surface damage, the same concept can be used on a sample surface coated with the absorbing material, where the CHOT is formed by selective removal of the coating from the surface avoiding the substrate damage.

This technique also has high potential for on-site and in-situ fabrication out of the laboratory setting, but requires prior surface preparation, precise control of the coating removal rate to ensure no substrate damage, with similar to LIFT considerations regarding the practicality of scanning for in-situ transducer fabrication.

Figure 3.10 shows the photographs of the SAW CHOTs fabricated with the reviewed methods.

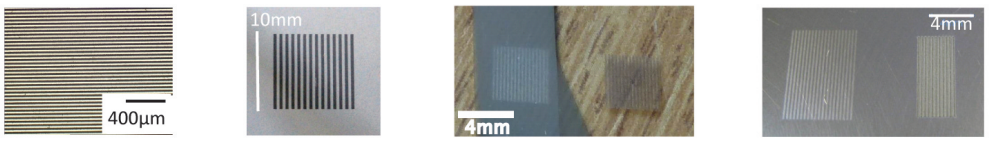

Figure 3.10: Photographs of CHOTs fabricated with: (a) photolithography , (b) direct deposition through a mask, (c) LIFT, and (d) etching.

3.2.2 Applicability requirements and restrictions

The choice of a suitable fabrication method largely depends on the CHOT target application and the type of the parts that the transducer is required to be placed on. In application to NDT of aeroengine components, this necessitates fabrication of the transducers on large and curved parts challenging for some of the methods. At the same time, unlike testing with other types of transducers or optical techniques, the use of CHOTs requires the presence of the transducers on the sample prior to the test, restricting their practical field applications to the components with pre-fabricated transducers. These factors prompted the development of the alternative fabrication methods to expand the range of the acceptable test parts and enable application of the transducers to the components at different stages: from permanent sensor placement during component fabrication to the manufacture of CHOTs in-situ.

The well-established micro-patterning techniques, very effective for fabrication of CHOTs under laboratory conditions with precise feature control and repeatability, are largely restrictive and hard to implement in industrial setting and on the actual parts. The current restrictions imposed by the microfabrication equipment onto the size and curvature of the test samples make this method unacceptable for CHOT fabrication on large parts, and those with complex curved surfaces (such as components of an aeroengine).

The development of the laser-based fabrication techniques addressed the sample-size restrictions of the laboratory-based fabrication, additionally enabling creation of the transducers on-site when they are required, and on the parts already in service, greatly expanding the range of CHOTs applicability. However, their use is to some extent complicated by the required sample scanning to produce the pattern and the associated positioning control. This might not prove difficult if the component to be tested can be removed, however would be hard to implement in-situ on the parts of assembly and those with complicated access paths.

3.2.3 Alternative fabrication concept: CHOTs on film carriers

The equipment requirements and process complexity of the micro-patterning methods place restrictions on the sizes and geometries of the samples, additionally limiting their application to a laboratory environment, whereas the laser-based techniques require scanning, precise laser control to avoid sample damage or placement of a donor carrier next to the sample. These factors make testing of the aeroengine parts in-situ, without requiring disassembly and removal of the parts, extremely complicated if the CHOTs are not pre-fabricated on the component due to the spatially-confined and complex access.

To remove these restrictions associated with direct sample-patterning and provide even greater

flexibility and the range of CHOTs applications, an alternative fabrication concept is proposed.

A portable CHOT can be produced on a film carrier in the laboratory environment to be later delivered and applied to the test part as required (figure 3.11). This method combines the control and repeatability of the laboratory-based fabrication with the ability to place CHOTs onto component in-situ and onto large and curved parts, simplifying their practical use. The development of a portable CHOT would additionally complement the instrumentation of the endoscopic pulser for the in-situ inspection of the aeroengine parts.

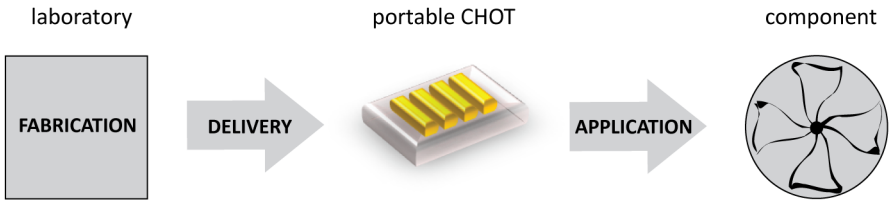

Figure 3.11: Illustration of the portable–CHOT concept.

Although such CHOTs would require a coupling medium as conventional PZTs, they provide a simple flexible solution for testing of the components without the pre-fabricated CHOTs, such as those already in service. Additionally, the portability enables them to be easily placed at multiple locations on the samples, being used as disposable transducers, and due to their small size – ensures the ease of delivery and application in confined spaces (unlike bulky conventional contact transducers).

3.3 Summary

The use of the cheap optical transducers in this work aims to bring the benefits offered by laser ultrasonics to the solution of a practical inspection task where the use of the conventional techniques is complicated or all together excluded by the bulkiness and complexity of the measurement systems and the spatially-confined access to required components. The CHOTs' operation principles, design and fabrication methods described in this chapter provide the basis for the creation of a compact, portable all-optical inspection system offering efficient ultrasonic generation and interferometric detection without requiring excessive optical and electronic systems, or stabilisation. Such a system combined with fibre-optic light delivery and an upgrade in the CHOTs fabrication methods has potential to enable flexible access and testing of the components in situ.

The CHOTs are optically-activated ultrasonic transducers employing principles of laser ultrasonics (section 2.2) to generate (g-CHOT) and detect (d-CHOT) acoustic waves. Located on the

surface of the sample, their use removes the need for additional optical elements and electronics, used by other methods to form the required intensity distribution on the surface or provide stabilisation in interferometric detection. The mode, directivity and frequency of operation is determined by the transducer geometry and can be customised to produce bulk or surface waves with plane or focused wavefronts, depending on the application requirements. The use of CHOTs in the present work and their description in this chapter is limited to the surface acoustic waves and plane wavefronts.

The design of the plane-SAW CHOTs represents an array of line sources/detectors providing efficient highly-directional and frequency-selective operation with additional benefit of allowing the higher input powers in the thermoelastic regime and the noise reduction due to the reduced system bandwidth. The spacing of the transducer elements is matched to the wavelength of the surface wave that is being generated or detected, considering wave velocity in the material of the substrate. Thereby the spectral filtering of the generation laser pulse and the propagating SAW is performed according to the selected transducer geometry (figure 3.3), with the bandwidth determined by the number of the illuminated lines.

The generation of surface waves by the g-CHOT (figure 3.1) requires pulsed illumination and is achieved by spatially-periodic modification of the surface absorption, where the material of the transducer is selected to provide the highest absorption contrast to the incident radiation. The versatility of the transducer to operate both as an absorber or a reflector enables efficient ultrasonic generation independently of the light absorption properties of the interrogated samples, enabling operation on weakly-absorbing and transparent substrates and enhancing generation on the strongly-absorbing materials.

The d-CHOT (figure 3.4) uses continuous-wave illumination and operates as a local on-sample interferometer using principles of the diffraction grating modulator. The alteration of its profile height by the propagating wave causes the redistribution of energy between the diffraction orders (figure 3.5) and permits ultrasonic sensing by monitoring intensity modulation in an isolated order (figure 3.6). Due to its higher sensitivity to the surface displacement and the higher light return, the specular reflection is used, where the optimal interferometric performance is achieved by setting the height of the transducer steps such to provide a phase difference $\phi_{st} = \lambda/4$ between the light reflected from the top and the base of the d-CHOT profile (figure 3.6b). As both 'interferometer arms' are located on the sample with a separation smaller than the optical wavelength, the system does not require path stabilisation and is robust to the environmental factors with high potential for industrial applications.

The CHOTs can be fabricated by a range of methods which have previously included well-established micro-patterning techniques such as photolithography and deposition through masks,

as well as more recently-developed laser deposition LIFT and laser etching. As the CHOTs have to be present on the sample for the test to take place, their realistic use in industry requires to extend the testing ability beyond the components with pre-fabricated transducers, prompting the development of the methods for in-situ fabrication or application of CHOTs.

While the first group of methods is suitable for pre-fabrication in the laboratory environment, they are hard to implement on the actual parts due to restrictions onto the sample sizes and curvatures. The second group overcomes these limitations and permits transducer fabrication in industrial settings on-site, however requiring precise positioning control and/or surface preparation, and is hard to implement in-situ and on the parts of the assembly.

The restrictions of these methods are associated with the direct on-component fabrication of the transducers, limited by the equipment and process requirement and the necessity to have full access to the test part. An alternative concept to create a portable CHOT has been proposed to remove these limitations. Fabrication of the transducers on film carriers would allow them to be transported, delivered and applied to components as required, combining the control and the repeatability of the laboratory-based fabrication with the ease of transducer use. This would additionally substantially expand the range of CHOTs applicability and testable parts, enabling testing of the large and curved parts and components in-situ.

The CHOTs simplicity and operation in compact optical arrangement are realised in the endoscopic pulser described in Chapter 4, where fibre-optic light delivery is used to provide flexible access for testing of hard-to-reach components in confined spaces or locations with complex access paths. This is complemented by the development of the portable CHOTs on film carriers (Chaper 5) enabling transducer delivery to the components already in service and testing in-situ. The functionality tests and performance characterisation of CHOTs are described in Chapter 6, and the combined system capabilities for non-destructive testing are discussed in Chapter 7.

Chapter 4

Endoscopic pulser instrumentation

As has been shown in Chapters 1 and 2, the use of optical fibres/endoscopes greatly enhances practical capabilities of the inspection system and contributes to its overall size reduction. Using CHOTs, described in the previous chapter, to perform laser-ultrasonic inspection allows further miniaturisation and simplification of the system instrumentation as excessive optical elements are not required to control intensity distribution on the sample or for optical-path stabilisation. In addition, simple CHOT activation by collimated beams removes the need for precise alignment, providing the ease of the system field use.

The endoscopic pulser instrumentation described in this chapter consists of the basic CHOTs optical setup combined with the fibre-optic light delivery to enable access to components out of direct line of sight or in confined spaces with complex access. Although the size of the current system exceeds the access limits for on-wing inspection (typical required endoscope diameter of 8 mm), combined with the results of the following chapters, it demonstrates the operational concept using off-the-shelf optical elements. Further reduction of the endoscope can be achieved by employing custom-design optics and fibres, where some preliminary work has been performed and possible prototype design options were discussed with optical fibre manufacturer SCHOTT. The system operation in its present configuration was demonstrated outside of the laboratory environment at the RCNDE Technology Transfer Event 2014, Nottingham, UK.

This chapter presents an overview of the endoscopic pulser and its technical layout, including the details on the role and the characteristics of the system components, and description of the required alignment. Further potential for system development is discussed.

4.1 System Overview

Considering the use of CHOTs in a coupled configuration, a basic measurement system consists of two transducers on the surface of the sample (g-CHOT + d-CHOT), generation and probing lasers to illuminate the corresponding CHOTs, minimal optics to expand and collimate the beams, a photodetector and an oscilloscope. The illuminated g-CHOT/sample absorbs/reflects the incident radiation from the generation laser, converting it into acoustic waves via the thermoelastic mechanism (Chapter 2, 3). The SAW propagating away from the g-CHOT or reflected by a defect (sample edge, etc.) is picked up by the d-CHOT and converted into intensity modulation in the diffraction orders of the reflected beam. The detection of ultrasound is then performed by an isolation of the zero diffraction order (specular reflection) using an iris diaphragm in front of the photodetector, and monitoring the corresponding output (Chapter 3).

The operation of the CHOTs system can be generally separated into three distinct channels based on the performed function: the *generation*, the *probing* and the *detection*. The block-diagram illustrating the structure and comprising elements of the CHOTs ultrasonic system is shown in figure 4.1, where the elements are grouped according to their contribution to one of the channels. The signal flow from element to element is indicated by arrows, with the main system inputs and outputs shown in bold. The two transducers located on the sample are shown in the shaded box, viewed with regard to their corresponding inputs and outputs. As the sample is an integral part of the ultrasonic system, it is included between the CHOTs to indicate the effect of the wave propagation between the transducers for their later characterisation (Chapter 6).

In the fibre-coupled setup, described in this section, the transmission of the generation and probing light is performed via optical fibres, and the collection of the returning probing light (containing ultrasonic information) – via an optical fibre bundle. The use of the fibre bundle allows to transfer the image of the diffraction orders from the sample to the user-side of the fibre, where the order selection takes place, greatly reducing the size of the probe accessing the sample. The optical layout of the endoscopic CHOTs system is shown in figure 4.2 and the photographs of the experimental arrangement in figure 4.3. The generation, probing and detection systems are enclosed, and combined with the corresponding optical fibres, form an *endoscopic pulser*. The generation channel consists of the pulsed generation laser, coupling optics, optical fibre, a collimating lens and the illuminated g-CHOT/sample. The probing channel includes the CW probing laser and a fibre-optic light delivery system. The detection channel is comprised of the illuminated d-CHOT, a collecting lens, optical fibre bundle, an expanding lens, an iris diaphragm for order selection, a photodetector, two band-pass filters (BPF), an amplifier and an oscilloscope.

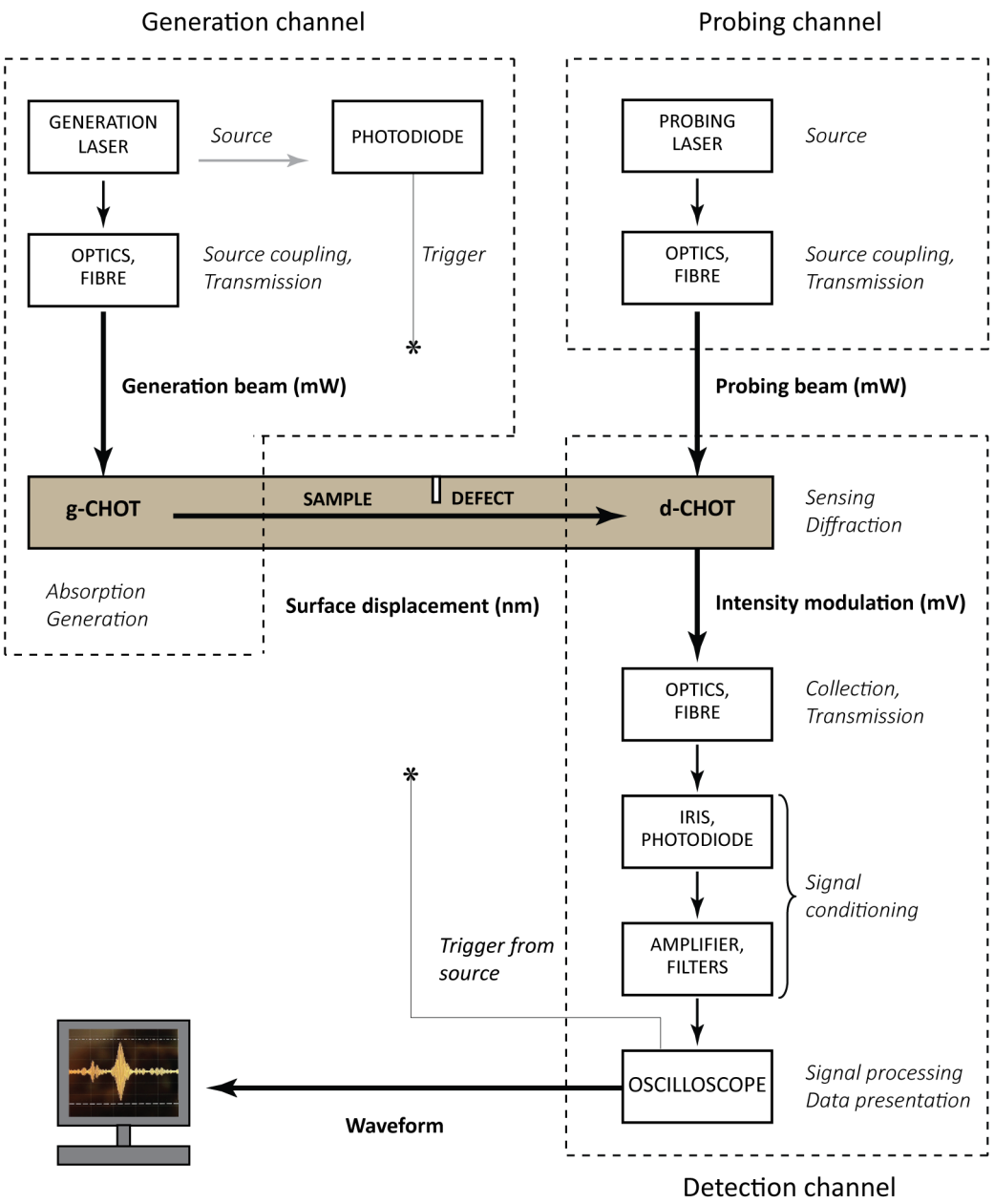

Figure 4.1: Block diagram of the CHOT measurement system and its components. The system elements are grouped based on the element contribution to generation, probing or detection. The main system inputs and outputs are indicated in bold.

Cameras can be additionally introduced into the system for remote observation and the ease of alignment of the laser beams on the sample and the diffraction orders with the iris. A more detailed description of the system elements is provided below.

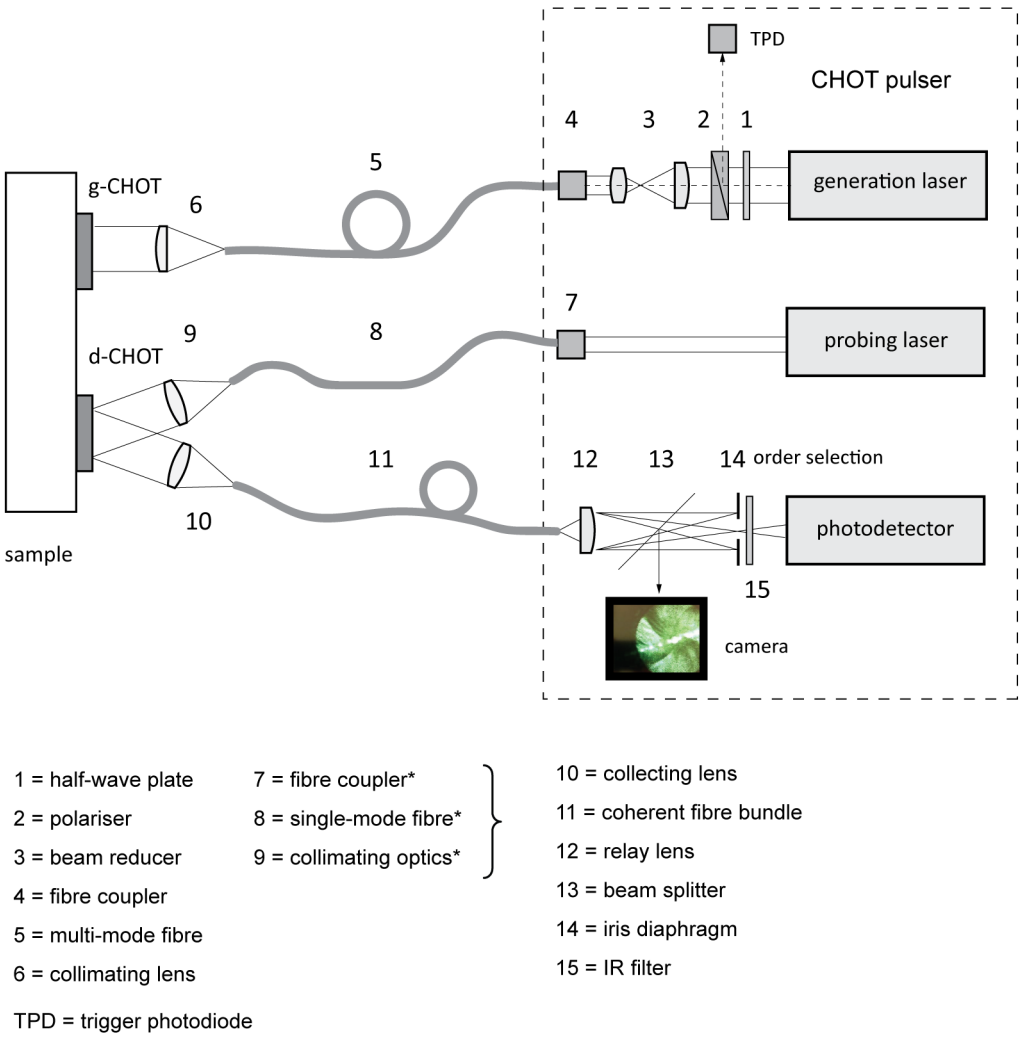

Figure 4.2: Optical layout of the endoscopic pulser. The items marked with '*' show the elements of a commercial fibre-delivery system KineFlex, and come as an assembly.

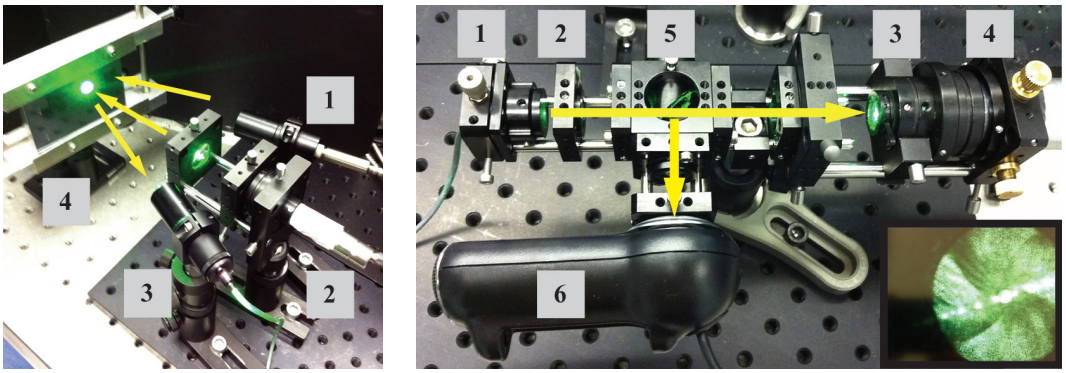

(a) (b)

Figure 4.3: Photograph of the experimental arrangement. (a) Sample testing showing exits of the delivery fibres and corresponding optics. 1 = Generation light delivery fibre, 2 = Probing light delivery fibre, 3 = Collection fibre bundle entry, 4 = Sample. (b) Detection system, showing the view of the iris and diffraction orders as seen from the camera (inset). 1 = Fibre bundle exit, 2 = Expanding lens, 3 = Iris diaphragm, 4 = Photodetector, 5 = Beamsplitter, 6 = Camera.

4.2 Elements of the system

4.2.1 Laser sources

Generation laser

The generation laser source is a pulsed (Q-switched) high-power Nd:YAG laser (Elforlight FQ 1064, class 4) with the following operational parameters: wavelength $\lambda = 1.064$ μm, pulse duration $\tau = 8$ ns, repetition rate $R = 1$ kHz, stability $< \pm 2\%$, and the output beam diameter $D = 4$ mm. The maximum average power output is $P_{avg} = 700$ mW, equating to the pulse energy $E = P_{avg}/R = 0.7$ mJ.

Selection of the generation laser

- *Optical wavelength* is determined based on the absorption characteristics of the material of the test part, where the appropriate choice of the g-CHOT material provides the absorption contrast (Chapter 3). The use of the g-CHOT expands the range of the suitable laser wavelengths, operating either via absorption by the sample or by the g-CHOT material. For example, the generation on an aluminium sample with relatively low absorption at the generation wavelength (6%) can be enhanced by selection of a stronger-absorbing g-CHOT material at the same wavelength, such as chromium (36%).

- *Pulse energy* determines the amplitude of the generated waves but is restricted by the ablation threshold of the test-part material if non-destructive operation is required. The ablation threshold for common metals and Q-switched lasers operating in the near-infrared is 1–10 MW/cm^2 [16]. The use of CHOTs allows to distribute the laser energy over a greater area permitting the increase of the input power without material damage (Chapter 2, 3). The diameter of the beam used in this work was $D \approx 5$ mm (area $A = (\pi/4)D^2 = 0.196$ cm^2) producing peak intensity in the beam $I = E/(\tau \mathrm{A}) = 446$ kW/cm^2. As it is below the threshold for common metals, the operation in the thermoelastic regime should be expected.

- *Pulse length* determines the spectral content of the laser pulse and the energy available at the selected generation frequency (Chapter 3). The bandwidth of the laser pulse thus limits maximum ultrasonic frequencies that can be generated with the chosen laser, where shorter pulses are required for high-frequency ultrasonic generation. The time-trace and the corresponding frequency content of the 8-ns laser pulse used in this work are shown in figure 4.4, displaying little signal reduction at the operational frequencies used in this work (5 MHz). An additional point worth mentioning is the electronic noise produced by the Q-switch. Although some pulse energy can be seen available in the region of 80 MHz, the signal detection at these frequencies is compromised by the electronic noise.

- *Repetition rate* is connected to the the number of signal waveforms that can be acquired at some fixed time-interval, with increased number of pulses producing faster signal averaging and increased inspection or scanning speed. At the same time, for the constant laser output power, it is inversely proportional to the peak intensity in the beam, so increasing the repetition rate reduces the peak beam intensity.

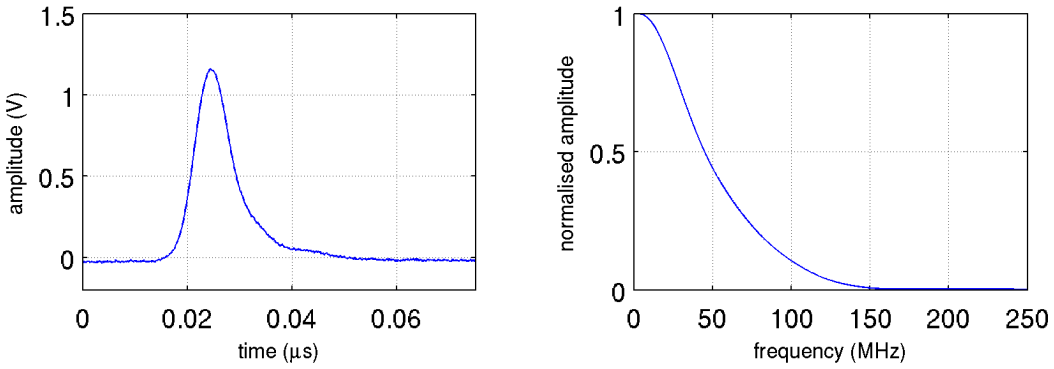

(a) Generation laser pulse

(b) Spectrum of the generation laser pulse

Figure 4.4: Characteristics of the generation laser pulse in time and frequency domain.

Probing laser

The probing laser used for detection is a continuous wave (CW) second harmonic Nd:YAG laser (Laser Quantum Torus, class 3B) operating at $\lambda = 532$ nm with power stability $< 1\%$, beam diameter 1.7 mm, and output power of 220 mW in TEM_{00}. Over the period of work, similar lasers with lower and higher output powers were used (60 mW and 405 mW, class 4). The corresponding change in the signal-to-noise ratio (considering thermoelastic regime) would be proportional to $\sqrt{P_{det}}$. The output power used in a particular test is stated alongside the result.

4.2.2 Transmission and coupling optics

Generation channel

The delivery of the generation beam to the g-CHOT is achieved by a multimode high-power optical fibre (Thorlabs MHP 550L02, 2 metres) with the damage threshold 50 kW/cm^2 (CW equivalent at 980 nm), core diameter of 550 μm, and numerical aperture NA 0.22. As the g-CHOT uses laser illumination simply as a heat source, the beam mode and polarisation are not required to be maintained by the fibre and a multi-mode fibre can be used.

The laser beam is coupled into the fibre using a telescopic optical system providing 5x beam-diameter reduction, and a fibre port coupler (Thorlabs PAF-SMA-11-C) with NA 0.2. The NA of the fibre determines the maximum acceptance angle of the incident light into the core. For efficient coupling and to avoid laser damage to cladding, the coupler should be chosen with NA matching or below that of the fibre. The actual average laser output was approximately 650 mW, and the coupling efficiency, determined as a fibre output-to-input ratio, was on average close to 75%. The coupling efficiency and/or the output power during the test is stated with the corresponding results. The distal end of the fibre contains a lens collimating the output beam to diameter $d \approx 5$ mm (defines the bandwidth of the generated SAW, Chapter 3).

Prior to the coupling optics, a combination of a polariser and a half-wave plate is placed in the path of the beam providing the means to control power input into the fibre, and a small amount of reflected light is directed to a photodiode to trigger signal acquisition.

Probing channel

The probing illumination from the laser is delivered to the d-CHOT via a fibre delivery system KineFLEX. The delivery system is comprised of the pre-focused and integrated optical assembly with the design matching parameters of the laser to provide transmission efficiencies of over 65%. It contains the beam coupling system, a single-mode fibre for $\lambda = 532$ nm (2 m length) and a collimating system on the distal end of the fibre producing beam diameter of 7 mm (defines the

detection bandwidth, Chapter 3). As the d-CHOT operation is phase sensitive, a single-mode fibre is used for optimal operation and to preserve Gaussian intensity distribution on the transducer.

The KineFLEX systems are used in precision measurement applications, provide high coupling efficiencies and increase system portability by reducing its size and the amount of required alignment. The laser coupling efficiency at the time of the test is stated with the results, and was on average close to 73%, providing average sample illumination with 43 mW, 160 mW and 295 mW for the 60 mW, 220 mW and 405 mW inputs respectively.

Detection channel

The collection and transmission of the probing light reflected from the sample (d-CHOT) to the photodetector is performed using a coherent leached fibre bundle (SCHOTT 1251167LFB), consisting of 18,000 individual fibre cores, each with diameter 11.6 μm, and the overall quality area diameter of 1.4 mm.

The use of coherent fibre bundles enables transmission of images by maintaining the spatial relations between the beams within the fibre, where the individual cores in the bundle are the equivalent of the pixels in a digital camera. This property, combined with the d-CHOT operation allows to spatially separate the ultrasonic sensing from the order selection and the electronic detection, by collecting the ultrasonic information at the sample and transferring it for detection at the user-end of the fibre. Due to the absence of the individual-core cladding, the use of such bundles is however associated with high transmission losses, with the measured transmission of 46–50%. In addition, the energy leakage takes place between the individual cores, most-likely producing a cross-talk if the split-use of the fibre is required (e.g figure 2.11b).

The diffracted light from the d-CHOT is collected and focused onto the facet of the bundle with a lens, and another collimating lens is used at the exit of the fibre to extract the diffraction orders and reduce the size of the beam. The choice of both lenses is connected to the operational frequency of the d-CHOT, where larger angular separations of the orders produced by higher frequencies would require higher NA of the collecting lens (although a single order can be collected, Chapter 3), whereas the lower frequencies would affect selection of the focal length of the collimating lens at the exit to provide sufficient order separation at the detector. The selection of the required diffraction order is performed by an iris diaphragm after which the light passes to the detector via an IR filter.

4.2.3 Signal acquisition and processing

Detection

A single-element photodetector circuit, custom-built at the Applied Optics Group, and based on BPX65 photodiode (200 MHz bandwidth, Appendix A.1), is used to detect the incident diffracted light. The detector sensitivity to wavelength of the probing illumination as well as to the ultrasonic-modulation frequency determines the efficiency of the photo-to-electric signal conversion and the output of the detector.

Filtering and amplification

The DC output from the detector is passed directly to the oscilloscope, whereas the RF output is directed to a chain of two 5 MHz band-pass filters (BPF, bandwidth $\approx$ 2 MHz) and two low noise amplifiers (Minicircuits ZFL500-LN, bandwidth 500 MHz). This arrangement is illustrated in figure 4.5. The ratio of the DC/RF outputs from the photodetector before the amplifier was measured as 0.0112. The use of DC output allows to monitor the amount of incident light received by the detector and aids the order alignment with the iris/detector.

The spectral characteristics of the filters and gain from the chain of two amplifiers were measured with Marconi 2382 spectral analyser and are shown in Appendix A.2 and A.3. The measured output increase with the use of the amplifier was $P(\text{dB}) = 60$ dB, related to the provided gain in power as:

$$P(\text{dB}) = 10 \log\left(\frac{P_{out}}{P_{in}}\right)$$

$$10^6 = \frac{P_{out}}{P_{in}}$$

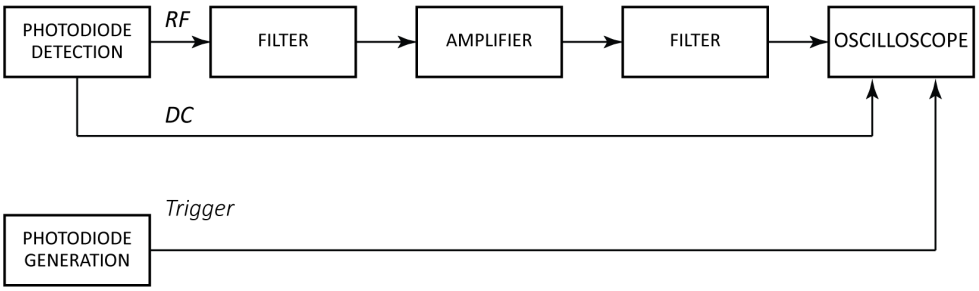

Figure 4.5: Block diagram illustrating signal chain during acquisition (joined amplifiers are shown as a single element).

The corresponding gain in voltage is:

$$V_{out} = 10^3 V_{in}$$

Signal acquisition

The signal acquisition was performed using oscilloscope LeCroy Waverunner 104Xi-A 1GHz (maximum acquisition rate 10 Gs/s), triggered by the generation laser pulse (figure 4.5). The trigger is provided by the Thorlabs PDA10A-EC photodiode located at the exit of the generation laser. In most cases the acquisition was performed averaging over a number of detected traces to improve signal SNR, where depending on the sampling rate up to 1,000 waveforms a second can be obtained corresponding to the repetition rate of the generation laser. The number of averaged waveforms is stated with the results.

4.2.4 Setup modification

Depending on the nature of the test, the system described in this section was additionally modified to include the translation stages (PI M-605.2DD) and a laser vibrometer (Polytec OVF-534), allowing to move the sample or the vibrometer, and perform surface scans. The particular setup used in the tests is provided in the corresponding sections.

4.3 The use of the endoscopic CHOTs pulser

4.3.1 Instrument alignment

Once the laser beams have been coupled to the corresponding optical fibres, only simple alignment is required during operation. More specifically, the alignment of the beams and collection optics with the appropriate transducers and reflected beam at the sample, and the order alignment with the iris at the user-side of the fibre.

Both CHOTs use collimated-beam activation, and the alignment of the illuminating beam involves simple positioning/direction of the beam onto the right transducer. As no focusing is required, the stand-off distance and the angle of the illumination are generally flexible. The alignment of detection optics with diffracted beam and the probing illumination with the d-CHOT are connected via reflection off the sample. The fibre bundle can be articulated to adapt the detection angle to the probing angle of incidence or a fixed angular setup can be used for particular stand-off distances and/or surface curvatures. Additional modifications can enable operation at normal incidence or using retroreflection (e.g Littrow diffraction configuration).

After the diffracted light has been collected and transmitted to the detector, the alignment of the diffraction orders and the iris is performed to select the required order. Some options include adjusting the sample holder (in a laboratory setting), adjusting the fibre mount at the user-side (for tests of large samples or in industrial conditions), or incorporating an automated/controlled deflection mirror between the fibre and the iris/detector.

4.3.2 Safety considerations

A valid concern regarding adaptation of the laser-ultrasonic systems in practical field applications is the high power densities of the laser sources, with associated health risk posed by accidental irradiation of the eyes or skin. Although the lasers used in this work are of class 3B and 4 (section 4.2.1) that require significant safety precautions, restricted access and user training, the fibre-coupled delivery of the probing and detection beams, described in this work, with the full enclosure of the laser pulser, provides major reduction of the associated risks. Combined with the sample enclosure, or the use in enclosed spaces such as an aeroengine, the safety of operation is maximised. This was illustrated by the demonstration of a fully-enclosed CHOTs system outside of the laboratory conditions at the RCNDE technology transfer event in 2014.

4.4 Further system development

4.4.1 Practical use

In order to enable practical field use of the system, specifically in applications where the endoscope is used to access hard-to-reach components in confined spaces without visual access, further modifications of the endoscopic pulser instrumentation should include the ease/automation of the alignment and provision of live images from the distal end of the fibre to enable navigation of the endoscope to the sample.

A commercially available endoscopic USB CMOS camera PE-157A was added to the experimental set up to deliver the image of the transducers and aid beam alignment on the sample (10 mm diameter, 2M fibre, 4 LED). In the pulser itself, a modified web-camera was incorporated into the setup (figure 4.3) enabling viewing of the diffraction orders with the iris on the screen of the oscilloscope and aiding their alignment. Such alignment (combined with automation) additionally enables full enclosure of the pulser.

The automation of the order alignment with the iris will provide further simplification of use, and can be accomplished by incorporating a deflection mirror between the exit of the fibre bundle and the iris/detector controlled using manual selection of the diffraction order and a feedback from

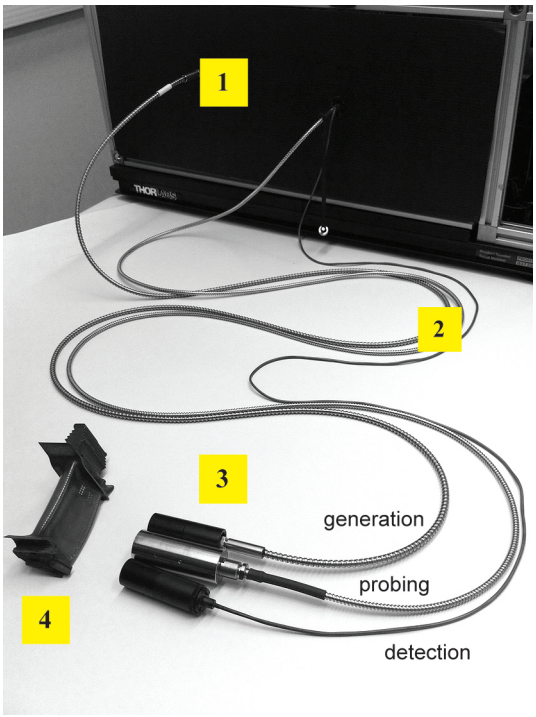

Figure 4.6: Endoscopic CHOT system at present. 1 = Pulser (lasers, coupling optics and detection system), 2 = Optical fibres corresponding to generation, probing and detection channels, 3 = Exit of the fibres with collimating/collecting optics, 4 = Test sample.

the DC levels on the detector.

4.4.2 Miniaturisation: channel combination concept

The present system shown in figure 4.6 uses off-the-shelf optical elements and three separate illumination-delivery fibres. The combined diameter of the fibres and the optical mounts at their exits at present exceed the acceptable endoscope diameter to access the engine components on-wing. The reduction of the overall endoscope diameter, in particular the size of the probe required to access the sample, is the priority of the further system development. Apart from the straightforward minimisation of the optical element sizes, not always possible, another solution can be found in the reduction of the number of channels (fibres) required to access the component.

It it proposed to combine the functions of the separate fibres, used in probing and detection channels, within a single fibre bundle. A frequently-found arrangement of the medical endoscopes includes the delivery of the illumination using outer circular part of the bundle, and collection of the returning light/image by its central part. Reversing this to suit the operation with CHOTs, the probing laser illumination can be coupled into a single core of the bundle, expanded by the

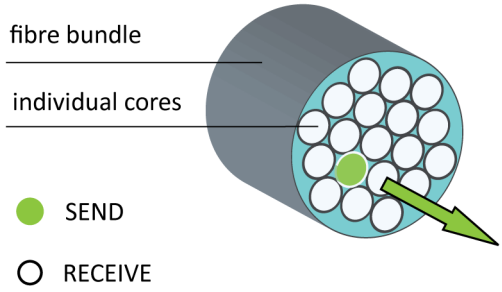

Figure 4.7: Combination of the probing and collection channels in a single fibre bundle for elimination of one of the fibres to reduce the diameter of the endoscope: concept illustration .

focusing (collimating) lens at the distal end of the fibre to illuminate the d-CHOT, and the rest of the bundle quality area (other cores) is used to collect and transmit the diffraction orders to the detector. The concept is illustrated in figure 4.7.

To date, only the first part of the proposed concept has been realised, using the fibre bundle of the detection channel. The probing beam was coupled into a single core of the bundle, and the collimated output used as probing illumination. The rest of the pulser was used unchanged, and the detection was performed using a separate fibre bundle.

Firstly, the experiment demonstrated the ability of the single core to transmit all of the probing beam power without the fibre damage. The absence of damage was confirmed by monitoring of the fibre exit before and after the laser irradiation using the setup camera. Figure 4.8a shows the compound photograph (two exposures) of the beam coupling into the core, where the desaturated close-up of the area confirms close to single-core coupling. Slight interference effects can be noticed around the illuminated area that are possibly due to the combination of diffraction from the illuminated bundle element with the light leaked/partially-coupled into the adjacent cores.

Secondly, due to its small diameter, the operation via a core of the bundle (not a single-mode fibre) did not seem to significantly alter the optical paths across the beam and the output from the d-CHOT. The signal detected by a separate bundle using probing illumination delivered via a single-core coupling is shown in figure 4.8 (glass sample; 2,000 averaged waveforms).

The next part of the experiment would include demonstration of the joint use of the bundle with the transmission of the diffraction orders from the sample. This requires additional optics and modification of the detection arrangement within the pulser, and is yet to be performed. Possible effects from the cross-talk/light leakage between the fibres in this case could be expected to affect the joint fibre use by both channels.

The use of the coherent fibre bundle additionally enables to replace the camera on the sample-

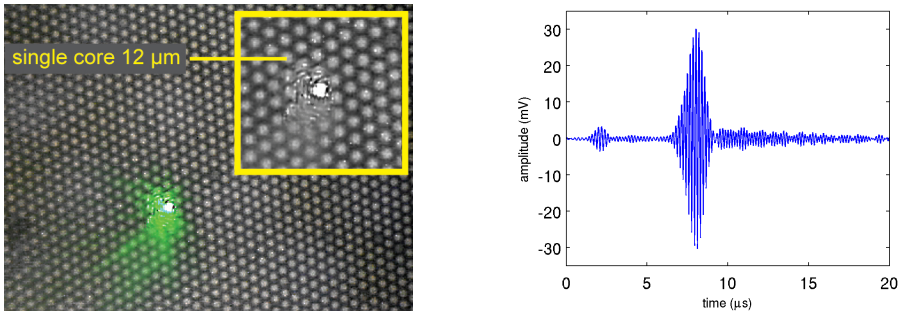

(a) Photograph of the fibre bundle exit

(b) Detected signal

Figure 4.8: Delivery of the probing illumination via coupling into a single core of the fibre bundle: investigation of system miniaturisation. Photograph (a) shows laser illumination coupling, with the close-up in the inset, and plot (b) shows signal detected using probing light expanded from the single core.

side of the endoscope. Potentially, the same fibre bundle can be used both to transmit the images for navigation of the endoscope and for alignment of the illumination with the transducers, as well as to collect the returning light. The use of the same fibre bundle to combine the functions of both channels will contribute to the overall reduction of the endoscope probe diameter.

4.5 Summary

The instrumentation of the endoscopic CHOTs pulser, its structure and elements were described viewing the operation of the system according to the performed functions of generation, probing and detection. The characteristics, selection and role of the system elements were provided grouping them into radiation sources, coupling and transmitting optics, and the electronic signal detection and acquisition components. The practical use of the system was described with regard to required alignment, operational safety and future system development past current capabilities. The system automation and endoscope miniaturisation would be the main priorities to enable system field application. The preliminary work on the miniaturisation of the endoscope size by combination of the probing and detection optical delivery was presented.

Chapter 5

Fabrication of CHOTs on film carriers

The fabrication procedures described in this chapter were developed to produce a portable CHOT, enabling application of the transducers on-site, to large and curved components. These procedures combine well-established microfabrication methods and materials with more recently-developed processes and the use of the purposefully-selected materials.

The feasibility of CHOT fabrication using film carriers was investigated for two concepts: 1) using photolithographic techniques and materials to produce sacrificial layers and CHOT carriers to enable separation of the transducers from the substrate, and 2) using commercially-available optically-clear adhesive transfer tapes. In both methods the CHOTs were created by metal deposition through a mask, using a sputter coater and a vacuum evaporator.

The fabrication procedures of a g-CHOT and a d-CHOT require to take into account the differences in their operation principles, which was achieved by corresponding adjustments of the devised procedures. Both fabrication concepts were used to create the g-CHOTs, whereas the d-CHOT was produced using only the second concept due to its simplicity. Fabrication of a d-CHOT using sacrificial layers and photolithographic techniques is also possible but would require a complex time-consuming procedure with multiple steps.

The proposed fabrication methods, step sequence and parameters were dynamically modified according to the intermediate findings to establish the best working procedure. The quality of the fabricated transducer carriers was evaluated by visual examination and optical microscopy. The functionality of the fabricated transducers was later assessed by performing a series of tests described in Chapter 6.

5.1 Equipment and materials

This section provides a description of the sample preparation, equipment and source materials used that are general to the fabrication of CHOTs in this work, and are not specific to the fabrication of CHOTs on film carriers. Specificity of the method or material in particular cases is noted in the text where applicable.

CHOT Mask

CHOT masks for 4 MHz and 5 MHz SAWs were produced on a 50 μm-thick sheet of brass by laser cutting at the University of Nottingham manufacturing workshop (figure 5.1). The spatial periods of the fabricated mask patterns Λ_f were measured to be 704 μm for a 4 MHz mask (design value $\Lambda_d = 726$ μm) and 559 μm for the 5 MHz mask (design value $\Lambda_d = 581$ μm). The mark-to-space ratios were determined as 0.944 and 1.055 correspondingly. The difference in the spatial period of the mask between its design and the fabricated value $\Delta\Lambda = \Lambda_d - \Lambda_f$ is 22 μm for 4 MHz mask and 22 μm for 5 MHz mask. These differences are expected to produce a shift in the central frequencies of the fabricated CHOTs equal to $\Delta f = c_R \cdot \Delta\Lambda/(\Lambda_d \cdot \Lambda_f)$. Considering Rayleigh wave velocity on Al $c_R = 2,905$ m/s, the frequency shifts are $\Delta f_{4\text{MHz}} = +0.125$ MHz and $\Delta f_{5\text{MHz}} = +0.196$ MHz.

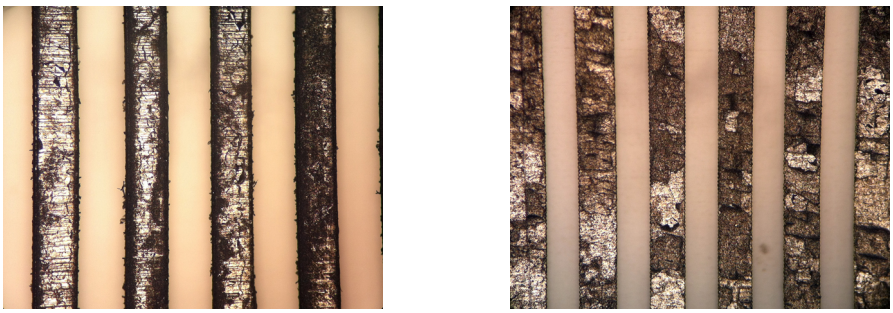

(a) 4 MHz mask (b) 5 MHz mask

Figure 5.1: Microscope images of the fabricated masks (darker areas correspond to metal and bright areas to cut-through slots).

Sample preparation

Precision glass windows from Comar (⌀25 mm, thickness 4 mm) were used as substrates. In all cases, prior to material deposition the samples underwent cleaning procedure to remove surface impurities consisting of sequential sonication for 8 minutes in ethylactate, acetone, methanol and isopropanol using an ultrasonic bath, and dried using nitrogen. The solvents were used in the order as listed to reduce the amount of residue left on the surface after each stage.

Equipment

Two types of equipment for material deposition were used with the fabricated masks to create a CHOT: a sputter coater Emitech K575XD and an Edwards 306A vacuum evaporator. The use of the mask with each system produced patterns unequal in quality, which could be explained by the difference in the mechanisms employed for material deposition in each case. Later, the choice of particular equipment was made prioritising the fabrication time or pattern quality requirements of each case, with the sputter coater providing faster operation times, and the vacuum evaporator being used for precise fabrication.

Sputtering is a process upon which the creation of the gaseous glow discharge (plasma) between an anode and a cathode target material results in a cathode being bombarded by the inert gas ions, eroding the target material and producing an omni-directional deposition of the high-speed sputtered atoms [143]. In a typical equipment arrangement, the target material is located in the chamber in the holder above the sample stage, and the sample is placed onto the rotation stage under the target (figure 5.2).

Evaporation is an alternative method to sputtering, where the source material is being heated above its melting point and evaporated in a vacuum, condensing on the surface of the sample. In this case the evaporated atoms travel directly to the sample without collisions with other particles, and so are deposited mostly from a single direction. In such setup, the sample is stationary, and is located above the source material (figure 5.3). In the Edwards 306A model material heating and evaporation is achieved by passing a large current through a resistive evaporation boat containing the source material.

The sputter coater is generally preferred for work with rough surfaces providing more even step coverage, compared to the vacuum evaporator where the deposition from a single direction

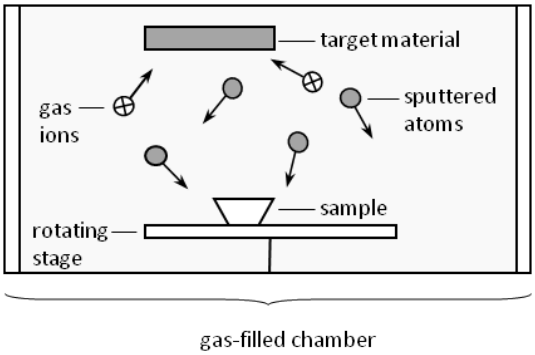

Figure 5.2: Typical arrangement during material deposition in a sputterer

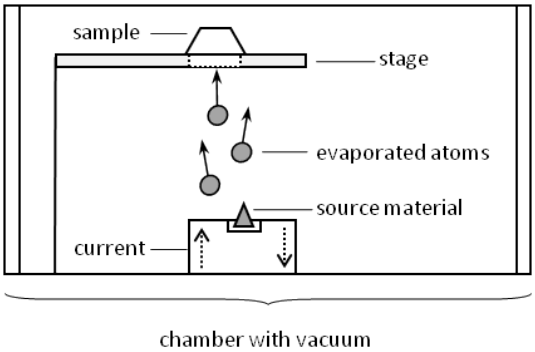

Figure 5.3: Typical arrangement during material deposition in an evaporator

produces undesirable shadowing effects. In the case of coating a sample through a mask, however, the effects are reversed.

In presence of a small gap between the mask and the surface of the sample, the multi-directional nature of material deposition in the sputter coater ensures penetration of the sputtered atoms into what should be the shadow regions under the mask, blurring the features of the pattern. This leads to certain disadvantages: 1) tightens the requirements to the flatness of the mask and the surface of the sample, 2) requires tight contact between the mask and the sample to be provided evenly across the mask. Additionally, 3) the movement of the sample stage during the deposition produces mask micro-shifts in instances where mask is not tightly attached to the sample, resulting in feature blur. The last two factors are limiting for the sputter coater in cases where contact with the substrate is undesirable (see fabrication of self-adhesive CHOTs, section 5.3).

In contrast, the direct path taken by the evaporated atoms through the mask in the vacuum evaporator and a stationary sample allow a small separation between the mask and the sample if required, without the loss of feature resolution (relative to the feature size). Generally, a better contact is also provided by the sample's own weight as it is placed on top of the mask in this arrangement.

The high-speed atoms sputtered onto the sample were also noted to penetrate into the material of the film substrates, which has to be considered when developing fabrication procedures using a sputter coater and film substrates.

Equipment Calibration

Both coating systems use film thickness monitor (FTM) to determine the thickness of the deposited film via a piezoelectric effect. The oscillating frequency of the quartz crystal comprising the FTM sensor is changed by the mass of the material being deposited on its surface. This change is detected electronically, and automatically converted into thickness using material density information provided by the operator.

Small differences, however, exist between the thickness indicated by FTM and the actual deposited layer measured independently on the sample. These result mainly from the physical arrangement where the indicated deposition is measured by FTM in close proximity to the sample but strictly in a different location (as the sensor can not obscure the sample) and at a different angle from the source.

In order to provide accurate indication of thickness, the tooling factor takes into account these inherent discrepancies by quantifying the relation between the measured and the indicated thickness. It has to be determined individually for different materials (due to the differences in the deposition rates), as well as corrected periodically during the crystal lifetime (the accumulation of

material on its surface reduces the sensitivity) and after each change of the FTM crystal:

$$T_{actual} = T_{indicated} \cdot TF = T_{indicated} \left(\frac{h_{measured}}{h_{indicated}} \right) \tag{5.1}$$

The knowledge of the tooling factor becomes particularly important during the fabrication of a d-CHOT, the operation of which is dependent on ensuring the accurate step height.

The tooling factor of the vacuum evaporator was determined for Cr, considering the target step height of 66 nm. A calibration sample was made by deposition of 60 nm of Cr ($h_{indicated}$) onto a glass substrate using a CHOT mask to produce a step profile. The resulting step height was considered to be indicative of the coating thickness. It was measured with the stylus surface profiler Alpha-Step D-120 (KLA Tencor) to be 75 nm ($h_{measured}$), averaging the height over the number of points across one step. Based on this data and according to equation 5.1 the tooling factor of the vacuum evaporator was calculated to be $TF = h_{measured}/h_{indicated} = 75$ nm/60 nm $= 1.25$.

Controlled deposition using the calculated tooling factor was performed and the step profile height measured to verify the determined quantity. To achieve the required step height of 66 nm with the TF of 1.25, the required indicated thickness of the deposited layer was determined to be 52.8 nm, where 52.9 nm of Cr was deposited. The average step height was measured as 66 nm confirming the calculated tooling factor was correct. The thickness of the deposited layer before and after the correction for the tooling factor is shown in figure 5.4 as step profiles of the fabricated CHOTs.

Similar procedures were later used for calibration and correction of the tooling factor as necessary.

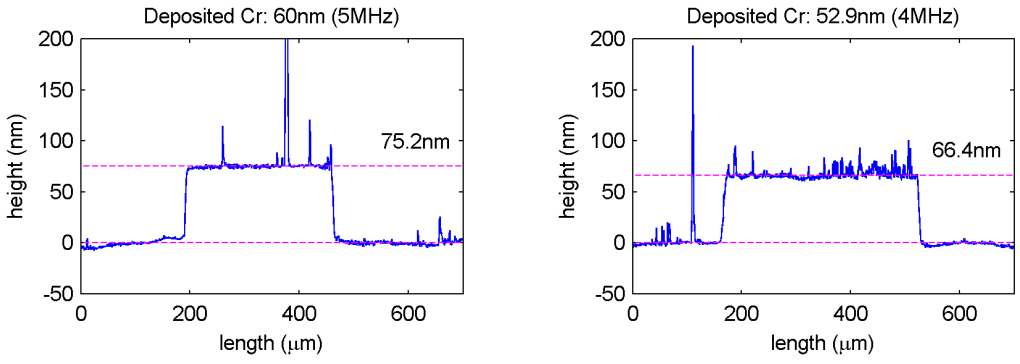

(a) (b)

Figure 5.4: Step profiles before (a) and after (b) evaporator calibration

Materials

Chromium (Cr) and silver (Ag) targets from Quorum were used for CHOT fabrication in the sputter coater. Chromium crystal sources of 99.99% purity and Ag wire source from Testbourn were used in a vacuum evaporator. All sources were cleaned by 8 minute sonication in isopropanol, and dried by nitrogen prior to deposition.

5.2 Transferable CHOTs using sacrificial layers

The first concept to create a portable CHOT consists of modifying the established fabrication procedure, where a CHOT is created directly on the sample, by introducing a sacrificial layer between the substrate and the CHOT. This layer is later chemically removed allowing the separation of the substrate and the transducer. An additional, containing, layer is required to act as a CHOT carrier and contain the pattern during and after its release.

Two methods were explored to produce CHOTs using sacrificial layers (figure 5.5). In method I the CHOT was created directly on top of the sacrificial layer separating it from the substrate, and the containing layer was fabricated last, covering the CHOT pattern (figure 5.5a). The use of polystyrene (PS) and a photoresist SU8 as CHOT containing layers was investigated. Method II is a modification of the procedure where the sequence of the fabrication steps was reversed based on the intermediate findings and observations. In this modified method the carrier film is produced on a sacrificial layer first, and the CHOT pattern is created last, on top of the carrier (figure 5.5b).

The described fabrication trials using sacrificial layer concept were carried out with g-CHOT

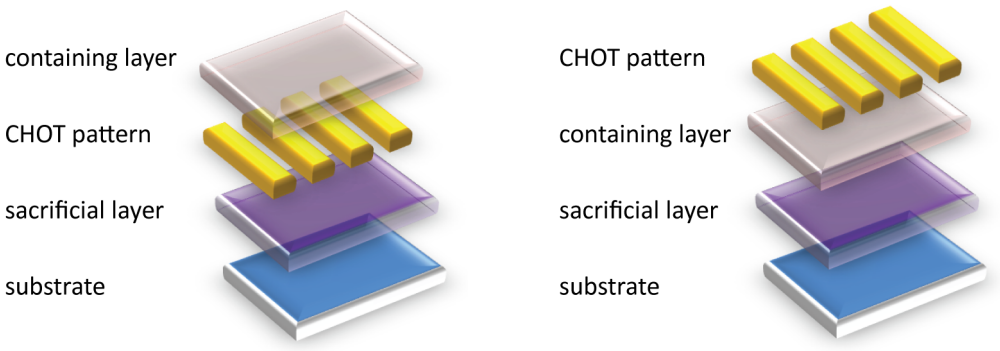

(a) (b)

Figure 5.5: CHOT fabrication sequence using sacrificial layers: Method I (a) and Method II (b)

patterns. Although a similar concept was devised for the d-CHOT fabrication, they were later produced using self-adhesive film (section 5.3.2). The g-CHOT patterns were made in the sputter coater, which was chosen over the vacuum evaporator for its faster operation that was beneficial in the multiple-step fabrication procedure.

5.2.1 Method I: Glass-BPRS-CHOT-PS (Protocol 1)

The creation of a solid sacrificial layer that can be chemically removed could be achieved using light-sensitive materials such as photoresists, commonly used in photolithography. Their ability to become soluble (positive photoresist) or insoluble (negative photoresist) to the resist developer after a UV exposure made them a suitable choice.

Photoresist BPRS-150 was used in the first trial as a sacrificial layer material. The selection of a positive photoresist (BPRS-150) would enable its easy removal after a UV exposure with the resist developer. The photoresist was spin-coated onto a glass substrate, baked and exposed to UV creating the sacrificial layer. The chromium (Cr) CHOT pattern was then produced onto the fabricated layer in the sputter-coater.

Polystyrene (PS) solution was prepared, spin-coated on top of the created BPRS-CHOT structure, covering the CHOT and baked, producing the containing layer. The release of the CHOT with the carrier was to be performed by submerging the sample into the resist developer to dissolve the sacrificial layer. In order to expose the layer of BPRS (now coated with PS) to resist developer, the outer edges of the structure were wiped with acetone prior to baking. The details of the process are shown in table 5.1. Baking of polystyrene and BPRS was performed in the Carbolite laboratory oven.

A disintegration of the CHOT pattern was observed during the lift-off stage, shortly after the sample was submerged. It was concluded to be the result of the effect of the developer on the PS layer containing the CHOT, leading to the dissipation of Cr into the solution.

Following this, the combination of materials used in the process was revised so as to provide better resistance of the containing layer to the chemical agent used to remove the sacrificial layer. The second trial of the method was carried out with the new combination of materials.

5.2.2 Method I : Glass-PS-CHOT-SU8 (Protocol 2)

The materials chosen for the second trial were PS for the sacrificial layer, and a negative photoresist SU-8 100 for the containing layer. In this trial toluene was used to remove the sacrificial layer and separate the transducer carrier from the substrate. The use of PS sacrificial layers was previously reported for successful release of the SU-8 structures as large as 50 cm^2 [144]. Here, the process

Table 5.1: Fabrication process of a g-CHOT using PS carrier, Method I (Protocol 1)

Sacrificial layer	**CHOT fabrication**	**Containing layer**	**Separation from substrate**
BPRS-150	Cromium (Cr)	PS 13k 5% solution	resist developer
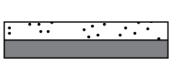	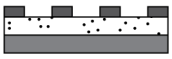	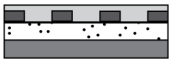	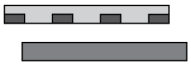
spin-coat: 30” at 3,000 rpm	sputter-coater deposition 60 nm (indicated)	spin-coat: 30” at 1,400 rpm	immerse resulting structure
bake: 30’ at 100 °C		bake: 60’ at 100 °C	
expose to UV: 80”			

was adapted for creation of the CHOT carrier.

The process consists of spin-coating and baking of a PS solution onto a glass substrate, deposition of the Cr pattern onto the solidified PS layer, followed by spin-coating of SU-8 on top of this PS-CHOT structure, and processing it according to the manufacturer's recommendations ([145]). The final structure produced by this method is placed into an agitator with toluene for pattern release, after which the separated carriers are removed and dried.

In this trial, the surface of the sample was pre-treated to improve adhesion of PS to glass by spin-coating of a small amount of toluene (substrate wetting). After being dispensed onto the substrate, the polystyrene solution was allowed to rest for 25 seconds before the start of spin-coating. Prior to spin-coating of the final layer of SU8, the photoresist was heated on a hot plate at 66 °C until it became fluid, and spread to cover the sample with a glass syringe. The details of the process are shown in table 5.2.

As in the previous trial, the sides of the sacrificial layer (PS, now coated with SU-8) were exposed by wiping the outer edges of the structure with acetone prior to baking. For both fabricated layers sufficient cooling to room temperature (21 °C) was allowed after the baking stages. The baked layer of polystyrene was left to cool in the oven to prevent forming of film stresses due to rapid temperature change. Baking and cooling of the SU-8 layer was performed on a hot-plate, and the temperature monitored with a digital infrared (Maplin N19FR) and an analogue contact hot plate thermometers.

Table 5.2: Fabrication process of a g-CHOT using SU-8 carrier, Method I (Protocol 2)

Sacrificial layer PS 13k/100k 10% solution	**CHOT fabrication** Cromium (Cr)	**Containing layer** SU8-100	**Separation from substrate** resist developer
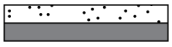	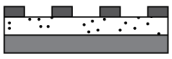	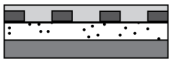	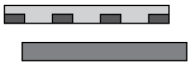
spin-coat toluene: 15” at 1,500 rpm	sputter-coater deposition 60 nm (indicated)	spin-coat: 10” at 500 rpm 30” at 2,500 rpm	immerse resulting structure
spin-coat PS: 30” at 700 rpm		soft-bake: 20’ at 66 °C 50’ at 95 °C	
bake: 60’ at 100 °C		expose to UV: 90” at $\lambda = 365$ nm	
		post-exposure bake: 1’ at 65 °C 12’ at 95 °C	
		develop: 5’ in EC solvent	

The process parameters shown in table 5.2 result from a number of fabrication trials and intermediate investigations, during which the working parameters were established and the process modified accordingly. Using this method and the combination of materials the CHOT carriers were successfully released from the substrates. The thickness of the separated carriers was measured with Mitutoyo digital micrometer to be 80 μm. The transducer release from the substrate was achieved in toluene using a sonication bath and heating in some trials, and an agitator and heating in others. Slight toluene warming and agitation proved to provide better quality of the released film.

It was noted that the resulting CHOT pattern in the fabricated structures had cracks (figure 5.6), which were found to be formed during the soft-baking stage of the containing layer of SU-8 (discussed below). It was further discovered that the use of PS with a different molecular weight was one possible solution to prevent cracking. Another suggested solution was to change the

Figure 5.6: Microscope images in transmission: CHOT on PS directly after Cr deposition (a) and in the final structure (b). The dark areas in the image correspond to the metal CHOT features.

fabrication order of the layers, which was implemented in Method II, described in subsection 5.2.3.

Pattern cracking investigation

A separate investigation was performed to identify the fabrication stage and the affected layer of the multi-layer structure where the cracking was occurring. The following possibilities leading to pattern destruction were initially considered:

- heat processes in the sputter-coater during the deposition of Cr leading to cracking of the PS layer itself
- the effect of SU-8 or its temperature during the deposition on top of the CHOT for spin-coating
- thermal expansion of Cr in the PS layer during the baking stages of SU-8
- thermal expansion differences between the PS and SU-8 layers during the baking stages of SU-8

A control sample was made where the condition of the layers was monitored at each stage of the

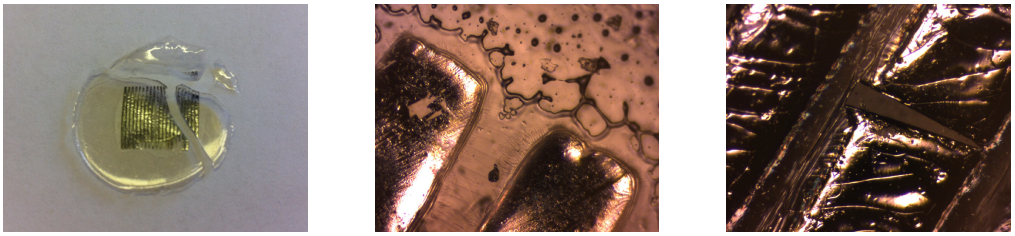

Figure 5.7: Released g-CHOT on an SU8 carrier (a) and its microscope images in reflection from the pattern side: lifted pattern (b) and crack details (c).

fabrication procedure (table 5.3). Comparing microscope images of the layers taken at each stage pattern cracking was observed after the soft-baking step of the containing layer. After the step of the process leading to pattern destruction was determined, it remained to identify which one of the three layers (PS, Cr, SU-8) was affected resulting in pattern damage.

In order to investigate the effect of baking onto isolated parts of the multi-layer structure, three control samples with layers corresponding to the fabrication sequence were made: a sample with a single layer of PS, a sample with PS and a Cr CHOT, and a sample with PS-CHOT that was spin-coated with SU-8 but untreated. Microscope images were again obtained after deposition of each layer to monitor the condition of the film and the pattern prior to the test.

Soft-baking of the sample spin-coated with SU-8 was then performed on the hot plate along with two control samples representing parts of the baked structure (table 5.4). At this stage, as was noted previously, the pattern cracking occurred in the PS-CHOT-SU8 sample a few minutes after the sample was heated. It was also observed at the same time in the control PS-CHOT sample, but not in the control sample containing single layer of PS. This, combined with the microscope images showing no pattern damage after deposition of layers but prior to soft-baking, indicated the PS-CHOT layer as the one affected by the treatment. The differences in thermal expansion rates between the metal Cr structures and the polymer PS layer during the heating were considered to be the cause of the cracks in the CHOT pattern.

The described test was repeated to confirm the findings. During this test, however, available 100k PS was used, not the 13k PS used previously keeping other procedures and quantities as previously described. During this trial pattern cracking was not observed. The following section

Table 5.3: Identifying the stage

Sacrificial layer	**CHOT fabrication**	**Containing layer**	**Separation from substrate**
PS 13k baked	deposited Cr pattern	SU-8 soft-baked	released CHOT carrier
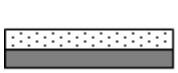	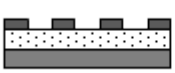	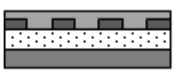	
	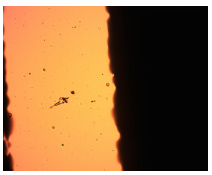	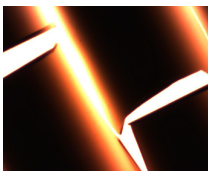	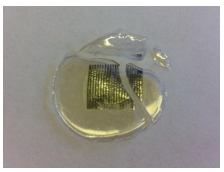

describes a separate investigation that was performed to confirm the effect from the differences in PS molecular weight onto the pattern integrity.

Table 5.4: Identification of the affected layers during the soft-baking stage

	PS layer only	**PS + Cr**	**PS + Cr + SU8**
	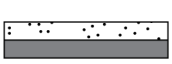	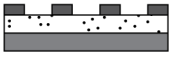	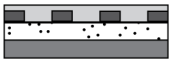
before heating		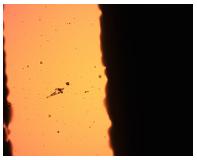	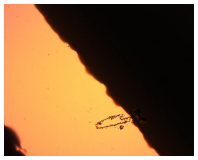
after heating		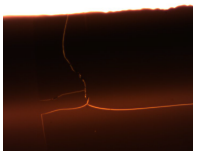	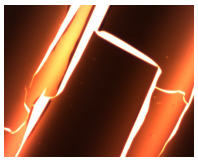

PS molecular weight investigation

To investigate the effect of the PS molecular weight onto the pattern integrity, two 10% solutions were made using PS of different molecular weights: 13k and 100k PS. A number of samples with each type of PS were made and all stages of the fabrication process were carried out for each set of samples, monitoring the structure condition at each stage by an optical microscope. The detailed process description and microscope images corresponding to each stage, as well as the separation of stages can be found in tables 5.5 and 5.6. As expected, fabricated PS-Cr-SU8 structure made using 100k PS as a base layer did not show the signs of pattern destruction, in contrast to the structure based on 13k PS where pattern cracking was observed. Both patterns from 13k and 100k trials were released from the substrates with some pattern damage that occurred during the release.

Spin-coating PS of different molecular weight at the same parameters produces layers of different thickness contributing to the release times, where a thicker layer of PS would result in a shorter release time. In this trial the release times were 195 minutes for 13k PS (thinner layer) and 90 minutes for 100k PS (thicker layer).

Table 5.5: Monitored stages of the fabrication process for PS of different molecular weights

Stage	**PS 13k**	**PS 100k**
PS: spin-coating		
PS: baking, cooling		
CHOT: Cr deposition	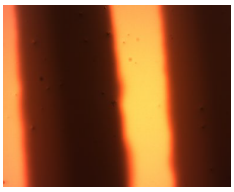	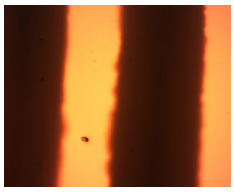
SU8: spin-coating	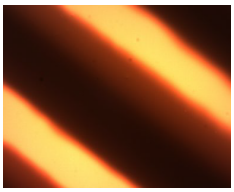	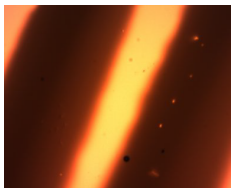
SU8: soft-baking 1	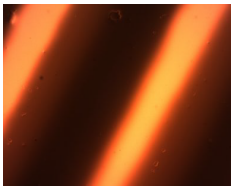	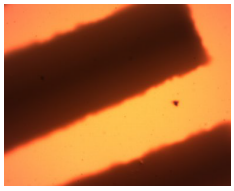
SU8: soft-baking 2, cooling	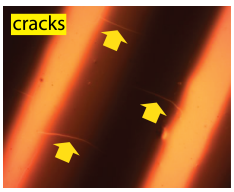	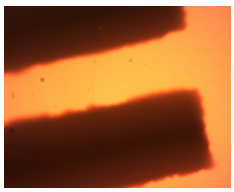
Exposing, baking		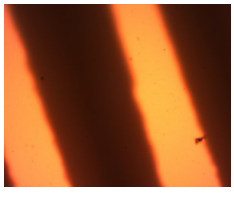
Developing	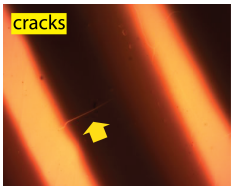	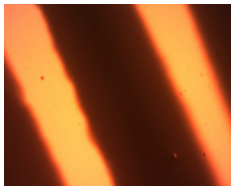

Table 5.6: Separation of layers during soft-baking stage for PS 13k and 100k MW

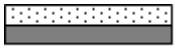	**PS layer only, 13k**	**PS layer only, 100k**
soft-baking 1	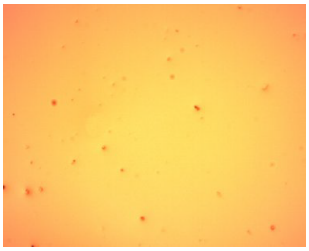	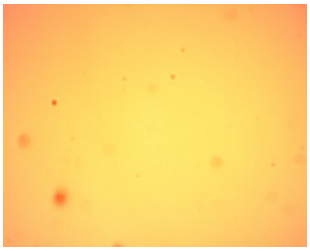
soft-baking 2	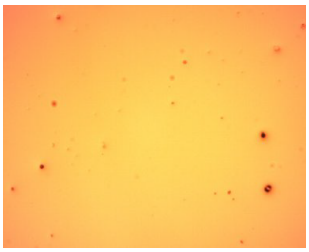	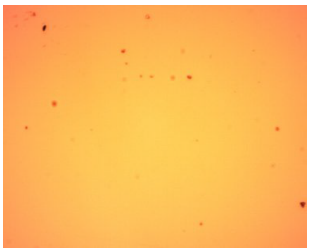
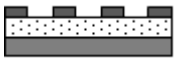	**PS 13k + Cr**	**PS 100k + Cr**
soft-baking 1	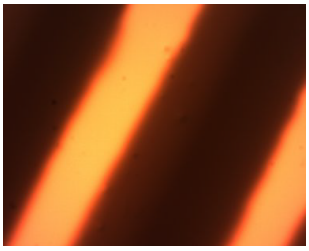	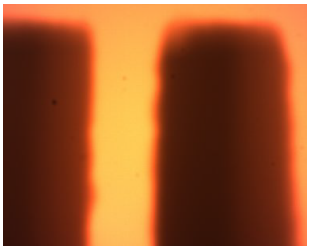
soft-baking 2	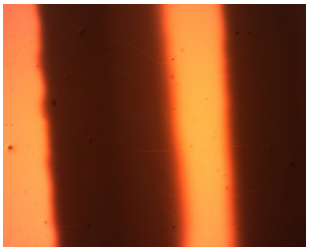	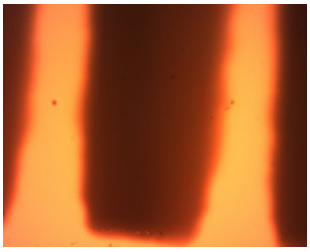

5.2.3 Method II : Glass-PS-SU8-CHOT

Although the use of PS with a higher molecular weight proved to be one solution to keep integrity of the CHOT, the process was modified by changing the order in which the layers are created and their respective treatment. In this modified process the containing layer is created directly on a sacrificial layer, forming the base for the pattern deposition, in contrast to Method I (section 5.2) where it was created on top of the pattern. Other stages of the process are kept unchanged. In this method, the setting of the SU-8 layer is performed before the creation of the metal pattern, therefore excluding the effects of heating onto the pattern integrity.

This method was used with the 100k PS. The SU-8 carrier with the g-CHOT was successfully released showing significant improvement in the quality of the film and the pattern, and no cracking. Figures 5.8 and 5.9 show the photograph and microscope images of the fabricated transferable CHOT on a film carrier in comparison to the CHOT produced directly on the sample.

The fabrication of CHOTs using sacrificial layers and their further tests demonstrated the feasibility to produce a functional transducer on a film carrier. This first generation of portable CHOTs

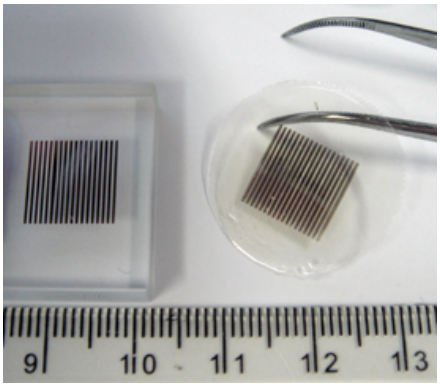

Figure 5.8: g-CHOTs produced directly on a glass sample (left) and on a film carrier (right).

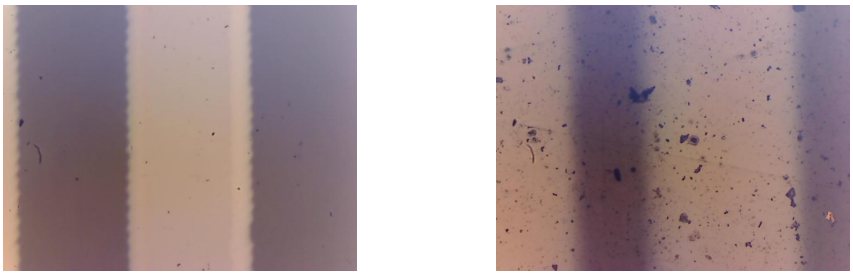

(a) (b)

Figure 5.9: Microscope images of 5 MHz g-CHOTs fabricated directly on glass (a), and on an SU8 film (b).

requires a couplant and can be reapplied. In instances where more permanent attachment of the transducer to the test part is desired and to facilitate the ease of application, a layer of adhesive could be added to the film carrier to act as the couplant and keep the transducer fixed on the surface. The second generation – self-adhesive CHOTs – was fabricated using commercially-available adhesive tapes to fulfil these functions. The use of commercially-available products simplifies the fabrication procedure, reducing the fabrication time and cost, and makes it reproducible without the need for specialist skills and equipment.

5.3 Self-adhesive CHOTs

The concept of the self-adhesive CHOTs is based on using a film structure consisting of three layers: a top base liner, a layer of adhesive and an adhesive protective liner at the bottom (figure 5.10a). The transducers are fabricated on the top liner with adhesive. They can then be transferred and attached to samples by 1) removing the protective liner to expose the adhesive, and 2) placing the CHOT carrier in contact with the surface of the sample and applying a slight pressure onto the film (figure 5.10b).

The selection of the film type should consider the operation principles of the CHOTs as well as the equipment and environment in which they are manufactured. The fabrication procedures are customised for the g- and a d-CHOT according to their operation principles, and considering test results of the CHOT carriers of the first generation presented in Chapter 6. As the pattern deposition is performed in a vacuum evaporator, one of the main requirements to the adhesive film is low outgassing and ability to withstand high temperatures.

Self-adhesive CHOTs for generation and detection of the plane surface acoustic waves at 4 and 5 MHz on aluminium were fabricated using deposition through a mask in a vacuum evaporator and a transparent adhesive transfer film from Lyntec as a carrier. The use of the vacuum evaporator

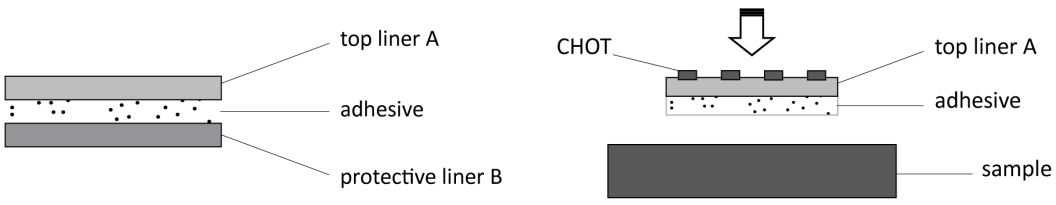

(a) Tape structure (b) Application to sample

Figure 5.10: Schematic diagrams of the adhesive transfer tape and application of portable transducer to the sample.

is preferred to the sputter coater in this case due to its ability to produce sharp features allowing the presence of a small gap between the sample and the mask, a desirable advantage for work with adhesive substrates.

5.3.1 Self-adhesive g-CHOT

The functionality tests of the first generation of portable g-CHOTs showed that the direct contact between the metal CHOT pattern and the sample was essential for transducer operation (Chapter 6). The fabrication of the g-CHOTs was therefore performed on the adhesive side of the film, allowing the CHOT to remain in contact with the sample surface upon attachment. Such arrangement requires the top liner of the film to be optically transparent to the radiation of the generation laser.

An additional option after transducer attachment is the removal of the top liner. This option is possible if the transducer is fabricated using adhesive transfer tapes which allow the separation of both liners for transfer of the adhesive layer onto the substrate. The optical transparency of the top layer in this case is not required as the transducer is being transferred onto the sample along with the adhesive, and the liner removed. Transducer functionality in both cases, and the effects of the film liner onto the propagating SAW are discussed further in Chapter 6.

The g-CHOT structures were created by evaporation of 80 nm of Chromium (Cr) through a mask onto the adhesive side of the carrier film. The protective liner was removed prior to deposition to expose the layer of adhesive. The film was then placed onto the mask, using 2 microscope slides (2 mm thickness) as spacers to separate the adhesive surface of the film from the mask. After the evaporation was complete and the film with the g-CHOT removed from the evaporator, the protective liner was reattached to cover the fabricated transducer. Table 5.7 illustrates the described process.

Initially, fabricated self-adhesive g-CHOTs displayed pattern cracking similar to the CHOTs fabricated on the PS layers, with the cracks orthogonal to the features of the CHOT. The pattern quality was marginally improved by leaving the film to cool in the vacuum evaporator for 30 minutes after the evaporation. As the test results showed later, the cracks in the pattern did not compromise CHOTs operation.

5.3.2 Self-adhesive d-CHOT

The d-CHOTs were fabricated directly on the top liner of the three-layer adhesive tape in two steps. First, the d-CHOT features/steps were created by evaporation through a mask of 66 nm of Cr – the step height required for d-CHOT operation with the 532 nm probing laser. The mask was

Table 5.7: Fabrication of self-adhesive g-CHOT

Separation of liner	**Deposition of Cr g-CHOT**	**Reapplication of liner B**	**Remove liners A and/or B for sensor attachment/transfer**
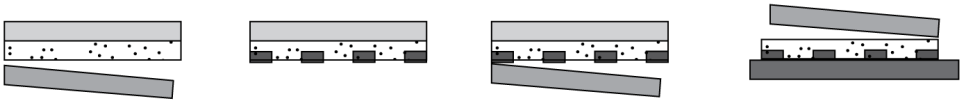			

then removed and 100 nm of Ag was evaporated on top of the CHOT features to create a reflective surface.

Upon the removal of the protective (bottom) liner and attachment of the film carrier to the sample, the d-CHOT remains on the top surface of the film, and operates through it. It is therefore required for the liner thickness to be sufficiently small. The individual liner thickness of the adhesive film used as a d-CHOT carrier was 35 μm (measured with Mitutoyo digital micrometer). The effects of the film carrier onto the operation of the d-CHOT and the propagation of the surface wave are discussed in Chapter 6.

5.3.3 Single-carrier sensors

The fabrication of the single-carrier CHOTs consists of the combination of steps described in the sections above. Both CHOTs are fabricated on a single strip of adhesive film aiding their application onto the sample and ensuring inter-sensor alignment. Figure 5.11 shows a photograph

Table 5.8: Fabrication of self-adhesive d-CHOT

Adhesive film	**Create d-CHOT profile**	**Coat with silver**	**Remove protective liner for sensor attachment**
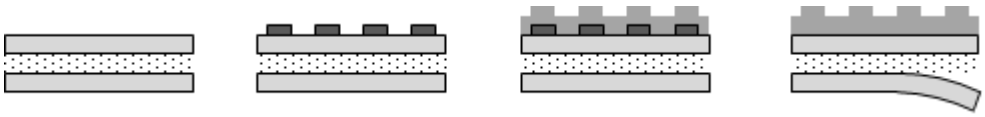			

of the fabricated CHOTs on a single carrier.

The protective liner is first removed from the part of the film to host a g-CHOT. Thus the adhesive side is exposed through a mask (using spacers) for evaporation of 80 nm of Cr creating a g-CHOT pattern. The protective liner is then reattached to cover the g-CHOT, and the carrier is turned upside down and placed directly onto the mask, aligning the fabricated g-CHOT with one of the corresponding CHOT windows on the mask. After this, the d-CHOT is created on the reverse side of the carrier (liner B) by evaporation of 66 nm of Cr to create the d-CHOT profile, followed by the removal of the mask and evaporation of 100 nm of Ag to create reflective surface.

Application of the single-carrier transducers in this case is achieved by 1) the removal of the underlying protective liners (separately covering the g-CHOT and rest of the carrier), and 2) placement of the common adhesive carrier with the transducers onto the sample surface and applying slight pressure onto the film.

5.4 Summary

This chapter described the fabrication methods developed to produce portable CHOTs on film carriers. Two fabrication concepts were investigated: the use of the sacrificial layers and the use of the commercially-available self-adhesive tapes. Both concepts were successfully implemented (with some intermediate process adjustments), the fabricated transducers characterised and tested. The test results of the transferable CHOTs, fabricated using sacrificial layers, and the self-adhesive CHOTs produced on adhesive tapes, are presented in Chapter 6.

The use of the adhesive transfer tape introduced an additional capability of the g-CHOT to be transferred onto the sample along with the layer of adhesive by removal of the carrier film after transducer attachment. This important property enables additional options for the use of the fabricated transducers, investigated and demonstrated in Chapters 6 and 7.

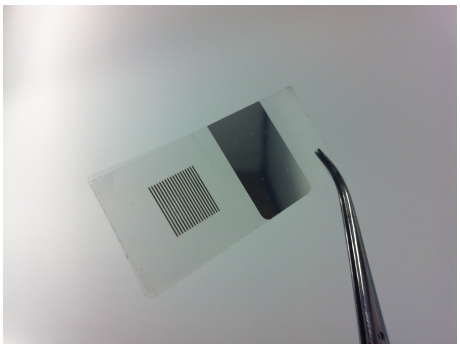

Figure 5.11: Fabricated single-carrier CHOTs

Chapter 6

Performance characterisation of the fabricated transducers

This chapter provides a quantitative description of the transducer performance. Both performance evaluation common to the CHOTs fabricated on samples directly and the self-adhesive CHOTs developed in this work (further referred to as 'OS' and 'SA' CHOTs for brevity) are presented, as well as the functionality test results and performance characterisation specific to the portable and self-adhesive CHOTs fabricated by the methods described in Chapter 5.

The performance evaluation approach was based on decoupling the system of CHOTs into its compound elements – the g-CHOT and the d-CHOT – and analysing their operation individually according to the performed function. As the independent use of CHOTs for generation and detection of ultrasound is possible, characterising their operation individually provides the most complete information compared to the analysis of the coupled CHOT system as a whole.

A brief investigation of the factors specifically affecting particular types of CHOTs considering their operation principles is included. Although such investigations are not complete in their own right due to the time constrains and further directions they opened for additional studies, by including them here an attempt has been made to provide the look into the complete set of the main performance-affecting, enhancing and limiting factors.

The g-CHOTs were characterised in terms of the generated surface acoustic wave and its parameters with respect to those expected from the pattern geometry. The transducer sensitivity to the input laser power and response linearity was measured in terms of the amplitudes of the generated surface displacement. The resulting calibration curves allow estimation of the expected transducer performance for given conditions. The experimental results showing the effect of the choice of the g-CHOT and substrate materials on the amplitudes of the generated waves are presented. Acoustic

fields produced by the g-CHOTs were visualised.

The functionality of the fabricated transferable and self-adhesive g-CHOTs was demonstrated and the generation mechanism confirmed. The transducer longevity and performance was evaluated over time and in continuous operation.

The d-CHOTs were characterised with respect to the output signal produced by the input surface displacement. Transducer sensitivity to the surface displacement and its linearity was measured to provide corresponding calibration curves. The response to the change in the probing power levels was also measured for a fixed surface displacement. The experimental results showing d-CHOT operation on a set of rough surfaces are presented. A comparison of the coupled CHOT operation is shown for the OS and SA CHOTs.

Instrumentation and common methodology

The transducer performance was evaluated in a number of test setups depending on the characteristics to be determined. The endoscopic pulser described in Chapter 4 was used for light delivery and collection to and from the CHOTs. In instances where the out-of-plane surface displacement was of interest, this setup (figure 6.1) was modified by the introduction of an optical vibrometer instead (section 6.1) or in addition (section 6.2) to the d-CHOT detection of SAW.

The Polytec vibrometer used to detect surface displacement in these tests was mounted on the PI translation stages (M-605.2DD) allowing it to move vertically across and horizontally along the sample. To perform the detection, it was then focused onto the reflective area on the sample in the region of interest. Such reflective areas were either specifically created on the sample by the deposition of 100 nm of Ag, or the existing reflective areas of the d-CHOTs were used depending

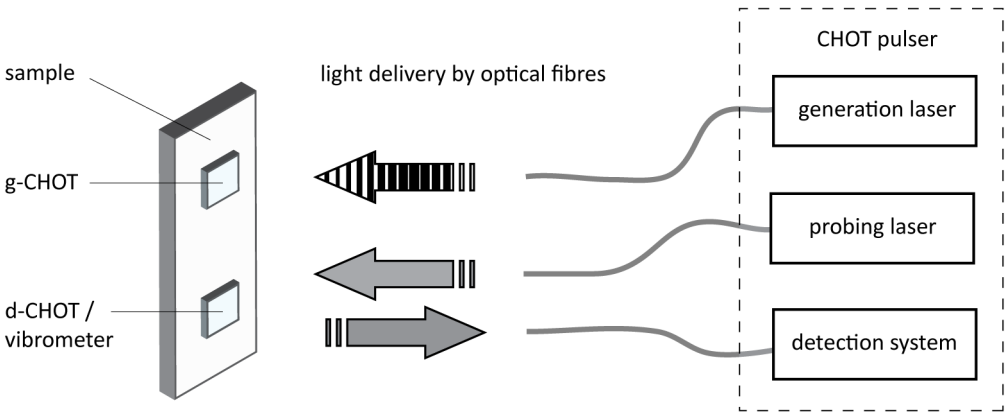

Figure 6.1: A schematic of the test setup used for performance evaluation of the fabricated CHOTs.

on the test.

Where the measurements were performed at a single point in front of the g-CHOTs, further alignment of the vibrometer detection point was performed vertically across the generated wavefront based on finding the maximum signal levels. This ensured the best alignment of a point-wise vibrometer detection to the centre of the generated wavefront for comparability of the measurements results.

To visualise the acoustic fields produced by the g-CHOTs (section 6.1.2 and 6.4.2) a scan of the sample area in front of the g-CHOT was performed by sequentially moving the vibrometer detection spot across and along the sample. During the scan the sample was kept stationary and the g-CHOT illuminated continuously. In this case an additional vertical and horizontal sample-plane to stage-plane alignment was performed to ensure consistent signal-to-noise levels across the scan area. This was achieved by monitoring signal levels corresponding to vibrometer focus on the sample and adjusting sample position accordingly.

Data acquisition and processing

The signal acquisition from the vibrometer was triggered by the generation laser pulses (at 1 kHz) providing coherent detection, particularly important during area scanning. Unless stated otherwise, a 5 MHz BPF was used during signal acquisition. The filter characteristics are given in Appendix A.2.

The raw traces acquired by the oscilloscope from the vibrometer in volts were converted to nm of surface displacement using 50 nm per volt sensitivity value provided by the equipment. The effect of the band-pass filter on the attenuation of the measured wave amplitude can be accounted for by using the reference traces taken without the filter.

In some cases the wave packets in the recorded signals were windowed using a Hann window centred on the peak of the wave packet. The fast Fourier transform of the signals was performed using a DFT MATLAB algorithm, and the Fourier amplitude values were converted into the time-signal PTP units for ease of result interpretation.

6.1 Performance evaluation: g-CHOT

The g-CHOT transforms optical energy of the generation laser into a SAW. The transducer output can therefore be characterised and measured in terms of the normal surface displacement produced by the generated wave (figure 6.2). Due to the natural material attenuation and distance-dependent amplitude reduction of the acoustic wave, the measurements of the surface displacement should be performed at a fixed distance from the source where comparable results are desired. This was

commonly achieved by keeping the distance between the generation and detection beams fixed or matching the arrival times of the detected wavefronts between the samples of the same test group.

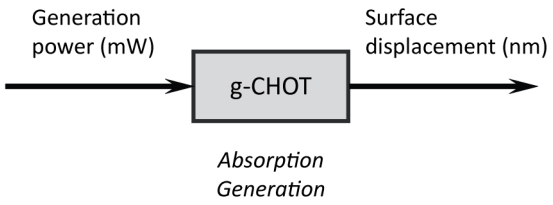

Figure 6.2: Schematic diagram of the g-CHOT inputs and outputs

The characteristics of the generated SAWs are defined by the transducer geometry and the choice of transducer and substrate materials (Chapter 3), by the size of the illuminated area and the distribution of energy on the g-CHOT. However, it is the characteristics defined by the transducer design that describe its performance. Therefore, transducer operation was evaluated with respect to the transducer geometry and material-dependent frequency and amplitude of the generated wave. The diagram in figure 6.3 illustrates the test arrangement used.

The beam diameter was maintained throughout the tests and possible small variation in the energy distribution due to the use of a multi-mode fibre for light delivery were considered negligible. These variations affect the shape of the acoustic wavefront and the spatial location of the wavefront maximum, and are excluded by appropriate selection of the measurement point across the wavefront.

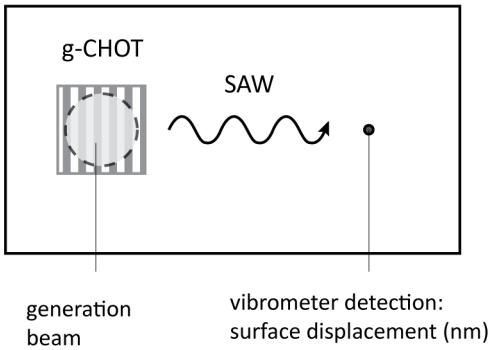

Figure 6.3: Schematic diagram of the g-CHOT performance evaluation test setup

6.1.1 Frequency and amplitude of the generated acoustic wave

The operational frequency of a transducer is one of its main characteristics, and a factor affecting transducer selection for particular applications. In case of a CHOT it is also defined by transducer geometry and dictates its design.

The wavelength of the generated wave Λ_{SAW} is determined by the spatial period of the g-CHOT fingers, with the corresponding acoustic frequency f further dependent on the Rayleigh wave velocity of the substrate c_R as $f = c_R/\Lambda_{SAW}$ (the operational frequency of the g-CHOT should therefore be quoted stating the substrate material).

The geometry of the fabricated g-CHOTs can be visualised by optical microscopy and their spatial profile measured with a stylus profiler. The actual operating frequency of the fabricated g-CHOTs obtained from the frequency spectrum of the generated wave can then be compared to the values expected from transducer design and its measured geometry.

Fabricated g-CHOTs

Figure 6.4 shows a typical profile of a g-CHOT produced in a vacuum evaporator and measured with a surface profiler. It was fabricated on crown glass (c_R = 3,127 m/s) using 5 MHz mask designed for aluminium (c_R = 2,905 m/s) with the corresponding Λ_{SAW} = 581 μm (Chapter 5).

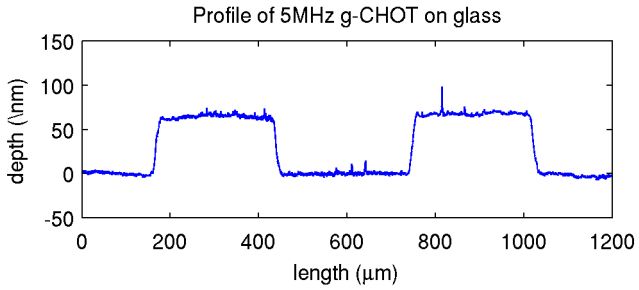

Figure 6.4: Geometry of a g-CHOT fabricated on glass by deposition through a mask.

Considering the velocity differences between these materials, the expected central frequency of the wave generated on glass is 5.38 MHz using the mask design value, and 5.59 MHz based on the measurements of the fabricated mask (Λ_{SAW} = 559 μm), 11.8% higher than for aluminium.

The average spatial period measured from the profiles of the fabricated OS g-CHOTs varied between Λ_{SAW} = 562–575 μm, with the corresponding expected frequencies in the range of 5.43–5.56 MHz. Such profile measurements, however, depend significantly on the angle between the

features of the CHOT and the path of the stylus, where deviation from the normal to the CHOT steps would result in overestimation of the profile length.

Microscope images of the OS and the SA g-CHOTs used to record generated SAWs and produced within a single deposition to ensure equal fabrication conditions are shown in figure 6.5.

Results and discussion

The SAWs generated by the fabricated g-CHOTs on a glass sample are shown in figures 6.6 and 6.7. The normal surface displacement produced by the propagating SAW was measured by the optical vibrometer in the setup shown in figures 6.1 and 6.3 averaging 500 waveforms at 5 GS/s and 470 mW average input IR power. The distance between the generation and the detection beam was fixed for both tests such that the detection beam was positioned at approximately 2 cm from the centre of the g-CHOT – a place corresponding to centre of a d-CHOT (in other tests). To determine the frequency content of the generated wave, the waveforms in figure 6.6 were recorded using no filters, whereas those in figure 6.7 recorded with a 5 MHz BPF. As this filter is further used with the vibrometer throughout the tests, recording both outputs at this point allows to consider the effect of the filter onto the amplitude and the frequency content of the measured SAW.

Although the source to detection point distance was fixed during the tests, comparing figures 6.6 and 6.7 (a) and (b) a slightly delayed arrival of the wavepacket from the SA g-CHOT can be noted. This was most likely caused by the propagation of the generated wave through the part of the carrier film surrounding the g-CHOT and altering wave velocity.

The frequency spectrum of the recorded unfiltered signals is shown in figure 6.8 and indicates the peak amplitudes corresponding to the central frequencies of 5.65 MHz and 5.11 MHz for the OS

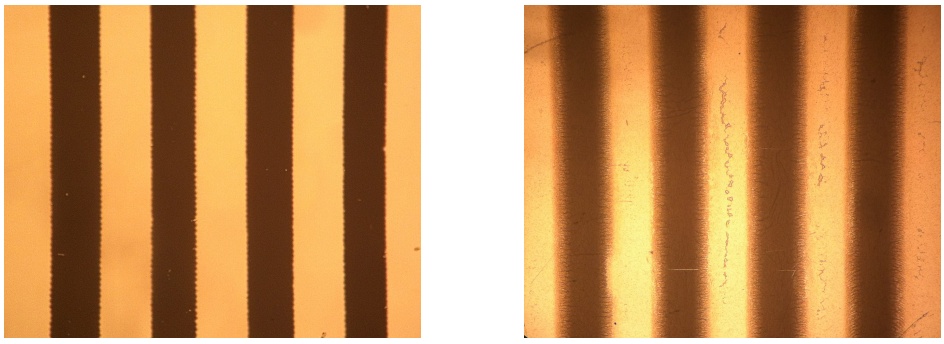

(a) (b)

Figure 6.5: Microscope images in transmission of the g-CHOTs fabricated (a) directly on glass (b) on adhesive carrier

and the SA g-CHOTs respectively, with the maximum corresponding deviations from the expected values of 4% (5.43 MHz) and 8% (5.56 MHz) .

The contributions from the following factors can lead to the deviations from the expected value: 1) the actual wave velocity in material could differ from the reference value, being also dependent on temperature; 2) the error in measurement of the CHOT's spatial period, which is highly dependent on sample orientation during the measurement. Considering these factors independently, the velocity would have to be at least 3,175 m/s or the spatial period would need to be 553 μm for the OS g-CHOT. Possible deformation of the carrier film during the fabrication and attachment of the SA g-CHOT could explain the lower central frequency of the generated wave compared to the OS g-CHOT.

The bandwidth of the detected SAW was determined as the full width at half maximum (FWHM) of the central frequency, corresponding to 1.26 MHz and 1.07 MHz for the OS and the SA g-CHOTs respectively. As the bandwidth is dependent on the number of the illuminated sources, it is expected to be similar for both tests with the constant diameter of the illumination beam. A small difference in these tests could be attributed to the higher signal amplitudes from the SA g-CHOT as well as the differences in the relative lateral positions of the beam and the g-CHOT producing an additional source in the second case.

The deviation in the central frequency of the generated wave from that of the 5 MHz BPF (when used in further tests) result in the shift of central frequency of the OS g-CHOT to 5.53 MHz and reduction in bandwidth from 1.26 MHz to 0.99 MHz. Due to the smaller frequency difference, the central frequency and bandwidth of the SA g-CHOT remain unaffected by the use of the filter.

The nature of the SA g-CHOT fabrication gives rise to a particular functional difference between the transducers that becomes evident when comparing their frequency spectra: the presence of the third harmonic in the spectrum of the OS g-CHOT, and its absence in the spectrum of the SA g-CHOT. This effect indeed could be observed in the microscope images of the fabricated transducers (figure 6.5) where the sharper features of the OS g-CHOT would produce higher frequency components as compared with the blurred gradient edges of the SA g-CHOT.

Another significant difference between the waves generated with the OS and the SA g-CHOTs is considerably higher amplitudes of the surface displacements produced by the latter: 3.7 times higher when no filter was used (compare figures 6.6(a) and 6.6(b)) and 6.1 times higher when the signal was filtered (figures 6.7(a) and 6.7(b))). This trend was consistent and observed during repeated tests and in other investigations where both types of CHOTs were used, with efficiency ratios between the OS and the SA g-CHOTs varying depending on the quality of transducer attachment and fabrication conditions. The higher efficiency difference of the filtered signals could be attributed to the removal of the third harmonic present in the OS g-CHOT signal by the BPF.

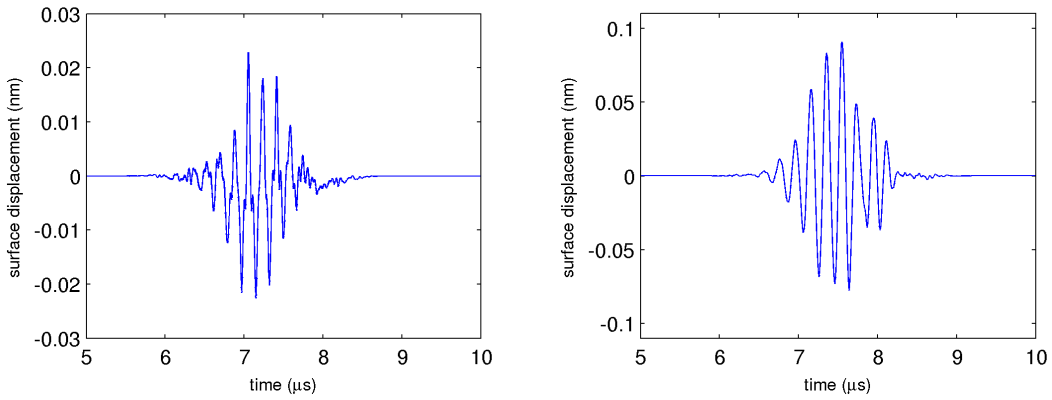

(a) OS g-CHOT (b) SA g-CHOT

Figure 6.6: Surface acoustic waves detected from g-CHOTs on glass (no filters)

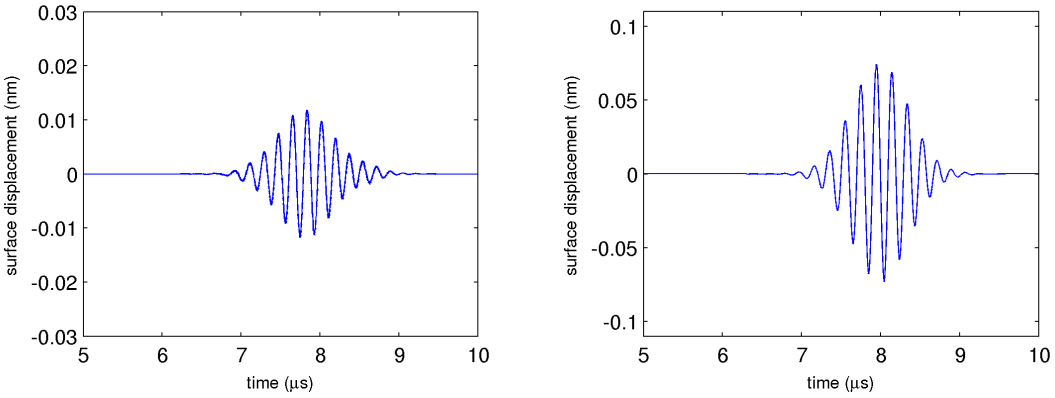

(a) OS g-CHOT (b) SA g-CHOT

Figure 6.7: Surface acoustic waves detected from g-CHOTs on glass (5 MHz BPF)

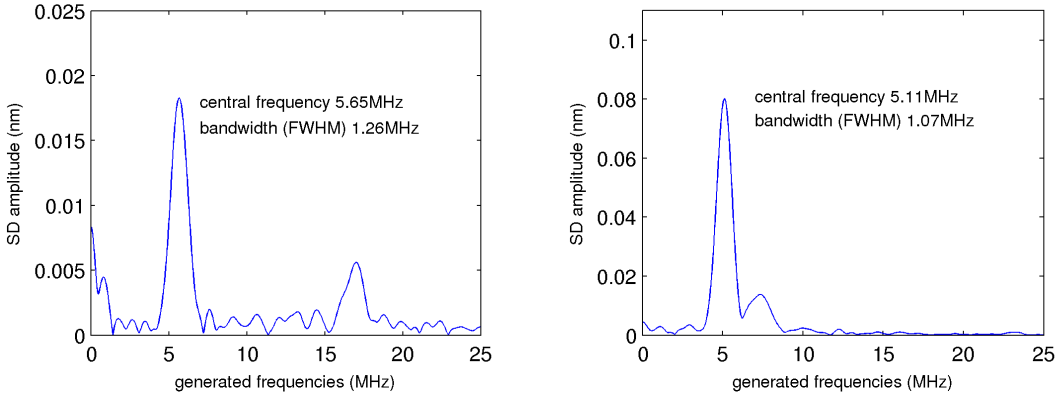

(a) OS g-CHOT (b) SA g-CHOT

Figure 6.8: Frequency spectrum of the generated SAWs corresponding to the fabricated geometry

It is reasonable to expect that a better pattern-to-sample bonding produced during the direct fabrication of the OS g-CHOTs would lead to more efficient acoustic coupling and stronger generation, considering the weaker bonding is provided by the SA g-CHOTs via the adhesive. Surprising at first, the higher generation efficiency displayed by the SA g-CHOTs can be explained by considering the effect of the CHOT carrier attached to the sample on the boundary conditions and the ultrasonic source.

Modification of the irradiated surface by transparent overlays is known [16,71,72,146], Fairand 74] to increase the laser generation efficiency in the thermoelastic regime, with possible contributions from a number of mechanisms. These include: 1) increased absorption at the layer-substrate interface; 2) possibility of the layer itself acting as a thermoelastic source due to its thermal expansion; 3) creation of a buried ultrasonic source and surface constrains at the layer-substrate boundary introducing strong stresses normal to the boundary which are absent during the generation at the free surface; 4) alteration of the thermoelastic source, with the radiation directivity pattern often resembling that of the ablation regime and determined by the boundary conditions and the differences in elastic properties of the layer and the substrate.

Significant amplitude enhancement of longitudinal waves was shown by Gutfield [147] from constrained metallic films acoustically bonded to the sample (with reported gain of 46 dB for Cr films), with common adhesive tapes reported to offer a sufficient constraint. The enhancement in generation of other acoustic modes was later shown by Hutchins [148] comparing the effects of different surface modifications, where most enhancement to the shear waves was reported from the constrained sources. Although some analytical models have been developed for longitudinal waves [149] and the effect on the surface waves is suggested in a number of works, the modification of the ultrasonic source has complex hard to model behaviour. In the present case, the system of ultrasonic CHOT sources constrained with the transparent carrier on the surface of the sample is complicated by the presence and possible contributions from the additional layer of adhesive and its thermal expansion.

The effect of the enhanced generation by the SA g-CHOTs and the results in section 6.1.4 point to the necessity for the opto-thermo-elastic model of a g-CHOT to be developed. The development of such a model in Comsol will be suggested as one of the directions of further work (Chapter 8).

6.1.2 The spatial distribution of the generated acoustic fields

The acoustic fields produced by the ultrasonic source are of particular interest in NDT applications, where the amplitudes of the flaw echoes are often employed for defect detection and characterisation. The distribution of acoustic pressure in the generated ultrasonic field and its directivity

pattern affect the amplitude of the returning echoes according to the location of the flaw within the field (relative to the source). Knowledge of the spatial field characteristics can therefore aid both the transducer selection and design for particular task as well as help with the interpretation of the test results. The acoustic fields produced by the g-CHOTs were visualised in this work for the first time, providing insight into the general field characteristics as well as additional means for performance comparison between the g-CHOTs and with conventional PZT transducers.

The generated acoustic fields were visualised for the OS/SA g-CHOTs from the previous section by performing a 20 x 25 mm scan of the sample surface in front of the transducer, approximately 12–13 mm from its centre. Similar geometries in both tests ensured directly comparable results with the start positions selected by matching the arrival times of the first-pass wave-packets. The vibrometer detection point was moved with 200 μm steps first across and then along the direction of wave propagation to create a C-scan, and the signals were recorded averaging 500 waveforms at 500 MS/s sampling rate and with 470 mW of transducer input power. The full scan time was approximately 3.5 hours and required the compromise between the scan resolution and sampling rate. The selected scan step allowed reasonable spatial resolution of the wavefront (average acoustic wavelength of about 575 μm), and the time-sampling provided 90 samples per cycle in the time signal.

The recorded scan data can be displayed and analysed at different levels of detail (Chapter 2) using figures 6.9 to 6.11 with the corresponding A, B and C-scans from the tests.

The A-scans in figure 6.9 show surface displacement against time recorded at a single point on the sample (selected in the centre of the field). These signals can be interpreted using the time-of-flight approach that considers the connection between the arrival time of the signals and the physical wave propagation paths, providing some useful information on the geometry of the sample. The first wavepacket in displayed signals is the forward wave propagating directly from the source (g-CHOT) to the detector (vibrometer), further referred to as a 'first-pass' detection/ultrasound. The second wavepacket in figure 6.9a is a back-wall echo produced by the rearward travelling wave (Chapter 3) from the edge of the sample nearest to the g-CHOT.

A point worthy of attention (further explored in section 6.4.2 but simply noted here) is a substantial reduction in the relative amplitude of the back-wall echo in the signal from the SA g-CHOT (figure 6.9b). One possible explanation is tilt between the g-CHOT and the edge with the reflected wave simply missing the detection point. Another explanation, that is later shown to be the cause of the amplitude drop, is the effect of the carrier film on the returning wave passing under the g-CHOT to the point of detection.

Comparing the first-pass signal arrival times between the OS/SA g-CHOTs, no delay from the SA g-CHOT (noted in the previous section) is visible as in this case the first-pass arrival times

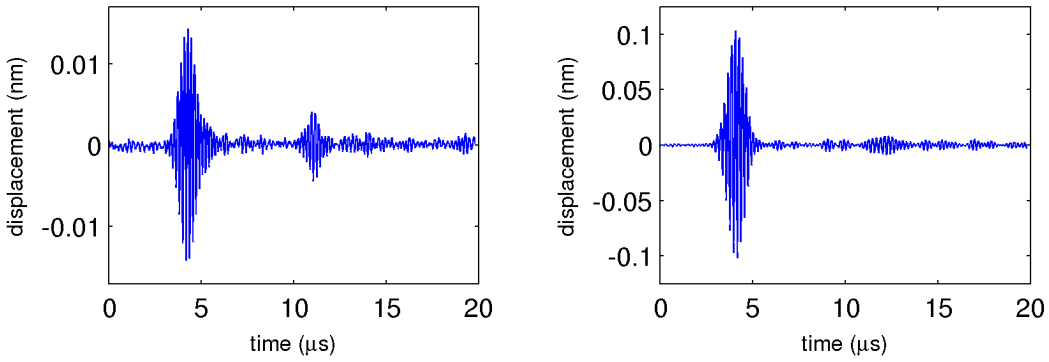

(a) OS g-CHOT (b) SA g-CHOT

Figure 6.9: A-scans of the generated surface wave

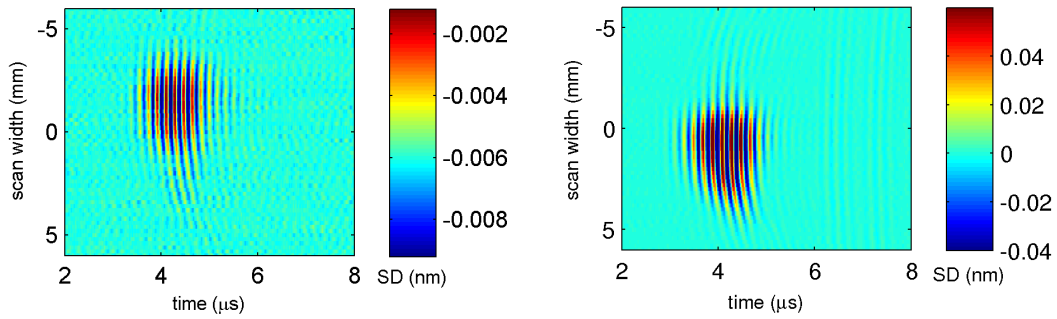

(a) OS g-CHOT (b) SA g-CHOT

Figure 6.10: B-scans showing propagating wavefront at one section of the sample

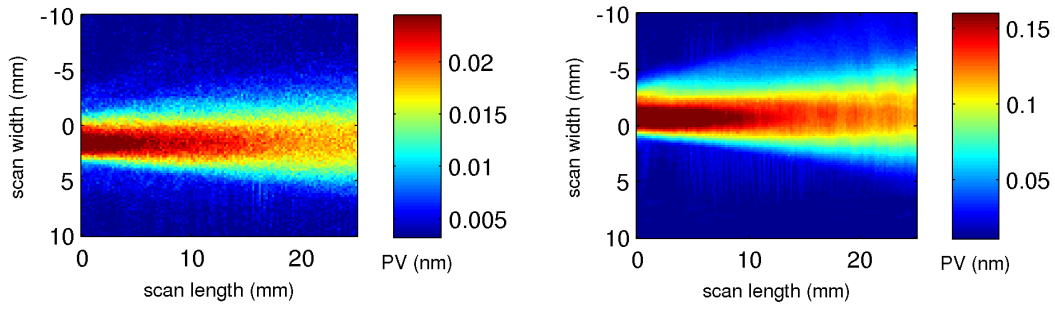

(a) OS g-CHOT (b) SA g-CHOT

Figure 6.11: C-scans showing PTP magnitude of surface displacement propagating along the sample - acoustic field

were matched between two tests before the start of the scan. The effect of the carrier can however be seen when comparing arrivals of a back-wall echo.

The B-scans in figure 6.10, comprised of the first line of A-scans, show a section across the wavefront at a fixed distance from the g-CHOT vs time, with the colour map indicating the amplitude of the recorded surface displacement. Only the time window containing the first-pass wave is shown for detail clarity.

The wavefront shape in the B-scan repeats the spatial distribution of the illuminated sources and corresponds to the laser beam profile on the g-CHOT in space (along the ordinate) and, via Rayleigh wave velocity and reversed, in time (along the abscissa). Some distortion of circular illumination visible in the vertical extension of the beam is due to the stray reflection from the laser mount, caused by the alignment to avoid laser beam entering the vibrometer. Additionally, the effects from the side lobes in the directivity pattern of the transducer would also contribute to the vertical distortion of the waveform. Slight curvature on the edges of the waveform is associated with the beam diameter and the vertical dimensions of the g-CHOT. The generated field is approximated as a superposition of the spherical waves from a series of point sources (using Huygen's principle), where individual source behaviour is more visible in the edge regions.

The C-scans in figure 6.11 were generated by combining a series of B-scans taken along the direction of wave propagation, and plotting the maximum PTP surface displacement from each scan in coordinates of the sample. These plots visualise the spatial distribution of the acoustic field on the sample (corresponding to the first-pass wave). The distribution of energy and the directivity patterns of the generated fields appear to be very similar for both OS/SA g-CHOTs, and the higher generation efficiency of the SA g-CHOT, noted previously, is manifested in noticeably-higher amplitudes throughout the field. Comparing the generated fields additionally allows evaluation of the effect and the quality of the SA carrier attachment, showing good transducer-sample contact in this test.

Analogous to the piezoelectric transducers, the generated beam can be characterised by its divergence angle and the location of the near/far-field zones.

Due to strong diffraction effects on the sound pressure in the near field of the transducer [31] and non-uniform beam intensity (especially for narrow-band transducers), it is hard to determine the size of the flaws located in this zone. The near-field distance (NFD) of the transducer can be determined using equation 6.1

$$NFD = r^2/\Lambda \tag{6.1}$$

$$NFD = 13.6 \text{ mm}$$

where $r = 2.8$ mm is the radius of the laser beam determined from the A, B and C-scans, and

$\Lambda = 575$ μm is the average acoustic wavelength.

The beam divergence angle $\theta/2$ (considering the edge of the sound beam) is determined by the relative size of the transducer and the acoustic wavelength using equation 6.2 [26], and agrees well with the experiment.

$$\sin\theta/2 = 0.61\Lambda/r \tag{6.2}$$

$$\theta/2 = 7.2^{\circ}$$

Considering the start scan location close to 13 mm from the centre of the transducer, the appearance and the divergence of the visualised fields, the scans illustrate the far-field region.

Increasing the size of the g-CHOT/illumination-beam diameter would improve the wavefront curvature and reduce the divergence of the sound beam, with the illumination of the whole g-CHOT producing divergence of 4°, however, increasing the near-field distance to 43 mm.

Figure 6.12 shows wavefront propagation on the sample by plotting the surface displacement in sample coordinates at three selected moments in time. The pattern of the propagating field in figure 6.12b is likely caused by internal reflections of the wave within the CHOT carrier, the effect observed during a detailed scan of the carrier surface and discussed in section 6.4.2.

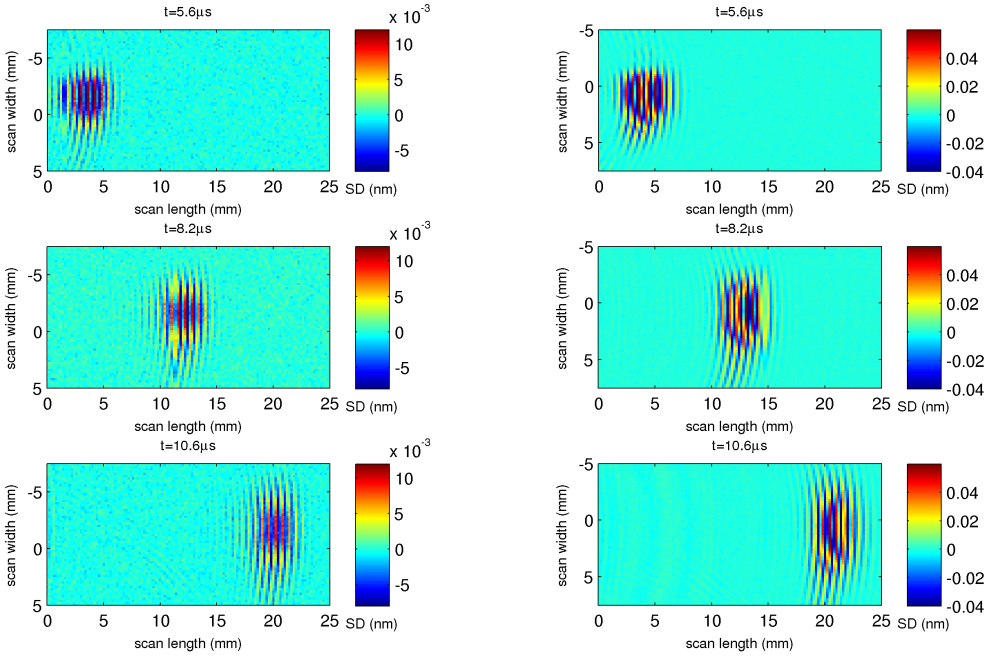

(a) OS g-CHOT

(b) SA g-CHOT

Figure 6.12: B-scans showing surface displacement on the sample at different times

6.1.3 Transducer response: generation output vs laser power input

In the previous section the g-CHOT performance was determined at a fixed input, the maximum of the generation laser power (470 mW). The transducer output for the range of inputs is represented by a calibration curve, analysing which the transducer response linearity, input sensitivity and the presence of hysteresis could be determined [150]. Such a calibration curve provides a good tool for performance comparison between fabricated transducers and for analysis of the elementary contributions and weights in the overall system performance.

The OS and the SA g-CHOT response was measured in the layout shown in figure 6.3 by varying the generation power in the range of 0–470 mW with 20 mW steps and recording the corresponding transducer output as PTP surface displacement.

Possible hysteresis in the CHOT response due to the rise of temperature and the change of the transducer state during the measurements would become apparent if the inputs are varied in turn in the opposite directions (as the output becomes dependent on the history of previous inputs). Considering this, the measurements were performed with the increase in the generation power followed by the decrease, and the loop repeated once to confirm the transducer behaviour, resulting in four sets of measurements.

The laser input power was controlled by the polariser and a half-wave-plate at the entry of the fibre and measured at its exit. The power levels in front and behind the g-CHOT (through glass) were first recorded for the set of steps. This data was used to set the input power according to the calibrated steps by monitoring power output behind the g-CHOT and avoiding the interruption of the generation beam during the test. A $\pm 5\%$ variation in the generation power was indicated by the power-meter and the measurement error was minimised by recording the average indicated power. The 0 power input was achieved by blocking the generation beam, and the signal acquisition was performed averaging 500 waveforms at 2.5 Gs/s. Due to the delay between the manual change of the input power and the acquisition of the signal, the test results should be treated as obtained at quasi-static conditions.

Figure 6.13 shows the full waveforms detected from both CHOTs at maximum average input power of 470 mW (note the scale differences between the (a) and (b) sub-figures). The change in the amplitudes of the generated waves with input laser power is illustrated in figure 6.14 where the first-pass wavepackets generated at 70 mW, 270 mW and 470 mW are shown windowed in the time domain.

The data points for the four calibration curves generated by plotting the PTP values of the detected waveforms against the corresponding power inputs are shown in figure 6.15. The amount of displacement produced by the g-CHOT is seen to proportionally increase/decrease with corre-

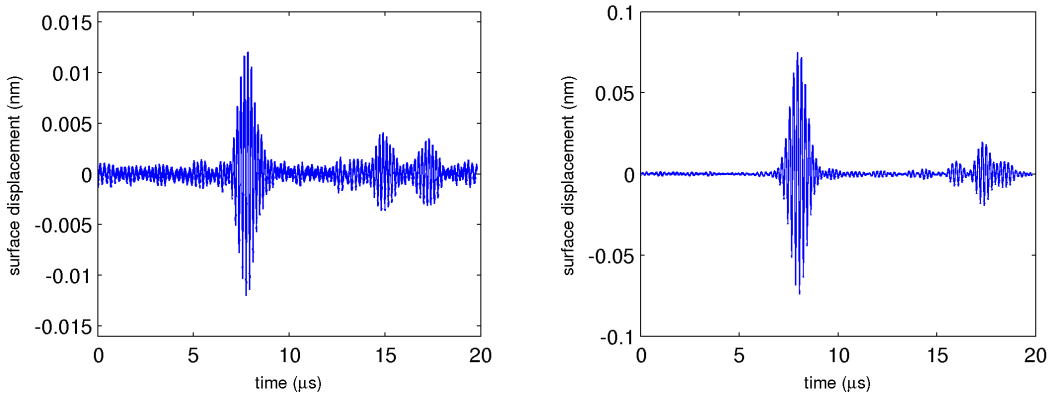

(a) OS g-CHOT (b) SA g-CHOT

Figure 6.13: Recorded waveforms corresponding to SAWs detected from g-CHOTs on glass at 470 mW input power (note different scales)

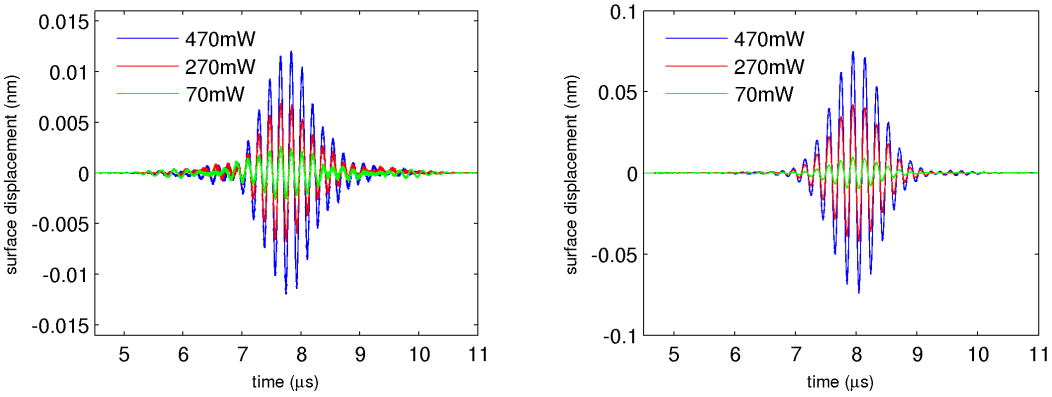

(a) OS g-CHOT (b) SA g-CHOT

Figure 6.14: Change in amplitude of SAW with input laser power

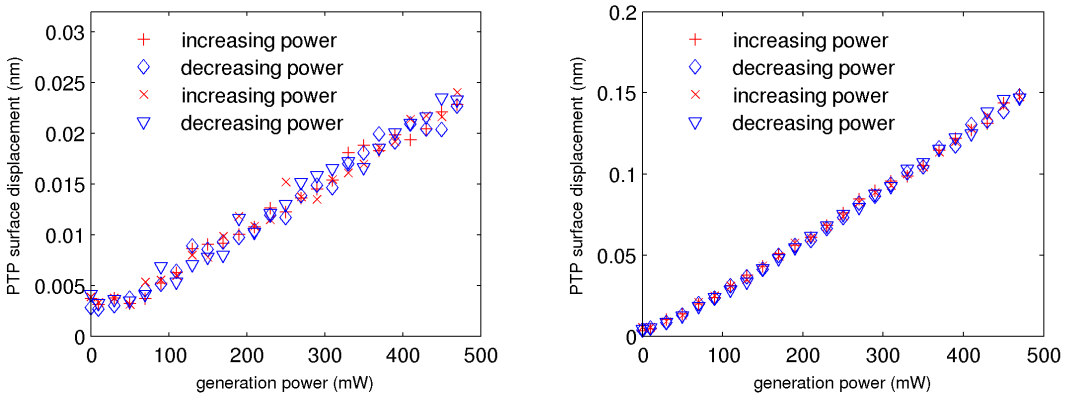

(a) OS g-CHOT (b) SA g-CHOT

Figure 6.15: g-CHOT response to the change in laser power input measured as PTP surface displacement

sponding power input, and the absence of hysteresis (for the given conditions) is evident from the figure. The vertical data offset at zero power input in this plot (especially visible in figure 6.15a due to smaller surface displacements) corresponds to the noise floor of the vibrometer, surface displacement below which can not be detected, and is inherent in the PTP-based analysis method.

Alternatively, the response curve can be similarly generated using central frequency amplitudes from the signal spectrum. This approach is demonstrated by the figure 6.16 where the spectra of the signals from figure 6.14 are displayed.

The calibration curves for the OS and the SA g-CHOTs generated by averaging of the central frequency amplitude values between the four sets of measurements are presented in figure 6.17 and are found to be well approximated by the linear fit displayed in the figure. The measured transducer response confirms the operation in the thermoelastic regime. At some level of the input power the curve is expected to reach saturation with no visible increase in the amplitude of the generated SAW despite the increase in the input laser power. This would eventually be followed by a sharp rapid drop indicative of the transducer/sample ablation.

Evaluating the g-CHOT performance numerically, the sensitivities of the transducers determined as the PTP surface displacement produced per unit of input power (the slope of the calibration curve) are 4.61 x 10^{-5} and 31.7 x 10^{-5} nm per mW for the OS and the SA g-CHOTs respectively, with the SA g-CHOT displaying 6.9 times higher sensitivity – the result consistent with 6.2 times higher generation efficiency noted in the previous section. The slope of the calibration curve and the measured sensitivity is affected by the distance from the g-CHOT at which the surface displacement is being measured, resulting in steeper slopes and higher sensitivities when measured closer to the g-CHOT and producing lower values if measured further away.

6.1.4 The effect of transducer and substrate materials onto the generation efficiency

In order to ensure the most efficient generation on a particular material, the material of the g-CHOT is selected based on its coefficient of absorption to create a greater absorption contrast with material of the substrate at the wavelength of the generation laser (Chapter 3). Although a study of material-dependent generation efficiency is outside of the scope of this work, a simple experiment was carried out to demonstrate the effect of material selection onto the amplitudes of the generated SAWs.

The surface displacement generated by g-CHOTs made of three different materials was measured on an 8 mm-thick BK-7 glass substrate, chosen for its high transparency (94%) to the generation wavelength (setup in figure 6.3). Due to substrate transparency, the ultrasonic genera-

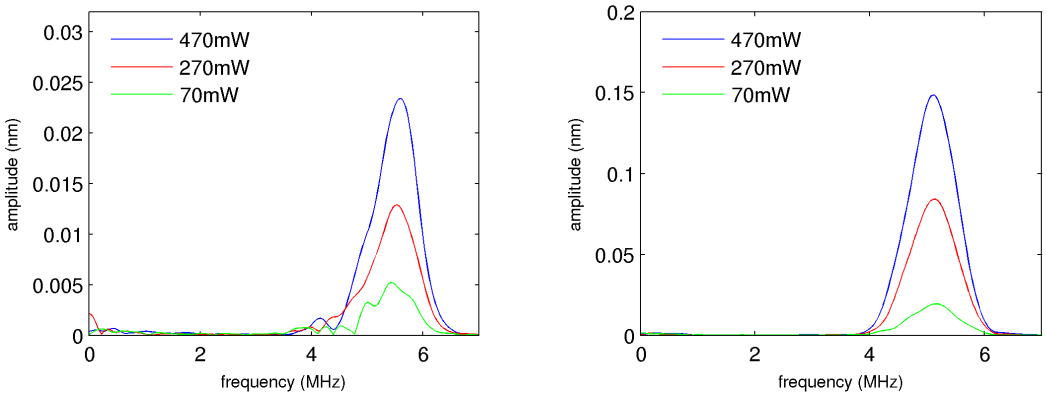

(a) OS g-CHOT (b) SA g-CHOT

Figure 6.16: Frequency spectra of the SAWs generated at different input powers

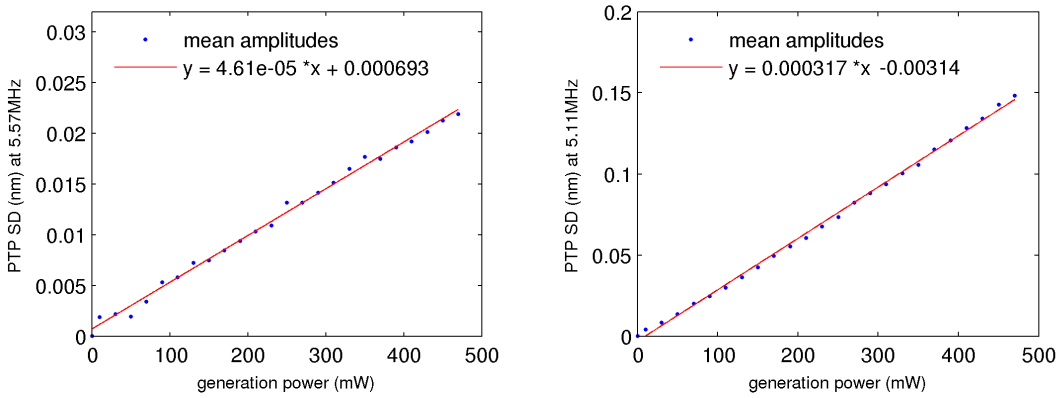

(a) OS g-CHOT (b) SA g-CHOT

Figure 6.17: g-CHOT response to the change in laser power input measured as PTP surface displacement at central frequency

tion originates exclusively from the absorption by the g-CHOT material and illustrates the effect of material-absorption differences. In addition, the generation by similar g-CHOTs was performed on aluminium, thereby modifying the absorption contrast in each case and illustrating the effect of the substrate-dependent efficiency of the same g-CHOT materials. To provide sufficient differences in absorption between the transducers and both substrates, and based on availability, silver (Ag), copper (Cu) and chromium (Cr) were chosen as g-CHOT materials.

Due to thickness dependency of the absorption in metal films, the Fresnel coefficients [151] describing the amplitude ratios for the reflected R and transmitted fields T, were used to determine sufficient g-CHOT thickness and corresponding absorptance, calculated as $A = 1-(T+R)$. Figure 6.18 shows example of the change in R/T/A ratios with thickness for Cr, and table 6.1 presents

the estimated absorption contrast for the 80 nm-thick g-CHOTs from selected materials on glass and aluminium samples.

Unlike in metals, where absorption is localised to the skin depth, gradual absorption on glass throughout its thickness (up to 3% for BK7, 10 mm at 1,064 nm) does not produce localised heating and associated stresses. Its absorption input was therefore disregarded and absorption contrast considered equal to the absorptance of the g-CHOT material itself. Absorption of 6% was considered for aluminium substrate.

The transducer material offering the best generation efficiency on particular substrate can be determined from the estimated absorption contrast (table 6.1) compared between the g-CHOT materials on that substrate, with chromium expected to outperform silver and copper both on glass and aluminium.

The change of substrate from glass to more absorbent aluminium shows different impact on the alteration of absorption contrast and corresponding function of the transducer. In case of Cr, the contrast reduction is expected to lower the generation efficiency, whereas a change of sign in case of Ag and Cu indicates the roles of transducer and the substrate are swapped and the substrate becomes the main absorbant. Additionally, the reversal of the comparative generation efficiencies between Ag and Cu on different substrates is noteworthy as a less absorbent material provides higher efficiency on a more absorbent substrate.

The 4 MHz g-CHOTs from Ag and Cu were fabricated using sputterer, and Cr g-CHOT deposited in the vacuum evaporator, with equipment calibration for each material performed prior

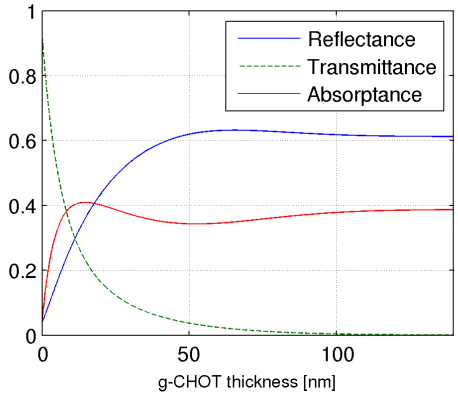

Figure 6.18: Thickness-dependent absorption of Cr on glass based on Fresnel coefficients, normal incidence and n=3.544, $\kappa = 4$

Table 6.1: Absorptance for selected g-CHOT materials based on Fresnel coefficients for normal incidence.

Material	Absorptance/ Contrast BK7	Contrast Al
Cr	0.363	0.303
Cu	0.028	-0.032
Ag	0.017	-0.043

to deposition. The surface displacement was recorded at fixed distances from the g-CHOTs (confirmed by matching the pulse arrival times) and at fixed generation power of 470 mW, averaging 500 waveforms. The resulting PTP surface displacement produced on glass and aluminium substrates is plotted in figure 6.19.

The comparison of the output on the same substrate seems to agree with the performance expected based on the differences in material absorption between the g-CHOTs (table 6.1) and associated transducer/substrate contrast. As expected, Cr provided the strongest generation on both substrates.

The reversal in the generation efficiency between the use of silver and copper on aluminium substrate is also evident from the plot, in agreement with the expected behaviour. The estimated negative contrast in this case supports the explanation of increased and reversed generation efficiency due to higher absorption by the substrate. However, the experimental confirmation of this effect would require observation of the phase shift in the detected signal from the same transducer material used on two different substrates, requiring precise control of the measurement conditions and test geometries, and was not be performed.

The test result on aluminium however contradicts the expected reduction in generation efficiency by Cr associated with lower absorption contrast, demonstrating almost double the increase in the output. Additionally, considering the relative magnitudes of the SAWs reveals further disproportionality of the generation efficiency with the respective absorption contrasts. For example, the generation using silver on aluminium (high absorption by substrate) is close to half that of chromium on the same substrate (high absorption by CHOT), despite its absorption contrast being seven times lower.

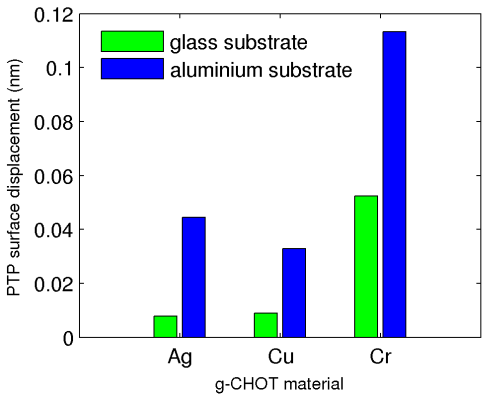

Figure 6.19: Effect of the g-CHOT and substrate materials onto the SAW output magnitude

The above observations from the test combined with disproportional and sometimes contradictory increase in the generation gain lead to believe that a higher overall generation efficiency is achieved on aluminium substrate. This allows to speculate that thermo-elastic material properties (e.g coefficient of thermal expansion, thermal conductivity, heat capacity, material density, elastic constants, etc.) should be considered during material selection besides the optical absorption contrast.

Although showing close agreement between the materials on the same substrate, in some circumstances the value of the absorption contrast did not prove to be a reliable indicator of the generation efficiency without consideration of the role of the transducer/substrate and other material properties.

The development of a thermo-elastic g-CHOT/substrate model with more experimental work is therefore suggested to explore this area further, and would be required to provide a reliable selection of the g-CHOT material.

6.2 Performance evaluation: d-CHOT

The d-CHOT converts surface displacement into intensity modulation of light (figure 6.20). The operation of the illuminated transducer can be considered to be comprised of two distinct states that jointly define the overall transducer performance: *static* – in absence of the input SAW, and *sensing*, when the d-CHOT is being deformed by the propagating wave.

In static mode the d-CHOT functions as a phase grating dividing the incident wavefront into diffraction orders and creating required intensity distribution between them with the initial phase contrast (see Chapter 3). The diffraction efficiency for each order in this state is fixed producing

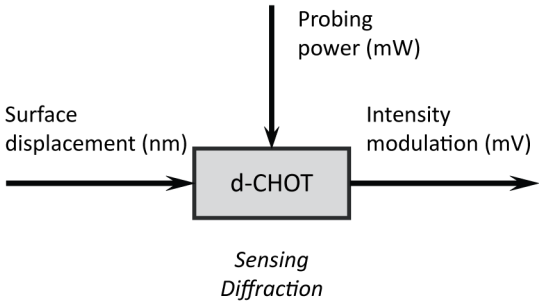

Figure 6.20: Schematic diagram of the d-CHOT inputs and outputs

constant signal output from selected order over time.

In sensing mode the time-varying phase shifts introduced by the passing SAW instantaneously modify the base (static grating) performance redistributing the energy between the diffraction orders. The signal detected from the chosen order in this case reproduces the corresponding modulation of intensity and enables the detection of SAW. The height of the d-CHOT steps in its static state (base operation point) establishes the rate of conversion between the phase and intensity and determines signal modulation depth during sensing (figure 3.6).

Although fundamental in defining d-CHOT operation, the isolated assessment of the static grating provides limited information on practical sensing performance, and was not analysed. Instead, present work focused on the evaluation of transducer operation in sensing mode, directly linked both to the underlying static performance and the input surface displacement.

Given the direct link with the order intensity, the magnitude of detected signal provides convenient metric to characterise the output of the transducer. For a reliable assessment of the d-CHOT performance it is important to recognise that the measured signal amplitude is not uniquely determined by the transducer but is additionally affected by the elements and losses in signal chain (Chapter 4) as well as the experimental arrangement and conduct. These factors are considered alongside the results, and their effects were isolated or minimised where possible.

The illumination of the d-CHOT by the probing beam represents the second independent input besides the SAW (figure 6.20) strongly contributing to the overall signal. In view of this, performance tests of the d-CHOTs were carried out at a fixed level of probing power, transducer sensitivity to which was evaluated separately with fixed input displacement (section 6.2.3). Any residual effects from temporal instability of the illumination level are reduced by signal averaging.

The d-CHOT performance was analysed for both OS/SA d-CHOTs in a similar fashion as it was done for the g-CHOTs in section 6.1. The test layout is illustrated in figure 6.21, where the input SAWs were produced using individual OS g-CHOTs, the displacement amplitude quantified with the vibrometer, and d-CHOT output signal recorded.

6.2.1 Detected signal

The magnitude of the surface displacement detected by the d-CHOT determines signal modulation depth and depends on the distance from the source (g-CHOT) at which the propagating SAW is 'intercepted' by the transducer. As the wave propagates towards the d-CHOT, its amplitude reduces as $1/\sqrt{r}$ with distance r due to geometrical beam spreading, and is further affected by material and surface quality of the sample with corresponding absorption and scattering (Chapter 2). The measured d-CHOT performance thus becomes relative to the distance at which the

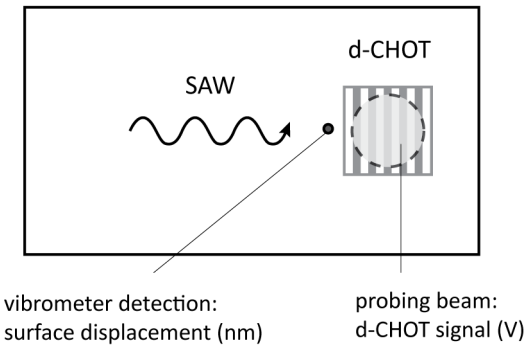

Figure 6.21: Schematic diagram of the d-CHOT performance evaluation test setup

input displacement is measured entering the transducer, with the measurements taken nearer the transducer resulting in a higher sensitivity than those performed farther away.

The measurements of input displacement carried out directly on the d-CHOT enable performance evaluation and transducer comparison independent of these factors. However, due to the presence of the carrier, the measurements on the SA d-CHOT do not accurately represent the actual transducer input, but rather describe the effective displacement produced on the carrier surface. In view of this, to enable fair performance comparison between the OS/SA d-CHOTs and reveal the effect of the carrier, the surface displacement was measured at two locations: at a fixed distance in front of the d-CHOT (as shown in figure 6.21) for performance and sensitivity measurements, and directly on it – to assess the effect of the carrier.

Fabricated transducers

The primary grating efficiency and sensitivity of the d-CHOT both to amplitude and frequency of the surface displacement are determined by the step height and spacing of the transducer (see Chapter 3) and are affected by its fabrication.

To eliminate the effect of the fabrication errors, resulting in different initial sensitivities, both the OS and the SA d-CHOTs used in performance evaluation tests were produced simultaneously during the same deposition, ensuring equal fabrication conditions. The largest depth of intensity modulation in the zero order and the highest sensitivity are achieved with the phase contrast in reflection of $\pi/2$ corresponding to the step height of $1/8\lambda$ (66.5 nm for $\lambda = 532$ nm). The equipment calibration described in Chapter 5 ensured accurate indication of the deposited layer thickness, and the profile height of particular d-CHOTs was not measured after fabrication. The effect of the step height on the grating performance was not separately evaluated as it is well-studied elsewhere and

the base operation point of the transducer is sufficiently-well controlled during the fabrication.

As the mask design permitted only two transducers to be produced simultaneously, the corresponding frequency-matching g-CHOTs were made on the sample separately. The OS/SA d-CHOTs were then fabricated/attached opposite, performing the best possible alignment with existing g-CHOTs. Due to separate fabrication, some signal amplitude reduction could be expected, arising from possible misalignment between the directivity of the d-CHOT and SAW wavefront.

The step spacing of the d-CHOT is designed to spatially match the acoustic wavelength of the propagating SAW for particular frequency. Generally, the frequency mismatch would reduce the amplitude of the detected signal due to lower sensitivity of the d-CHOT to SAWs at frequencies outside of its fundamental. The amount of reduction depends on the frequency spectra of both, the SAW and the d-CHOT, and their respective bandwidths. The use of the matching-frequency CHOT pairs fabricated with the same masks minimised possible frequency mismatch in presented work, and the step spacing of the fabricated d-CHOTs was not specifically measured, assuming similarity to that of previously measured g-CHOTs (figure 6.4).

Specific test considerations

The amplitude of the signal is further affected by the factors that determine the amount of light reaching the detector (DC level), including the probing power level, surface roughness and reflectivity, the separation of the orders, the relative order/iris sizes and further order alignment with the photo-sensitive area of the detector.

Clear separation of the orders ensures full modulation depth from selected order is detected without reduction by contributions from overlapping orders. It is initially determined by the CHOT operation frequency (or step spacing Λ, as $m\lambda/\Lambda - \sin\alpha = \sin\beta$, Chapter 3) and further affected by surface roughness. Sufficient separation of the orders was controlled experimentally by using appropriate optics (lens) to expand the beam from the fibre bundle (Chapter 4) and by controlling the diameter of the iris to isolate the order of interest. The iris diameter was then fixed during the tests and the best possible alignment of the order achieved by finding the maximum output signal in each case.

The effects of surface roughness are complex but generally affect both the amount of light in a specular direction as well as the order size and separation due to scattering. This point is further briefly discussed in section 6.2.4 where the operation of OS/SA d-CHOTs is compared on rough surfaces, although the effect was not explicitly studied. The use of the glass samples with smooth surface excluded the effects of the substrate surface condition in performance evaluation tests. The contribution from the intrinsic roughness of the carrier film of the SA d-CHOT is part of the transducer performance but could also be excluded from the results by normalisation to DC

output from the photodetector.

The incidence angle of probing illumination with respect to the d-CHOT was previously shown to have minimal impact on signal amplitude for angles up to 35° [1]. However, this estimation is limited to the geometrical reduction of effective step height and relatively large surface displacements (0.5 nm), without consideration of other factors such as conical diffraction or surface condition. When operating with rough surfaces, the angle of incidence partially defines how rough the surface appears to the incident radiation [152], and therefore is expected to have more significant impact on signal amplitude. Regardless of the surface condition, the illumination incidence angle was fixed with respect to the samples during the tests where comparable results were desired.

Possible differences in detector sensitivity to the wavelength and modulation frequency of the incident light affect the output from the photodetector (Chapter 4) and should be generally considered when comparable results are required. In this work they were eliminated by using the same detector throughout the tests.

Results and discussion

Figures 6.22 and 6.23 show the input SAWs detected with vibrometer in front of and at the d-CHOTs, and their respective frequency spectra. The signals (shown windowed) were recorded using no filters to preserve the original frequency content, averaging 500 waveforms at 5 GS/s with 470 mW input generation power. Similar front measurement position for both samples was confirmed by matching the arrival times of the corresponding wave packets (first-pass), whereas equidistant positioning on the d-CHOTs was achieved by moving the vibrometer from the front to the centre of the d-CHOT by the same number of steps controlled by the stages.

The differences in fabrication and quality of the g-CHOTs is the possible cause of the differences in the amplitudes of SAWs detected in front of the d-CHOTs. The comparison of their frequency spectra (figure 6.23, dashed red line) confirms poorer quality of the OS g-CHOT in the first case. Although the difference in the input SAW amplitudes affect the amplitudes of the corresponding d-CHOT signals, the sensitivity evaluation is not affected as the output is considered relevant to the magnitude of input.

A striking difference in the frequency spectra of the surface displacement detected at the d-CHOTs reveals the effect of the carrier onto the propagating wave in case of the SA d-CHOT (figure 6.23 solid blue). The relative reduction of the amplitude at the central frequency of the wave measured in front and at the d-CHOT (dashed red vs solid blue) is characteristic of the wave attenuation, in the OS d-CHOT case (figure 6.23a) simply attributed to the propagation between two measurement points. In the case of the SA d-CHOT (6.23b) it is additionally affected by the presence of the carrier, dropping by almost 40% from the value where the carrier is absent

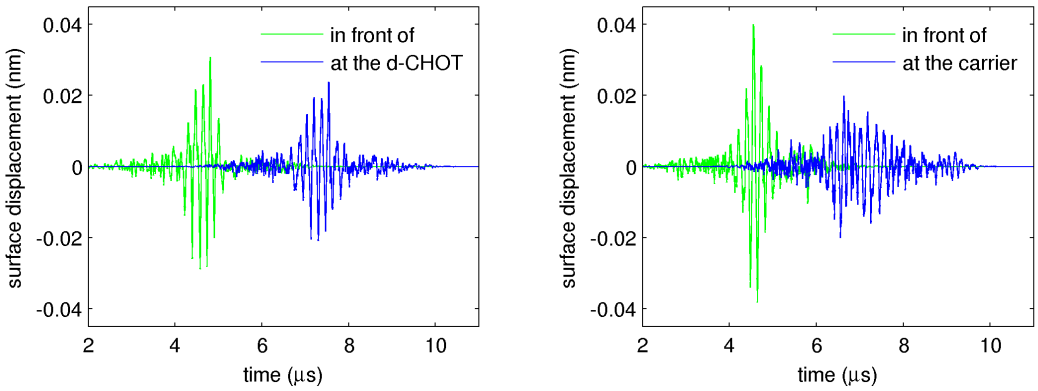

(a) OS d-CHOT (b) SA d-CHOT

Figure 6.22: Incoming SAWs detected in front of and at the d-CHOTs (470 mW generation power)

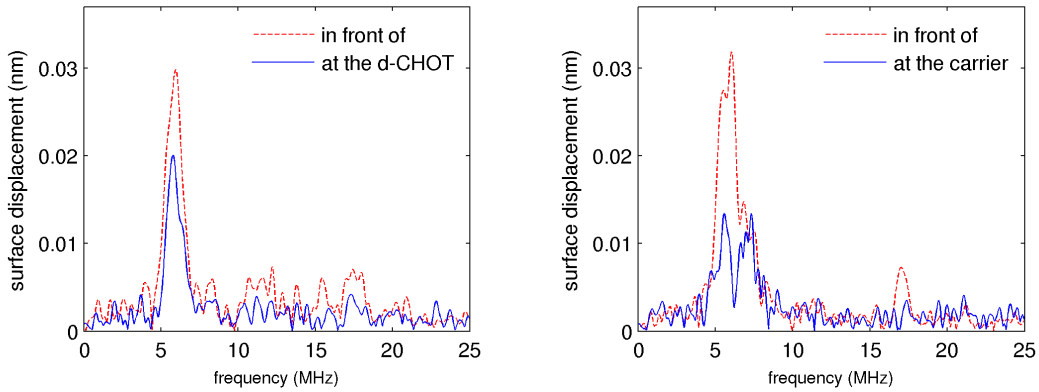

(a) OS d-CHOT (b) SA d-CHOT

Figure 6.23: Frequency spectra of the SAWs detected in front of and on the d-CHOTs

(comparing figures 6.23a and 6.23b, solid blue).

Whereas some wave attenuation by the carrier could be expected, the most interesting effect is presented by the distinct split of the central lobe in the spectrum of the wave on the SA d-CHOT. Corresponding wave energy transfer from the central frequency can also explain the additional reduction of central frequency amplitude. Close examination of the signal in the SA case shows what appears to be two arrivals at 6.4 μs and 7.4 μs, which when windowed separately correspond to 7.3 MHz and 5.5 MHz components respectively.

Figures 6.24 and 6.25 show windowed signals detected from the d-CHOTs and their respective frequency spectra (note the scale differences between the sub-figures). Similarly to the vibrometer detection, signals were recorded using no filters or amplifiers, averaging 500 waveforms at 5 GS/s, with 410 mW of input generation power and 310 mW of probing power.

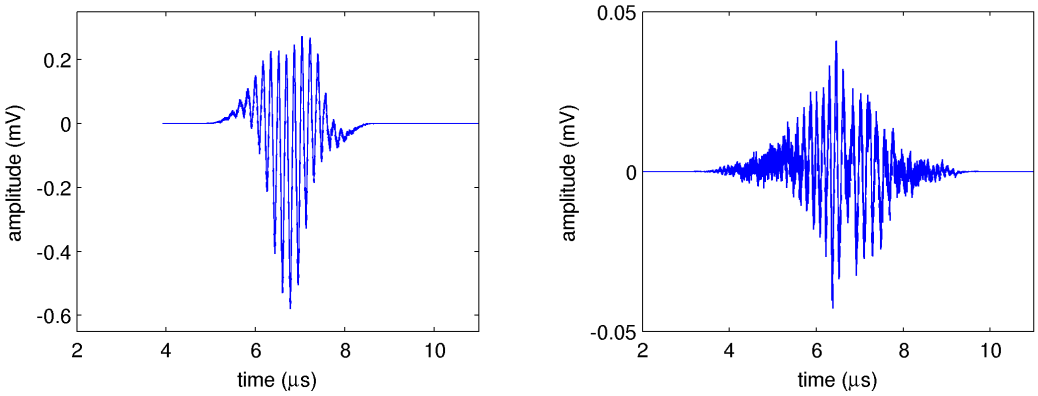

(a) OS d-CHOT (b) SA d-CHOT

Figure 6.24: Signals detected from the d-CHOTs corresponding to the input SAWs

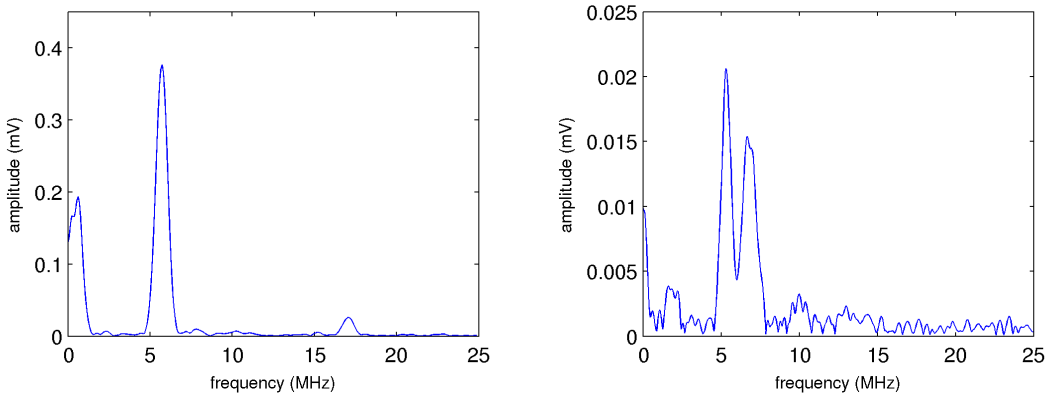

(a) OS d-CHOT (b) SA d-CHOT

Figure 6.25: Frequency spectra of the d-CHOT output signals

The spectra of the d-CHOT signals show very good agreement with those of the input displacement detected at the d-CHOT with the vibrometer. In particular – the clear split of the wave energy between two components in the SA d-CHOT spectrum (figure 6.25b), replicating the behaviour observed in vibrometer measurements on the carrier (figure 6.23b). Here, the analysis of the corresponding time signal (figure 6.24b) similarly shows two arrivals at 6.2 μs and 7.2 μs, associated with 6.7 MHz and 5.3 MHz spectral components. The bandwidth of the d-CHOT limits its sensitivity to the SAW at 7.3 MHz detected on the carrier with the vibrometer, and explains the shift from 7.3 MHz to 6.7 MHz in the spectrum of the CHOT signal.

Figure 6.26 shows frequency transition in the full vibrometer and d-CHOT signals when analysed using Cmor wavelet, and confirms previous analysis.

The ability of the d-CHOT to detect both frequencies suggests similar wavelengths Λ of both

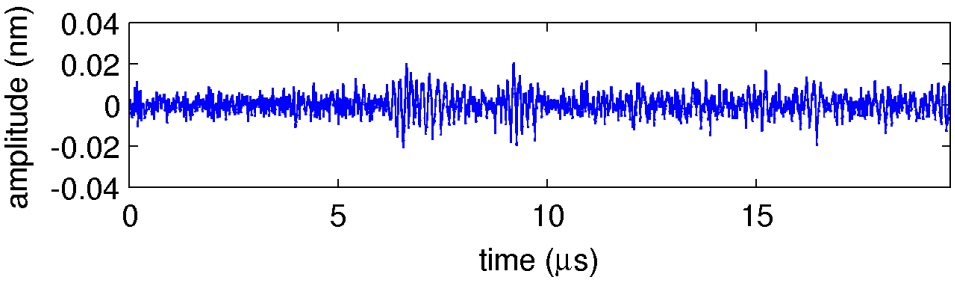

(a) SAW detected by the vibrometer

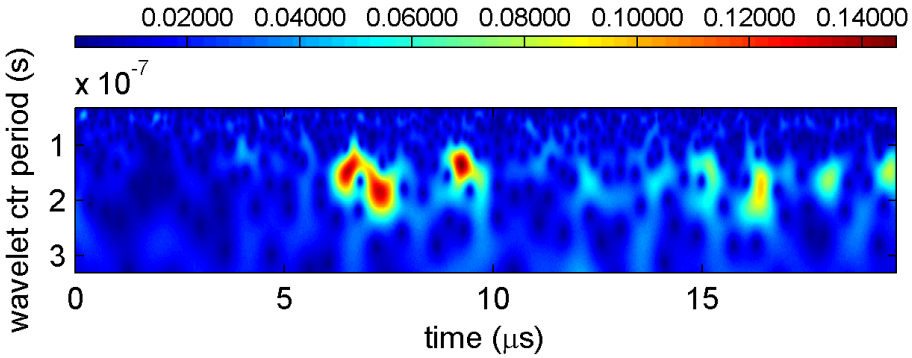

(b) Vibrometer signal frequency content

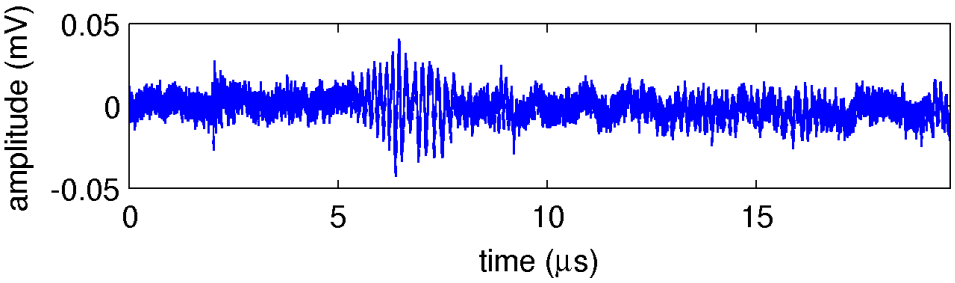

(c) SAW detected by the SA d-CHOT

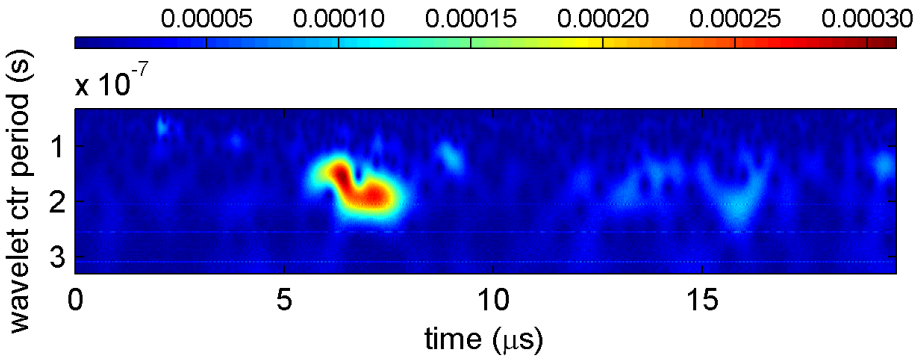

(d) D-CHOT signal frequency content

Figure 6.26: Detected vibrometer and d-CHOT signals and their wavelet decomposition

waves, close to the d-CHOT spatial period. The velocity of the faster arrival C_{R1} can then be found by solving the system of equations 6.3, where $C_{R2} = 3{,}127$ m/s is the Rayleigh wave velocity on glass.

$$\begin{cases} f_1\Lambda = C_{R1} \\ f_2\Lambda = C_{R2} \end{cases} \tag{6.3}$$

$$C_{R1} = (f_1/f_2)C_{R2} = 1.32C_{R2} = 4{,}150 \text{ m/s}$$

Noting the time difference between both arrivals Δt is 0.98 μs and 1 μs for the detection with vibrometer and the d-CHOT respectively, the difference in the path length of the faster 7.3 MHz arrival is found as follows:

$$\Delta l = \Delta C_R \Delta t = (4{,}150 - 3{,}127)10^{-6} = -1.02 \text{ mm}$$

Considering test geometry (the vibrometer detection at the centre of the d-CHOT, the size of the d-CHOT = 10 mm), 1 mm path difference between the arrivals implies the origin of the faster higher-frequency wave to be on the SA carrier.

One possible cause for the displayed effect is the dispersion and reflections within the carrier region, although a significant amount of modeling and experimental work would be required to fully explain and confirm the observed behaviour.

Due to the use of the 5 MHz BPF, the higher-frequency component is not observed in the later measurements, and could potentially be reduced or eliminated by changing or removal of the carrier material and tapering or angling of the carrier edges.

6.2.2 Transducer response: signal modulation vs surface displacement

The d-CHOT response in the previous section was analysed for the input SAW of a fixed magnitude. By recording the output signal for a range of SAW magnitudes, the d-CHOT calibration curves could be obtained, allowing the evaluation of transducer sensitivity and linearity of response, as well as providing the means for transducer comparison.

The OS/SA d-CHOT response was measured on a glass sample in the layout shown in figure 6.21. The d-CHOT probing power was fixed at 310 mW and the SAW magnitude controlled by changing the input power to the OS g-CHOTs in the range of 0–470 mW with 20 mW steps as described in section 6.1. The resulting surface displacement (at each power level) was measured with the vibrometer in front of the d-CHOT, equidistantly in both tests, and transducer output recorded. Considering its effect on the signal amplitude, the DC light level on the photo-detector was recorded during the measurement along with the RF d-CHOT signal.

The measurement of the surface displacement and the d-CHOT output were not simultaneous, performing the vibrometer measurement first and recording the d-CHOT output after. In both cases, the signals were acquired averaging 500 waveforms at 2.5 Gs/s. The electronic system including two 5 MHz BPFs and an amplifier (Chapter 4) was used with the d-CHOTs, and a 5 MHz BPF was used with the vibrometer.

Figure 6.27 shows the input SAWs generated at 470 mW and detected in front of the d-CHOTs. The corresponding OS/SA d-CHOT signals are presented in figure 6.28 (note the scale differences between the sub-figures). Despite maintaining the source-detector distance in both tests, a small delay in the arrival of the SA d-CHOT signal (figure 6.28b) can be noted. Consistent with the delay observed in the arrival of SAWs generated with the SA g-CHOTs (section 6.1, figures 6.7a and 6.7b), it appears to be caused by the presence of the carrier, with possible changes of wave velocity and a delay in the grating carrier response to deformation.

To evaluate the presence of hysteresis, the inputs were varied in turn in opposite directions: the increase of the SAW magnitude was followed by a decrease, and the loop repeated once to confirm the transducer behaviour, resulting in four sets of measurements.

The SAW outputs of the individual OS g-CHOTs were characterised as described in section 6.1 by using the linear fit to the mean central frequency amplitudes (figure 6.29), using these values as the surface displacement input in performance evaluation. The gradient difference between the g-CHOT outputs confirms the poorer quality of the OS g-CHOT in the first case (noted previously).

The change in the magnitude of the d-CHOT signal with input surface displacement is illustrated in figure 6.30, where the first-pass wavepackets are shown windowed for three levels of surface displacement generated at 70 mW, 270 mW and 470 mW (using corresponding fit values).

The four data sets generated by plotting the PTP values of the detected waveforms against the corresponding PTP surface displacement using the g-CHOT output fit are shown in figure 6.31. Linearity of signal response to the input displacement during sensing, observed in these results, indicates the base operation point of the d-CHOT in its static state is close to optimal. The vertical data offset at zero surface displacement (especially visible in figure 6.31b) corresponds to the noise floor of the CHOTs detection system and determines its detection limits (in the present setup). Comparing figures 6.31a and 6.31b, the smallest detectable PTP displacement with the OS d-CHOT is 6 x 10^{-4} nm in contrast to 54 x 10^{-4} nm detectable with the SA d-CHOT.

Similarly to the analysis of the g-CHOTs in section 6.1, the central frequency amplitudes from the signal spectra can be used to generate the calibration curves. Figures 6.32 and 6.33 show the spectra of the signals from figure 6.28 and corresponding calibration curves generated using the mean Fourier amplitudes between the four sets of measurements. The sensitivities of the transducers determined from the slope of the calibration curves are 21.9 V and 1.9 V per nm for the

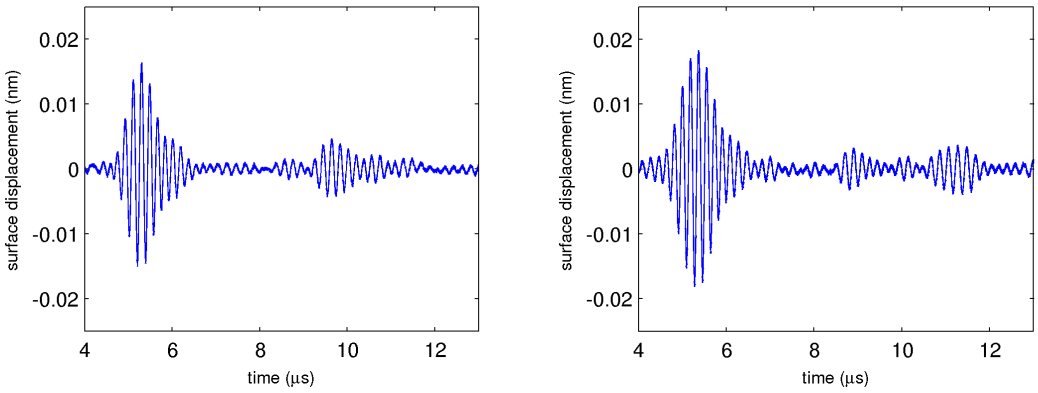

(a) OS d-CHOT (b) SA d-CHOT

Figure 6.27: d-CHOT input: surface waves detected in front of the d-CHOTs

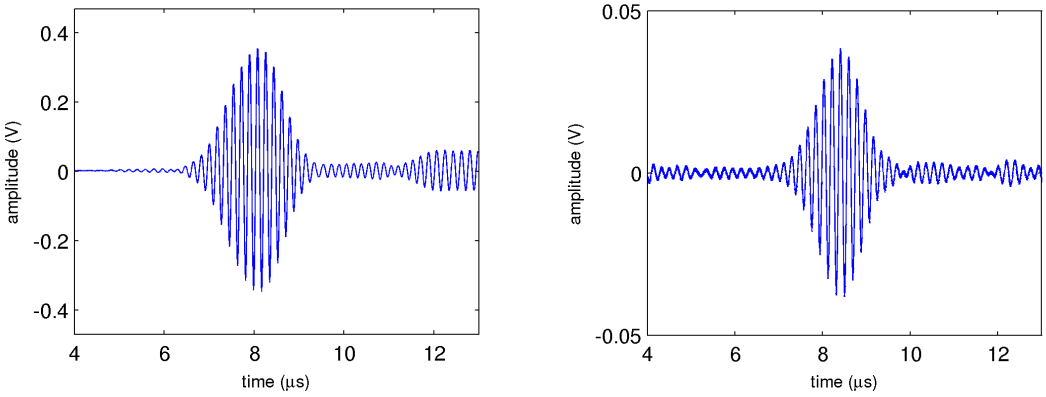

(a) OS d-CHOT (b) SA d-CHOT

Figure 6.28: Signals detected from the d-CHOTs as response to the surface displacement input

OS and the SA d-CHOTs respectively, showing 11.5 times higher gain in the output signal per unit of input displacement produced by the d-CHOT fabricated directly on sample. Considering equal initial sensitivities of both d-CHOTs provided by their simultaneous fabrication, the differences both in sensitivity and the minimum detectable displacement of the SA d-CHOT can be originally attributed to the presence of the 35 μm-thick carrier with 15 μm-thick layer of adhesive. The reduction of the layer thickness can then be expected to improve the transducer performance.

Looking at figure 6.31a, the four data points corresponding to the set of 'decreasing power' measurements are seen noticeably offset from the rest of the curve and other measurements. The drop in signal amplitudes at these points during the measurements is the result of the temporary decrease in the DC light levels on the photo-detector (figure 6.34a). Normalisation of the response curve to the corresponding DC levels shows to remove the offset, confirming its cause (figure 6.34b).

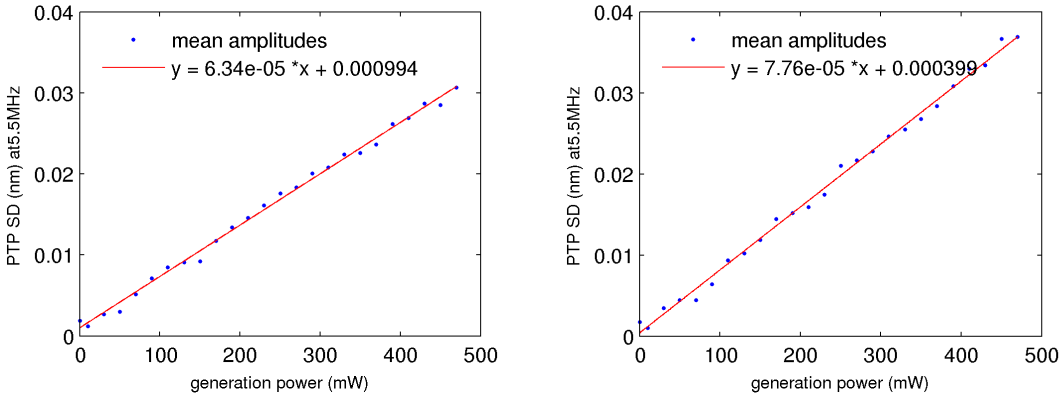

(a) OS d-CHOT (b) SA d-CHOT

Figure 6.29: d-CHOT input surface displacement PTP amplitudes

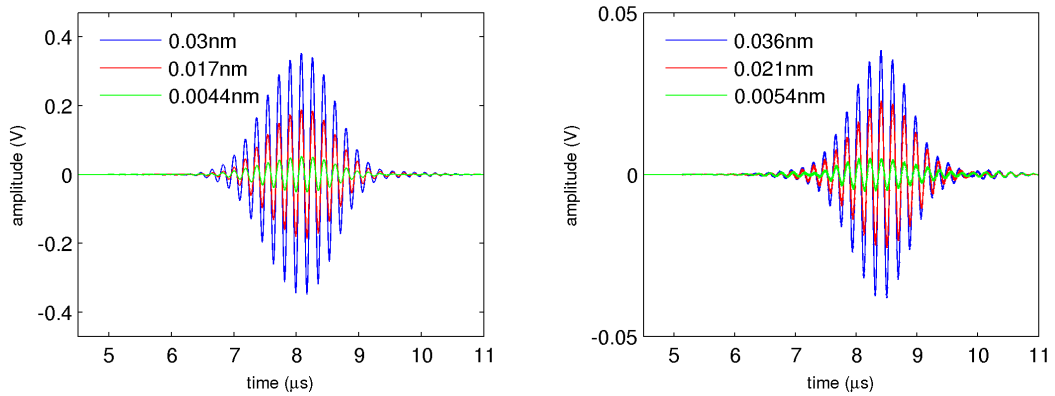

(a) OS d-CHOT (b) SA d-CHOT

Figure 6.30: Change of signal amplitudes with input surface displacement

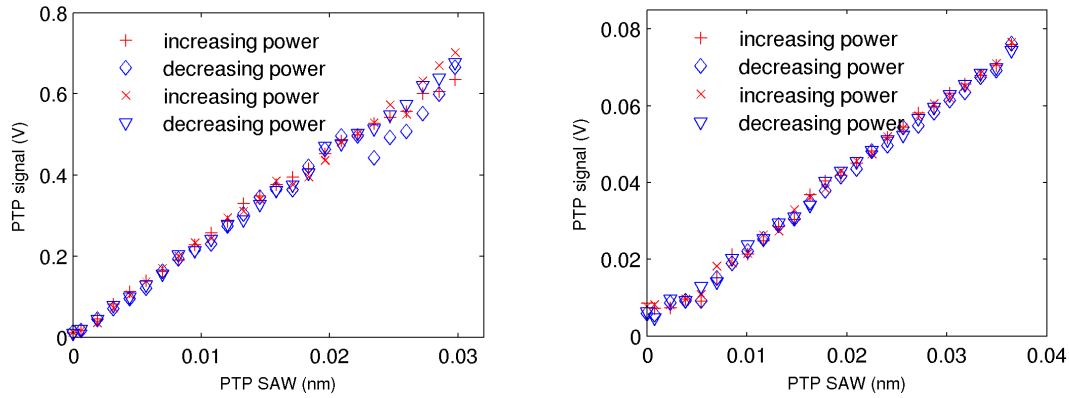

(a) OS d-CHOT (b) SA d-CHOT

Figure 6.31: d-CHOT response to the change in input surface displacement measured as signal PTP

The normalisation to the DC output removes the effects of the light levels, determined by external factors, on the signal amplitude, providing description of the independent d-CHOT light-to-signal conversion efficiency. The calibration curves for the OS/SA d-CHOTs normalised to the corresponding DC light levels during the measurements plotted in figure 6.35 display very similar conversion efficiencies by both types of d-CHOTs, as could be expected from simultaneous fabrication of both gratings. Taking into account different gain in the DC and RF channels (DC/RF = 0.0112) and the use of the amplifier (Chapter 4), the sensitivity in terms of the signal modulation depth per nm of surface displacement corresponds to 38.3 x 10^{-5} and 41.4 x 10^{-5} for the OS and the SA d-CHOTs respectively.

Although beneficial for comparison of the d-CHOT 'goodness', due to the removal of transducer

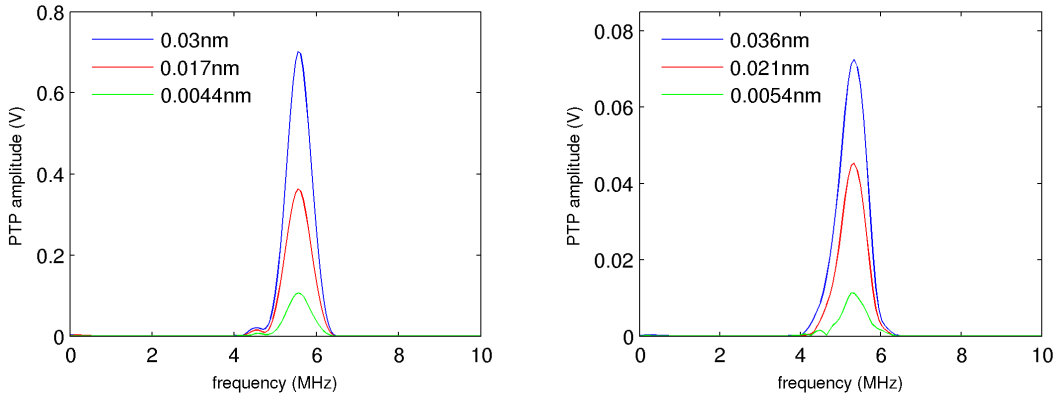

(a) OS d-CHOT (b) SA d-CHOT

Figure 6.32: Frequency spectra of d-CHOT signal at different surface displacement inputs

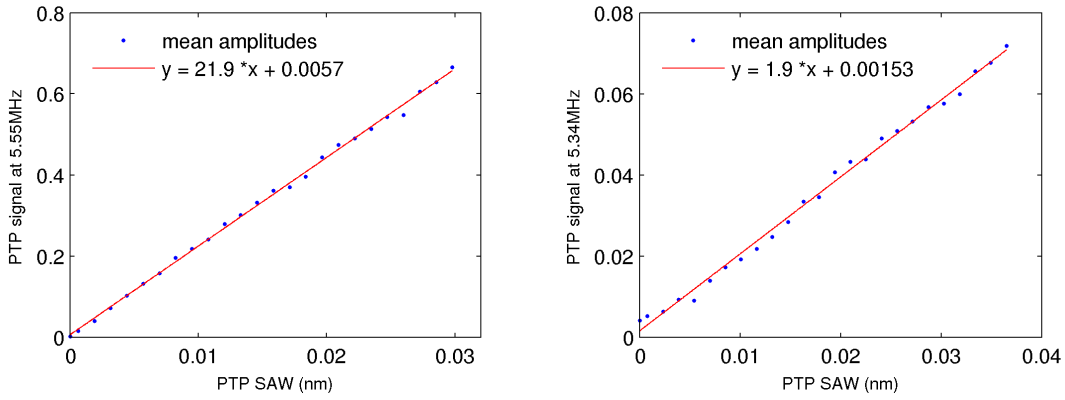

(a) OS d-CHOT (b) SA d-CHOT

Figure 6.33: d-CHOT response to the change in input surface displacement as PTP signal at central frequency (average of four sets)

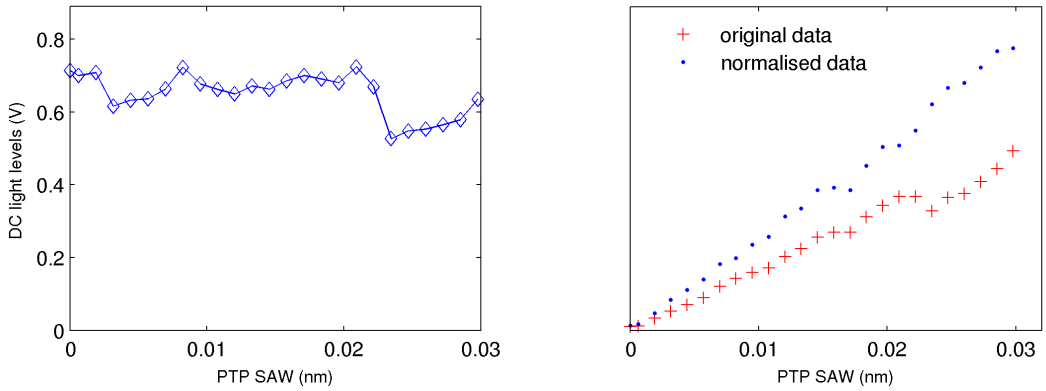

(a) DC light levels during the test (b) Normalisation example

Figure 6.34: Example of data normalisation to DC light levels (a) variation of DC during the test, (b) response comparison before and after normalisation

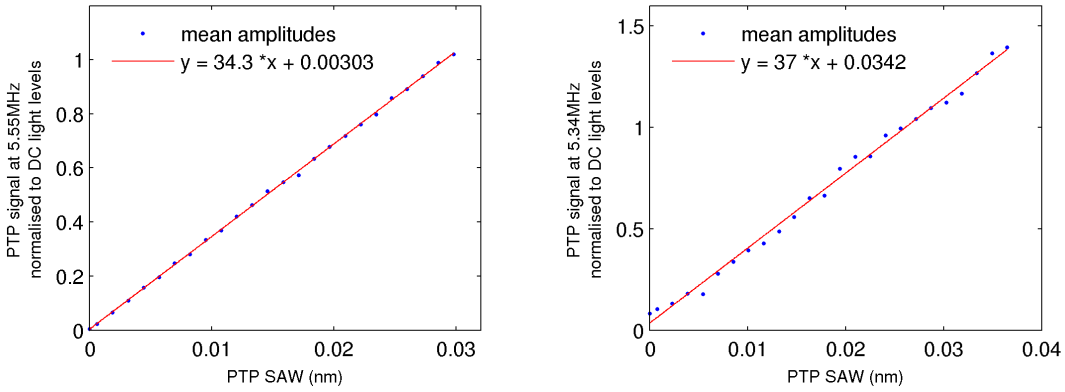

(a) OS d-CHOT (b) SA d-CHOT

Figure 6.35: d-CHOT response to the change in input surface displacement normalised to the corresponding DC light levels

performance-affecting operational differences between the OS/SA d-CHOTs (clearly demonstrated in figure 6.33), the normalisation is not used further.

6.2.3 Probing power response

The second d-CHOT input contributing to the overall signal magnitude is the amount of probing power illuminating the d-CHOT (figure 6.20). Independent evaluation of its effect on the output signal allows to quantify signal gain from the probing power contribution in the overall system as well as set the requirements to laser power instability based on permissible signal variation.

The sensitivity of the output to the probing power was determined for both OS/SA d-CHOTs from the previous section by recording the magnitude of the output signal for different levels of probing power. The generation power provided to the g-CHOT was fixed at 470 mW, providing a fixed SAW input to the d-CHOTs during the test. The levels of probing power were changed in the range 0–310 mW by placing an appropriate neutral density filter at the exit of the fibre, and were restricted to the available filters. The signals were recorded in the same configuration and with the same settings as in the previous section.

Figure 6.36 shows the d-CHOT response to the change of probing power using the PTP signal magnitude at its central frequency. Similarly to the comparison between the OS/SA d-CHOT response to the input surface displacement (figure 6.33), the SA d-CHOT demonstrated a 10.2 times lower sensitivity to probing power. This result is consistent and should be considered together with the corresponding lower DC and signal levels produced by the SA d-CHOT as shown in the previous section.

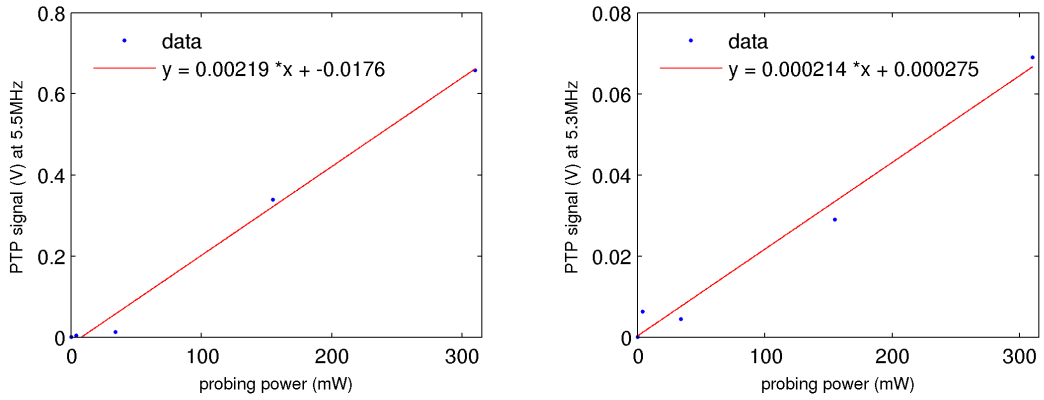

(a) OS d-CHOT (b) SA d-CHOT

Figure 6.36: Transducer response to probing power.

6.2.4 Effects of surface roughness

The operation of the transducers on the real surfaces, especially those of the metal parts, is affected by the surface roughness, often associated with the part fabrication process. Whereas the laser ultrasonic generation is likely to be enhanced by the surface roughness, recalling the operational principle of the d-CHOT (Chapter 3), it is expected to be a significant limiting factor in the transducer operation.

The surface roughness is not an intrinsic property of the object but a measure relative to the wavelength and angle of the incident light as well as, in this case, the dimensions of the d-CHOT

features. A number of approaches can be adopted to describe the effects of the surface roughness onto the incident light, which in general causes scattering around or from the specular direction reducing the energy in the main beam. The detailed description of the scattered fields is however complex, depending on particular surface realisation, and such a study is not intended in this work. Nevertheless, an insight into the practical operation of the d-CHOTs on rough surfaces is provided in this section and the comparison between the OS and the SA transducers is demonstrated.

Among other methods to characterise surface roughness, random rough surfaces can be described in terms of the root mean square (RMS) of individual height deviations $S(x)$ from a smooth reference (the mean line μ):

$$S_{RMS} = \sqrt{\frac{1}{n}\sum_{m=1}^{n}(S(x_m) - \mu)^2}$$

The spatial distribution of these deviations along the surface can be further described by their correlation length L_c.

Most real surfaces are rough on multiple scales, and a particular surface realisation can be represented as a superposition of the sinusoidal surfaces of different wavelengths and amplitudes. Relating the surface description to the size of the d-CHOT features (D - lateral size of the whole d-CHOT, h - step height, a - step spacing), the roughness effects of the following basic surface realisations can be considered:

- **low amplitude** $S_{RMS} < h$**, low frequency** $L_c/2 >> D$**:** may result in small transducer curvature producing slightly converging/diverging wavefronts with little effect on d-CHOT operation
- **high amplitude** $S_{RMS} > h$**, low frequency** $L_c/2 > D$**:** could produce tilt and curvature of the d-CHOT distorting the wavefronts with some operational impact
- **low amplitude** $S_{RMS} << h$**, high frequency** $L_c << a$**:** causes localised scattering of the specular reflections affecting the order energy/size/separation but not impairing d-CHOT functionality
- **high amplitude** $S_{RMS} > h$**, high frequency** $L_c << a$**:** results in surface self-shadowing and reduced reflectivity, with considerable operational impact
- **amplitude** $S_{RMS} \sim h$ **and frequency** $L_c/2 \sim a$ **comparable to d-CHOT features:** the worst case, with critical effect of the relative CHOT and surface–profile dimensions where complete loss of functionality is highly–likely to occur

Additional consideration of roughness should be given with respect to the wavelength of the probing light λ. The height variations within the correlation length of the 'smooth' surface produce phase difference $\Delta\phi < \pi/2$ in the specular direction [152]. Averaged across the surface this criterion becomes $S_{RMS} \cdot \cos\theta < \lambda/8$, where θ is the angle of incidence. For normal incidence and $\lambda = 0.532$ μm this means $RMS < 66$ nm, where the height deviations above $\lambda/4 = 133$ nm produce no specular refection at all due to destructive interference in this direction ($\Delta\phi = \pi$). It could be concluded that at roughness $S_{RMS} \sim \lambda$, where $\lambda << L_c$, the operation of the d-CHOT is limited by optical scattering irrespectively of the relative roughness/CHOT dimensions.

Limiting the discussion to the case of $L_c << a$ when the d-CHOT operation is only affected by the diffuse roughness scattering but not impaired, figure 6.37 illustrates the impact on the intensity, size and separation of the diffraction orders for the most common cases, and the associated effect on the detected signal. The images in figure 6.38 show the black-screen projection of the diffracted wavefront demonstrating the typical appearance of the diffraction orders from d-CHOTs fabricated on different substrates.

Considering the fabrication of both d-CHOTs, a superior operation of the SA d-CHOT on the rough surfaces can be inferred, as the roughness of the resulting transducer is mostly determined by its substrate. The fabrication of the SA d-CHOT on a carrier film in this case limits the roughness of the substrate to that of the polymer film, additionally smoothing the underlying surface profile. Thus operational limits of the OS d-CHOTs dictated by the surface roughness are expected to be reasonably extended for the SA d-CHOTs, enabling operation on rougher samples.

To provide a comparison of operation capabilities of the OS/SA d-CHOTs on rough surfaces, both types of transducers were tested on three aluminium samples of different polishing quality: 1) sufficiently-well polished surface, 2) same, sanded with 1,000 grit and 3) same, sanded with 800 grit. Only half of the sample area was sanded, maintaining the original polishing quality of the other half to exclude the effects of roughness onto the generation efficiencies. The frequency-matched pairs of 4 MHz OS g/d CHOTs were then fabricated placing the g-CHOT on the smooth side, and the d-CHOT on the sanded side of the surface. The SA d-CHOTs were fabricated separately, and then attached to the rough side of the sample in a similar configuration, with the generation by the OS g-CHOT.

The produced surface quality was evaluated using optical microscopy and by performing an 80 x 80 μm surface scan with atomic-force microscope (AFM) to quantitatively describe the area profile. Both, the sample surface and the clear SA carrier film attached to respective samples were scanned, and the corresponding results are presented in table 6.2.

The following parameters are used for description of surface roughness: S_a – mean height deviations, S_{rms} – rms height deviations, and S_m – the distance between the highest peak and

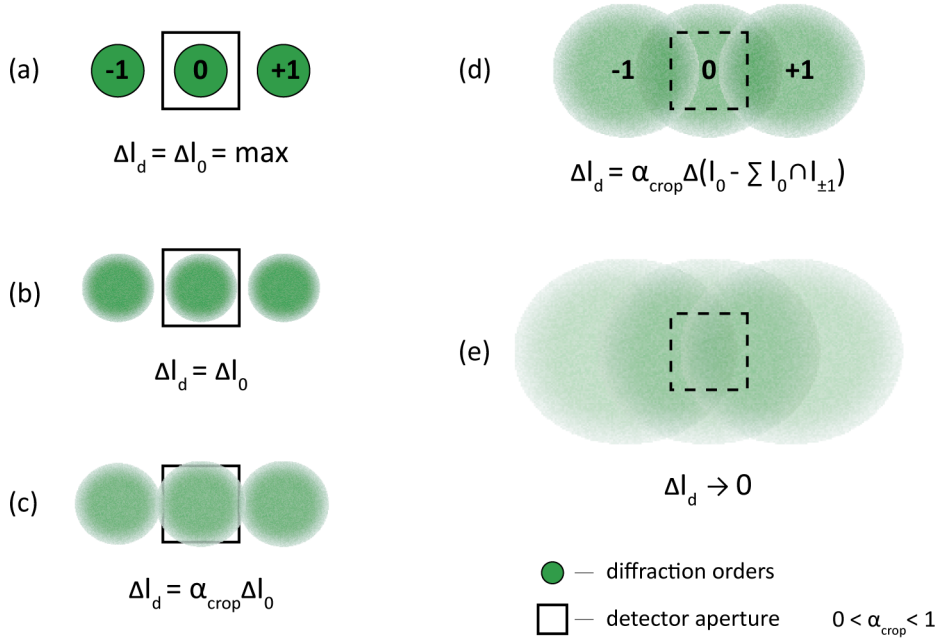

Figure 6.37: The effect of increase in the surface roughness on the diffraction orders and the detected intensity modulation: (a) mirror surface quality, maximum signal modulation; (b) roughness-caused order scattering; (c) order scattering and cropping by detector aperture, reduced signal amplitude; (d) order scattering and overlapping, reduction in registered modulation due to destructive interference in the overlap regions, amplitude reduction due to order cropping; (e) strong scattering, overlap and cropping, drop of registered signal to zero

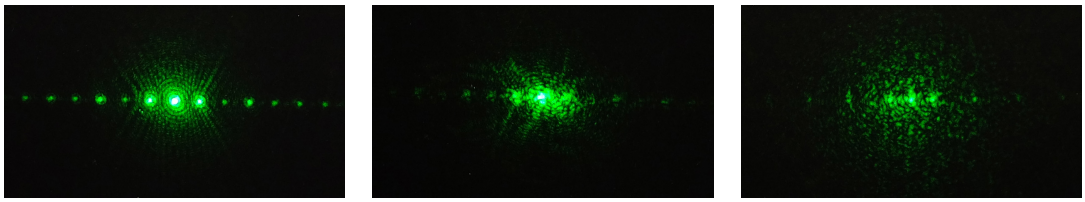

(a) Glass sample OS d-CHOT (b) Glass sample SA d-CHOT (c) Polished aluminium OS d-CHOT

Figure 6.38: Effects of the substrate roughness onto diffraction orders scattering: photographs of the diffracted field projections on a black screen

Table 6.2: Surface characterisation

Sample 1	**Sample 2**	**Sample 3**
polished	grit 1,000	grit 800
Microscope images in reflection 5x		
	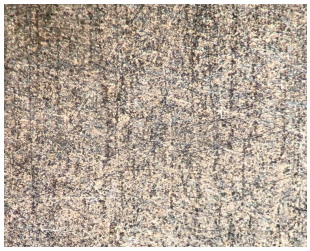	
AFM surface scans (data in μm): sample		
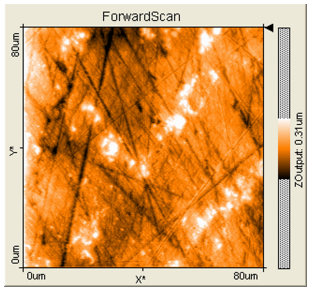	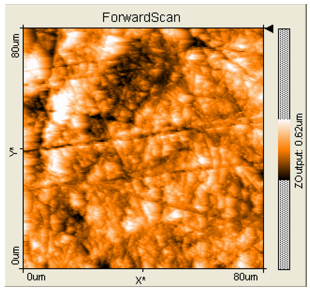	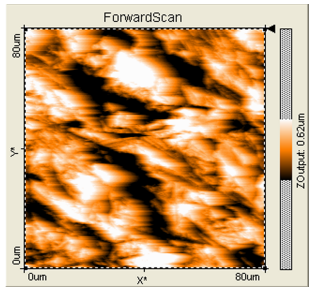
$S_a = 0.0445$	$S_a = 0.0947$	$S_a = 0.186$
$S_{rms} = 0.0589$	$S_{rms} = 0.122$	$S_{rms} = 0.234$
$S_m = 0.00256$	$S_m = 0.00501$	$S_m = 0.00498$
AFM surface scans (data in μm): SA carrier film		
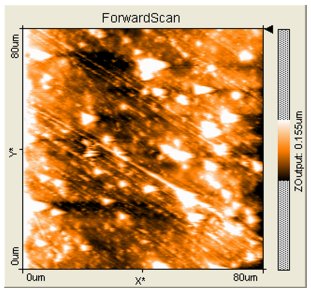		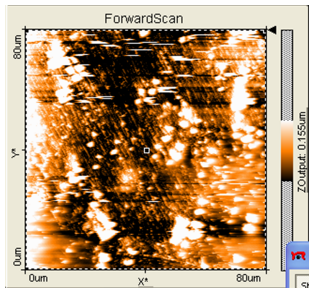
$S_a = 0.0369$		$S_a = 0.0598$
$S_{rms} = 0.0503$		$S_{rms} = 0.0817$
$S_m = 0.00151$		$S_m = 0.00193$

the lowest valley. Although the scan size, limited to 80 μm by the AFM capabilities, does not provide information on roughness frequencies (correlation lengths) comparable to the d-CHOT lateral dimensions $L_c/2 \sim a$, the RMS values of the area (compared to the phase difference criteria of $\lambda/4 = 133$ nm) indicate that the d-CHOT operation in most cases would likely be limited by the localised optical scattering.

The scans of the SA carrier on the rough surfaces reveal the smoothing effect of the polymer carrier onto the underlying surface profile (from $S_{rms} = 0.234$ μm to 0.0817 μm), as well as characterising the intrinsic roughness of the carrier itself.

The fields reflected from the d-CHOTs were imaged onto the black screen, and the output signal recorded averaging 1,000 waveforms at 470 mW generation and 310 mW probing powers. Although possible efficiency differences arising from separate fabrication of CHOT pairs do not allow a direct numerical comparison of the results, the SAW output from the g-CHOTs was measured in each case (at around 11 mm in front of the g-CHOT) to enable comparison with respect to the detected wave magnitude. The corresponding test results are displayed in table 6.3.

Comparison of the field images clearly shows strong scattering effects of the surface roughness in case of the OS d-CHOTs (table 6.3, top) and their appreciable reduction with the use of the

Table 6.3: Effects of the surface roughness onto diffraction orders and detected signals

Sample 1		**Sample 2**		**Sample 3**	
Images of black-screen projection of the diffracted fields from OS d-CHOTs					
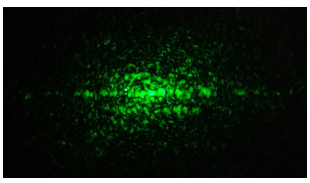		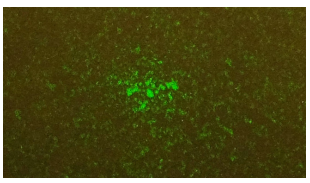		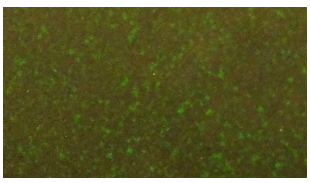	
PTP SAW in	PTP signal out	PTP SAW in	PTP signal out	PTP SAW in	PTP signal out
0.077 nm	0.314 mV	0.066 nm	–	0.076 nm	–
Images of black-screen projection of the diffracted fields from SA d-CHOTs					
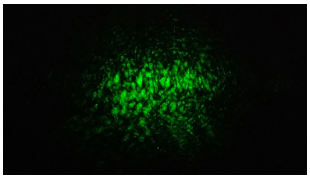		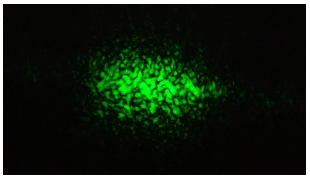		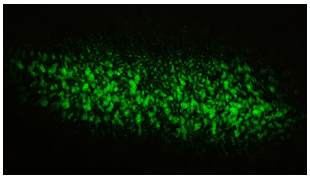	
PTP SAW in	PTP signal out	PTP SAW in	PTP signal out	PTP SAW in	PTP signal out
0.078nm	0.179 mV	0.086 nm	0.307mV	0.080 nm	0.080 mV

SA d-CHOTs (table 6.3, bottom), which agrees with the indications from the surface and carrier AFM scans (table 6.2) and supports the suggestion of the smoothing action of the SA carrier. The faint presence (only visible at full laser power, imaged with no filters) and complete absence of the specular reflections from the OS d-CHOTs on samples 2 and 3 correlates with the exceedance of the expected RMS heights limit of 133 nm for the wavelength of the probing laser.

The OS d-CHOT showed successful operation only on sample 1, with no detection on samples 2 and 3. The SA d-CHOTs performed rather well with reliable detection on all three samples (with some additional signal amplitude differences attributed to d-CHOT fabrication).

The experimental results presented in this section demonstrated some effects and restrictions imposed by the rough surfaces onto the d-CHOT operation and provided the first evidence of the beneficial use of the SA d-CHOTs to extend the range of d-CHOT applicability.

6.3 Coupled-CHOTs system response

Considering the performance of the individual CHOTs and significant differences between the OS and the SA types in particular, the evaluation of the coupled transducer operation is of additional interest. A straight-forward performance comparison of the individual transducers is not easily transferred to the coupled systems, as the jointly operated SA CHOTs combine higher generation efficiency with the lower sensitivity of detection, compared to a pair of coupled OS CHOTs. A layer of carrier film is additionally present between the single-carrier SA transducers.

Using performance analysis similar to that provided in sections 6.1 and 6.2 for the individual CHOTs, two pairs of coupled 5 MHz CHOTs were tested on the glass sample: the OS CHOTs fabricated directly on glass and the SA CHOTs fabricated on a single carrier and attached to the sample. As the mask design allowed simultaneous fabrication of a single pair of CHOTs, the OS and the SA CHOT pairs were produced separately and some differences in the initial d-CHOT sensitivities are possible within the fabrication error.

A coupled-transducer performance was assessed with respect to the main system inputs and outputs: the input generation power to the g-CHOT, and the detected output signal from the d-CHOT. During the test, the probing power was fixed at 310 mW, the generation power was reduced from 470 mW to 0 mW with 40 mW steps, and the output signal recorded averaging 500 waveforms at 2.5 MS/s using corresponding d-CHOT detection setup.

Figures 6.39 and 6.40 show coupled-transducer response in time and frequency domain at three levels of input power (70 mW, 270 mW and 470 mW), and figure 6.41 presents the corresponding response curves generated by plotting the signal PTP central frequency amplitudes against the input generation power.

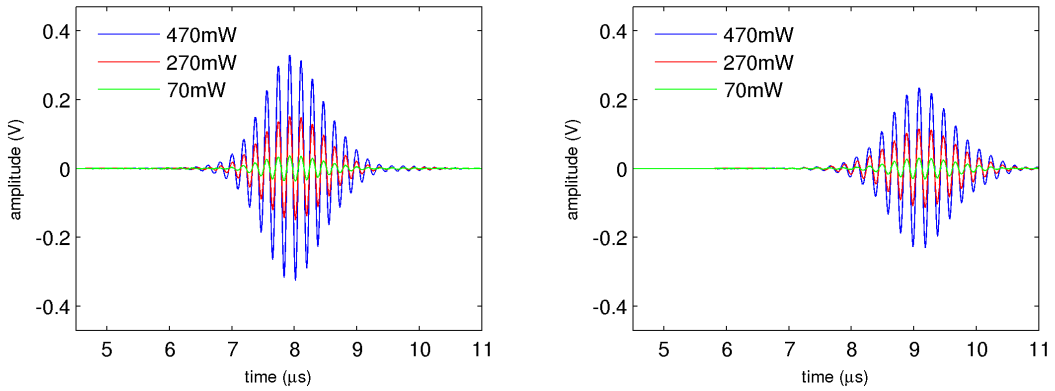

(a) Coupled OS CHOTs (b) Coupled SA CHOTs

Figure 6.39: Change of signal amplitudes with input power

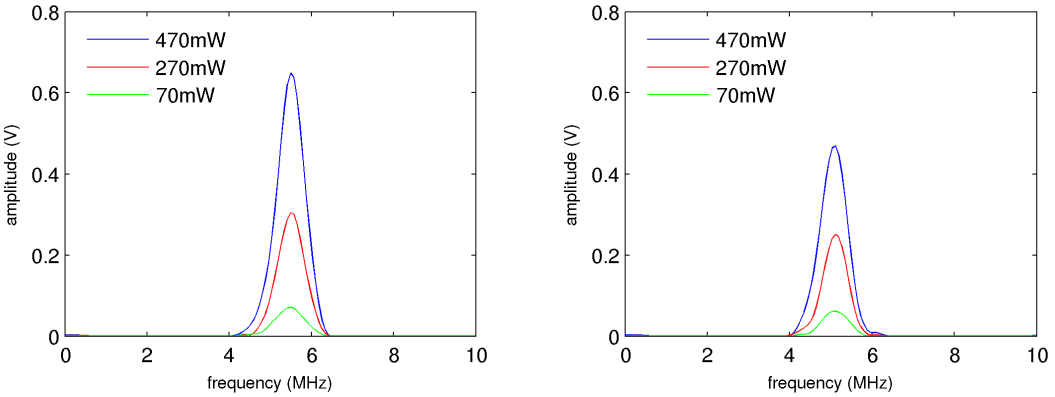

(a) Coupled OS CHOTs (b) Coupled SA CHOTs

Figure 6.40: Frequency spectra of coupled CHOTs signal at different power inputs

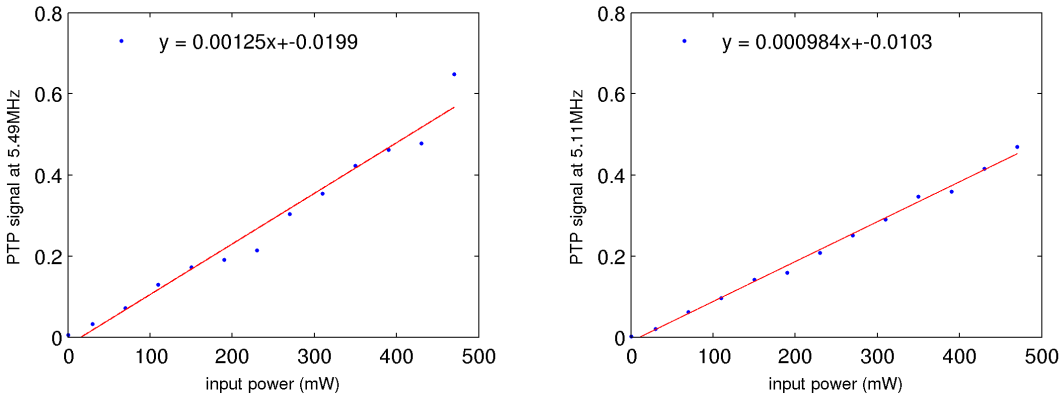

(a) Coupled OS CHOTs (b) Coupled SA CHOTs

Figure 6.41: Coupled CHOT response to the change in input power

A delay in signal arrival is again visible in the time trace from the coupled SA CHOTs (figure 6.39b), consistent with the previous observations during the separate SA g/d CHOTs tests. Maintaining fixed source-to-detector distance throughout the tests, the appearance of the delay exclusively in the SA CHOT tests allows it to be attributed to the presence of the carrier. Almost 3.5 times longer time-delay (about 1 μs) is observed using single-carrier coupled-CHOTs compared to that of the individual SA g/d CHOTs (0.3 μs), most likely caused by the presence of additional 10 mm carrier between the transducers.

Despite the poorer sensitivity of the SA d-CHOT, signal amplitudes from the coupled CHOTs do not differ as dramatically between the OS and the SA transducers, and their response curves (figure 6.41) also suggest a comparable performance.

Although comparison of the coupled OS/SA CHOTs does not show significant differences in the first-pass detection, the application to NDT in pulse-echo configuration makes it necessary to consider the detection of echoes. Of particular interest is the use of the SA CHOTs, where considerable echo-amplitude reduction was noted during the previous tests (figures 6.9 and 6.26). The comparison of the signals from the coupled OS/SA CHOTs in a similar test geometry with the corresponding detected echoes is shown in figure 6.42, where despite the comparable first-pass detection amplitudes, the echoes are indeed seen affected. The echo amplitudes relative to the direct wave are 21% and 12% for the OS and the SA coupled CHOTs respectively, showing almost

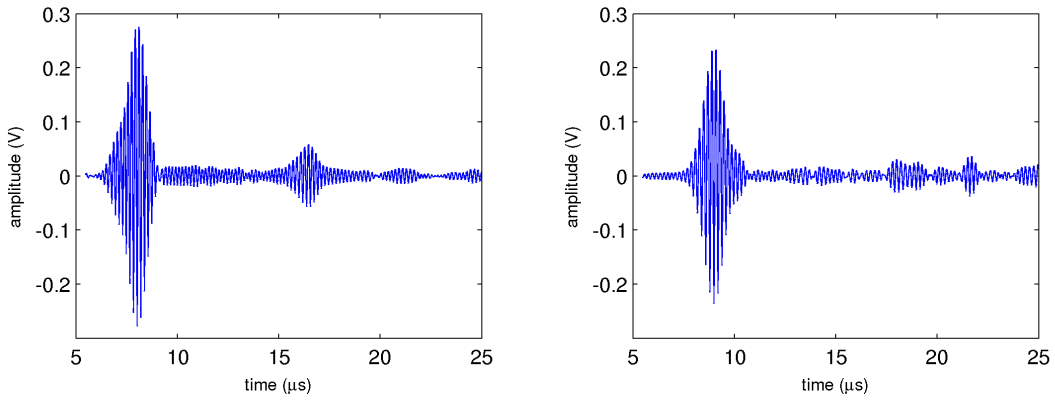

(a) Coupled OS CHOTs (b) Coupled SA CHOTs

Figure 6.42: Operation of the coupled CHOTs in a pulse-echo configuration showing the detection of echoes corresponding to the same sample geometry, where the first wavepacket is a direct first-pass detected wave, and the second is the near-edge echo

a 50% drop in echo amplitude where the coupled SA CHOTs were used (figure 6.42b).

The consistent manifestation of this effect with the SA CHOTs implies it is caused by the carrier, which could present a serious drawback for their use in the pulse-echo configuration. More comprehensive investigation of this effect is carried out in section 6.4.2.

6.4 Functionality tests specific to CHOTs on film carriers

The focus of this section is on specific functionality tests of the transferable and self-adhesive CHOTs, fabricated with methods described in Chapter 5, as well as the investigation of their unique properties and effects associated with the use of the film carriers.

The functionality and the generation mechanism of the fabricated portable g-CHOTs was first confirmed to verify the effectiveness of the proposed concept and validate the chosen fabrication method. A process for fabrication of the SA g-CHOTs was then accordingly devised using the conclusions from these tests.

The ability to reuse the transferable g-CHOTs due to the absence of adhesive layer was studied, whereas the self-adhesive CHOTs were evaluated for bonding longevity and performance stability over time and in continuous operation, restricting the test to the g-CHOTs operating at higher power inputs. Additional functionality was demonstrated for the SA g-CHOT modified by removal of the top liner (CHOT carrier) after transducer attachment to the sample. The effect of the d-CHOT carrier onto the amplitude of the propagating SAW was investigated to evaluate the feasibility of its use in pulse-echo mode. The overall functionality of the SA g/d CHOTs can be seen from the tests in sections 6.1 – 6.2, and the results of their initial tests are not included.

The test setup shown in figure 6.1 was used, where the transferable g-CHOTs were attached to the sample using an industrial gel couplant, and the SA g/d CHOTs – by removal of the protective bottom liner to expose their adhesive layers prior to attachment.

6.4.1 Ultrasonic generation with transferable g-CHOTs

Functionality

The functionality of the fabricated transducers was demonstrated by performing detection of the SAWs generated by the transferred SU8 g-CHOT structure under laser illumination (figure 6.3). The 5 MHz g-CHOTs were tested on glass and aluminium samples, using both types of detection: a vibrometer and the frequency-matching OS d-CHOT. The signals were recorded using 430 mW of generation and 120 mW of detection power (d-CHOT detection), and averaging 1,000 waveforms.

The operation of the transferred g-CHOTs is shown in figure 6.43, where the displayed results

were selected to demonstrate both types of detection and a range of substrates. The signals detected from the SU8 g-CHOTs under the IR illumination are presented in the middle, whereas the top plots show comparable operation of a similar OS g-CHOT on the same substrate. The bottom plots illustrate the absence of detected signal with blocked IR illumination, thus confirming the ultrasonic generation by the g-CHOT structure.

Confirmation of the ultrasonic source

The origin of successful generation demonstrated by the transferred g-CHOT could be attributed to two possible sources. In the first case the source is located on the carrier, with the g-CHOT absorbing the laser radiation and acting as a transducer (the desired function). In the second, the source is located on the sample of the surface with the g-CHOT spatially modulating laser illumination and absorption by the sample, acting as a mask [98].

Although the detection of SAWs shown on the glass sample, transparent to the generation

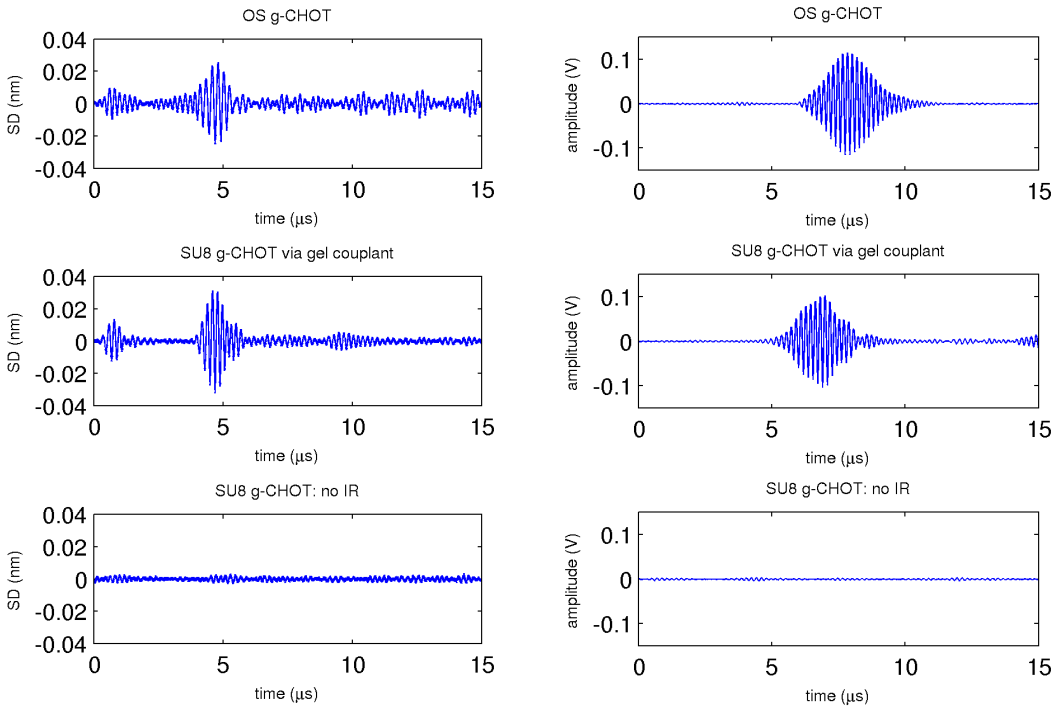

(a) Generation on Al (vibrometer detection)

(b) Generation on glass (d-CHOT detection)

Figure 6.43: Comparison of the ultrasonic generation by the OS g-CHOTs and transferable g-CHOTs on SU8 carriers on Al and glass samples, using vibrometer and OS d-CHOT detection

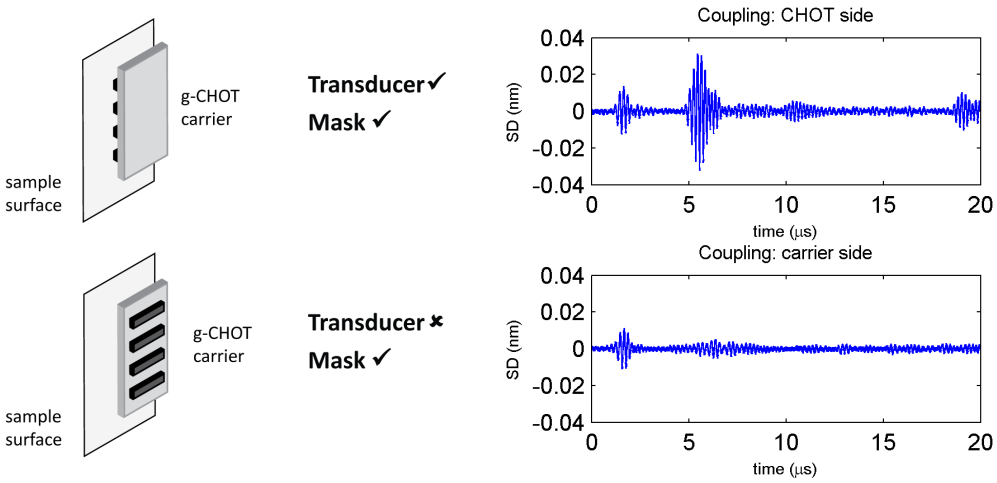

Figure 6.44: Isolation of the generation mechanisms on Al by reverse coupling of the g-CHOT. Top: patterned surface coupled to the sample; Bottom: carrier coupled to the sample

wavelength, confirms the g-CHOT as the ultrasonic source, a further investigation performed on an aluminium sample allows isolation of the two generation mechanisms. In this test the transducer was in turn coupled to the sample by reversing its CHOT and the carrier sides, respectively changing the role of the g-CHOT from a transducer to a mask (figure 6.44). The vibrometer detection was used, averaging 1,000 waveforms. The clear detection of SAW in the first case (g-CHOT = transducer, top plot) and its absence in the second (g-CHOT = mask, bottom plot) confirm the preservation of the generation mechanism employed by the OS g-CHOTs in their portable alternative.

The test additionally indicated the importance of close contact of the portable g-CHOT features with the sample, consequently directing the fabrication process of the SA g-CHOTs (Chapter 5).

Repeatability

As the transferable g-CHOTs do not contain a layer of adhesive and can be easily removed from the sample, the possibility of their repeated application can be considered and was verified by performing a series of test cycles on an aluminium sample.

The 5 MHz g-CHOT on an SU8 carrier was attached to the sample using industrial gel couplant, after which the PTP magnitude of the generated SAW was recorded with the vibrometer at a fixed distance in front of the transducer (figure 6.3). The g-CHOT was then removed from the sample and the carrier cleaned with IPA and a soft tissue. After this the cycle was repeated until the

signal could no longer be distinguished from noise. Figure 6.45a shows the diagram of the test cycle and figure 6.45b presents the corresponding test results plotting the PTP SAW amplitude against the test number.

The distance between the generation beam and the detection vibrometer spot was fixed during the tests (providing equidistant amplitude assessment) and the signal was recorded at 425 mW generation power averaging 1,000 waveforms. Although the relative vertical positions of the generation beam and the vibrometer detection spot were aligned, the angular position of the g-CHOT could differ with each attachment, introducing a small misalignment with corresponding effects onto the measured signal amplitude. The inclusion of this effect into the measurement results additionally characterises the effects of the CHOT portability.

The rapid drop of SAW amplitudes during the first third of the measurements resulted from the build up of couplant on the surface of the sample. The confirmation of this effect is seen in the immediate increase of signal levels after the aluminium sample surface was cleaned (points marked with red square in figure 6.45). The overall slow decrease in the generation output ending with the sharp drop is a consequence of the gradual pattern erosion by the chemical and physical cleaning of the CHOT carrier between the tests.

Despite the eventual g-CHOT wear, the test demonstrated the ability to reuse the fabricated transferable g-CHOTs multiple times. Although due to reduced generation such use would not be considered for serious measurements, it could provide rather acceptable means for determination of further transducer placement and alignment on the part.

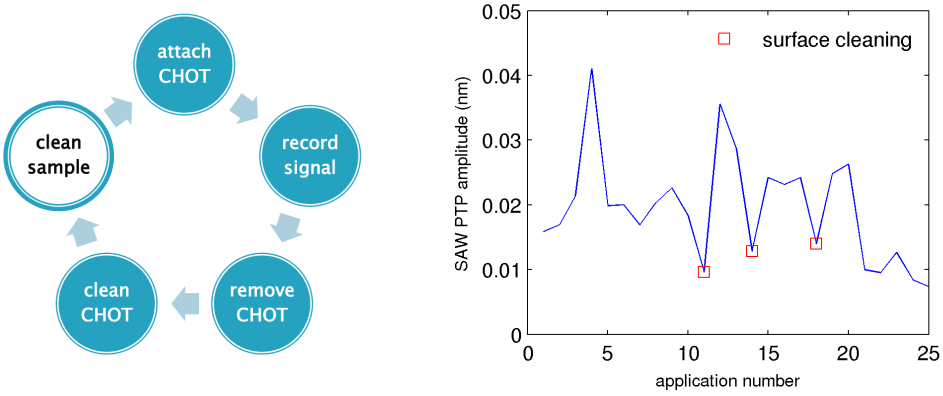

(a) Test cycle

(b) g-CHOT output during repeated applications

Figure 6.45: Reapplication of the transferable g-CHOTs: test cycle (a) and transducer output (b)

6.4.2 Self-adhesive CHOTs

Functionality and stability over time

The localised heating and high power densities experienced during the ultrasonic generation can be anticipated to impact the properties and bonding of the adhesive and the carrier layers, and consequently affect the performance of the SA g-CHOT. To evaluate transducer bonding longevity and adhesive integrity during use, the transducer performance was recorded over time and in continuous operation.

A 4 MHz SA g-CHOT attached to a glass sample was continuously illuminated for the total period of 5 hours. The transducer output was then characterised by the vibrometer, recording the generated SAW in front of the transducer at 2.5-minute intervals (averaged 1,000 waveforms). The original test was performed 7 days after transducer attachment, and then repeated later at increased time intervals roughly in 2 weeks, 2 months, and 1 year.

Figure 6.46 shows the corresponding results where the PTP surface displacement in the generated wave is plotted against time for each test. Here the set of tests performed within 2 months of the transducer attachment displays very similar output levels, and was performed at equal experimental conditions with the average generation power of 420 mW. Due to setup disruptions between the tests over a longer time period and associated differences in test conditions, including positional differences of the beam on the g-CHOT and vibrometer detection, it is hard to directly compare these output levels with the output of a one-year test (performed at 430 mW). Nevertheless, the long-term test showed a similar output stability over time and did not indicate the loss of functionality.

Overall, the transducer demonstrated a stable output in continuous operation (in individual

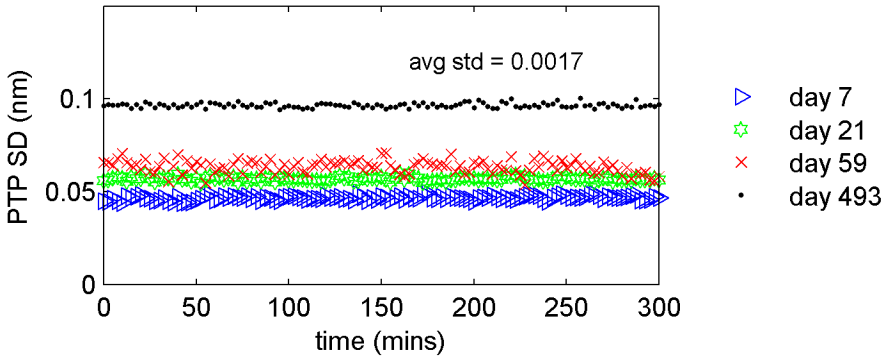

Figure 6.46: Output of the 4 MHz SA g-CHOT on glass shown as peak-to-peak surface displacement during continuous operation for 5 hours, and over time.

tests as well as during a two-month period at equal conditions) without the loss of functionality throughout the one-year time period. The average standard deviation in each test was 0.0017 nm or 2.5%, comparable to the power fluctuation of the generation laser (Chapter 4).

The output stability in the individual tests indicates the coupling integrity of the g-CHOT to the sample is not affected by possible absorption and temperature effects in the adhesive/carrier layers resulting from continuous illumination. The consistency of this behaviour observed among repeated tests illustrates bonding longevity and suggests no significant changes take place in the adhesive over time (e.g. drying out). Provided the use of the same carriers, the conclusions regarding transducer bonding can be applied to the SA d-CHOTs.

Ultrasonic generation with removed carrier

An additional capability permitted by the fabrication of the SA g-CHOT on the adhesive transfer film (Chapter 5) is the removal of the top liner (CHOT carrier) after transducer attachment to the sample, with the adhesive layer and the fabricated structure remaining in place (figure 6.47). The removal of the surface loading will be shown to be desirable and beneficial in particular circumstances (Chapter 7). The efficiency of thus modified transducer can be expected to be affected by the removal of surface constrains (discussed previously), and functionality possibly impaired as the result of the loss or weakening of the bond with the sample.

To investigate the effects on functionality of the transducer, the acoustic field of the 5 MHz SA g-CHOT attached to a glass sample was scanned before and after the removal of the top liner. An area of 20 x 22 mm in front of the g-CHOT was scanned with the vibrometer with 200 μm steps, and the signal recorded at 50 MS/s averaging 500 waveforms, at 470 mW generation power. The C-scans for both cases are shown in figure 6.48 where the maximum PTP SD at each measurement position is colour-coded and presented in coordinates of the sample.

The comparison of the generated fields shows little effect of the layer removal onto their structure or directivity patterns, where sufficient integrity of the g-CHOT structure/contact after the removal

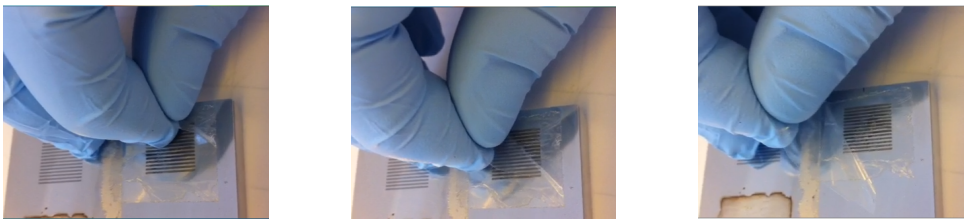

Figure 6.47: Video frames showing the removal of the CHOT carrier (top liner) from the 4 MHz SA g-CHOT attached to Al sample. The 4 MHz OS g-CHOT is seen on the left.

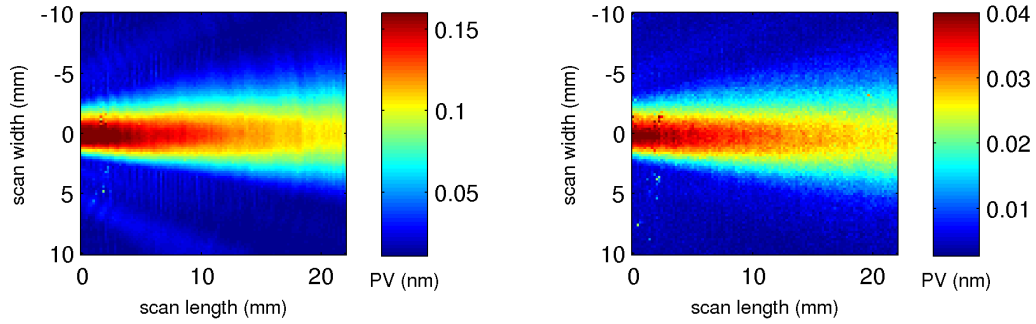

(a) SA g-CHOT with carrier

(b) SA g-CHOT with carrier removed

Figure 6.48: Acoustic fields generated by the SA g-CHOT before and after the removal of the carrier, demonstrating optional functionality of the transducer

of the carrier can be concluded. A considerable reduction of SAW magnitudes observed at the same time brings the operation of the transducer to the levels comparable with the generation by the OS g-CHOTs, additionally supporting the conclusions regarding the role of the top layer in the enhanced generation by the SA g-CHOTs. The optional modification of the SA g-CHOT has thus been shown to offer still effective although reduced ultrasonic generation.

Effect of the carrier onto the amplitude of the propagating SAW

In a typical coupled-CHOTs setup operating in a pitch-catch configuration, the d-CHOT is located in the path of the generated SAW to perform its detection. Although this does not present a problem for the operation of the OS CHOTs in the pulse-echo configuration, with portability of the SA d-CHOTs an adhesive/polymer loading is introduced at the place of transducer attachment to the surface, and consequently into the path of the propagating wave. The alteration of behaviour and characteristics of the propagating SAW by the presence of this extra layer could therefore be expected, and was noted during the previous tests (section 6.1.2) as significant reduction in the echo amplitudes. Consequently, the main concern with regard to the pulse-echo NDT application of the SA d-CHOTs is the impact of the carrier on defect detection ability, in part determined by the amplitude of the wave.

To investigate and quantify the effects of the carrier onto the amplitude of the propagating SAW, three acoustic field scans were performed using 4 MHz SA g-CHOT on a glass sample. An area of 20 x 22 mm in front of the transducer was scanned with 200 μm steps, using 420 mW generation power and averaging 500 waveforms. The first scan (figure 6.49a) provided the baseline SAW energy distribution without the surface alteration by the d-CHOT carrier. A 6.6 x 9 mm (length x width) piece of clear SA carrier (no d-CHOT) was then attached to the surface in the path

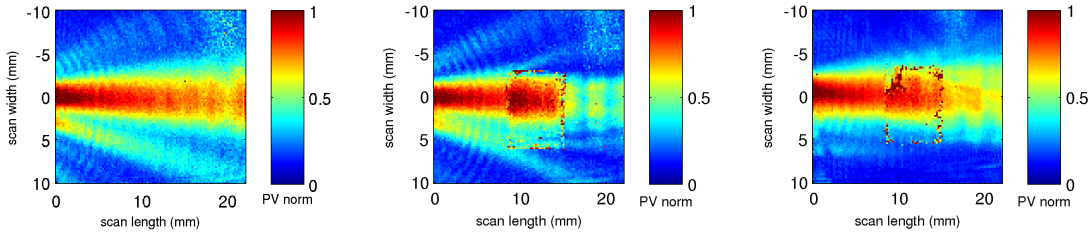

(a) baseline scan (b) carrier (c) adhesive only

Figure 6.49: Acoustic fields illustrating the effect of the carrier onto the propagting wave.

of the SAW, representing the presence of the SA d-CHOT, and the second scan performed (figure 6.49b). Using additional capability of the SA carriers, the third scan (figure 6.49c) was performed after the removal of the top liner, with isolated layer of adhesive remaining on the surface.

The impact of the carrier is evident from comparison of the three scans, most notably – the overall strong amplitude reduction of the SAW past the carrier (figure 6.49b) with a sudden increase in amplitude at the carrier entry. At the same time, this effect appears reduced by removal of the top liner (figure 6.49c), with some recovery of SAW amplitude towards the baseline levels.

The PTP SD in each scan was integrated across the wavefront, using only the central 2 mm of the beam to exclude the beam spreading effects, and normalised to unity at the beginning of the scan. The SAW attenuation can then be visualised and evaluated by plotting the integrated field against propagation distance as shown in figure 6.50a. As noted from the corresponding C-scans, a sudden amplitude increase occurs at the carrier entry followed by the rapid drop past the carrier, with an average reduction from the base levels of approximately 36% and about 8% after the SA carrier and the adhesive respectively (figure 6.50a, red and blue curves). The increase in

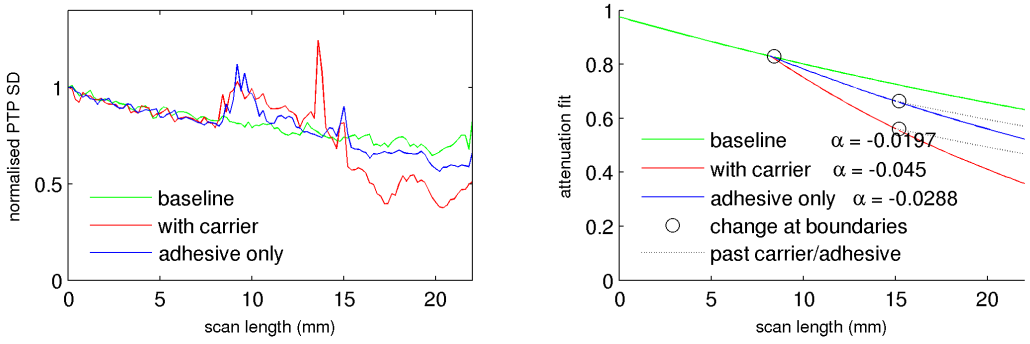

(a) Integrated field (b) Fitted attenuation curves

Figure 6.50: Integrated and normalised PTP field of the propagating SAW along the sample

the SD amplitudes on the carrier is likely caused by the differences of material elastic properties of the polymer compared to glass. The sharp peaks at the edges of the carrier/adhesive are the measurement artefacts which are excluded from further data analysis.

The degree of SAW amplitude reduction past the SA carrier is mainly determined by its frequency-dependent attenuation and length. The exponential fit to the measured data (equation 6.4) is displayed in figure 6.50b and describes the attenuation of SAW on unaltered surface and at corresponding modifying layers. The changes in attenuation rate are seen to occur at the points marking the layer edges, with 2.28 and 1.46 times increase of attenuation coefficients on the carrier and adhesive. The dotted lines represent the base rate of attenuation closely resembling mean amplitude reduction measured after the layer. Due to strong interference with the sample-edge echo in this area, the mean value is used.

$$\begin{cases} A_{base} = 0.97 \cdot \exp[-0.0197 \cdot L] \\ A_{carrier} = 1.02 \cdot \exp[-0.0450 \cdot L] \\ A_{adhesive} = 0.94 \cdot \exp[-0.0288 \cdot L] \end{cases} \tag{6.4}$$

where A is the wave amplitude, and L is the propagation distance (length) of the modifying layer.

Using the fitted attenuation curves, amplitude reduction of 36% can be expected by a 10 mm SA d-CHOT (size used in this work) and 23% by the layer of adhesive of the same size.

From figures 6.50a and 6.50b, the actual drop in SAW magnitude after the carrier appears bigger than expected from its sole attenuation. The anticipated reduction by the adhesive however agrees well with the measured levels. The detailed scan of the central part of the sample with the carrier, performed with 35 μm step (figure 6.51) reveals interference in the carrier and suggests additional losses of wave energy via the internal reflections at the carrier edges. The removal of energy by reflections is further supported by the examination of the central section of the corresponding B-scan, shown in figure 6.52 where in-carrier reflections are revealed. A faint reflection observed at the entry to the carrier in figure 6.52 combined with diffraction seen at the carrier edges in figure 6.49b suggest an additional consideration could be given to the shape and form of the SA carrier

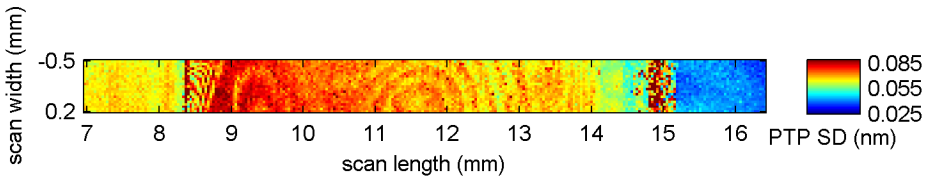

Figure 6.51: Section of a detailed scan of the SAW propagating across the SA carrier

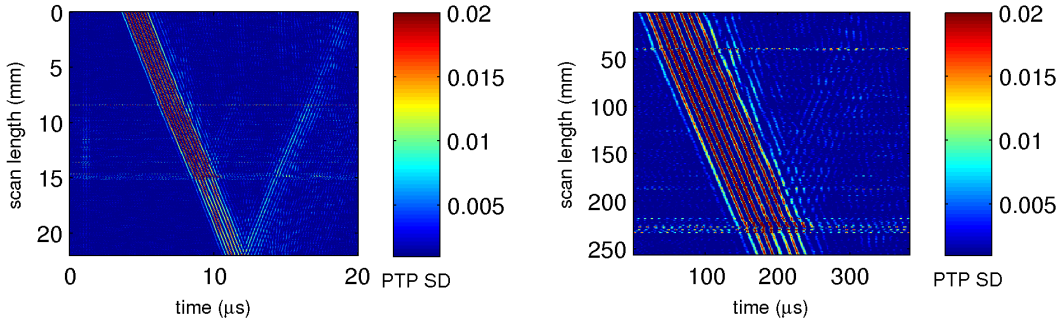

(a) Detailed B-scan

(b) Detailed B-scan: carrier section enlarged

Figure 6.52: B-scans showing propagating SD (PTP) along the sample with attached SA carrier.

edges to reduce the losses.

A change in the wave velocity is also visible from the B-scan where the average group velocity values in the areas before/on/after the carrier are 3,285 m/s, 2,840 m/s and 3,300 m/s. The slower velocity on the SA carrier agrees with and explains the delay consistently observed in signal arrival times from the SA CHOTs.

6.5 Summary and performance comparison

In order to lend support for practical applications of CHOTs, this chapter demonstrated the performance, operation capabilities and selected limitations of the fabricated transducers for both types of g/d-CHOTs, providing comparison between the OS CHOTs and their portable SA option developed in this work. The previous work was thereby extended to provide quantitative description of transducer performance, and introduced the means for comparison not only between the fabricated CHOTs but, more generally, with other conventional methods. The secondary findings of the presented investigations opened new directions for further studies, including those not considered in previous works, potentially contributing to the wider field of ultrasonics. The key results and implications from the studies presented in this chapter are summarised below.

The functionality of the portable CHOTs, developed according to the proposed concept and fabrication method, was first demonstrated for transferable SU8-carrier g-CHOTs, confirming the location of the ultrasonic source on the carrier and the preservation of the generation mechanism employed by the OS g-CHOTs in their portable alternative. Following the fabrication of the SA CHOTs, the transducer performance was evaluated for both types of OS/SA CHOTs, separately assessing their generation and detection functions.

A considerably-higher generation efficiency of the SA g-CHOTs was observed, with six-times

higher output PTP surface displacement and closely-matching ratios in sensitivity to the power input compared with the OS g-CHOTs at equal conditions (31.7 x 10^{-5} vs 4.61 x 10^{-5} nm per mW). Surprising at first, considering weaker bond with the sample, this effect was concluded and partially confirmed to be attributed to the presence of the SA carrier. Although this conclusion is generally supported by other works demonstrating enhanced laser ultrasonic generation by the use of transparent overlays or other modifications of the irradiated surface, the studies were mainly restricted to longitudinal waves with few analytical models, to the knowledge of the author. The determination of the generation-enhancement mechanism requires additional experimental work and the development of the opto-acoustic g-CHOT model – a direction suggested for further work. Building on the observed behaviour, a polymer coating or attachment of a clear SA carrier to the OS g-CHOTs can be anticipated to increase their generation efficiency.

A functional difference arising from the nature of CHOT fabrication was manifested in the absence of the third harmonic in the spectrum of the SA g-CHOT despite its presence in the OS g-CHOT spectrum. The difference in the frequency content of the OS/SA alternatives could be beneficial for application-appropriate selection of the transducer, whether the presence of additional frequencies is undesirable or, conversely, the use of the higher harmonics can be made.

The acoustic fields produced by the g-CHOTs were visualised for the first time and general field characteristics such as near-field-distance and beam divergence were determined (NFD= 13.6 mm, $\theta/2 = 7.2°$), enabling functional comparison with conventional transducers. The developed SA g-CHOTs were shown to produce fields of similar structure and directivity patterns to their OS version.

The effect of the transducer material on the generation efficiency was investigated and showed close agreement with the expected performance between different g-CHOT materials on the same substrate. The discrepancies with the similar tests performed on a different substrate however pointed out insufficiency of using material absorption contrast as the sole means to describe the g-CHOT operation, disregarding substrate/g-CHOT material properties beyond absorption. As the choice of the g-CHOT material is customised to provide the most efficient generation on material of the sample, more knowledge is required on the effect of other material properties to enable transducer practical application. This finding further supports the need for creation of a more complicated g-CHOT model, as mentioned previously.

The optional modification of the SA g-CHOT by removal of the carrier after transducer attachment was shown to offer effective although reduced ultrasonic generation (close to the OS g-CHOT levels), without the loss of transducer functionality and with little effect onto the directivity pattern of the acoustic field. The ability to remove surface loading will be shown to benefit SA CHOTs applications in pulse-echo mode in Chapter 7.

An eleven-times higher sensitivity to the input displacement was demonstrated by the OS d-CHOTs (21.9 V vs 1.9 V per nm) with comparable ratios of sensitivity to the probing laser power. The minimal detectable PTP surface displacement was determined as 6 x 10^{-4} nm and 54 x 10^{-4} nm for the OS/SA d-CHOTs respectively. The lower sensitivity of the SA d-CHOT can be reasonably attributed to the lower light return provided by the SA d-CHOT, shown during the transducer sensitivity tests to the probing power.

Despite the poorer sensitivity of the SA d-CHOT, its combination with more efficient generation by the SA g-CHOT in the coupled system demonstrated performance comparable with the coupled OS CHOTs in the pitch-catch configuration.

The methodology for numerical performance evaluation was developed and transducer calibration curves describing its response for a range of inputs were produced and used to determine individual transducer sensitivities quoted earlier. The use of the calibration curves provides a useful tool for performance comparison of the fabricated transducers and analysis of their contributions in the overall system. This can be used to set the requirements to the measurement system for CHOTs integration or estimate the expected system performance when changes are introduced. All tested transducers demonstrated linear response to the corresponding inputs and absence of hysteresis.

The areas anticipated to be affected by the introduction of carriers were investigated and associated effects quantified.

The high power densities and localised heating during ultrasonic generation with possible absorption and structural changes in the adhesive showed no measurable or visible impact on transducer output and bonding integrity in continuous operation, displaying 2.5% stability (within the deviations in input power). The tests over extended time intervals during the twelve months after transducer attachment did not show degradation of coupling or in output stability.

The impact of the d-CHOT carrier introduced into the path of the propagating SAW onto the operation of CHOTs in pulse-echo mode and the corresponding defect-detection ability was investigated, revealing the alteration of amplitude, frequency spectrum and velocity of the propagating SAW.

The comparison of the base acoustic field with those altered by the presence of the carrier and a single layer of adhesive showed a rapid drop after the carrier reducing wave amplitude to 64% of the base level, and some amplitude recovery to 92% after the removal of the carrier. The attenuation coefficients were determined by performing exponential fit to the corresponding integrated acoustic fields, displaying 2.28 and 1.46 times increase from the base level on the carrier and the isolated adhesive accordingly.

Separately, the comparison of the SAW frequency spectra before and after the entry to the

carrier uncovered the split of the wave energy between two distinct frequency components, a slower 5.5 MHz and a faster 7.3 MHz. This split was repeated in the spectrum of the SA d-CHOT signal, indicating similar wavelengths of both arrivals which allowed to evaluate the velocity of the second frequency component C_{R1} = 4,150 m/s and its origin on the carrier. The displayed behaviour could be explained by possible dispersion and reflections within the carrier region (confirmed in later investigations); however, a significant amount of experimental and modelling work would be further required to confirm the cause.

The presence of internal reflections and interference effects within the carrier as well as weak reflections at the carrier entry were demonstrated in the detailed scan of the propagating SAW. This explained larger loss of energy observed after the carrier than expected from its sole attenuation, and compared to the isolated adhesive, suggesting additional consideration should be given to the shape/form of the carrier edges to reduce the losses.

Additionally, wave velocity reduction to 2,840 m/s was observed on the carrier, consistent with the signal arrival delays noted throughout the tests of the SA CHOTs.

The expected effects and restrictions imposed by the rough surfaces onto the d-CHOT operation were outlined. Comparative tests of the OS/SA d-CHOTs on rough aluminium samples demonstrated the predicted extended tolerance of the SA d-CHOTs to the surface roughness, still performing on the samples where the OS d-CHOT operation was impaired by strong optical scattering. The presented evidence shows the potential to expand the applicability of CHOTs to include the range of parts with surface quality previously unacceptable for detection with OS d-CHOTs. The reflectivity of the SA d-CHOT limited by the roughness of the carrier provides an additional benefit by enabling operation on non-reflective rough surfaces as will be shown in Chapter 7.

Chapter 7

Ultrasonic NDT with endoscopic CHOTs

This chapter demonstrates the NDT capabilities of CHOTs combined with the endoscopic pulser. The detection of machined slots representing surface-breaking flaws is shown both on controlled and industrial samples, with comparison to the equivalent inspections by a conventional wedge piezoelectric transducer of the same frequency. The operation in the pulse-echo and pitch-catch configurations is shown on industrial samples with complex shapes and untreated rough surfaces. Further potential was demonstrated with respect to continuous-pass inspection (sample in motion) and structural health monitoring.

The tests presented in this chapter were performed using the endoscopic pulser (Chapter 4) in configuration shown in figure 6.1.

7.1 Inspection on controlled Al samples with slots in pulse-echo configuration

The flaw-detection capabilities were assessed using coupled 4 MHz OS CHOTs on Al samples, operating in pulse-echo configuration. Rectangular-profile slots representing surface-breaking cracks of different depths (table 7.1) were produced by milling on three, polished to a high degree, Al samples (figure 7.1). The CHOTs were then fabricated on the samples in alignment with the slots, and the fourth, defect-free, sample was used for calibration measurements. A comparison with conventional methods is provided by performing an equivalent inspection with a 4 MHz wedge piezoelectric transducer coupled to the sample using industrial-type gel couplant.

Table 7.1: Parameters of the manufactured slots

Sample #	Slot depth		Slot width		Slot length
0	–		–		–
1	$2\Lambda_{SAW}$	1.46mm	$1/3\Lambda_{SAW}$	0.28mm	8mm
2	$1\Lambda_{SAW}$	0.75mm	$1/3\Lambda_{SAW}$	0.24mm	8mm
3	$1/2\Lambda_{SAW}$	0.39mm	$1/3\Lambda_{SAW}$	0.25mm	8mm

The test geometry and dimensions of the samples and introduced slots were designed with the following considerations: sample thickness – to exclude generation of Lamb waves (10 mm, sufficient at 4 MHz); inspection geometry and locations of slots – to allow clear resolution of the echoes, and representative of the characteristic locations of cracks from the bottom surface of a blade dovetail ($\sim$ 10 mm); slot dimensions – to represent the macroscopic appearance common to dovetail fractures; fabrication of two slots – to enable equivalent comparative inspection with the wedge transducer. The dimensions and quality of the slots were verified by white-light interferometry (Appendix B), where two slots on a single sample were shown to be identical within the fabrication tolerances.

The propagation paths determined by the corresponding test geometries during the CHOT/PZT inspections are shown in figure 7.2, where the expected echoes are labelled accordingly ('a', 'b','c' and 'd'). The test of the clear sample provides the defect-free base signal for comparison with the traces where the slots are present, and the echo detected from the top far edge (marked 'd') can be used as a position marker, similar to establishing a time-gate for inspection area of interest.

The operation of the coupled CHOTs is equivalent to the use of two transducers in a pitch-catch configuration placed next to each other. This produces an additional 'direct-pass' echo (marked 'a') corresponding to the outgoing wave picked up by the d-CHOT (figure 7.2a, note also the

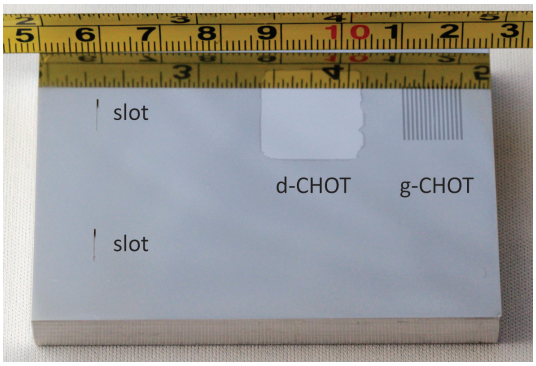

Figure 7.1: Photograph of the Al sample with machined slots and coupled OS CHOTs.

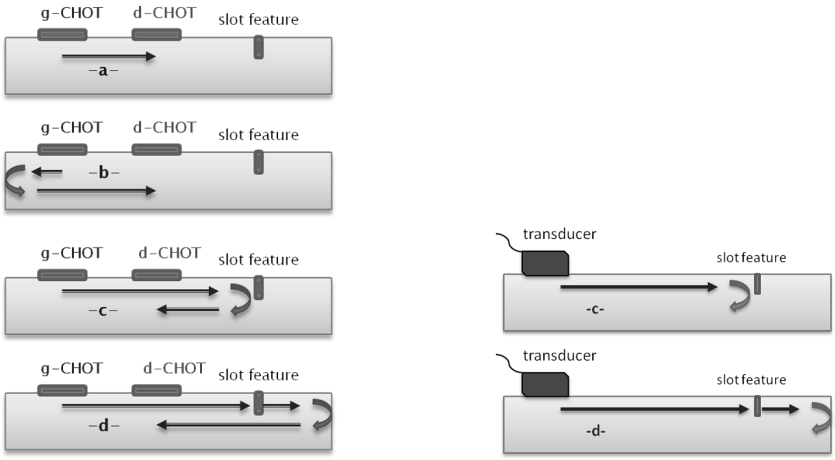

(a) Coupled CHOTs (b) Wedge transducer

Figure 7.2: Propagation paths corresponding to the test geometries.

echo 'b' produced by the rearward-travelling wave). The first-pass detection represents a direct system response and can be used as a means of self-calibration. The PTP value of the first pass objectively characterises the coupled CHOTs - sample system, including both, the generation and detection efficiency, and can be used to normalise the data. Such normalisation allows elimination of unavoidable differences in sample surface quality and efficiencies of the fabricated CHOTs from sample to sample, enabling direct comparison of the results.

During the CHOT test, the generation laser energy measured at the exit of the fibre was 0.48 mJ/pulse. A different CW probing laser with a smaller power output than the one described in Chapter 4 was used, providing 40 mW power at the exit of the fibre at 65% coupling efficiency. Signal acquisition was performed averaging 1,000 waveforms. In an equivalent inspection with a wedge transducer the signals were averaged over 64 measurements. Figure 7.3 presents the corresponding experimental results from the four samples in both tests.

Comparing the CHOT A-scans from the samples with slots to that of the clear sample (bottom trace, figure 7.3a), an additional echo (marked 'c') resulting from the introduced slots is clearly visible in all three tests, showing the ability to detect the slots down to depth $\Lambda_{SAW}/2$. The magnitude of the slot echoes plotted against the depth-to-wavelength ratio shows increasing echo amplitudes for deeper slots (figure 7.4), conforming to the expected behaviour [28]. At the same time, in the test with the wedge transducer (figure 7.3b) the differences in the coupling quality/pressure between the tests are seen to affect the amplitudes of the detected echoes.

Replacing the OS g-CHOT in the same configuration with the SA g-CHOT shows the impact of the carrier film onto the echo amplitudes. The effect is illustrated in figure 7.5. The near-edge

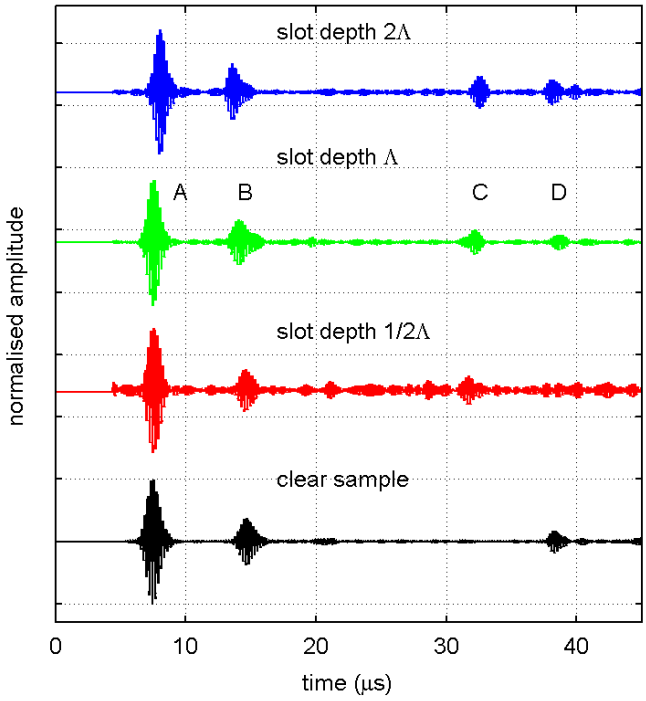

(a) Coupled OS CHOTs

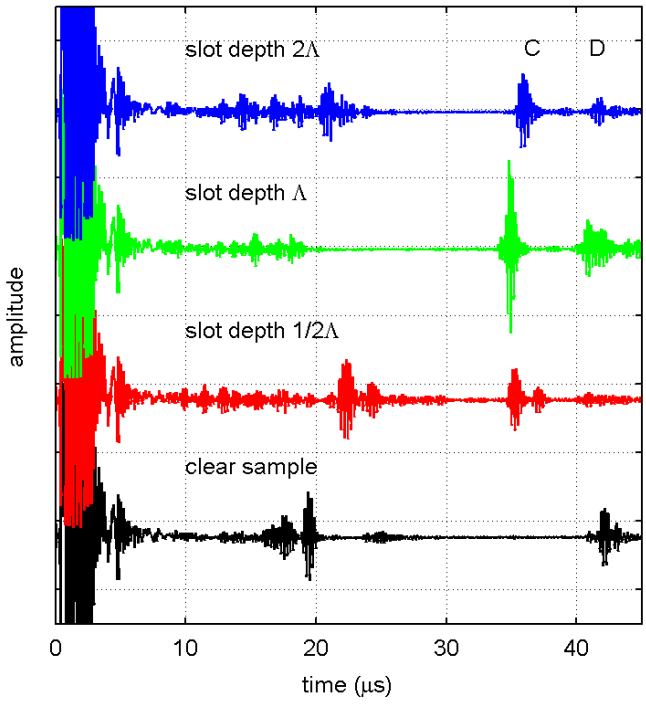

(b) Wedge transducer

Figure 7.3: Comparative results of inspection of controlled Al samples with slots at 4 MHz.

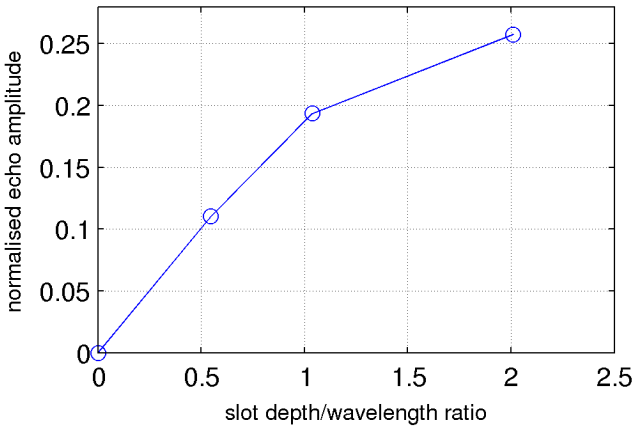

Figure 7.4: Nomalised PTP echo amplitudes detected by 4 MHz coupled OS CHOTs on Al sample from rectangular slots of depth $0.5\Lambda_{SAW}$, Λ_{SAW} and $2\Lambda_{SAW}$.

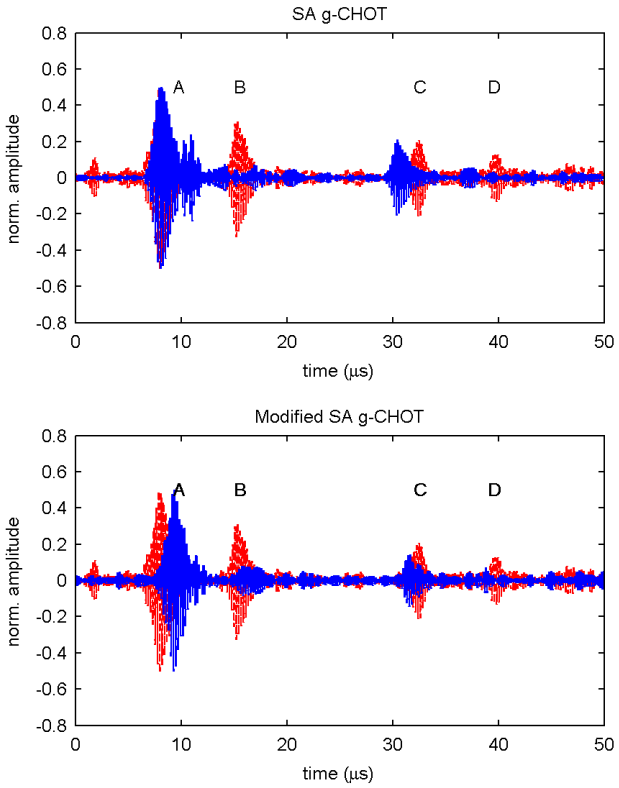

Figure 7.5: Comparison of the inspection results from the coupled OS CHOTs (dashed red) with the same configuration where the OS g-CHOT was replaced with the SA g-CHOT with (top) and without (bottom) the top liner, demonstrating the effects of the CHOT carrier.

echo 'B' produced by the rearward-travelling wave and present in the original trace from the OS g-CHOT (dashed red), is seen to be almost blocked with the introduction of the SA carrier (top) and partially recovered after the removal of the top liner (bottom). This confirms the conclusions in section 6.4.2 regarding the effects of the carrier, demonstrating its impact onto the inspection results. As the g-CHOT carrier is not in the way of the forward-propagating wave, in this test the slot detection is unaffected.

The comparison of the OS CHOTs inspection results with those from a conventional PZT demonstrated the ability of the CHOT system to detect surface defects, producing easy-to-interpret A-scans of a similar nature, with the benefit of self-calibration. Although the use of the SA CHOTs in pulse-echo configurations is evidently limited by the presence of the carrier, the ability to remove it without the loss of g-CHOT functionality opens the possibility to reverse the positions of CHOTs to enable pulse-echo operation (section 7.2.2).

7.2 Inspections performed on industrial samples

The tests of controlled Al samples demonstrated the NDT capabilities of the endoscopic CHOTs. However, the complex material structure, geometries and surface conditions of the real parts, as well as the required inspection distances, introduce additional challenges for the inspection. The CHOTs capability is therefore best demonstrated by a test of an industrial part, additionally allowing exploitation of the full potential offered by the developed SA CHOTs.

7.2.1 Calibration Al-alloy sample: pulse-echo configuration

The first industrial sample for inspection was a 3 mm-thick highly-polished Al-alloy calibration plate (figure 7.6) with two slots of different sizes/depths fabricated by EDM spark erosion (electrical discharge machining). Such calibration samples are fabricated representative of the part to be inspected, and used to set a time gate of the field inspection system to monitor the region of interest [3]. The detection of the calibration slots is then performed with a wedge PZT transducer in pulse-echo configuration, placing it at marked positions on the sample.

In this work, the procedure was replicated with the coupled CHOTs and the conventional (wedge transducer) method to demonstrate comparative operation on an industrial part in a practically-used inspection setting. Figure 7.6a shows the relative positions of the transducers during the test.

(a) full sample (b) close-up

Figure 7.6: Photograph of the calibration Al-alloy sample with marked locations of the test geometry (a) and two EDM slots (b) The marked scan area corresponds to the results of the acoustic field scan shown in figure 7.8.

Sample characterisation

The acoustic material properties of the sample were evaluated using SRAS (spatially-resolved acoustic spectroscopy) system developed at the University of Nottingham [153]. The results of the scan in comparison to a conventional non-specific aluminium alloy (figure 7.7) revealed large grain sizes (100–400 μm) and a degree of material structure inhomogeneity, with the mean SAW velocity of 2,925 m/s. The dimensions of the two EDM slots were measured with the stylus profiler (Appendix C.1), where the slot width/depth/length were 100 μm/110 μm/1 mm and 140 μm/180 μm/2 mm for the first and the second slot respectively. Due to the relative aspect ratios of the slots and the size of the stylus tip, the bottom of the slots was not reached and the quoted depth values represent a lower estimate.

Generated acoustic fields

The generated acoustic fields from 4 MHz OS g-CHOT, fabricated on the sample, and a 4 MHz wedge piezoelectric transducer coupled to the sample via phenyl salicylate, were visualised (in two separate tests) with an optical vibrometer, performing a scan of a 20 x 120 mm area in front of the transducers (figure 7.6a) at 200 μm steps. During the test, the wedge transducer was placed at the positioning marker, whereas the g-CHOT, fabricated in a coupled configuration with the d-CHOT, was located further back from the marker in an equivalent test. The thickness of the sample was calculated to be sufficient for the excitation of the Rayleigh and not Lamb waves at this frequency (Appendix C.3).

The traces from the PZT transducer were recorded averaged over 64 measurements at 100 MS/s. The size of the sample combined with the spatial scan resolution and the need to average CHOTs waveforms for improved SNR resulted in very long scan times, to reduce which the g-CHOT field was recorded at lower time-resolution of 50 MS/s, and averaged over 1,000 measurements.

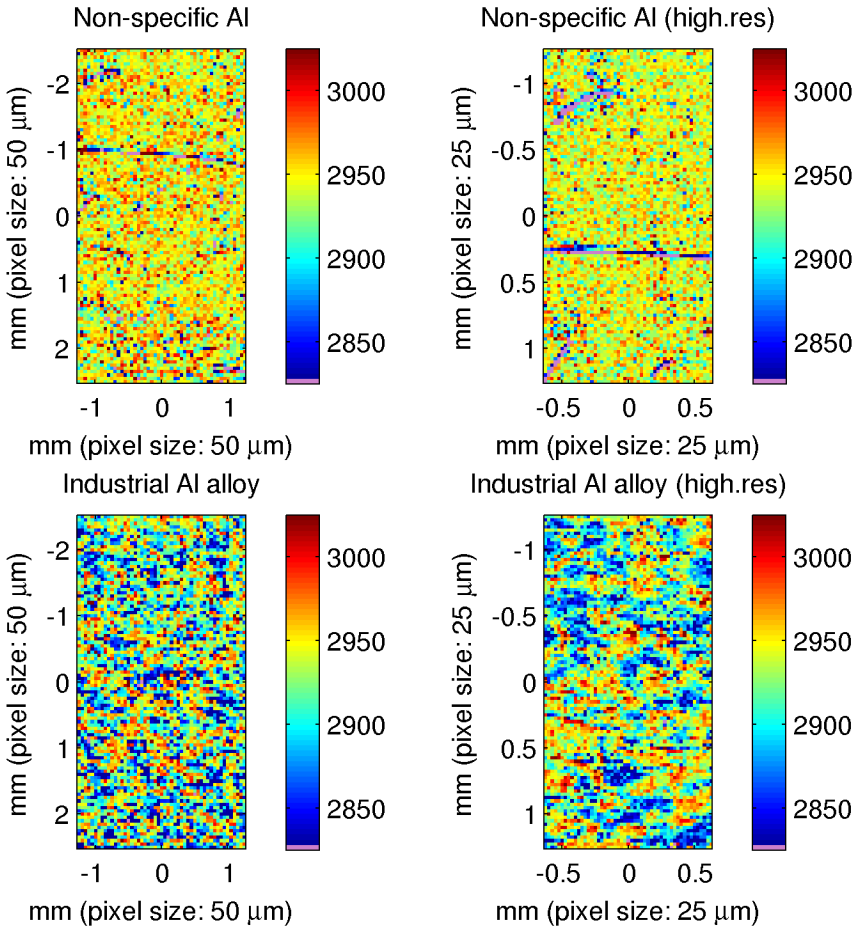

Figure 7.7: Comparison of the acoustic structures of a sample from non-specific Al with the industrial Al-alloy calibration sample. Images were obtained using SRAS technique and illustrate the velocity maps of propagating 164 MHz SAWs (colorbar). Large grain size and inhomogeneity of the industrial sample are evident.

The generation energy was 0.43 mJ/pulse. Figure 7.8 shows the corresponding C-scans for both transducers, with the colour-map representing the maximum PTP surface displacement at each point on the sample.

The propagating acoustic fields in both cases are seen to reach the slots (visible as short vertical lines between 110–120 mm of the scan) despite the inhomogeneous grain structure of the sample (figure 7.7), with the effects of diffraction clearly visible in figure 7.8a. Here the bright area in the lower part of the scan past 100 mm is the artefact of detection, confirmed by recorded optical gain (Appendix C.2), and is not a reflection from the notch. The scan region of the sample at around 20 mm in both tests shows the artefacts from the higher surface roughness in that area.

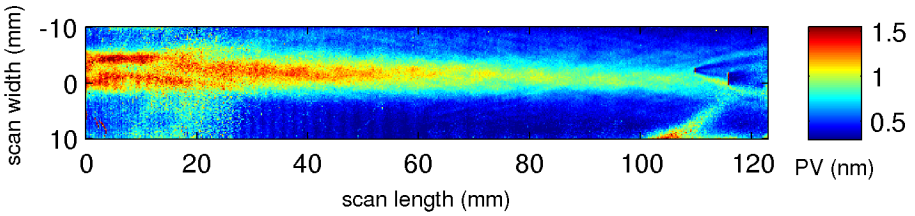

(a) Acoustic field from a 4 MHz wedge transducer

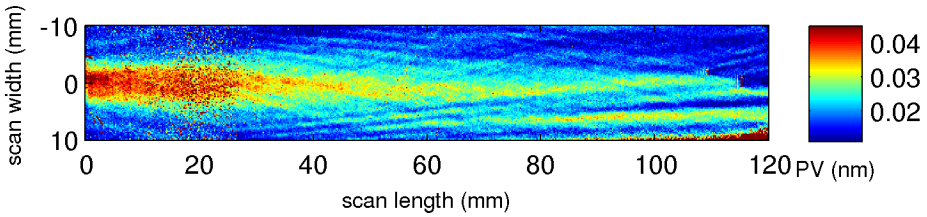

(b) Acoustic field from a 4 MHz OS g-CHOT

Figure 7.8: Comparison of acoustic fields generated on a calibration Al-alloy sample (scan across the area shown in figure 7.6, the notches are visible as vertical lines between 110–120 mm).

The acoustic field generated by the g-CHOT (figure 7.8b) displays similar diffraction effects at the slot as with the wedge transducer in figure 7.8a. Their visibility is however obstructed by the wave propagating back towards the transducers after being reflected from the edge of the sample. Multiple reflections from the edges of the sample can be seen in the scan, appearing to be caused by the side lobes of the generated filed. This marks a difference with the field generated by the PZT. Additionally, the amplitudes of the generated surface displacement can be compared in both cases, with the difference of over an order of magnitude between the two transducers.

More detailed interaction of the acoustic field generated with the g-CHOT with the calibration notches was visualised by performing a scan of the ROI at increased spatial resolution. The 12 x 12 mm area around the slots was scanned with 50 μm steps, recording 1,000 waveforms at 50 MS/s. The resulting C-scan presented in figure 7.9 displays both, the effects of diffraction at the slot and the interference with the returning echoes. The propagation of the wavefront across this region is shown with more detail by a number of time frames in figure 7.10.

Overall, the field generated by the g-CHOT was shown to reach and interact with the slots in a similar manner to the wedge piezoelectric transducer despite the inhomogeneous grain structure of the sample and lower amplitude of the surface displacement.

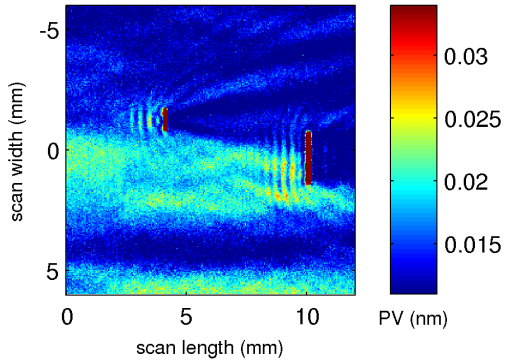

Figure 7.9: Acoustic field from a 4 MHz OS g-CHOT: interaction with slots

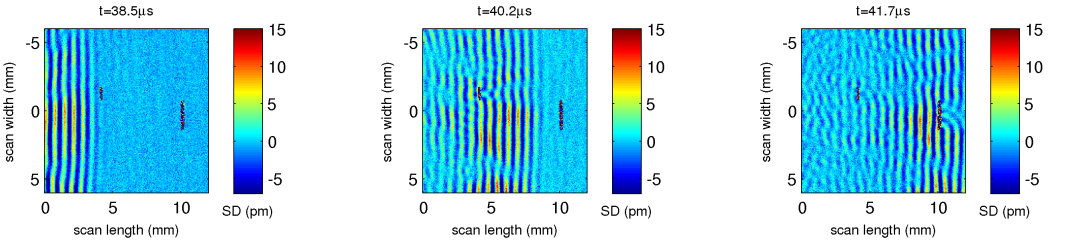

(a) oncoming wavefront (b) interaction with first slot (c) interaction with second slot

Figure 7.10: Propagation of the SAW wavefront across the ROI (4 MHz OS g-CHOT)

Slot detection

In this test, the wedge transducer was coupled to the sample using industrial gel couplant, and the detected signal recorded by averaging 64 waveforms. In a similar inspection, the g and the d-CHOTs were used in a coupled configuration, with the generation and detection powers 0.47 mJ/pulse and 315 mW respectively, averaging the detected signal over 25,000 measurements. The results of both inspections plotted as a function of distance from the corresponding transducers (based on the measured mean sample velocity of 2,925 m/s) are shown in figure 7.11 at the full time-scale, and as a close-up of the region of interest (ROI) on the sample in figure 7.12.

The first three detected wave packets in figure 7.11a correspond to the direct pass and the rear top/bottom edge reflections detected by the OS d-CHOT. The echoes marked ‘A‘, ‘B’ and ‘C’ corresponding to the two slots and the far edge of the sample (figure 7.6b) are hard to see due to the amplitude differences with the direct pass. The close-up of the ROI in figure 7.12a shows the three resolved echoes corresponding to the inspected geometry.

The comparison of the results with the PZT transducer inspection (figures 7.11b and 7.12b) validates the detection of slots with the CHOTs, although with markedly-higher SNR from the

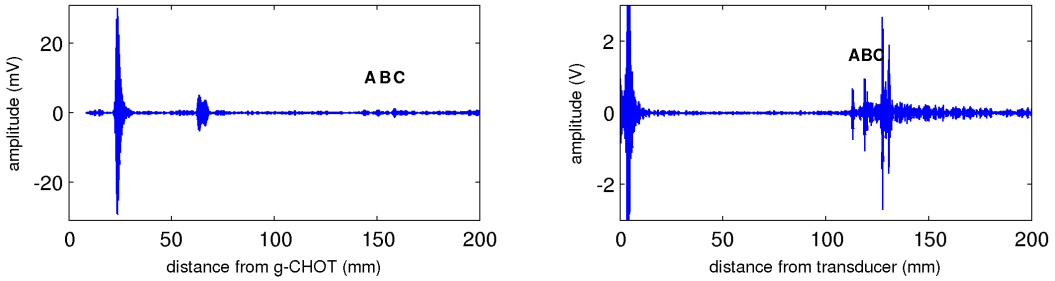

(a) 4 MHz coupled OS CHOTs: 25,000 waveforms (b) 4 MHz wedge transducer: 64 waveforms

Figure 7.11: Full traces from inspection of the calibration sample

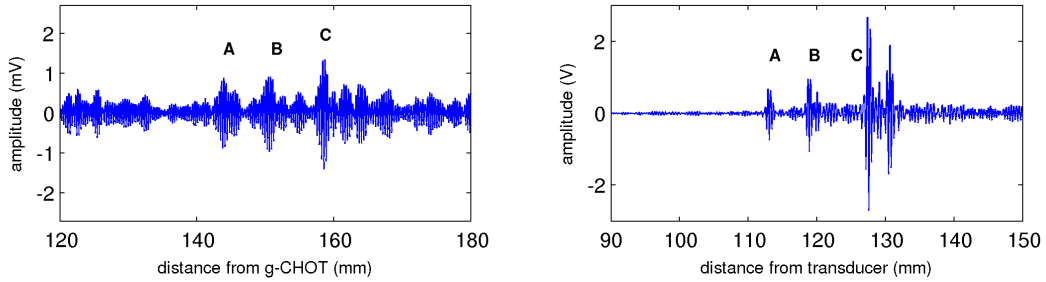

(a) 4 MHz coupled OS CHOTs: 25,000 waveforms (b) 4 MHz wedge transducer: 64 waveforms

Figure 7.12: A close-up of the region of interest containing slots on the calibration sample

contact transducer, where the SNR of the CHOT inspection is limited by a coherent noise. At the same time, considering the results of the acoustic field scans (figure 7.8), the surface displacement produced by the g-CHOT is also over an order of magnitude lower.

Similarly, a pair of 5MHz SA CHOTs was used to perform the inspection in a pulse-echo configuration. Considering the low amplitudes of the slot echoes obtained with the OS CHOTs at marked propagation distance and substantial amplitude reduction by the d-CHOT carrier (section 6.4.2), the CHOTs were positioned at reduced distance, within 25 mm from the first slot. The signal detected at 0.47 mJ/pulse, 310 mW and averaged over 5,000 measurements is shown in figure 7.13, where the echoes corresponding to the slots and the edge of the sample can be identified and are marked ‘A’, ‘B’ and ‘C’.

Despite the lower SNR in the OS CHOT signal (where some allowance could be made considering longer propagation distance, non-flexible alignment and generally lower amplitudes of the generated SAWs), the test demonstrated the CHOT system ability to fulfil the required inspection on an industrial part with complex grain structure and large propagation distance (subject to actual inspection thresholds). Although functionality of the SA CHOTs in pulse-echo configuration

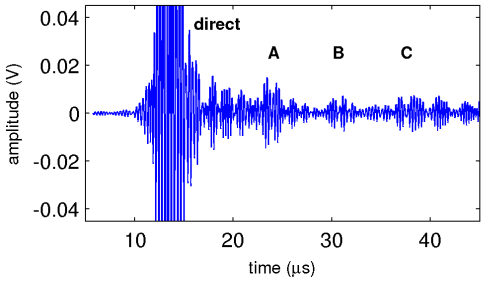

Figure 7.13: 5MHz coupled SA CHOTs in pulse-echo configuration

was limited by the propagation distances and attenuation by the d-CHOT carrier, the slots at close proximity to the CHOTs were detected.

7.2.2 Section of a blade-root: SA CHOTs in reversed pulse-echo configuration

The second type of tested industrial samples was a section of the aeroengine blade root (Ti-64) with the grain structure visible to the naked eye, and unpolished rough surface. This sample is representative of the components with complex geometries and surface curvature, and its shape and surface finish provided ideal opportunity to utilise the benefits offered by the SA CHOTs.

The test was performed with 5 MHz SA CHOTs placed on the sample in reversed pulse-echo configuration (figure 7.14a). By placing the d-CHOT out of the way of the forward-propagating wave (behind the g-CHOT), the effects of the carrier can be excluded by using the SA g-CHOT in its modified state - with the top liner removed (section 6.4.2). In this case the reduced generation

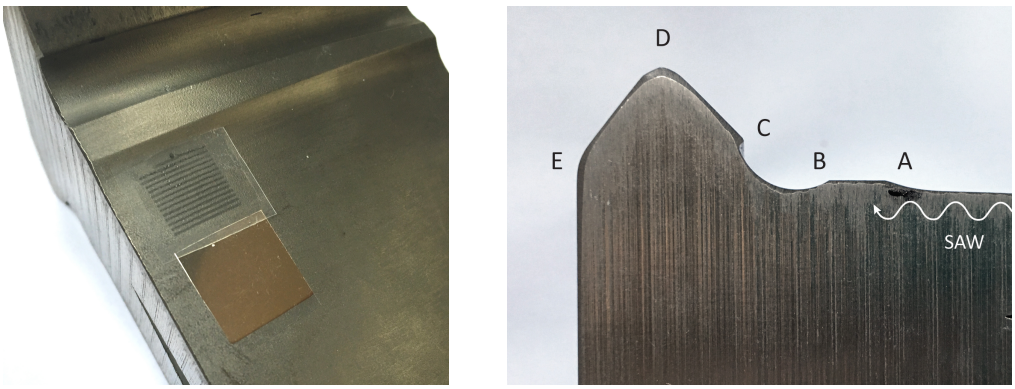

(a) CHOT placement (b) surface profile

Figure 7.14: Photographs of the inspected blade root section: Ti-64.

efficiency was preferred to the attenuation introduced by the d-CHOT carrier.

An example of a signal recorded at 0.47 mJ/pulse and 310 mW, averaged over 5,000 measurements is shown in figure 7.15a, where the expected echo arrival times corresponding to the surface profile (figure 7.14b) and the mean Ti velocity of 2,958 m/s are marked 'A', 'B' and 'C' accordingly. Figure 7.15b shows the mean signal from 9 trials. The traces are plotted as a function of distance from the farthermost transducer and give good agreement with the nearest reference points of the sample geometry. The changing curvature of the reference features across the sample makes their detection challenging as the angle of the returning SAW differs accordingly. Due to the generation laser beam illuminating only a part of the g-CHOT, its relative position on the transducer, combined with the above effect of the sample geometry, determined the angle of the SAW arrival and the magnitude of detected echoes. The mean of the 9 trials taken by varying position of the generation beam on the g-CHOT averaged the detection of the same reference feature across the transducer and enhanced SNR.

The low signal levels in the individual measurements are caused by the low light return to the photodetector, partially due to the alignment difficulties of the fixed-mount optics with the curved sample, but mainly resulting from high distortion of the returning field by the surface curvature, producing astigmatic fields. A photograph of the diffraction orders taken at the iris (where selection of the zero order takes place) illustrates the combined effects of the sample curvature and surface roughness (figure 7.16), where the distortion of optical field is accompanied by the spread of energy out of the diffraction orders and the associated loss in the signal levels.

This test demonstrated not only the functionality of the SA CHOTs on a challenging industrial part, but also the feasibility of operation in reversed pulse-echo configuration using the modified SA g-CHOT, where potential agreement with the sample geometry could be observed in the de-

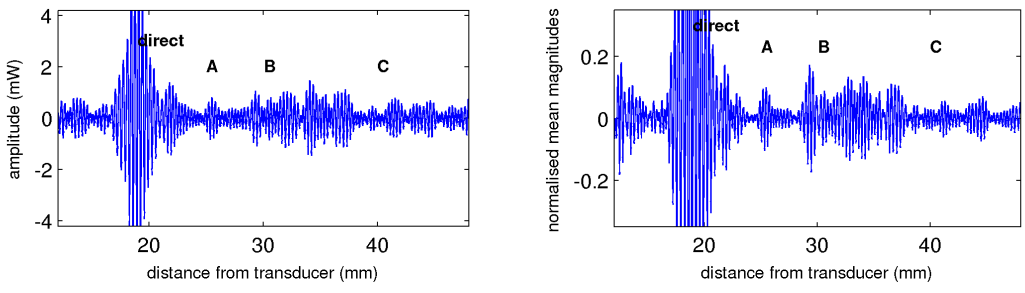

(a) Single test: 5000 traces

(b) Average over 9 trials

Figure 7.15: Inspection results of the blade-root section with 5MHz SA CHOTs in reversed pulse-echo configuration.

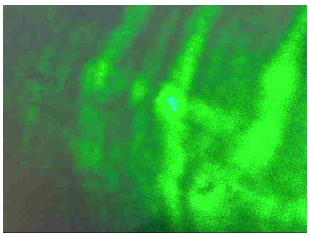

Figure 7.16: The returning optical field containing diffraction orders and displaying the effects from the surface curvature and roughness.

tected signal. It additionally confirmed the ability of the SA d-CHOT to operate on parts with characteristic to the component surface roughness, and indicated practical effects from the surface curvature onto the returning field as well as echo identification challenges presented by the geometry of the sample.

7.2.3 Section of an aeroengine disk: SA CHOTs in pulse-echo and pitch-catch configurations

Another example of CHOTs application to real parts is operation on a section of the aeroengine disk. One of the most challenging samples tested with CHOTs in terms of surface conditions, it demonstrated the benefits as well as the limitations of practical applications of the developed SA CHOTs.

The test sample was a 7 mm-thick section of an aeroengine disk, with a dark, unpolished surface and evident tooling marks. The large size of the sample would make it unsuitable for fabrication of the OS CHOTs in the sputterer or vacuum evaporator (Chapter 5), providing a good example where the use of portable CHOTs would be beneficial. After the surface was wiped with IPA and allowed to dry, 5 MHz SA CHOTs were attached to the sample in pulse-echo and pitch-catch configurations shown in figure 7.17. The surface finish is visible in a close-up image of the g-CHOT in the inset (figure 7.17b), and the effect on the surface of the d-CHOT – in the main frame of the photo.

High generation efficiency was not anticipated on this sample as the alloy composition and absorption at the generation wavelength were unknown, and the g-CHOT material was not changed to tailor the absorption contrast with the sample (the Cr g-CHOT was used).

In terms of detection, such non-reflective rough surface is extremely challenging for most optical detection methods including the d-CHOTs due to light absorption and scattering. The operation of the SA d-CHOTs on rough surfaces was shown to decrease the effects of roughness and extend the range of d-CHOT applicability (section 6.2.4). Another advantage that becomes evident in

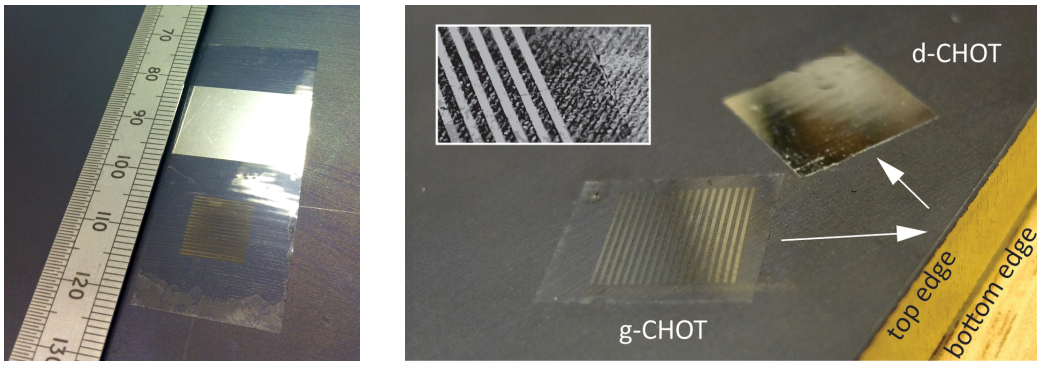

(a) (b)

Figure 7.17: 5 MHz SA CHOTs on untreated section of an aeroengine disk (a) in pulse-echo configuration on a single carrier, (b) in pitch-catch configuration, (inset) close-up of the g-CHOT with exaggerated contrast showing surface roughness.

this test is the introduction of its own highly-reflective area by the SA d-CHOT, making optical detection independent of the sample reflectivity and thus overcoming one of the main barriers for application of all-optical LU systems in industry.

In the first test the single-carrier CHOTs in a pulse-echo configuration (figure 7.17a) were used to direct the wave along the sample profile shown in figure 7.18a, where the prominent geometry features are marked with 'A', 'B' and 'C'. The propagation distance from the g-CHOT to the feature 'C' was approximately 143 mm, the generation and detection powers were 0.42 mJ/pulse and 115 mW respectively.

Despite the possibility of low absorption contrast (e.g the absorption of Ti sample would be very close to that of Cr CHOT), a clearly-detectable signal was obtained in direct pass (figure 7.18b, 30,000 waveforms averaged). The signal amplitude was also likely to be reduced due to the

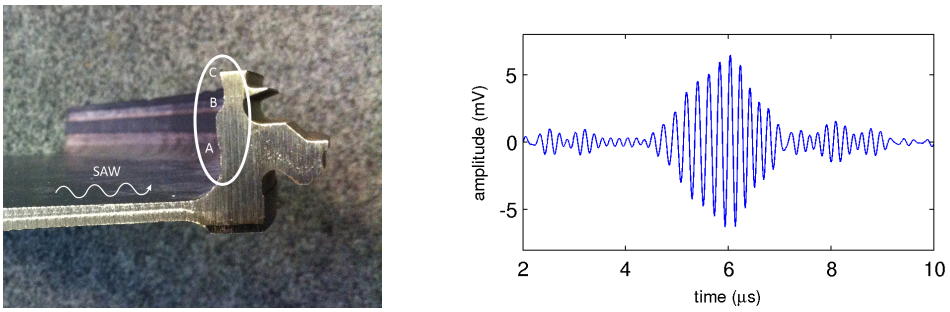

(a) sample geometry (b) first-pass detection

Figure 7.18: The geometry of the sample (a) and the signal detected in the first-pass (b)

difficulties in the alignment of such a large sample with the limited-articulation fixed-mount optics.

The detection of geometry echoes was strongly affected by combined attenuation introduced by the carrier of the SA d-CHOT (section 6.4.2), high surface roughness and strong material attenuation. Figure 7.19 shows a comparison of the signal detected with SA CHOTs (5 MHz, 30,000 waveforms) and a wedge piezoelectric transducer (4 MHz, 1,000 waveforms) from the same area on the sample. The location of the wedge transducer was slightly closer to the feature 'C', at approximately 112 mm. The expected echo times of arrival from the marked profile features (figure 7.18a) are respectively indicated in the plots. The time arrivals from the same sample region differ in two cases according to the differences in position and detection arrangement of the coupled CHOTs and the wedge transducer. The result comparison between the inspections shows similarly-detected echoes by the CHOTs and the wedge transducer, in agreement with the test geometry. The lower SNR in the CHOTs signal and the presence of additional echoes however complicates signal interpretation compared to the wedge transducer and indicates corresponding operational challenges.

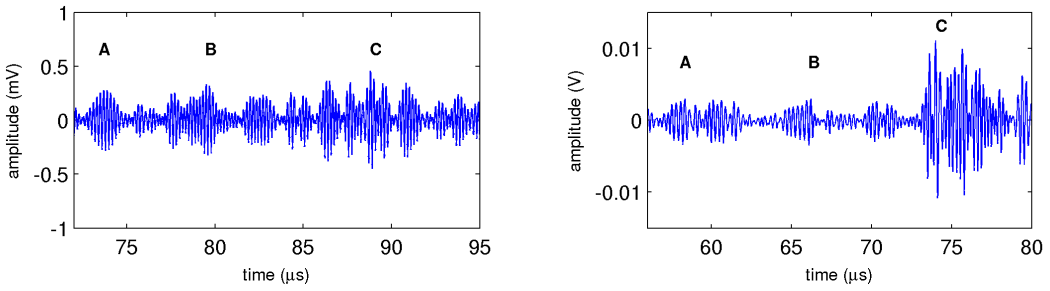

(a) 5 MHz coupled SA CHOTs: 30,000 waveforms

(b) 4 MHz wedge transducer: 1,000 waveforms

Figure 7.19: Signals detected from the area of interest on an aeroengine disk section

In the second test, the SA CHOTs were placed at an angle to the edge of the sample (figure 7.17b) operating in a pitch-catch configuration with reduced propagation distances, simpler geometry and excluding the effects of the d-CHOT carrier. The generation and detection powers were 0.47 mJ/pulse and 310 mW respectively. The signal detected by averaging over 15,000 waveforms is shown in figure 7.20, where the echoes from the top and the bottom edge of the sample can be easily identified (geometry shown in figure 7.17b).

The successful operation on this sample, particularly challenging for the d-CHOT, demonstrated its functionality on untreated rough surfaces. This, combined with additional ability to inspect non-reflective parts, minimises one and partly-overcomes another of the most common restrictions on the applicability of the optical techniques.

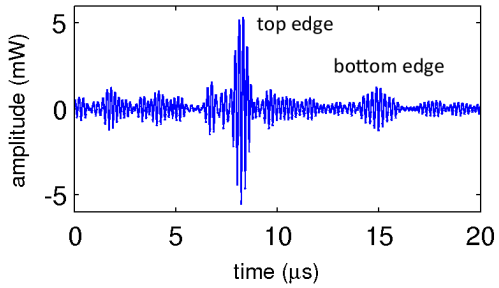

Figure 7.20: 5 MHz coupled SA CHOTs on a section of aeroengine disk in pitch-catch configuration: 15,000 waveforms

The inspection distances and operation in a pulse-echo configuration, however, proved challenging for the SA CHOTs, with the test results indicating the best performance is achieved in a pitch-catch arrangement. Additionally, the relative direction of the dominant roughness features (directional tool marks) and the d-CHOT steps had to be considered prior to transducer placement. Whereas the functionality of the d-CHOT was maintained when transducer features were parallel to the tooling grooves, it was compromised when used with the orthogonal orientation.

7.3 Additional capabilities

7.3.1 Active structural health monitoring (NDT inspection)

The stationary locations of the transducers provide a fixed reference point on the sample that could be used to perform high-fidelity monitoring of the region within the transducer coverage. This allows CHOTs to be considered for structural-health monitoring applications, in particular of components where the location with high probability of fracture is known apriori.

The concept is demonstrated using coupled 4 MHz OS CHOTs on an Al sample in a pulse-echo configuration. A surface defect in the form of a line/slot perpendicular to the propagating wavefront was gradually introduced into the sample to simulate the growth of the flaw. The process was performed manually using an engraving tool, and the sample in its holder had to be removed from the system. After the flaw was introduced, the sample was returned and the signal recorded. The test was performed at 0.47 mJ/pulse generation energy, 110 mW probing power, and averaging 1,000 waveforms.

Figure 7.21 shows the signals recorded in the absence of the defect and after a sufficiently-deep flaw was introduced. The echoes corresponding to the sample geometry and the region of interest are marked accordingly. The presence of an additional echo in the ROI is indicative of the

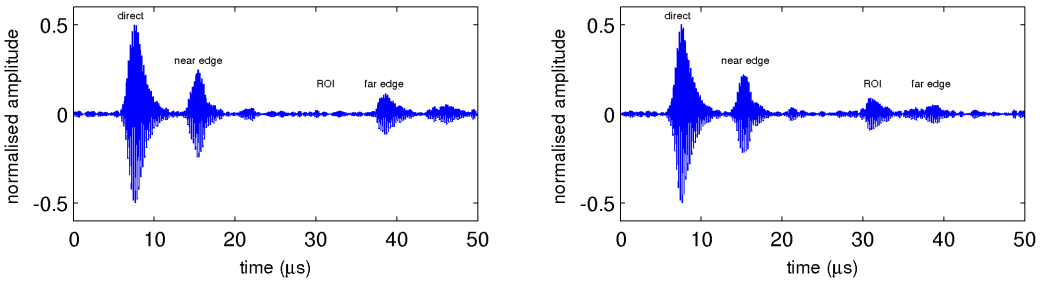

(a) Existing sample geometry

(b) Appearance of flaw

Figure 7.21: Signals from coupled 4 MHz OS CHOTs in a pulse-echo configuration on Al sample before (a) and after (b) the introduction of the defect in the region of interest.

surface flaw. Besides indicating the defect initiation, by monitoring the amplitude of this echo over time, the growth of the defect can be assessed and its rate determined for condition monitoring. Figure 7.22 shows two examples of analysing the recorded data for this purpose – by monitoring the increase of the echo amplitude (figure 7.22a), and using a differential B-scan (figure 7.22b) where the difference of each successive measurement with the baseline signal is plotted against time-of-flight (sample location) and time of inspection (defect depth).

The angular deviation of the introduced flaw during the test can be seen to reduce the echo amplitudes in some measurements. Additionally, despite the fixed physical alignment, the phase-sensitive differential detection was not optimal in this case: the removal of the sample combined with partial illumination of the CHOT resulted in small phase shifts of the static geometry echoes

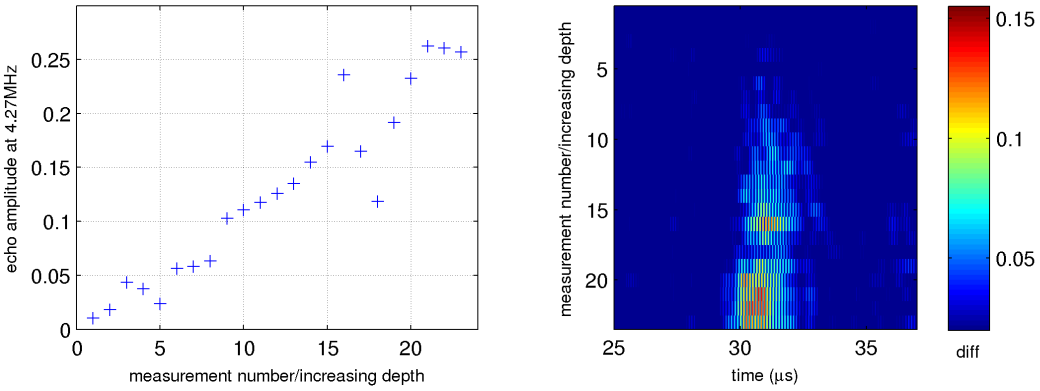

(a) Flaw echo amplitude (normalised)

(b) Differential detection (only ROI shown)

Figure 7.22: Condition monitoring with coupled 4 MHz OS CHOTs on an Al sample, demonstrating the initiation and growth of the flaw.

making them appear in the differential signal. This can be avoided using a top-hat profile illumination covering the whole area of the CHOT, and by monitoring only the region of interest.

The experiment demonstrated the capability of the endoscopic CHOT system for active structural health monitoring by detection of the initiation and growth of the simulated surface flaw over time, as well as the high repeatability of inspection expected from the fixed-transducer placement.

7.3.2 Automation and moving samples

The benefits of the non-contact excitation and fixed locations of the CHOTs on the sample enable inspection of the moving parts, allowing potentially-automated continuous-pass inspection.

The concept was demonstrated using one of the controlled Al sample with slots (section 7.1) mounted on a horizontal translation stage. The illumination from the endoscopic pulser was initially aligned with 4 MHz coupled OS CHOTs on the sample, and fixed. The sample was then alternately moved out of/back into the illuminated zone, repeating the process and monitoring the live signal on the oscilloscope at the same time. Figure 7.23 displays the video time-frames illustrating the experimental arrangement.

The detected signal corresponded to the sample geometry shown in figure 7.2a where the extra echo indicated the presence of the slot. As the CHOTs moved into the corresponding generation and probing beams, the signal gradually appeared on the oscilloscope, disappearing as gradually when the sample was moved out. The response speed of the system depended both on the sample velocity and the number of required trace averaging.

Although the signal was not recorded, the experiment showed practical capabilities of the system for defect detection on the samples in motion, and the ease of the inspection. It has to be said that the detection/appearance of the slot echo depended on the speed of inspection and signal averaging (SNR).

7.4 Summary

The practical capabilities of the endoscopic CHOT system to perform ultrasonic inspection were investigated on a set of controlled samples and representative industrial parts, using the OS and the developed SA CHOTs.

The detection of the rectangular-profile slots of depths down to $\Lambda_{SAW}/2$ by the 4 MHz OS CHOTs in pulse-echo configuration was successfully performed on controlled Al samples and Al-alloy industrial calibration plate with complex grain structure and at large propagation distances. In both cases the results from a comparable inspection performed with conventional 4 MHz wedge PZT transducer were presented.

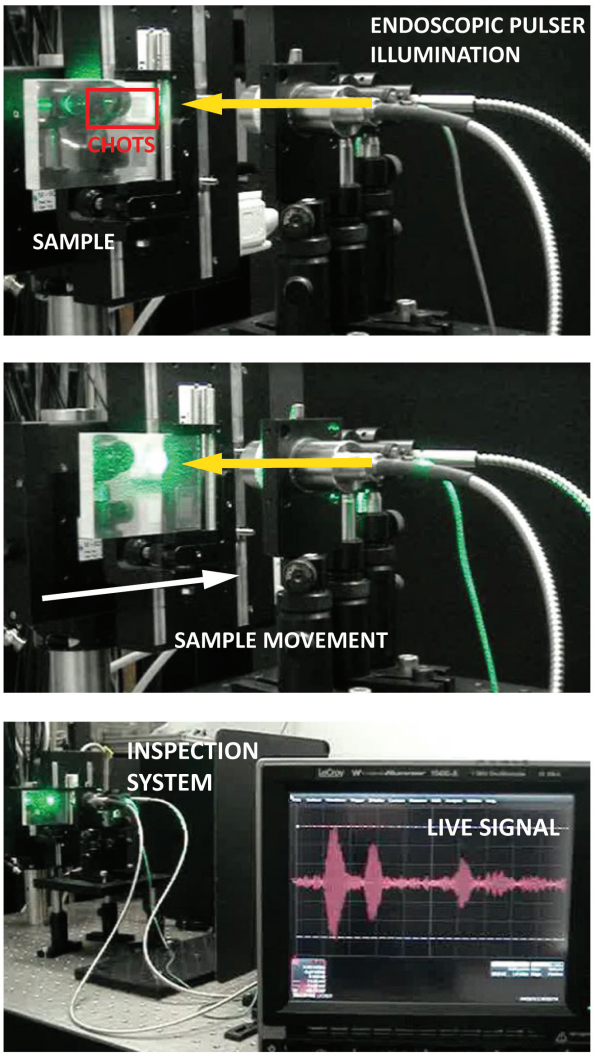

Figure 7.23: Video frames showing inspection of an Al sample in motion

Although providing lower SNR than the wedge transducer, the CHOTs demonstrated their ability to fulfil the required inspection, producing easy-to-interpret A-scans of a conventional nature with the additional benefit of self-calibration. One difference from the wedge transducer inspection, evident in the A-scans, is the presence of the rearward-travelling wave that may cause unwanted back reflections, which could complicate signal interpretation depending on sample geometry. This effect is reduced when the g-CHOT is used with a carrier, and enables operation of the coupled CHOTs with reversed transducer placements, shown to be beneficial during the use of the SA CHOTs.

The acoustic fields generated by the g-CHOT and the wedge transducer on the calibration plate were visualised, and a detailed scan of the g-CHOT field in the area of interest demonstrated

wave interaction with the slots. Despite evidently-lower magnitudes of the surface displacement produced by the g-CHOT, both fields displayed similar diffraction effects upon reaching the slots. The presence of the side lobes in the g-CHOT field appeared to produce additional reflections from the sides of the narrow sample, potentially contributing to the reduction in the SNR of detected signal, and indicating factors for additional consideration.

The SA CHOTs displayed limited inspection functionality in the pulse-echo arrangement with significant echo attenuation caused by the presence of the d-CHOT carrier, making pulse-echo inspection with the SA CHOTs impractical (for the current fabrication and carriers). However, the pulse-echo operation with reversed transducer placements and modified g-CHOT produced rather satisfactory results on a challenging sample. The best performance by the SA CHOTs was demonstrated in a pitch-catch configuration with clear echo resolution.

The pulse-echo operation on the blade-root section displayed good correlation of detected signal with the complex geometry of the sample profile. However, a further study is needed to determine the practical limitations with regard to the resolution of the closely-located sample features, considering the extended wave-packet duration in time domain. Also, the tests in this work employed limited TOF amplitude-based feature detection, whereas the use of more sophisticated signal processing could prove beneficial.

The test performed on the blade root section showed CHOTs operation on the curved surfaces (challenging for the rigid PZT transducers and EMATs), at the same time demonstrating the effectiveness of the SA d-CHOT and the associated effects of curvature onto the returning optical field. Despite the field spread and astigmatism resulting in low signal return, the functionality of the d-CHOT was not impaired, although a more accurate alignment was required. Depending on the surface curvature at the point of transducer attachment, the divergence/convergence of the returning beam would place restrictions on operational stand-off distance. It is possible to suggest that provided the shape of the component at the place of attachment is known, the design of the d-CHOT transducer can accommodate optical correction of the reflected beam. The test additionally confirmed the feasibility of operation in the reversed pulse-echo arrangement with the modified SA g-CHOT.

Considering another aspect of testing, one of the most restrictive for optical detection, successful d-CHOT operation was demonstrated on samples with varying degree of surface roughness – from highly-polished controlled Al samples, well-polished Al-alloy calibration plate to the rough surface of the blade root, and even on the most optically-challenging untreated machined surface of the aeroengine disk. The surface conditions of the two representative aeroengine parts, not acceptable for testing with the OS d-CHOTs, provided excellent demonstration of the advantages of the developed SA d-CHOTs, easing operational requirements to surface finish and extending the range

of the testable parts and CHOTs applicability.

An additional benefit provided by the SA d-CHOTs, and evident from the test of the disk section, is the ability to operate independently of the sample surface reflectance. The reflective surface required for optical detection is introduced with the d-CHOT carrier, where the scattering effects are further determined by the carrier roughness as shown in section 6.2.4.

Relatively low SNR produced on industrial samples can be attributed to a number of factors: generation efficiency of the g-CHOT, diffracted-field distortion by the surface curvature, roughness-caused scattering, wave attenuation due to material properties and grain structure (combined with large propagation distances), and some difficulties in alignment of the limited-articulation fixed-mount optics. The improvement of signal levels can be expected from increase of the g-CHOT generation efficiency by tailored selection of transducer material for material of the sample, corresponding design of the d-CHOT to provide optical correction of the curvature-distorted field, reduction of the d-CHOT carrier roughness, and increase in the probing power.

Additionally-investigated CHOTs' capabilities included the application to the structural-health monitoring and inspection of the samples in motion. The condition-monitoring potential was demonstrated by observing the expected indications of the flaw initiation and growth displayed in a sequence of signals recorded from the coupled CHOTs as the simulated surface flaw was introduced on Al sample. Placing the sample on the translation stage and monitoring live signal as the sample was moved in and out of alignment with laser illumination showed practical capabilities of the system for defect detection on moving parts (challenging for contact methods), and potential for an automated inspection.

Overall, the first evidence of the CHOTs NDT and SHM capabilities was presented. The promising results were shown by the SA CHOTs on the representative aeroengine parts that varied in material, geometry and surface conditions. The tests demonstrated the feasibility of operation on the target industrial components and indicated further areas for improvement.

The displayed capabilities of the developed SA CHOTs on rough surfaces, combined with the ability to inspect non-reflective parts, address both of the most serious restrictions on the applicability of the optical techniques in general, and broaden the application range of CHOTs in particular.

Chapter 8

Conclusions and suggestions for further work

This work presented the instrumentation of the endoscopic CHOTs pulser combining the use of the Cheap Optical Transducers (CHOTs) with fibre-optic light delivery in a compact, portable and non-contact ultrasonic inspection system.

The work addressed four main areas associated with the development of the inspection system for practical applications: the fibre-optic instrumentation, the upgrade of the fabrication method to enable application of the transducers on large, curved components in-situ and complement the endoscopic pulser for field applications, characterisation of the transducer performance to enable comparison with conventional techniques and provide quantitative evaluation of the practical system capabilities, and demonstration of the NDT potential of the system on representative industrial samples.

8.1 Conclusions and main contributions of work

The main contributions of this work listed below achieved but are not limited to the initially set goals, as the secondary finding opened new directions for study and provided additional capabilities not anticipated at the start.

- The optical fibres were combined with the CHOT operation and composed a fully-optical ultrasonic inspection system able to deliver laser-ultrasonic testing to components out of direct line of sight, or with complex access. The compact optical arrangement and environmental robustness offered by the use of CHOTs removes the need for excessive auxiliary

optics required by most laser ultrasonic techniques to form the required ultrasonic source or for environmental stabilisation of the interferometric detection. This maximised the benefits of fibre-optic delivery by minimising the size of the instrumentation required to access the sample.

- Portable CHOTs were produced using film carriers to allow transducer fabrication in controlled laboratory environment with further transfer and delivery to the component in-situ to complement the endoscopic pulser for in-service testing. The portability of the transducer overcomes the restrictions on the size and shape of the test samples, imposed by the laboratory-based direct on-sample fabrication used previously. Additionally, the use of the carriers demonstrated greater tolerances of optical detection to surface roughness than the OS d-CHOT, expanding the range of CHOTs applicability. More generally, it overcomes some of the main barriers of transition of the optical techniques to industry by reducing the requirements to the surface finish of the test part and enabling operation on non-reflective samples.

- Quantitative evaluation of the transducer performance was carried out, introducing the means for comparison not only between the fabricated CHOTs but, more generally, with other conventional methods and lending support for practical transducer applications.

- The potential of the endoscopic CHOTs for non-destructive testing was demonstrated by detection of surface features and sample geometry on representative industrial samples. Additionally, the benefits of the developed SA CHOTs became evident by retaining the d-CHOT functionality on an unpolished, non reflective surface of the aeroengine disk with visible tool marks, which other optical detection techniques, including the OS d-CHOTs would find extremely challenging.

Limitations of study

The investigations in this thesis were concerned with demonstration of the CHOTs capabilities in particular context, where the study performed was limited to the use of the surface acoustic waves, metal samples, and detection of surface-breaking defects, normal to the propagating wavefront. The range of frequencies was 4 and 5 MHz, typical for type of inspection used for aeroengine blade testing.

The combined diameters of the fibres used in the endoscopic pulser and the size of the collimating optics currently exceed the acceptable size of the instrumentation able to use endoscopic access inside the engine.

The fabrication method used to produce the SA CHOTs is currently limited to the frequencies below 20 MHz (for the SA g-CHOT, on aluminium). This limitation stems partially from the presence of adhesive on the surface of the carrier, that excludes the ability to use photolithographic fabrication, and partially from the use of the metal mask for material deposition, frequencies of which are restricted by the physical ability to fabricate such finely-spaced slots in a thin metal sheet.

The use of the developed SA CHOTs in pulse-echo configuration has limited capabilities due to high attenuation of the propagating wave by the carrier of the d-CHOT.

8.2 Thesis summary and key findings

Background

The use of the endoscopic CHOTs pulser was proposed in Chapter 1 to address the challenges of in-situ testing of the aeroengine components by combining two of the routinely-used inspection techniques with the addition of non-contact laser-ultrasonic operation. The motivation for and the context in which the current work is viewed were described in the first two chapters, including the review of the common inspection practices used in aerospace sector, the role of the ultrasonic inspection in NDT with particular focus on the use of the Rayleigh waves. The common techniques for ultrasonic generation and detection were reviewed where particular attention was given to the laser-ultrasonic generation and detection methods for surface acoustic waves and previous work in the field aimed to increase the efficiency of optical generation and detection.

This was followed by the description of CHOTs operation principles, design and practical considerations for selection of transducer and relevant instrumentation parameters based on the previous CHOTs development and within the context of the practical application. Special attention was paid to the review of the established direct on-sample fabrication methods restricting transducer-to-sample application to the laboratory environment. More recently developed laser-based methods allowing fabrication of the transducers outside of the laboratory setting and on-site were also reviewed, and the concept of the portable CHOT using film carriers proposed (Chapter 3).

Instrumentation

Chapter 4 presented the endoscopic pulser instrumentation, with the review of the system structure and the role of its elements, separating them based on the performed function into the generation, probing and detection channels. The properties and characteristics of the elements were presented.

The concept for further system miniaturisation based on the reduction of the number of fibres used to deliver the illumination to the test component was proposed. The use of the same fibre bundle for delivery of the probing illumination and collection of the diffracted light was investigated, with the results of the preliminary work demonstrating the ability to use a single core of the bundle for delivery of probing illumination. Practical system use considerations and suggestions for further system automation were presented.

Fabrication of portable CHOTs

Two concepts to create portable CHOTs using film carriers were investigated in Chapter 5, describing the developed fabrication processes and the corresponding results and challenges. The first concept consisted of creation of the CHOT pattern using sacrificial layers that can be chemically removed releasing the transducer on a carrier film. The second concept involved the use of the commercially-available adhesive transfer tapes to create self-adhesive CHOTs. Both concepts produced the CHOTs on film carriers, with the first type being transferable and requiring a couplant, and the second type being self-adhesive without the need for surface preparation. An important capability of the g-CHOT was introduced by the use of the adhesive transfer films. It allowed the transducer to be transferred onto the sample with the layer of adhesive by removal of the carrier film after transducer attachment. This ability was later shown to compensate for the attenuation introduced by the SA carrier and enabled the use of the SA CHOTs in pulse-echo configuration (Chapter 7). The functionality of the developed portable CHOTs was tested and the ultrasonic generation mechanism confirmed in Chapter 6.

Performance characterisation

The characterisation of the CHOTs operation, specific capabilities and limitations were discussed in Chapter6 for both types, the OS and the SA CHOTs, and where possible compared between them. The calibration curves were obtained for the transducers describing their response to the corresponding inputs and providing the means for transducer comparison, and acoustic fields visualised and compared.

Considerably higher generation efficiency was observed from the SA g-CHOT that was attributed to the presence of the carrier providing the surface constraint. Although it was partially confirmed, further work is required to model the ultrasonic source. The comparison of the generated acoustic fields showed that the use of the carrier did not alter the structure or the directivity of the generated wavefront. Additional functionality of the SA g-CHOT was demonstrated in a modified state – when transducer was transferred to the sample and the carrier film removed. Similarly, the structure of the generated acoustic field was not changed by the removal of the carrier,

although the generation efficiency was reduced. The SA g-CHOT tests performed over time and in continuous operation showed the temperature effects from the laser illumination or possible disintegration of adhesive over time did not affect the stability of performance or transducer bonding integrity.

As the choice of the g-CHOT material is customised to provide the most efficient generation on material of the sample, the effect of transducer material onto generation efficiency was investigated. It showed the discrepancies with the expected performance when evaluated simply based on the differences in absorption between the CHOT and the substrate material. The development of the CHOT generation model would be required to enable material selection for the best generation efficiency on particular substrates.

The OS d-CHOT demonstrated significantly higher detection sensitivity than the SA d-CHOT that was attributed to the higher light return from the OS d-CHOT, confirmed by sensitivity tests to the probing power. Despite the poorer sensitivity of the SA d-CHOT, its combination with more efficient generation by the SA g-CHOT in the coupled system demonstrated performance comparable with the coupled OS CHOTs in the pitch-catch configuration.

The areas anticipated to be affected by the introduction of carriers were investigated and associated effects quantified. The main impact potentially affecting the use of the SA CHOTs for NDT application is the attenuation of the propagating SAW by the SA carrier of the d-CHOT in the pulse-echo configuration, with significant amplitude reduction past the transducer, and some wave velocity alteration. Comparison of the acoustic fields propagating across the surface without the SA carrier with those where the carrier was placed in the path of the wavefront allowed determine the attenuation of the film. It similarly showed that if the transducer carrier is removed with the layer of adhesive remaining on the sample, the attenuation is significantly reduced. This provided the means to enable operation of the SA CHOTS in pulse-echo configuration by reversing their relative positions and using the g-CHOT in its modified state, with the carrier removed.

Separately, the comparison of the SAW frequency spectra before and after the entry to the carrier (measured with a vibrometer) displayed the split of the wave energy between two distinct frequency components propagating with different velocities, and repeated in the spectrum of signal detected with the d-CHOT. The displayed behaviour could be explained by possible dispersion and reflections within the carrier region (confirmed in later investigations), however a significant amount of experimental and modelling work would be further required to confirm the cause.

Comparative tests of the OS/SA d-CHOTs on rough aluminium samples demonstrated the extended tolerance of the SA d-CHOTs to the surface roughness expanding the applicability of CHOTs to include the range of parts with surface quality previously unacceptable for detection with OS d-CHOTs.

NDT capabilities

The feasibility to use the endoscopic CHOTs pulser for practical NDT applications was demonstrated on a number of controlled and representative industrial samples, where the OS and the SA CHOTs were used in a coupled configuration in a pulse-echo and a pitch-catch arrangement (Chapter 7). The defect detection capabilities were shown by both OS and the SA CHOTs, and comparison with the wedge transducer provided.

The functionality of the SA CHOTs was shown on the sections of the blade root and the aeroengine disk with surface conditions challenging to conventional optical techniques, and even the OS d-CHOTs, providing evidence of the ability to inspect actual parts and the suitability of the CHOTs use for the considered inspection task. Potential use of the system for active structural health monitoring and inspection of samples in motion was demonstrated.

8.3 Suggestion for further work

A number of investigations performed in this work indicated the need for development of a comprehensive model of the g-CHOT ultrasonic generation. The model development was started in Comsol, and when completed should confirm the mechanism of the enhanced ultrasonic generation observed from the SA g-CHOT and would help to model the effect of the carrier. It would additionally enable determination of the most suitable material of the g-CHOT for particular substrate. The effects of the carrier onto the frequency and velocities of the propagating wave should be investigated further.

Although the SA CHOTs performed rather well on the industrial sample, further work could be performed with regard to selection of the carrier and its parameters to further enhance ultrasonic generation and increase the light return from the d-CHOT.

The design of the d-CHOT can be customised to correct the distortion of the returning beam in order to increase signal levels.

Other methods to fabricate the transducers can be investigated to expand their capabilities.

To support the transition of the system to practical use, the suggested automation of alignment should be performed with further system miniaturisation. Further investigation of the started work on the joint use of the same fibre bundle to reduce the diameter of the endoscope can provide the basis for future prototype designs. The use of the robotic and crawling systems can be combined with the CHOTs or CHOTs' endoscopic pulser to deliver the transducers to test components and guide the endoscope, or combined with the operation of the crawling laser welding systems for inspection and repair of the part.

Although the use of the system was described within the context of NDT and simple pass/fail

detection, other inspection techniques can be investigated such as coating thickness monitoring or chemical testing.

8.4 Final remarks

The evidence provided in this work supports the concept of the practical application of the endoscopic CHOTs system for industrial NDT applications, with the work carried out to enable the transition of the technique to industry. It is hoped that further development of the system will be realised in a prototype and tested in an aeroengine environment and the work presented here will encourage confidence in further adoption and development of optical inspection methods in industry.

The work in this thesis has been presented at a number of academic conferences and industry-organised events, and has been published.

List of delivered presentations

- 2013, 2014, 2014: IOP Anglo-French Physical Acoustics Conference (AFPAC)
- 2013, 2014: IOP Optics + Ultrasound day conference, UON
- 2013: 5th International Symposium on NDT in aerospace, Singapore
- 2015: RCNDE Technology transfer event, Bristol
- 2015: Presentation at Rolls-Royce plc, Derby
- 2015: The 4th International Symposium on Laser Ultrasonics and Advanced Sensing, Chicago

Industrial and public engagement events

- 2014, 2015: RCNDE Technology Transfer Events
- 2014: Farnborough International Airshow: demonstration of the developed SA CHOTs in the Innovation Zone as part of the UON IAT display.

Publications

- 'Fabrication of Cheap Optical Transducers (CHOTs) on film carriers for in-situ application and generation of surface acoustic waves', Journal of Physics: Conference Series AFPAC 2014
- 2013 'Integrative solution for in-situ ultrasonic inspection of aero-engine blades using endoscopic Cheap Optical Transducers (CHOTs)', The e-Journal of Nondestructive Testing, ndt.net

Awards

The paper presented at the 5th International Symposium on NDT in aerospace received The Best Paper Award.

Appendix A

Signal acquisition: elements characteristics

A.1 Photodiode in detection channel

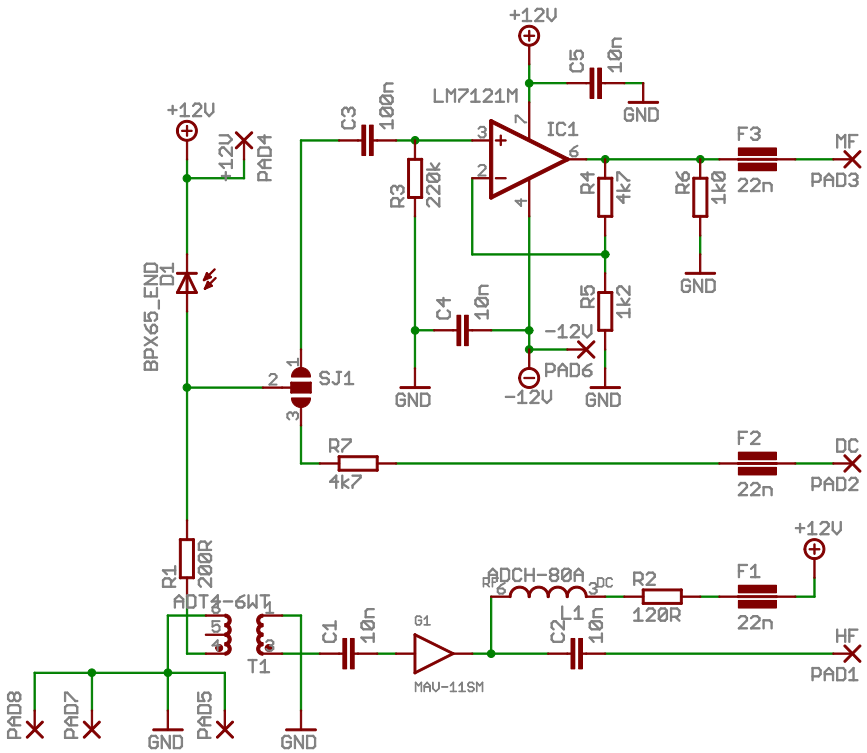

A.2 Filter characteristics

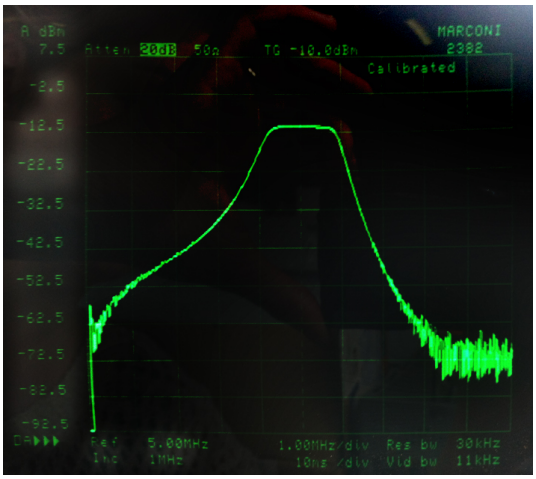

Figure A.1: Characteristics of the 5MHz BPF used in detection channel.

A.3 Amplifier characteristics

(a) Before amplifier

(b) After amplifier

Figure A.2: Determination of gain from two Minicircuits ZFL500-LN amplifiers used with the CHOT system.

Appendix B

Controlled aluminium samples: rectangular slot characterisation with white light interferometry

SAMPLE 1 DATA

X Profile

Rq	0.00 mm
Ra	0.00 mm
Rt	0.01 mm
Rp	-0.48 mm
Rv	-0.50 mm

Angle	-
Curve	-0.68 m
Terms	None
Avg Ht	-0.49 mm
Area	-0.31 mm2

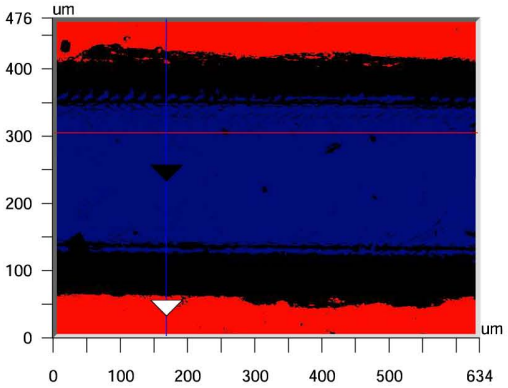

Y Profile

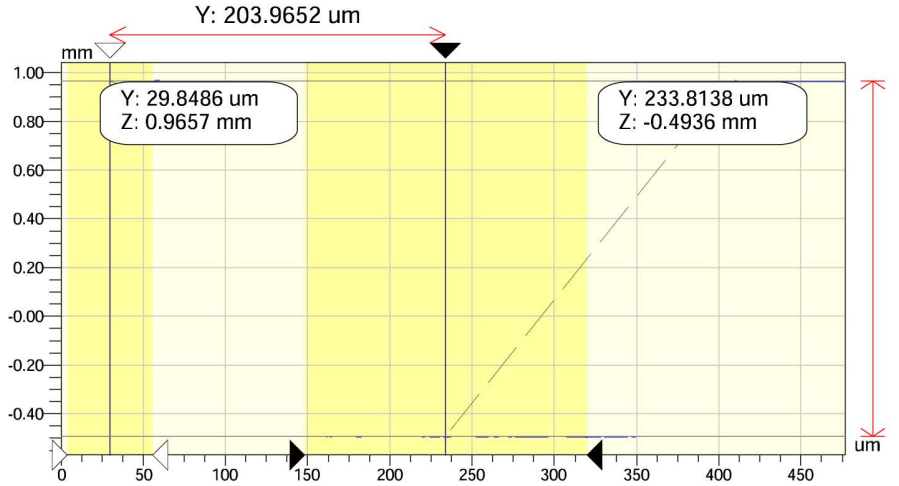

X	166.80	-	-	um
Y	304.81	-	-	um
Ht	-0.49	-	-	mm
Dist			-	um
Angle			-	°

Rq	0.62 mm
Ra	0.52 mm
Rt	1.46 mm
Rp	0.97 mm
Rv	-0.49 mm

Angle	-1.43 rad
Curve	1.76 mm
Terms	None
Avg Ht	-0.16 mm
Area	-0.03 mm2

Title:

Note:

SAMPLE 2 DATA

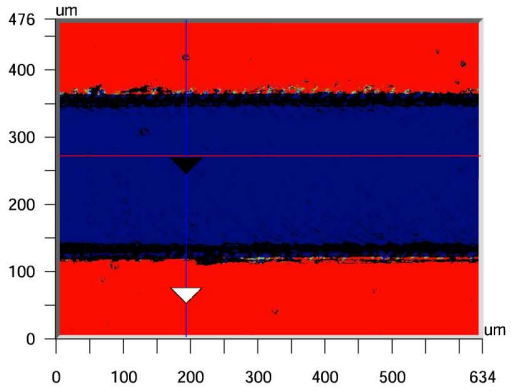

X Profile

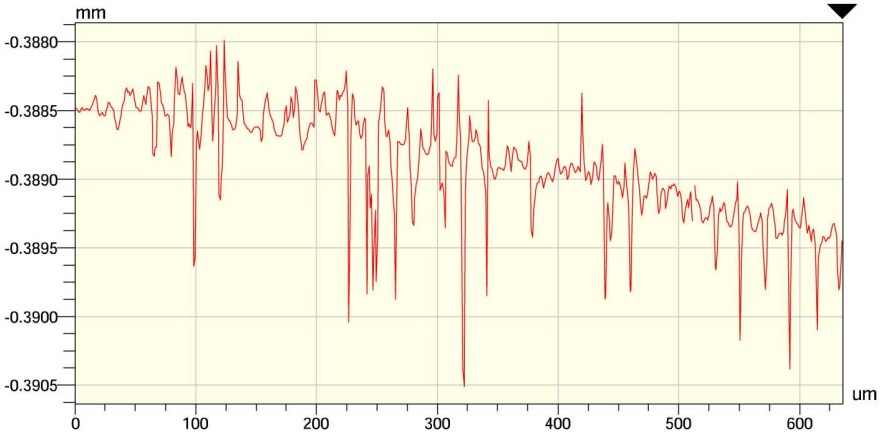

Rq	0.00 mm
Ra	0.00 mm
Rt	0.00 mm
Rp	-0.39 mm
Rv	-0.39 mm

Angle	-1.53 mrad
Curve	-0.35 m
Terms	None
Avg Ht	-0.39 mm
Area	-0.25 mm2

Y Profile

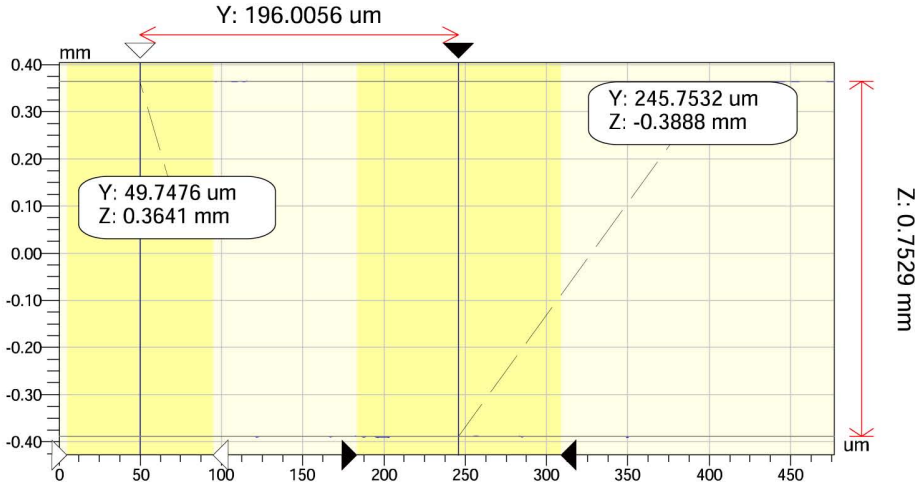

X	191.63	-	-	um
Y	272.05	-	-	um
Ht	-388.70	-	-	um
Dist			-	um
Angle			-	°

Rq	0.37 mm
Ra	0.36 mm
Rt	0.76 mm
Rp	0.37 mm
Rv	-0.39 mm

Angle	-1.32 rad
Curve	-4.18 mm
Terms	None
Avg Ht	-0.10 mm
Area	-0.02 mm2

Title:

Note:

SAMPLE 3 DATA

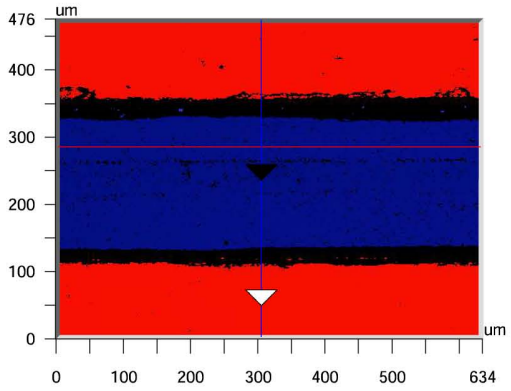

X Profile

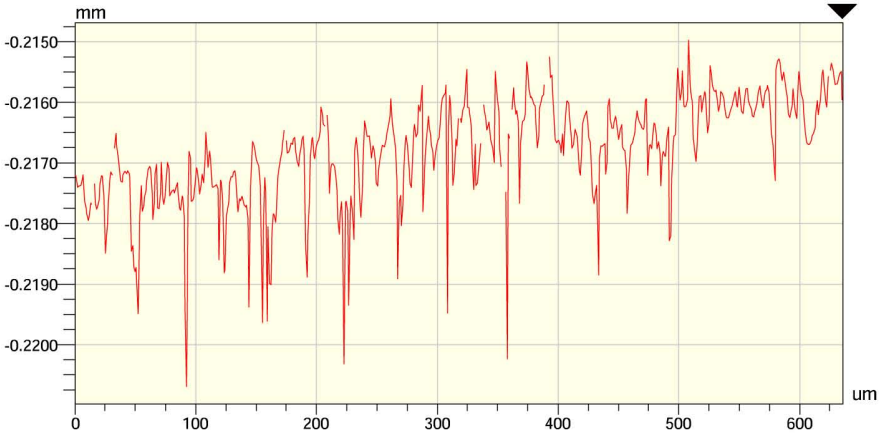

Rq	0.00 mm
Ra	0.00 mm
Rt	0.01 mm
Rp	-0.21 mm
Rv	-0.22 mm

Angle	1.97 mrad
Curve	-1.20 m
Terms	None
Avg Ht	-0.22 mm
Area	-0.14 mm2

Y Profile

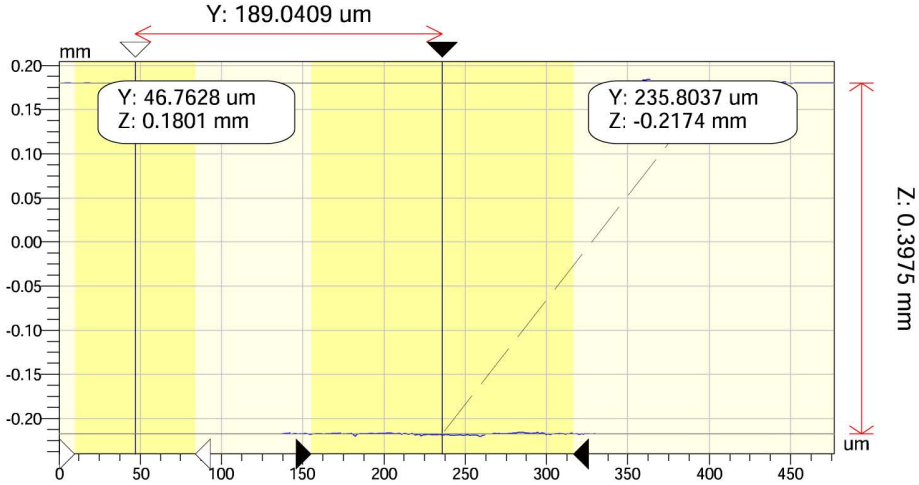

X	304.81	-	-	um
Y	284.96	-	-	um
Ht	-215.89	-	-	um
Dist			-	um
Angle			-	°

Rq	0.19 mm
Ra	0.19 mm
Rt	0.40 mm
Rp	0.18 mm
Rv	-0.22 mm

Angle	-1.13 rad
Curve	0.18 mm
Terms	None
Avg Ht	-0.06 mm
Area	-0.01 mm2

Title:

Note:

Mag: 10.0 X
Mode: VSI

Surface Data

Date: 26/09/2012
Time: 09:51:32

SAMPLE 2 SURFACE DATA

Surface Statistics:

Ra: 206.48 nm
Rq: 288.65 nm
Rz: 3.99 um
Rt: 5.69 um

Set-up Parameters:

Size: 284 X 197
Sampling: 992.88 nm

Processed Options:

Terms Removed:
None
Filtering:
None

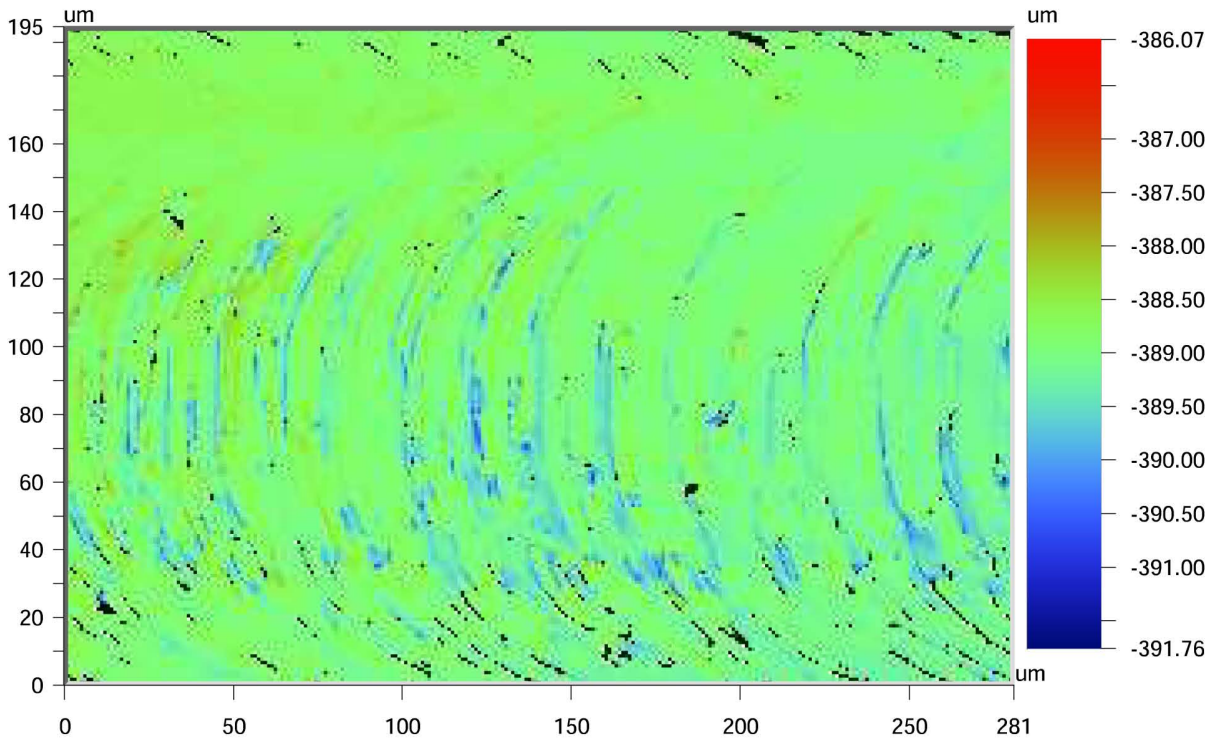

Title: Subregion
Note: X offset:191 Y offset:148 Resolution:

Appendix C

Industrial Al-alloy calibration sample

C.1 Measured profiles of the slots

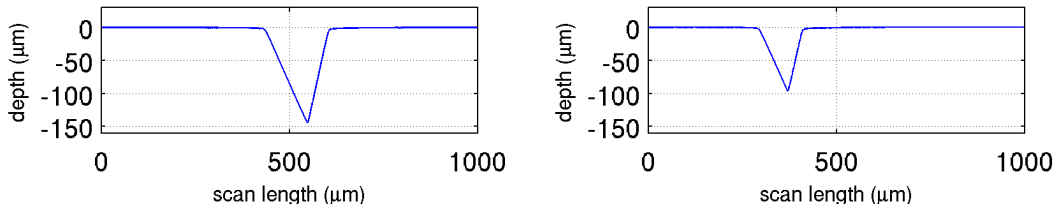

(a) farthermost slot (b) nearest slot

Figure C.1: Profiles of the EDM slots on calibration Al-alloy sample measured with surface profiler; due to the aspect ratios of the slot profiles, the stylus could not provide the full depth measurement.

C.2 Optical gain data for transducer acoustic field scan

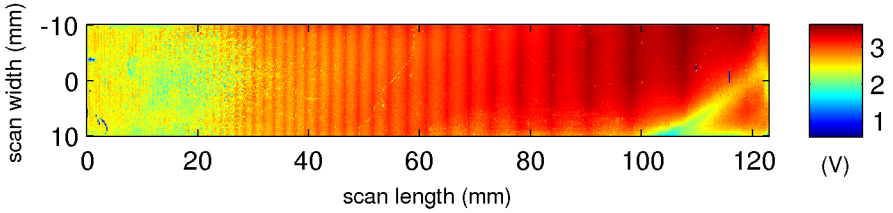

Figure C.2: Optical gain data from the acoustic field scan of the 4 MHz wedge transducer.

C.3 Lamb wave dispersion curves for aluminium

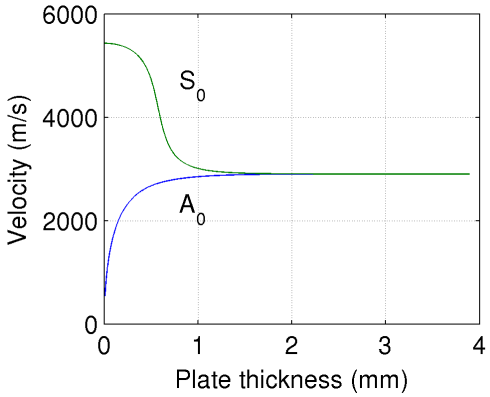

Figure C.3: Lamb wave velocities of the fundamental zero-order modes for aluminium.

Bibliography

[1] T. Stratoudaki *et al.*, "Cheap optical transducers (CHOTs) for narrowband ultrasonic applications," *Measurement Science and Technology*, vol. 18, pp. 843–851, 2007.

[2] Federal Aviation Administration, *The Aviation Maintenance Technician Handbook: General (FAA-H-8083-30)*, ch. 8. Oklahoma, USA: United States Department of Transportation, 2008.

[3] Federal Aviation Administration, AFS-640, *Acceptable Methods, Techniques, and Practices: Aircraft Inspection and Repair (Advisory Circular 43.13-1B)*, ch. 5. Oklahoma, USA: United States Department of Transportation, 1998.

[4] Civil Aviation Authority, *CAP 562, Civil Aircraft Airworthiness Information and Procedures*, ch. F. Norwich, UK: The Stationery Office, 2013.

[5] Y. Bar-Cohen, "Emerging NDE technologies and challenges at the beginning of the 3rd millennium," *e-Journal of Nondestructive Testing, ISSN 1435-4934*, vol. 5, no. 1, 2000.

[6] J. R. Barton and F. N. Kusenberger, "Fatigue damage detection," in *Metal Fatigue Damage: Mechanisms, Detection, Avoidance, and Repair*, pp. 123–227, Philadelphia: American Society for Testing and Materials, 1971. STP 495.

[7] M. Siegel, "Robotic assistants for aircraft inspectors," *IEEE Instrumentation & Measurement Magazine*, vol. 1, no. 1, pp. 16–30, 1998.

[8] J. Shang *et al.*, "Design of a climbing robot for inspecting aircraft wings and fuselage," *Industrial Robot: An International Journal*, vol. 34, no. 6, pp. 495–502, 2007.

[9] Y. Bar-Cohen and P. Backes, "Scanning large aerospace structures using open-architecture crawlers," in *National Space and Missile Materials Symposium*, (San Diego), 2000.

[10] M. Choquet *et al.*, "Laser ultrasonic inspection of the composite structure of an aircraft in a maintenance hangar," *Review of Progress in Quantitative Nondestructive Evaluation*, vol. 14, p. 545, 1995.

[11] O. Pettilon *et al.*, "Applications of laser based ultrasonics for aerospace industry," in *ECNDT 98*, e-Journal of Nondestructive Testing, ISSN 1435-4934, 1998.

[12] T. L. Adair *et al.*, "Blending borescope inspection (BBI) maintenence service equates to cost savings," in *AUTOTESTCON '98. IEEE Systems Readiness Technology Conference*, pp. 486–493, 1998.

[13] Rolls-Royce plc, "A method of inspecting and/or repairing component and a device for inspecting and/or reapairing a component," 05 2011. Inventors: L C Jones and H Litzenberg, Patent GB 2474834 A.

[14] W. Tian, M. Pan, and D. Chen, "Integrative in-situ detection of defects in aeroengine blades combining borescope and Eddy current techniques," in *18th world conference on on nondestructive testing*, (Durban), e-Journal of Nondestructive Testing, ISSN 1435-4934, 2012.

[15] Y. Xiong, D. Dong, and J. Duan, "The development and manufacture of fixed ultrasonic inspection reference reflectors and transducers for compressor blade dovetails," in *Smart materials, structures & NDT in aerospace, NDT in Canada 2011*, (Montreal), e-Journal of Nondestructive Testing, ISSN 1435-4934, 2011.

[16] C. B. Scruby and L. E. Drain, *Laser ultrasonics: Techniques and Applications*. Bristol, UK: Adam Hilger, 1990.

[17] B. Park *et al.*, "Laser ultrasonic imaging and damage detection for a rotation structure," *Structural Health Monitoring*, vol. 12, no. 5-6, pp. 494–506, 2013.

[18] M. Ochiai, "Development and applications of laser-ultrasonic testing in nuclear industry," in *1st International Symposium on Laser Ultrasonics: Science, Technology and Applications*, 2008.

[19] P. N. T. Wells, "Ultrasound imaging," *Physics in Medicine and Biology*, vol. 51, pp. 83–98, 2006.

[20] D. Miller *et al.*, "Overview of theraputic ultrasound applications and safety considerations," *Journal of Ultrasound in Medicine*, vol. 31 (4), pp. 623–634, 2012.

[21] H. Mulvana, S. Cochran, and M. Hill, "Ultrasound assisted particle and cell manipulation on-chip," *Advanced Drug Delivery Reviews*, vol. 65, pp. 1–11, 2013.

[22] R. G. Maev, *Advances in Acoustic Microscopy and High Resolution Imaging: From Principles to Applications*. Berlin: Wiley-VCH, 2013.

[23] J. D. Achenbach, *Wave Propagation in Elastic Solids*. Amsterdam; Oxford: North-Holland, 1975.

[24] P. A. Mante *et al.*, "THz acoustic phonon spectroscopy and nanoscopy by using piezoelectric semiconductor heterostructures," *Ultrasonics*, vol. 56, pp. 52–65, 2015.

[25] A. Minachi, P. D. Panetta, and S. Nakahama, "Turbine blades inspection using high frequency ultrasonic technique," in *AIP Conference Proceedings*, vol. 557, pp. 1634–1641, 2001.

[26] D. Ensminger, *Ultrasonics: Fundamentals, Technology, Applications*. New York: Marcel Dekker, 1988.

[27] "Tables of physical & chemical constants (16th edition 1995), 2.4.1 the speed and attenuation of sound." Kaye & Laby online, Version 1.0 (2005). www.kayelaby.npl.co.uk.

[28] I. A. Viktorov, *Rayleigh and Lamb waves: Physical Theory and Applications*. New York: Plenum Press, 1967.

[29] J. Blitz and G. Simpson, *Ultrasonic Methods of Non-Destructive Testing*, ch. 2, p. 23. Cambridge, UK: University Press, 1996.

[30] W. A. Grandia and C. M. Fortunko, "NDE applications of air-coupled ultrasonic transducers," in *IEEE Ultrasonics Symopsium*, vol. 1, pp. 697–709, 1995.

[31] J. Blitz and G. Simpson, *Ultrasonic Methods of Non-Destructive Testing*. Cambridge, UK: University Press, 1996.

[32] X. Zhao *et al.*, "Active health monitoring of an aircraft wing with embedded piezoelectric sensor/actuator network: defect detection, localization and growth monitoring," *Smart Materials and Structures*, vol. 16, pp. 1208 –, 2007.

[33] D. C. Wright *et al.*, "1000 gates - a novel approach and method for ultrasonic inspection of aero-engine disc forgings." Presentation at British Institute of NDT Conference, Telford, UK, 2013.

[34] M. G. Silk, "The determination of crack penetration using ultrasonic surface waves," *NDT International*, pp. 290–297, 1976.

[35] P. A. Doyle and C. M. Scala, "Crack depth measurement by ultrasonics: a review," *Ultrasonics*, vol. 16, pp. 164–170, 1978.

[36] B. G. Kim and S. Lee, "Direct and continuous measurement of depth-dependent reflection coefficients of Rayleigh waves for surface discontinuity: normal slot," *Journal of Acoustic Society of America*, vol. 104, pp. 2733–2740, 1998.

[37] J. A. Cooper *et al.*, "Surface acoustic wave interactions with cracks and slots: a noncontacting study using lasers," *IEEE Transactions on Ultrasonics,Ferroelectrics and Frequency Control*, vol. 33, no. 5, pp. 462–470, 1986.

[38] R. J. Blake and L. J. Bond, "A general model for Rayleigh wave-surface feature scattering problems," *Review of Progress in Quantitative Nondestructive Evaluation*, vol. 9, pp. 77–84, 1990.

[39] X. Jian, "Surface-breaking crack gauging with the use of laser-generated Rayleigh waves," *Journal of Applied Physics*, vol. 100, 2006. 064907; doi: 10.1063/1.2353892.

[40] B. Masserey and E. Mazza, "Ultrasonic sizing of short surface cracks," *Ultrasonics*, vol. 46, pp. 195–204, 2007.

[41] U. B. Halabe and R. Franklin, "Detection of flaws in structural members using spectral analysis of ultrasonic signals," *Nondestructive Testing and Evaluation*, vol. 15, no. 3-4, pp. 215–236, 1998.

[42] J. G. Rasmussen, "Ultrasonic inspection of turbine and compressor rotor blades for cracks and other flaws," *Nondestructive testing*, vol. 16 (3), pp. 228–236, 1958.

[43] J. G. Rasmussen, "Prediction of fatigue failuire using ultrasonic surface waves," *Nondestructive testing*, vol. 20 (2), pp. 103–110, 1962.

[44] B. Harris-Maddox, "Ultrasonic testing and flight safety," *Flight International*, vol. 83 (2817), pp. 330–331, 1963.

[45] B. Harris-Maddox, "The ultrasonic testing of B66 compressor blades," *Aircraft Engineering and Aerospace Technology*, vol. 35, pp. 293–296, 1963.

[46] Federal Aviation Administration, *The Aviation Maintenance Handbook: Powerplant (FAA-H-8083-32)*, ch. 10. Oklahoma, USA: United States Department of Transportation, 2012.

[47] Oklahoma State Univ Stillwater School of Mechanical and Aerospace Engineering, "A study of ultrasonics for flaw detection in turbojet engines," 1963. Retrieved from http://www.dtic.mil/get-tr-doc/pdf?AD=AD0436289.

[48] V. V. Kosachev, Y. N. Lokhov, and V. N. Chukov, "Theory of attenuation of Rayleigh surface acoustic waves on a free randomly rough surface of a solid," *Soviet Physics, Journal of Experimental and Theoretical Physics*, vol. 67, pp. 1825–1830, 1988.

[49] A. A. Maradulin and D. L. Mills, "Attenuation of Rayleigh surface waves by surface roughness," *Applied Physics Letters*, vol. 28, pp. 573–575, 1976.

[50] S. V. Biryukov *et al.*, *Surface Acoustic Waves in Inhomogeneous Media*. Berlin: Springer-Verlag, 1995.

[51] R. V. Goldstein and J. Lewandowski, "Surface roughness induced attenuation and changes in the propagation velocity of long Rayleigh-type waves," *Acta Mechanica*, vol. 91, pp. 235–243, 1992.

[52] B. W. Drinkwater and P. D. Wilcox, "Ultrasonic arrays for non-destructive evaluation: A review," *NDT & E International*, vol. 39, pp. 525–541, 2006.

[53] M. C. Remillieu *et al.*, "Review of air-coupled transduction for nondestructive testing and evaluation," *Acoustics Today*, vol. 10(3), pp. 36–45, 2014.

[54] D. A. Hutchins and A. Neild, *Ultrasonic Transducers*, ch. 12, pp. 374–407. Cambridge, UK: Woodhead Publishing Limited, 2012.

[55] Z. Sun *et al.*, "A methodological review of piezoelectric based acoustic wave generation and detection techniques for structural health monitoring," *International Journal of Aerospace Engineering*, vol. 2013, 2013. Article ID 928627, 22 pages.

[56] X. Chen *et al.*, "A laser-activated mems transducer for efficient generation of narrowband longitudinal ultrasonic waves," *IEEE Transactions on Ultrasonics,Ferroelectrics and Frequency Control*, vol. 58 (2), pp. 470–476, 2011.

[57] D. A. Hutchins *et al.*, "Air-coupled piezoelectric detection of laser-generated ultrasound," *IEEE Transactions on Ultrasonics,Ferroelectrics and Frequency Control*, vol. 41 (6), pp. 796–805, 1994.

[58] D. Cerniglia, K. Y. Jhang, and B. B. Djordjevic, "Non-contact ultrasonic testing of aircraft lap joints," in *Proceedings of the 15th WCNDT*, p. 161, 2000.

[59] D. A. Hutchins, "Pilsed lasers for quantitative ultrasonic NDE," *Review of Progress in Quantitative Nondestructive Evaluation*, vol. 11, pp. 561–568, 1992.

[60] S. Dixon *et al.*, "Detection of cracks in metal sheets using pulsed laser generated ultrasound and EMAT detection," *Ultrasonics*, vol. 51 (1), pp. 7–16, 2011.

[61] K. T. Wu *et al.*, "Integrated piezoelectric ultrasonic receivers on metals for laser generated ultrasound," in *1st International Symposium on Laser Ultrasonics: Science, Technology and Applications*, 2008.

[62] M. Kobayashi *et al.*, "High-temperature integrated and flexible ultrasonic transducers for nondestructive testing," *NDT & E International*, vol. 42 (2), pp. 157–161, 2009.

[63] C. J. L. Lane, "The inspection of curved components using flexible ultrasonic arrays and shape sensing fibres," *Case Studies in Nondestructive Testing and Evaluation*, vol. 1, pp. 13–18, 2014.

[64] J. Shih *et al.*, "Applications of flexible ultrasonic transducer array for defect detection at 150°," *Sensors*, vol. 13, pp. 975–983, 2013.

[65] C. R. Bowen *et al.*, "Flexible piezoelectric transducer for ultrasonic inspection of non-planar components," *Ultrasonics*, vol. 48, pp. 367–375, 2008.

[66] Y. Y. Kim and Y. E. Kwon, "Review of magnetostrictive patch transducers and applications in ultrasonic nondestructive testing of waveguides," *Ultrasonics*, vol. 62, pp. 3–19, 2015.

[67] J. W. Wagner, "Breaking the sensitivity barrier: the challenge for laser-ultrasonics," in *IEEE Ultrasonics Symopsium*, vol. 2, pp. 791–800, 1992.

[68] J. P. Monchalin, "Laser ultrasonics: from the laboratory to industry," in *AIP Conference Proceedings*, vol. 700 (3), pp. 3–31, 2004.

[69] C. K. Jen *et al.*, "NDE using laser generated ultrasound and integrated ultrasonic transducer receivers," in *IEEE International Ultrasonics Symposium Proceedings*, pp. 1516–1519, 2008.

[70] K. C. Baldwin, T. P. Berndt, and M. J. Ehrlich, "Narrowband laser generation/air-coupled detection: ultrasonic system for on-line process control of composites," *Ultrasonics*, vol. 37, pp. 329–334, 1999.

[71] R. J. Dewhurst *et al.*, "Quantitative measurements of laser-generated acoustic waveforms," *Journal of Applied Physics*, vol. 53, pp. 4064–4071, 1982.

[72] S. J. Davies *et al.*, "Laser-generated ultrasound: its properties, mechanisms and multifarious applications," *Journal of Physics D: Applied Physics*, vol. 26, no. 3, pp. 329–348, 1993.

[73] R. M. White, "Generation of elastic waves by transient surface heating," *Journal of Applied Physics*, vol. 34, pp. 3559–3567, 1963.

[74] V. V. Krylov, "Directivity patterns of laser-generated sound in solids: effects of optical and thermal parameters." arXiv:1402.6024 [physics.optics], 2014. https://dspace.lboro.ac.uk/2134/18519.

[75] J. D. Achenbach, "Simplifications for the calculation of surface wave pulses generated by laser-irradiation," *The Journal of Acoustical Society of America*, vol. 116, no. 3, pp. 1481–1487, 2004.

[76] A. M. Aindow, R. J. Dewhurst, and S. B. Palmer, "Laser-generation of directional surface acoustic wave pulses in metals," *Optics Communications*, vol. 42, no. 2, pp. 116–120, 1982.

[77] A. M. Aindow *et al.*, "Laser-generated ultrasonic pulses at free metal surfaces," *Journal of the Acoustical Society of America*, vol. 69, no. 2, pp. 449–455, 1981.

[78] S. Kenderian, B. B. Djordjevic, and R. E. Green, "Sensitivity of point- and line-source laser-generated acoustic wave to surface flaws," *IEEE Transactions on Ultrasonics,Ferroelectrics and Frequency Control*, vol. 50, no. 8, pp. 1057–1064, 2003.

[79] C. Chenu, D. Royer, and M. Fink, "Defect detection by surface acoustic waves generated by a multiple beam laser," in *Ultrasonics Symposium 1995, IEEE Proceedings*, vol. 1, pp. 821–824, 1995.

[80] C. I. Swift, S. G. Pierce, and B. Culshaw, "Generation of a steerable ultrasonic beam using a phased array of low power semiconductor laser sources and fiber optic delivery," *Smart Materials and Structures*, vol. 16, pp. 728–732, 2007.

[81] P. Cielo and C. K. Jen, "Laser generation of convergent acoustic waves and applications to materials evaluation," in *Ultrasonics Symposium 1986, IEEE Proceedings*, pp. 515–526, 1986.

[82] C. K. Jen *et al.*, "Laser generation of annular converging surface acoustic waves," in *Ultrasonics Symposium 1984, IEEE Proceedings*, pp. 660–665, 1984.

[83] M. Liu *et al.*, "Noncontacting optical-generation of focused surface acoustic waves using a customized zoneplate," *Electronics Letters*, vol. 31, no. 4, pp. 264–265, 1995.

[84] M. Clark, S. D. Sharples, and M. G. Somekh, "Noncontact continuous wavefront/diffractive acoustic elements for rayleigh wave control," *Applied Physics Letters*, vol. 74, no. 24, pp. 3604–3606, 1999.

[85] R. E. Lee and R. M. White, "Excitation of surface elastic waves by transient surface heating," *Applied Physics Letters*, vol. 12, no. 1, pp. 12–14, 1968.

[86] G. Cachier, "Optical excitation of highamplitude surface waves," *Applied Physics Letters*, vol. 17, no. 10, pp. 419–421, 1970.

[87] S. K. J Huang and J. D. Achenbach, "Laser-generation of narrow-band surface waves," in *Ultrasonics Symposium 1991, IEEE Proceedings*, vol. 1, pp. 537–541, 1991.

[88] F. L. di Scalea *et al.*, "Advances in optical methods for non-contact nondestructive evaluation," in *AIP Conference Proceedings*, vol. 497, pp. 149–155, 1999.

[89] Y. H. Berthelot and J. Jarzynski, "Directional laser generation and detection of ultrasound with arrays of optical fibers," *Review of Progress in Quantitative Nondestructive Evaluation*, vol. 9, pp. 463–470, 1990.

[90] J. S. Yang *et al.*, "Laser phased array generated ultrasound for nondestructive evaluation of ceramic materials," *Journal of Nondestructive Evaluation*, vol. 16, no. 1, pp. 1–9, 1997.

[91] M. H. Noroy, D. Royer, and M. Fink, "The laser-generated ultrasonic phased array: analysis and experiments," *Journal of Acoustical Society of America*, vol. 94, no. 4, pp. 1934–1943, 1993.

[92] A. D. W. McKie *et al.*, "Laser generation of narrow-band and directed ultrasound," *Ultrasonics*, vol. 27, no. 6, pp. 323–330, 1989.

[93] J. W. Wagner *et al.*, "Modulated laser array sources for generation of narrowband and directed ultrasound," *Journal of Nondestructive Evaluation*, vol. 9, no. 4, pp. 263–270, 1990.

[94] T. W. Murray, M. Marince, and J. W. Wagner, "Narrow-band and directed ultrasound generated by laser arrays," in *Ultrasonics Symposium 1993, IEEE Proceedings*, pp. 623–626, 1993.

[95] T. W. Murray, J. B. D. Jr, and J. W. Wagner, "Experimental evaluation of enhanced generation of ultrasonic waves using an array of laser sources," *Ultrasonics*, vol. 34, pp. 69–77, 1996.

[96] C. U. R Pierce and J. Jarzynski, "Temporal modulation of a laser source for the generation of ultrasonic waves," *Ultrasonics*, vol. 33, no. 2, pp. 133–137, 1995.

[97] D. Royer and E. Dieulesaint, *Elastic Waves in Solids II - Generation, Acousto-optic Interaction, Applications*. New York: Springer, 1999.

[98] F. L. di Scalea *et al.*, "Remote laser generation of narrow-band surface waves through optical fibers," *Transactions on Ultrasonics, Ferroelectrics, and Frequency Control*, vol. 46, no. 6, pp. 1551–1557, 1999.

[99] M. Clark *et al.*, "Frequency control in laser ultrasound with computer generated holography," *Applied Physics Letters*, vol. 72, no. 16, pp. 1963–1965, 1998.

[100] H. N. A Harata and T. Sawada, "Laserinduced surface acoustic waves and photothermal surface gratings generated by crossing two pulsed laser beams," *Applied Physics Letters*, vol. 57, no. 2, p. 132, 1990.

[101] H. Nishino *et al.*, "Excitation of high frequency surface acoustic waves by phase velocity scanning of a laser interference fringe," *Applied Physics Letters*, vol. 62, no. 17, p. 2036, 1993.

[102] R. E. Lee and D. W. Jackson, "An optical detector based on surface-acoustic-wave generation," in *Ultrasonics Symposium 1975, IEEE Proceedings*, pp. 126–129, 1975.

[103] B. Bonello *et al.*, "Surface acoustic waves in the GHz range generated by periodically patterned metalic stripes illuminated by an ultrashort laser pulse," *Journal of Acoustical Society of America*, vol. 110, no. 4, pp. 1943–1949, 2001.

[104] A. Arca *et al.*, "CHOTs optical transducers," *Nondestructive Testing and Evaluation*, vol. 26, no. 4, pp. 353–366, 2011.

[105] T. Stratoudaki *et al.*, "Cheap optical transducers (CHOTs) for generation and detection of longitudinal waves," in *IEEE Proceedings*, vol. 18, pp. 961–964, 2012.

[106] J. A. Fox, "Effect of water and paint coatings on laser-irradiated targets," *Applied Physica Letters*, vol. 24, no. 10, pp. 461–464, 1974.

[107] J. W. Wagner, "Optical detection of ultrasound," *Physical Acoustics*, vol. 19, pp. 201–266, 1990.

[108] R. J. Dewhurst and Q. Shan, "Optical remote measurement of ultrasound," *Measurement Science and Technology*, vol. 10, pp. R139–R168, 1999.

[109] J. P. Monchalin, "Optical detection of ultrasound," *Transactions on Ultrasonics, Ferroelectrics, and Frequency Control*, vol. 33, no. 5, pp. 485–499, 1986.

[110] A. S. Murfin *et al.*, "Laser-ultrasound detection systems: a comparative study with Rayleigh waves," *Mesurement Science and Technology*, vol. 11, pp. 1208–1219, 2000.

[111] A. Korpel, L. J. Laub, and H. C. Sievering, "Measurement of acoustic surface wave propagation characteristics by reflected light," *Applied Physics Letters*, vol. 10, no. 10, pp. 295–297, 1967.

[112] G. I. Stegeman, "Optical probing of surface waves and surface wave devices," *IEEE Transactions on Sonics and Ultrasonics*, vol. SU-23, no. 1, pp. 33–63, 1976.

[113] T. W. Murray, H. Tuovinen, and S. Krishnaswamy, "Adaptive optical array receivers for detection of surface acoustic waves," *Applied Optics*, vol. 39, no. 19, pp. 3276–3284, 2000.

[114] . Solgaard, E. S. A. Sandejas, and D. M. Bloom, "Deformable grating optical modulator," *Optics Letters*, vol. 17, no. 9, pp. 688–690, 1992.

[115] N. A. Hall *et al.*, "Capacitive micromachined ultrasonic transducers with diffraction-based integrated optical displacement detection," *IEEE Transactions on Ultrasonics,Ferroelectrics and Frequency Control*, vol. 50, no. 11, pp. 1570–1580, 2003.

[116] B. Culshaw *et al.*, "The detection of ultrasound using fiber-optic sensors," *IEEE Sensors Journal*, vol. 8, no. 7, pp. 1360–1367, 2008.

[117] A. J. A. Bruinsma and J. A. Vogel, "Ultrasonic noncontact inspection system with optical fiber methods," *Applied Optics*, vol. 27, no. 22, pp. 4690–4695, 1988.

[118] H. Nakano and S. Nagai, "Crack measurements by laser ultrasonic at high temperatures," *Japan Journal of Applied Physics*, vol. 32, pp. 2540–2542, 1993.

[119] A. S. B Mitra and D. J. Booth, "An optical fibre interferometer for remote detection of laser generated ultrasonics," *Measurement Science and Technology*, vol. 9, pp. 1432–1436, 1998.

[120] J. E. Bowers *et al.*, "An all fiber-optic sensor for surface acoustic wave measurements," *Journal of Lightwave Technology*, vol. LT-1, no. 2, pp. 429–436, 1983.

[121] I. Pelivanov *et al.*, "A new fibre-optic non-contact compact laser-ultrasound scanner for fast non-destructive testing and evaluation of aircraft composites," *Journal of Applied Physics*, vol. 115, p. 113105, 2014.

[122] H. C. Wang, S. Fleming, and Y. C. Lee, "A remote, non-destructive laser ultrasonic material evaluation system with simplified optical fibre interferometer detection," *Journal of Nondestructive Evaluation*, vol. 28, pp. 75–83, 2009.

[123] S. G. Pierce, R. E. Corbett, and R. J. Dewhurst, "An actively-stabilised fibre-optic interferometer for laser-ultrasonic flaw detection," *Review of Progress in Quantitative Nondestructive Evaluation,*, vol. 12, pp. 587–593, 1993.

[124] K. A. Murphy *et al.*, "Miniaturized fiber-optic Michelson-type interferometric sensors," *Applied Optics*, vol. 30, no. 34, pp. 5063–5067, 1999.

[125] P. C. Beard and T. N. Mills, "Extrinsic optical-fiber ultrasound sensor using a thin polymer film as a low-finesse FabryPerot interferometer," *Applied Optics*, vol. 35, no. 4, pp. 663–675, 1996.

[126] T. Stratoudaki *et al.*, "How to make optically excitable Cheap Optical Transducers (CHOTs): Fabrication methods.." Submitted to Sensors, 2015.

[127] I. J. Collison *et al.*, "Measurement of elastic nonlinearity using remote laser ultrasonics and CHeap Optical Transducers and dual frequency surface acoustic waves.," *Ultrasonics*, vol. 48, no. 6-7, pp. 471–477, 2008.

[128] A. Arca *et al.*, "Evanescent CHOTs for the optical generation and detection of ultrahigh frequency SAWs," *Journal of Physics: Conference Series*, vol. 269, p. 012012, 2011.

[129] H. N. Lin *et al.*, "Study of vibrational modes of gold nanostructures by picosecond ultrasonics," *Journal of Applied Physics*, vol. 73, pp. 37–45, 1993.

[130] D. H. Hurley and K. L. Telschow, "Picosecond surface acoustic waves using a suboptical wavelength absorption grating," *Physical Review B*, vol. 66, p. 153301, 2002.

[131] G. A. Antonelli, P. Zannitto, and H. J. Maris, "New method for the generation of surface acoustic waves of high frequency," *Physica B*, vol. 316-317, pp. 377–379, 2002.

[132] M. Siemens *et al.*, "EUV detection of high-frequency surface acoustic waves," in *Lasers and Electro-Optics, 2009 and 2009 Conference on Quantum electronics and Laser Science Conference. CLEO/QELS 2009.*, pp. 1–2, 2009.

[133] D. H. Hurley, "Optical generation and spatially distinct interferometric detection of ultrahigh frequency surface acoustic waves," *Applied Physics Letters*, vol. 88, p. 191106, 2006.

[134] M. Ohring, *The Materials Science of Thin Films*. London,UK: Academic Pressr, 1992.

[135] C. K. Charalambos and D. I. Siapkas, "General transfer-matrix method for optical multilayer systems with coherent, partially coherent, and incoherent interference," *Applied Optics*, vol. 41, no. 19, pp. 3978–3987, 2002.

[136] S. Uma *et al.*, "Elastomer-based diffractive optical modulator," *IEEE Journal of Selected Topics in Quantum Electronics*, vol. 10, no. 3, 2004.

[137] O. Solgaard, *Photonic Mycrosystems: Micro and Nanotechnology Applied to Optical Devices and Systems.* New York: Springer, 2009.

[138] J. A. Rogers *et al.*, "Elastomeric binary phase gratings for measuring acceleration, displacement, strain, and stress," *Review of Scientific Instrumentation*, vol. 67, no. 9, pp. 3310–3319, 1996.

[139] J. W. Goodman, *Introduction to Fourier Optics.* New York: McGraw-Hill, 1988.

[140] C. A. Mack, *Fundamental Principles of Optical Lithography: The Science of Microfabrication.* Chichester, UK: John Wiley & Sons, 2007.

[141] F. J. Adrian *et al.*, "A study of the mechanism of metal deposition by the laser-induced forward transfer process," *Journal of Vacuum Science Technology B*, vol. 5, pp. 1490–1494, 1987.

[142] D. A. Willis and V. Grosu, "Microdroplet deposition by laser-induced forward transfer," *Applied Physics Letters*, vol. 86, p. 244103, 2005.

[143] Quorumtech, *Sputter coating technical brief.*

[144] L. Cheng *et al.*, "Releasing su-8 structures using polystyrene as a sacrificial material," *J.Sna A*, vol. 114, pp. 123–128, 2004.

[145] MicroChem, " SU-8 50-100 ."

[146] V. V. Krylov and T. V. Shtentsel, "Laser generation of sound in a layered solid medium," *Soviet Physics - Acoustics*, vol. 33, pp. 159–160, 1987.

[147] R. J. von Gutfeld and R. L. Melcher, "20-MHz acoustic waves from pulsed thermoelastic expansions of constrained surfaces," *Applied Physics Letters*, vol. 30, pp. 257–259, 1977.

[148] D. A. Hutchins, R. J. Dewhurst, and S. B. Palmer, "Laser generated ultrasound at modified metal surfaces," *Ultrasonics*, vol. 19, pp. 103–108, 1981.

[149] J. Wang *et al.*, "Influence of transparent coating thickness on thermoelastic force source and laser generated ultrasound waves," *Applied Surface Science*, vol. 255, pp. 7172–7178, 2009.

[150] J. P. Bently, *Principles of Measurement Systems.* England: Prentice Hall, 2005.

[151] S. A. Akhmanov and S. Y. Nikitin, *Physical Optics.* Oxford: Clarendon Press, 1997.

[152] J. A. Ogilvy, *Theory of wave scattering from random rough surfaces.* Bristol, UK: Adam Hilger, 1991.

[153] R. J. Smith *et al.*, "Spatially resolved acoustic spectroscopy for rapid imaging of material microstructure and grain orientation," *Mesurement Science and technology*, vol. 25, no. 5, p. 055902, 2014.